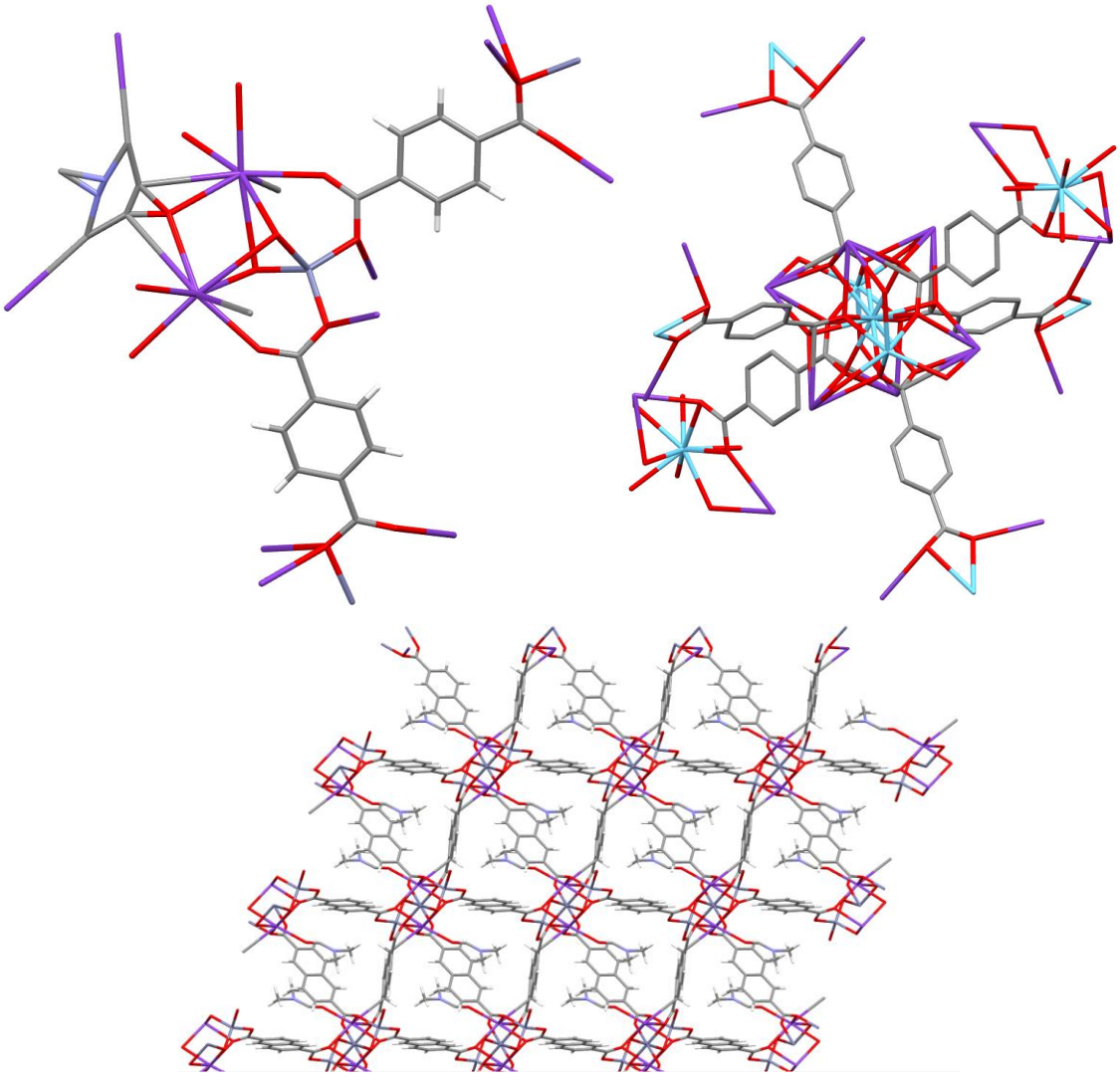
University of Nottingham
UK | CHINA | MALAYSIA



Olukayode Adedayo Babarinde

Adsorption Performance of Mixed Metal-Alkali Metal-Organic Frameworks

A thesis submitted to the University of Nottingham in fulfilment of the requirements for the Degree of Doctor of Philosophy

Olukayode Adedayo Babarinde, MSc

September 2023

Declaration

Apart from where specific reference is made to other sources, the work presented in this report is the original work of the author. It has not been submitted for any other degree either in whole or in part.

Signed: 

Date: 29/09/2023

Abstract

This work describes the solvothermal synthesis of zinc and lanthanum-based mixed metal-alkali metal-organic frameworks (MOF) with carboxylate linkers with benzene 1,4 dicarboxylic acid (H_2BDC), 1,3,5-tris(4-carboxyphenyl) benzene (BTB), and 2,6-Naphthalenedicarboxylic acid (H_2NDC). The successful synthesis of Zinc-Potassium (ZnKMOF), Zinc-Lithium (ZnLiMOF), and Lanthanum-Potassium (LaK) MOF was affirmed by several analytical techniques such as XRD, TGA, SEM, and EDX in this research. ZnKBTB MOF is a straightforward type 1 isotherm for Nitrogen and Hydrogen, indicating microporosity (width < 2nm) with a BET surface area around 200 $m^2 g^{-1}$ and pore volume ~ 0.17 cm^3. While ZnKBTB and ZnLiBTB displayed strong CO_2 adsorption capacity depicted by a concave curve at all temperature and relative pressure ranges, ZnKBDC and ZnKNDC MOFs displayed linear plot associated with Type III Isotherm indicating non-porosity for the adsorption of H_2, N_2 and CH_4 gases at both 273K and 298K. Interestingly, ZnKBDC and ZnKNDC MOFs showed minimal Type I adsorption (described by a lower concave curve) at 77 K. We then deduced that the adsorption in this experiment is dependent on the ligand employed and on the probability of pore channel blockage by the alkali metal in the MOF. The study of the trend in CO_2/N_2 selectivity shows that the higher the CO_2 adsorption capacity in both ZnKBTB and ZnLiBTB MOFs, the lower the CO_2/N_2 selectivity because ZnLiBTB possesses higher CO_2/N_2 selectivity of 32.32 while ZnKBTB was 24.13 at 800 mmHg and 298 K. Therefore, the adsorption capacity for CO_2 increased in the order of $K^+ > Li^+$. The heat of adsorption, $Q_{st,}$ falls in a range of 30.83 to 19.85 kJ/mol at high loading conditions (ZnKBTB; 34.38 - 30.83 $kJmol^{-1}$ and ZnLiBTB; 29.17 $kJmol^{-1}$ – 19.85 $kJmol^{-1}$), thus exhibiting our MOFs with features favouring high loading of CO_2 at low pressure and high heat of adsorptions, which are comparable to values attained by MOFs having open metal sites. The isosteric heat for CO_2 on LaKBDC MOF shows that the carbon dioxide adsorption (CO_2) on LaKBDC MOF exhibits a decreasing trend with higher uptake (thus higher pressure); this is common to all potassium-based MOFs studied. Selectivity studies show LaKBDC showed similar selectivity for CO_2/N_2 and CO_2/H_2 around 13.9 while displaying higher selectivity for CO_2/CH_4, thus predicting its useful separation potential for CO_2/CH_4.

Acknowledgments

I like to express my profound gratitude to Prof. Neil Robert Champness for supervising this research and for all his encouragement, staunch support, guidance and understanding during this research. You are indeed a true research leader and mentor to me, thanks for your huge contributions to my career. I am also very grateful to Prof. David Amabilino, Dr Matthew Cliffe and Dr Debbie Kays for accepting the role of my supervisor after Prof. Neil Champness left the University of Nottingham. I am grateful to my financial sponsors, Tertiary Education Trust Fund, TETFund Nigeria, Nigerian Defence Academy, and my employer, Nigerian Army Education Corps, Nigerian Army, and Nigerian Armed Forces, for releasing me to embark on this PhD programme. A special appreciation to my mentors, Colonel (Dr) A. Olayiwola (Rtd), Major General I.M. Jallo, Major General S.Z. Kazaure, Major General (Assoc. Prof) S. Ibrahim, Captain (Prof) D.K. Garba (Rtd), and Brigadier General O.A. Fadairo, I acknowledge your huge support and contribution to my PhD journey. I am eternally grateful for inspirational leadership daily raising higher goals for me to achieve. Thanks to Prof. (Mrs) A.O. Aliyu, Prof. D.M. Faruruwa and the Chemistry department at Nigerian Defence Academy, Kaduna, for your encouragement and support before and during this programme. I am very grateful to Defence Attache, Nigerian High Commission London, headed by Major General Baffa, for all the administrative support I enjoyed during this study. I will not forget the huge support of the entire Champness group of B52. The collaborative effort to get things done rightly in B52 was laudable. I commend the huge support of postdoctoral researchers in the Champness group, especially Dr Nicholas Pearce, Dr Georgia Orton and Dr Sarah Griffin. You are all simply the best; what a great time in the busy laboratory environment despite the disruption by covid - 19 pandemic. To my fellow researchers Dr Joseph Ogar, Dr Nathan Anderson, Dr Rosemary Young, Dr Arjun l, Dr Mark, Marysia, Alex, Asia, Claire, Jen and Musa thanks for all the cakes and play times together. Ferdinando, thanks for supplying DPP ligands. I am truly grateful to you all. So many thanks to Dr David Madden (University of Cambridge) and Leo Scott Blankenship (Mokaya Group, University of Nottingham) for helping with the gas adsorption studies, Dr Stephen Argent for helping with crystallography and Dr Richard Cousins for the Scanning Electron Microscopy (SEM) with Energy Dispersive X-Ray Analysis (EDX) analysis. Also, thanks to all the technical staff at Nottingham: Shazad Aslam, Kevin Butler, Mark Guyler and Ben Pointer-Gleadhill for their help with NMR and mass spectrometry and Tong Liu for the elemental analysis. I can't help but appreciate the support of my family: my darling wife, Bukoye, daughter, Moyosooreoluwa and sons Monifeooreoluwa, Monjolaooreoluwa, and the twins, Mojibolaooreoluwa and Mojijolaooreoluwa. Special thanks to my parents and the entire Mr & Mrs Adeleke and Ruth Babarinde, Elder & Mrs Olusayo, and Titilayo Oyerinde families for your care and understanding throughout this programme. I love you all. You are all pillars of support and encouragement through this journey. All Glory to my Lord Jesus Christ God, Almighty, the giver of life. To him alone be the glory and honour forever.

List of Symbols and Abbreviations

BDC	Terephthalic acid (Benzene dicarboxylic acid)
BET	Brunauer-Emmet-Teller
BTB	1,3,5-Tris(4-carboxyphenyl)benzene
a	Unit cell parameter
b	Unit cell parameter
3D	Three-dimensional
c	Unit cell parameter
CHN	Carbon, Hydrogen and Nitrogen analysis
CP	Coordination Polymer
DMF	N, N- Dimethylformamide
DMSO	Dimethylsulfoxide
DEF	N,N-Diethylformamide
EPR	Electron Paramagnetic Resonance
ESI	Electrospray Ionisation
EDX	Energy dispersive X-ray spectroscopy
et al.	and others
HKUST-1	Hong Kong University of Science and Technology Structure –
H_2NDC	2,6-Naphthalenedicarboxylic acid
IR	Infrared
IRMOF	Isoreticular MOF
IUPAC	International Union of Pure and Applied Chemistry
MeOH	Methanol
MIL	Materials of Institut Lavoisier
MOF	Metal-Organic Framework
MM-MOF	Mixed metal MOF
MALDI	Matrix Assisted Laser Desorption Ionisation
MS	Mass Spectrometry
MTV	Multivariant MOF

NDI	Naphthalene Dimide
NH_2-BDC	2-Aminoterephthalic acid
NMR	Nuclear magnetic resonance
ODT	Optimum degradation temperature
PSM	Post-synthetic modification
PXRD	Powder X-ray diffraction
SALE	Solvent-assisted linker exchange
SEM	Scanning electron microscopy
SBU	Secondary Building Unit
SXRD	Single-crystal X-ray diffraction
TGA	Thermogravimetric analysis
UTSA	University of Texas at San Antonio

CONTENTS

Chapter 1: General introduction and Objectives 1

1.1 General introduction 1

1.2 Synthesis of Metal-Organic Frameworks 3

1.2.1 The Design strategies of MOF 3

1.2.2 Synthetic Strategies towards mixed-metal MOFs 4

1.2.3 Direct synthesis approach or one-pot reaction for Mixed Metal MOF…...5

1.2.4 Synthesis of MM MOFs using post-synthetic exchange 6

1.2.5 The Carboxylate linkers and Nitrogen donor linkers 7

1.2.6. Methods of crystallization 12

1.2.7. Electrochemical Synthesis 17

1.2.8 Mechanochemical Synthesis 18

1.2.9 Sonochemical Synthesis 20

1.2.10 Microwave assisted synthesis 21

1.2.11 Purification and activation Strategies 22

1.3 Application of MOFs in catalysis, gas storage, organic electronic and photovoltaic devices ..... .23

1.3.1 Catalysis ..... .23

1.3.2 Gas Adsorption……26

1.3.2.1 Gas adsorption applications……27

1.3.2.2 Hydrogen adsorption……27

1.3.2.3 Sensing……..28

1.4 Aims and Objectives……31

1.5 References……..…….33

Chapter 2: Characterization techniques 45

2.0. Reagents and Purification..... 45
2.1 General Synthesis of Mixed-Metal Metal-Organic Framework..... 45
2.2. X-ray Diffraction (XRD) 46
2.3 Scanning Electron Microscopy with Energy Dispersive X-Ray Analysis (EDX) 47
2.4 Elemental Analysis (EA)…….47
2.5 Infrared Spectroscopy (FTIR)……47
2.6 Gas adsorption..... 47
2.7 Determination of Surface area and porosity……50
2.8 An Ideal Adsorbed Solution Theory (IAST) Method for Gas Separation Study ……...51
2.9 Isosteric heat of adsorption, Qst 51
2.10 Thermogravimetric Analysis (TGA)……..57
2.11 References 59
Chapter 3: Synthesis of Zinc/Alkali Metal-Organic Frameworks..... 62
3.0 Introduction..... 62
3.1 Experimental..... 65
3.1.1 Reagents 65
3.2 Synthesis of Mixed-Metal Organic Frameworks ZnKBDC 65
3.2.1 Synthesis of ZnKBDC MOF..... 65
3.2.2 Synthesis of ZnKNDC MOF 66
3.2.3 Synthesis of ZnKBTB MOF 67
3.3 XRD Analysis..... 67
3.3.1 PXRD Analysis……..72
3.3.2 TGA Analysis……74
3.3.3 Scanning Electron Microscopy (SEM) / Energy Dispersive X-Ray Analysis (EDX)……..……..77

3.4 FTIR Spectroscopy……...79

3.5 Zinc Lithium MOF System……..……..83

3.6 PXRD Analysis of ZnLiBDC and ZnLiNDC…….90

3.7 SEM/EDX Analysis of ZnLiMOFs…….92

3.8 Conclusion and further studies…….94

3.9 References 96

Chapter 4: Gas Adsorption and Separation Studies of Novel Bimetallic Metal Organic Frameworks synthesized from Zinc and Alkali Metal (Potassium and Lithium) 99

4.1 Introduction 99

4.2 Hydrogen Adsorption Studies 101

4.3 Oxygen Adsorption Studies 103

4.4 Brunauer–Emmett–Teller (BET) Surface Area Analysis 104

4.5 Carbon dioxide (CO_2) adsorption properties of ZnKMOF and ZnLiMOF System……..107

4.6. N_2 Adsorption Studies 109

4.7 The Isosteric Heat of Adsorption, Q_{st} ZnKBTB and ZnLiBTB 111

4.8 Ideal adsorbed solution theory (IAST) ZnKBTB and ZnLiBTB MOFs..... 113

4.9 Comparative Studies with other Mixed Metal – Alkali Metal-Organic Framework..... 116

4.10 Conclusion…….119

4.11 References……121

Chapter 5: Adsorption Studies of Lanthanum/Alkali Metal-Organic Frameworks……124

5.0 Introduction 124

5.1 Experimental 125

5.1.0 Materials 125

5.1.1 Attempt to Synthesis of LaKNDC MOF……126
5.1.2 Attempt to Synthesis of LaKBTB MOF……126
5.1.3 Attempt to Synthesis of LaLiBDC MOF……129
5.1.4 Attempt to Synthesis of LaLiNDC MOF……..131
5.1.5 Attempt to Synthesis of LaLiBTB MOF……...133
5.1.6 Synthesis of LaKBDC MOF……135
5.2.0 Results and Discussions……136
5.2.1 PXRD Analysis of LaKBDC MOF……..136
5.2.2 FTIR and TGA analysis……..141
5.2.3 SEM/EDX Analysis of LaKBDC MOF……...142
5.3 Gas Adsorption Studies……..146
5.3.1 CO_2, N_2, CH_4 and H_2 Adsorption Isotherms for LaKBDC at 273 K and 298 K of LaKBDC MOF……..147
5.3.2 Isosteric heat for CO_2 on LaKBDC……147
5.3.3 Ideal Adsorbed Solution Theory (IAST)……148
5.3.4 Comparative Studies of LaKMOF with other Mixed Metal – Alkali Metal-Organic Framework 149
5.4 Conclusion 153
5.4 References 155
Chapter 6: Conclusions and Future Directions 157
References…… 160
Appendix…… 161

Chapter 1: General Introduction and Objectives

1.1 General Introduction

Metal-organic frameworks (MOFs), or porous coordination polymers (PCPs), are constructed from inorganic nodes with organic linkers that generate framework structures with large internal surface areas (Figure 1.1). They have emerged as a promising class of materials possessing high porosity, diverse composition, and tuneable pore structures.[1-3] Metal-Organic Frameworks (MOFs) are hybrid microporous materials with inorganic unsaturated metal nodes coordinated with organic linkers.[1-3] Due to their large pore volume and adequate surface areas, MOFs have displayed high efficiency as nanomaterials, finding usage in different industrial technologies such as sensing, biomedicine, catalytic, gas storage, energy, luminescence[9] and sequestration applications.[3-9]

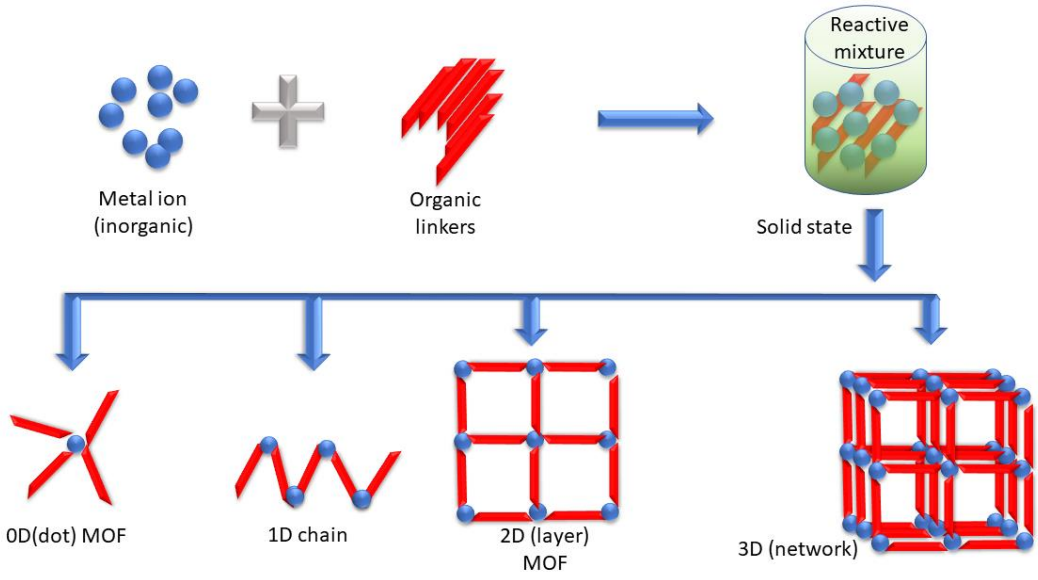


Figure 1.1: Building blocks of metal-organic framework[1]

The history of MOF synthesis dates back to 1965 when Tomic reported a set of coordination polymers made using di- and tetratopic carboxylic acid linkers coordinated to di-, tri-, or tetravalent metals.[7,8] It was found that the polymer properties, such as the thermal stability, correlate with the valency of the coordinated metal and the number of potential coordination sites on the linker of the polymers.[8] The group of

compounds/materials possessing this set of properties were later named 'metal−organic frameworks' (MOFs).

About 25 years after Tomic's report, Hoskins and Robson[9] hypothesized that a wide range of scaffold-like materials with infinite 3D frameworks should be tuneable and accessible with additional potential for industrial applications.[9] They suggested that despite possessing large empty cavities and low densities, the materials should remain open and accessible while maintaining high thermal, chemical, and mechanical stability. In addition, potential applications such as molecular sieving, ion exchange, and catalysis were predicted. A few years later, Yaghi et al.[10] named these compounds metal−organic frameworks (MOFs) when they used the hydrothermal synthesis method to obtain a 3D crystalline and open material.[10] In 1997, Kitagawa *et al*.[11] reported the first application of MOFs for methane gas storage. This was immediately followed by Yaghi *et al*.[10] widely reported MOF-5 synthesis as a framework that also displayed permanent porosity (demonstrated in Kitagawa's paper) without structural collapse when guest solvent molecules were evacuated from its pores.[12]

With this new development comes computational chemistry predictions and rational design by Ferey *et al*.[13], which guided the synthesis of a highly stable MOF with very large pores (30−34 Å) and high surface area.[13] This fascinating development in MOF research has given birth to thousands of MOF structures in the Cambridge Structural Database, including frameworks with densities as low as 0.13 g/cm^3, [14] pore volumes up to 90% free volume,[15] and Brunauer− Emmett−Teller (BET) areas greater than 6000 m^2/g.[15-17]

To date, endless varieties of MOF structures are still being hypothesized, designed, and constructed from a combination of a variety of metal clusters or ions (as inorganic nodes) and organic linkers using different successful methods while still exploring wide applications in industry, environment, and daily life issues. A huge variety of potential applications are being researched daily due to the highly modular and tuneable nature of MOFs. However, applications have been reported in catalysis,[18-20] gas storage and separation,[20,21] water,[22,23] chemical separations,[24,25] drug delivery,[26,27] light harvesting and energy conversion,[28] chemical sensing,[29],[30,] air pollution control,[22,23] conductivity,[31] the degradation of chemical warfare agents[32,33] and ion-exchange.[7,33,34]

1.2 Synthesis of Metal-Organic Frameworks

There are a wide variety of methods that have been used to synthesize MOFs[35,36] Generally, the conditions for MOF synthesis should be chosen so that metal−ligand bond formation and breaking allow for structure propagation. Dynamic bonds are key to forming crystalline and ordered materials so that any erroneous bonding that may cause disorder or premature structure termination can be corrected. Common methods used here include traditional synthesis (solvothermal and non-solvothermal), electrochemical synthesis, microwave-assisted synthesis, mechanochemical synthesis, green synthesis and sonochemical synthesis.[7,8,35,36] Some MOFs are difficult to synthesize anew, therefore various post-synthetic methods designed include post-synthetic modification (PSM),[37] solvent-assisted linker exchange (SALE),[38] and transmetalation.[39]

1.2.1 The Design strategies of MOF

The modular nature of MOFs allows for great synthetic tunability, offering fine chemical and structural control. The creativity in synthetic design makes MOFs exhibit properties such as conductivity, stability, porosity and particle morphology that can be designed for applications.[7] Hence, MOF materials possess tuneable pore sizes, structure diversity, and other advantages. The chemist is meant to understand the physicochemical properties of both organic linker and metal nodes, which will enhance their combination in the suitable reaction solvent. The target properties of the resulting MOF direct the selection of the right reaction routes to obtain MOF structures for specific applications. At the early stage of MOFs' synthesis, direct assembly of new MOFs from metal nodes and organic linkers was the main approach, with early publications describing the coordination characteristics of the first-row transition metals such as Zn, Cu and Co with carboxylate groups under hydrothermal and solvothermal conditions to form exciting crystals. However, as science develops, many more techniques are still unfolding based on the properties of the organic linker, the metal nodes, the anticipated physicochemical properties as well as the potential applications of the resulting MOF system.[7,40]

1.2.2 Synthetic Strategies towards mixed-metal MOFs

Bu *et al*.[41] described the metal-ligand bond existing within the monometallic MOFs ‘’as a simple Lewis acid (metal ion node)–Lewis base (ligand) interaction’’.[40,41] This strong bond ensures the stability of monometallic MOFs against hydrolysis, especially in water. The ligands are typically O or N-donors. Commonly used O-donor Ligands are carboxylates. To achieve carboxylate interactions, metals with high charges (typically M^{3+} or M^{4+}) will form strong Lewis acids that will bond with the strong COO^- Lewis base. As for the linker, a higher stability is obtained if the pK_a of the ligand is increased. This strategy was introduced by Jeffrey Long and his group, who synthesized a pyrazolate MOF (pKa = 19.8).[42] The famous ZIFs (zeolitic imidazole frameworks) rely on the same principle, the imidazolate having a pKa of 18.6.[41]

Leus *et al*.[40] and Hambley *et al*.[42,43] worked on studying the nature of metal–ligand covalency from the bonding in carboxylate ligands. They asserted that the fraction of covalency increases as the oxidation state of the metal cation increases.[43] Hence, metals with higher oxidation states create more stable mixed MOFs. The oxidation state of the participating metals must be determined to ascertain overall charge balance and MOF stability after synthesis. The reaction must be designed to allow metal substitution/replacement (doping) with a more acidic metal ion to achieve the stability of the final product. Also, metal substitution with a lower valent ion will cause a charge deficit that exchangeable cations must balance.[40]

In addition, the size (ionic radius) of the different cations is related to their preference to occur in certain anion coordination[44,45] helps predict the stability of crystalline phases. The stability of the MOF structure is controlled by the solvent molecules residing within the MOF cavities. Also, the pressure generated within the synthesis reactor is an important parameter in the crystallization of MOFs. Scholars agreed that understanding the thermodynamics and kinetics of MM MOF formation, though still not been well explained, would be highly advantageous to MOF chemistry.[40,46]

1.2.3 Direct synthesis approach or one-pot reaction for Mixed Metal MOF (MM MOF)

MOF synthesis by direct synthesis is reported to be unpredictable in many ways. However, the main aim of a one-pot reaction for MM-MOF is to help produce MM MOFs in a simply controlled synthesis such that the introduced metal cations should

react concurrently to allow controlled incorporation as well as prevent the formation of single cation frameworks (which is not the desired product). This synthesis method was demonstrated by Serre *et al*.[47] when a direct synthesis obtained the bimetallic MIL-53(Cr/Fe) framework. In their research, a less reactive Fe^0 was introduced to slow down the reaction of iron components and allow a controlled introduction of metals Fe^{3+} (labile) and Cr^{3+} (inert) by controlling the reactivity of the metal ions.[40,47]

Another direct synthesis strategy used to obtain bimetallic MIL-127 materials;[48] was the control of metal ratio to obtain the proposed structure in a method termed as secondary building unit approach (SBU). All the mixed MOF-74 materials were prepared by a one-pot solvothermal synthesis, varying the effects of solvent and temperature of the reaction. The literature further suggested that while the impact of the temperature was more pronounced as it hugely influences the nucleation and the crystal growth, the solvent only had a minimal influence on the introduced cations.[49]

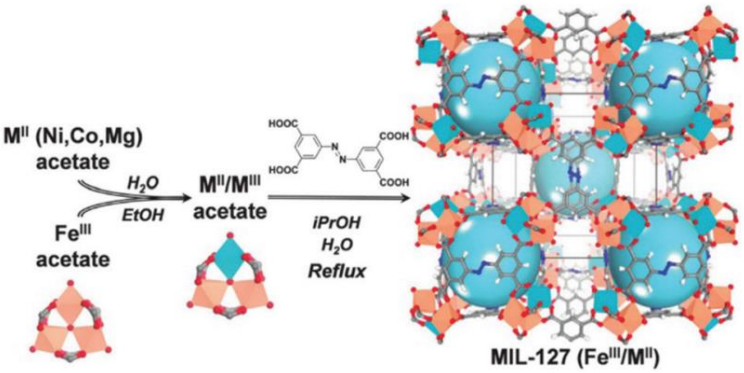


Figure 1.2: Schematic representation of the SBU approach for the synthesis of mixed-metal MIL-127.[48]

In most cases, 2 metal ions are mixed in one SBU to create bimetallic MOFs (Figure 1.2). However, Yaghi and co-workers demonstrated that up to 10 divalent metals could be included in one structure in a system termed multivariate MOF shown in Figure 1.3.[50]

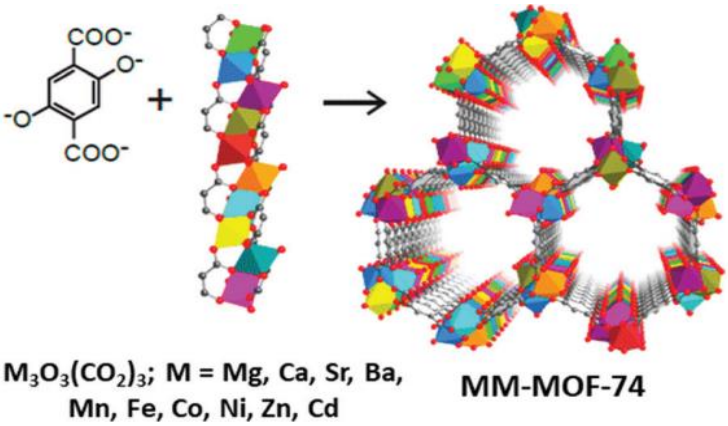


Figure 1.3: Multivariate MOF-74 materials having up to 10 various metals within their structure.[50]

1.2.4 Synthesis of MM MOFs using the post-synthetic exchange

The post-synthetic exchange method enables the synthesis of mixed-metal MOFs that are impossible through a direct synthesis approach. More reports on post-synthetic modifications succeeded in synthesizing mixed-linkers MOF than the metal ion exchange to synthesize MM-MOFs. The transmetallation or exchange of the metal nodes typically proceeds by immersing the MOF in a metal ion solution, typically nitrates or chlorides, for several days at room or elevated temperatures to have an (incomplete) transmetallation.[7]

Lah *et al*.[51] identified factors that influenced the kinetics and the thermodynamics of the metal exchange process, including the choice of solvent, the concentration of the metal ion solution and the exchange temperature. The team synthesized the Zn analogue of HKUST-1 in which Cu2+ ions replaced the Zn^{2+} ions by soaking HKUST-1 into a methanolic solution of $Cu(NO_3)_2.2.5H_2O$ at ambient temperature. They concluded that metal centres connected via a flexible organic linker are more reactive than those linked to a rigid organic linker. The post-synthetic exchange strategy has also introduced redox-active di- and trivalent first-row transition metals into MOFs. In general, the post-synthetic exchange of metal ions has synthesized mixed–metal MOFs from less stable MOFs that have labile metal-ligand bonds, ‘‘inert’’, chemically and thermally stable robust MOFs[51] like UiO, MIL and ZIF-based materials [52]

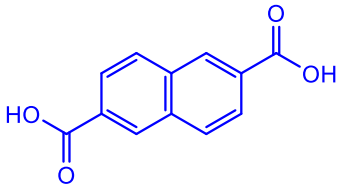
Additionally, cation exchange via post-synthetic strategies was associated with some demerits, which included high contact times and the unpredictability of the exchange rate, especially using the immersion period.[40] Long et al.53 utilized a microwave-

assisted method to mitigate these demerits to prepare MM-MOFs via the post-synthetic method. In that study, UiO-66 was selected to introduce Ti^{4+}. Hence, the Titanium, Ti metal salt, $TiCp_2Cl_2$, and UiO-66 were combined in DMF, after which the mixture was transferred into a microwave reactor and kept at 120 ^oC for 4 hours to synthesize the envisaged UiO-66(Ti/Zr) MM MOF material.[53,56]

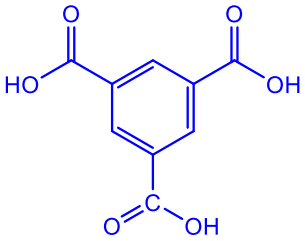
1.2.5 The Carboxylate linkers and Nitrogen donor linkers

The structure and physical and chemical properties of the Metal-Organic Frameworks (MOFs) are strongly influenced by the nature of metal clusters and organic linkers, which are essential to the successful synthesis of coordination polymers with multidimensional networks.[40] Majority of metal-organic frameworks are made from multitopic ligands possessing carboxylate functionality. Most of these classes of ligands can be synthesized in the laboratory using accepted procedures and high-yielding synthetic routes. Some patented aromatic carboxylate ligands are commercially available and cheap. Common examples include naphthalene-2,6-dicarboxylic acid (H_2NDC), 1,1'-biphenyl]-4,4'-dicarboxylic acid, (H_2BPDC), 1,3,5-tricarboxybenzene (Trimesic acid, H_3BTC), 1,3,5-tris(4-carboxyphenyl) benzene, (H_3BTB or BTB=benzenetribenzoate) and 1,3,5- benzene tricarboxylic acid (H_3BTC). Any organic ligands suitable for MOF synthesis should form coordination bonds with secondary building units (SBU), the central metal. Also, for specific potential applications, the choice of organic ligand helps to control the pore volume and surface area of MOFs due to the geometry and chemical properties of multivalent, aromatic carboxylic acids.[5-59] Figure 1.4 lists some aromatic carboxylate organic linkers used in MOF Synthesis.

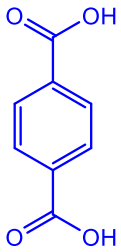
Many MOFs were synthesized from aromatic carboxylate groups such as benzene-carboxylate groups due to their rigidity and capacity for the formation of rigid metal carboxylate clusters. Ligands with this linear orientation mostly generate square planar or cubic MOFs.



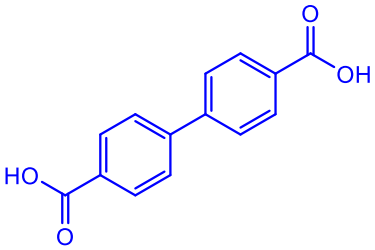
Naphthalene-2,6-dicarboxylic acid (2,6 NDC)



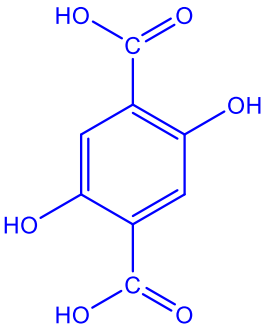
Benzene-1,3,5-tricarboxylic acid (Trimesic acid, BTC)



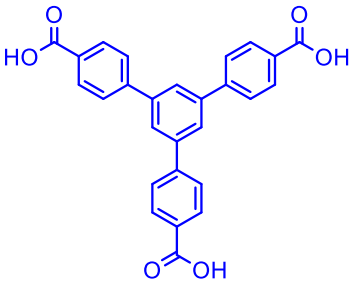
Benzene 1,4 dicarbocylic acid (H_2BDC)



[1,1'-biphenyl]-4,4'-dicarboxylic acid (BPDC)



2,5-dihydroxy-4-(1-hydroxyvinyl)benzoic acid (2,5-dihydroxyterephthalic acid



1,3,5-Tris(4-carboxyphenyl)benzene (BTB)

Figure 1.4: List of some aromatic carboxylate organic linkers used in MOF synthesis.

Ligands are deliberately functionalized to have carboxylic acids due to carboxylic acid's possession of high acidity (pK_a ~ 4), which enables facile in situ deprotonation. Also, it is thought that the formation of well-ordered, crystalline MOFs is probably because the metal–carboxylate bond formation can be reversible under relatively mild conditions. Therefore, the negative charges on the carboxylates are countered with the positive charge of the metal centre when coordination occurs in a framework structure. Consequently, counter ions within the pores of the frameworks will be eliminated.

There are different coordination characteristics carboxylate linkers exhibit during synthesis, the design strategies for each MOF are dependent on the coordination modes of the linkers. Figure 1.5 and 1.6 shows different coordination modes of two commonly used linkers (1,3,5-benzenetricarboxylic acid and 1,4-benzenedicarboxylic acid) with metal ions, M.[60,61,]

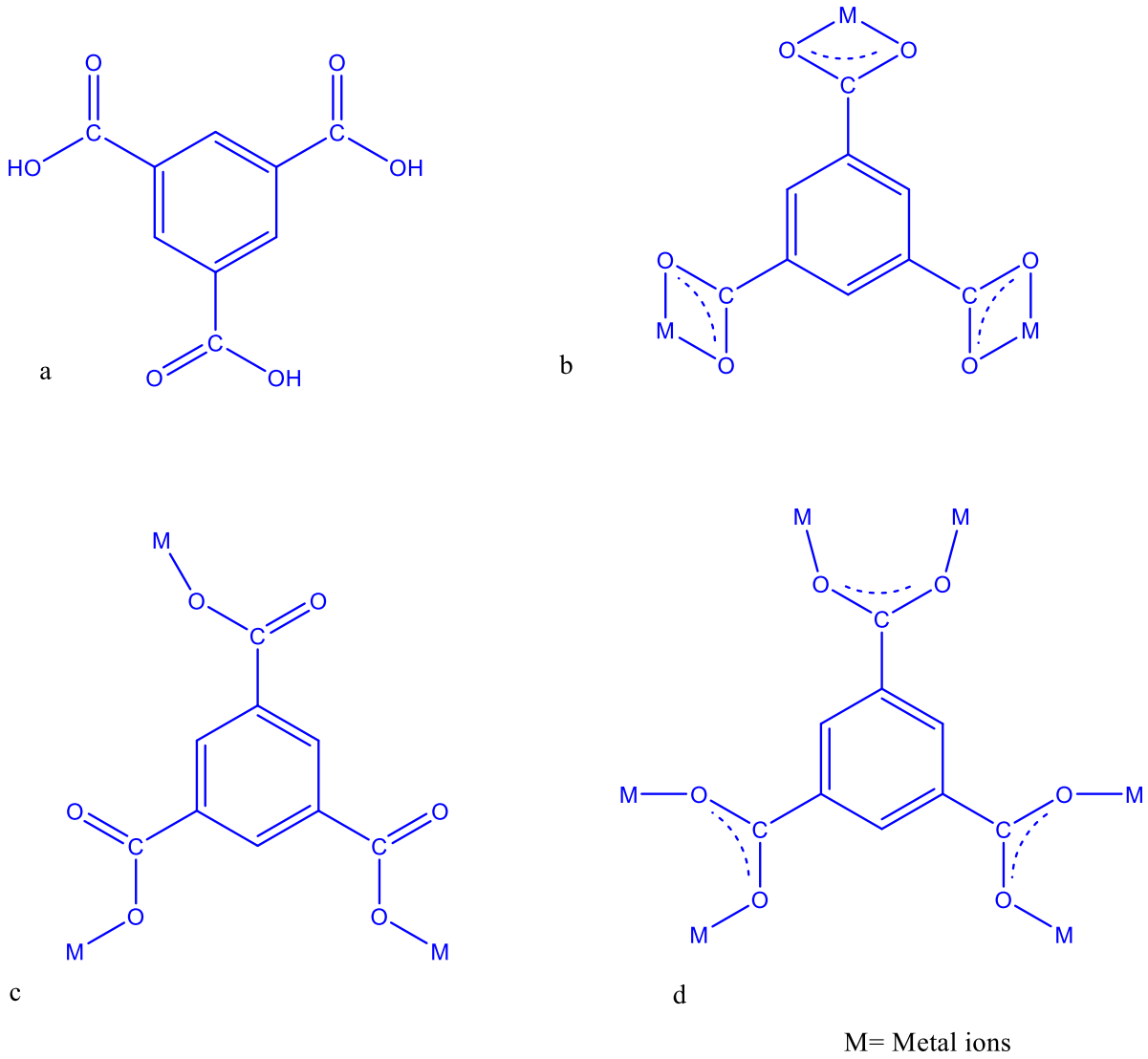


Figure 1.5 (a) 1,3,5-benzenetricarboxylic acid and (b-d) examples of multidentate coordination modes of 1,3,5-benzenetricarboxylic acid.[61]

The introduction of a base modulator may be required here for the construction of the planned porous three-dimensional network that will enhance framework rigidity and thermal stability. This is because the complete deprotonation of 1,3,5- benzene tricarboxylic acid (H_3BTC) is required for metal ions to bind in a multidentate mode, as

exhibited in figures 1.5 (b-d).[60,62-63] Therefore, the dimensionality of the resulting MOF is mainly dependent on the solvent used in the synthesis, and the strength of base employed for the deprotonation of H_3BTC.[60]

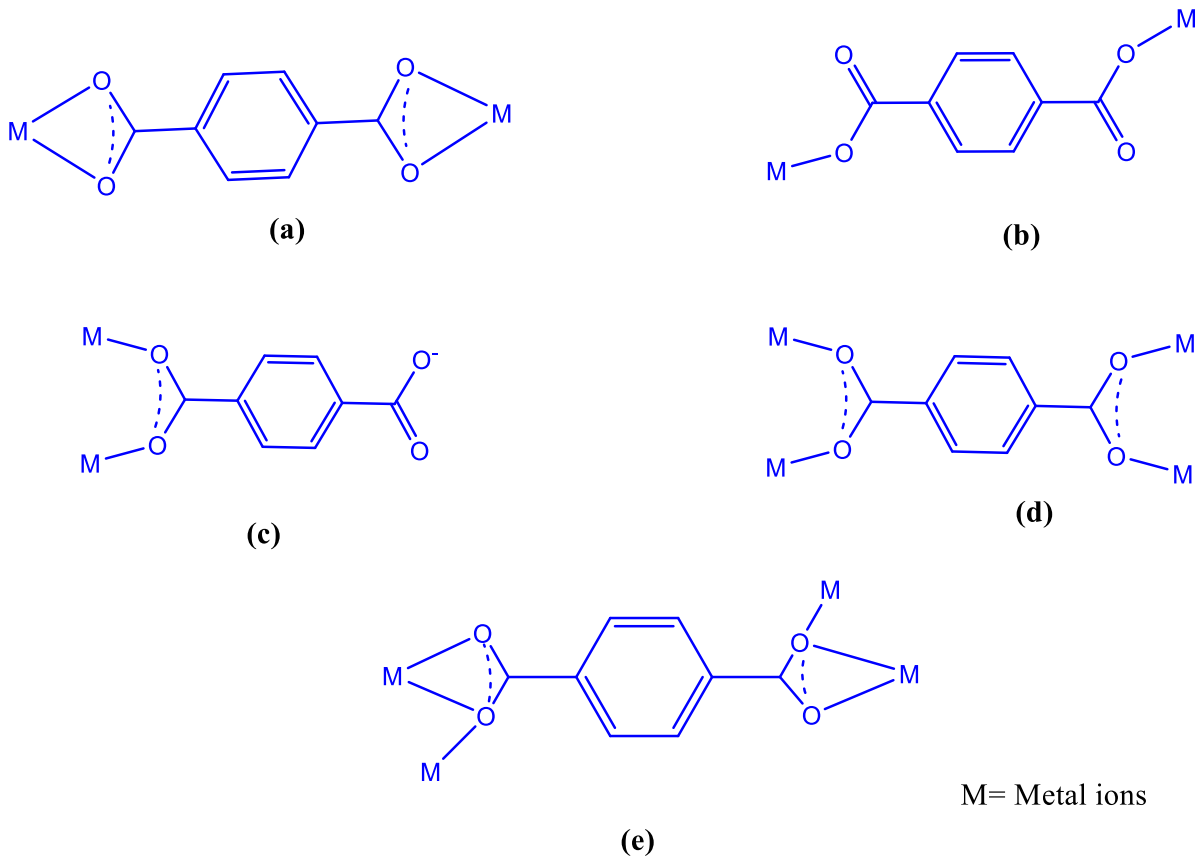


Figure 1.6: Common coordination modes of 1,4-benzenedicarboxylic acid in MOFs: (a) chelating bis-bidentate,[62] (b) bis-monodentate,[63] (c) mono-bidentate, (d) bridging bis-bidentate, (e) chelating/bridging bis-bidentate.[60,62,63]

Nitrogen-containing ligands[64] : The two major contributors of organic building blocks in MOFs are carboxylate-based linkers and N-donor ligands. N-donor linkers broadly constitute two types: charged and neutral donor, with each type offering differing characteristic features.[64-67]

The chemistry of charged ligand-based MOFs has evolved rapidly over the years and has been surveyed consistently in literature[64-67] and; hence more attention has been devoted to reports of MOFs constructed out of neutral N-donor ligands in the present review.

N-donor ligands are a class of linkers that constitute five-membered heterocycle azolate, and the coordination mode is via sp^2 N-donor atoms upon deprotonation. MOFs are generally classified into neutral and ionic, based on the charge of the framework backbone. Ionic MOFs are further divided into cationic and anionic. N donor linkers can give both neutral and ionic frameworks based on the connectivity of the linker, coordination geometry and metal coordination environment.[64]

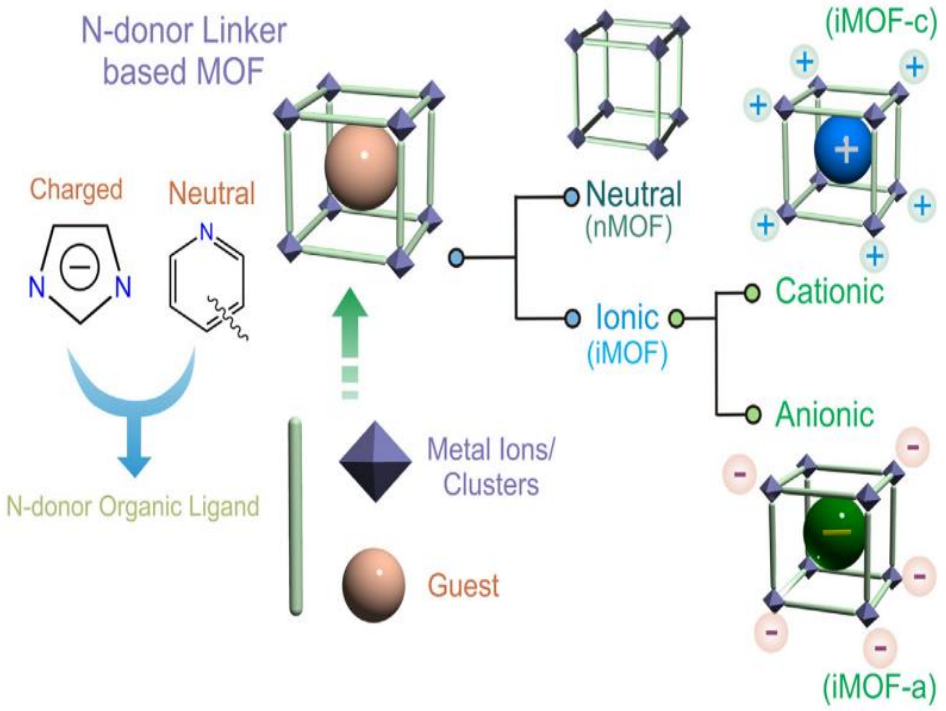


Figure 1.7: Pictorial Classification of MOFs formed from N-donor linkers.[64]

Notably, the coordination ability of the N-donor group and the anion employed in the reaction medium will typically determine the properties of the resulting MOF, which may either be neutral or ionic (mostly cationic), as shown in Figure 1.7 above. For example, weakly coordinating anions such as hexafluorophosphate $[PF_6]^-$ mostly remain uncoordinated within the void spaces of the MOFs. The solvent molecules will usually occupy the vacant coordinating sites and complete the coordination sphere while strong coordinating anions like thiocyanate $[SCN]^-$ bind to the metal nodes. In the latter case, the solvent molecules occupy the vacant coordinating sites, if any, and complete the coordination sphere. Neutral N-donor ligands have been employed with O-donor ligands as co-linkers to extend the network of metal-carboxylates,[68] hexatopic

3,4-di(3,5-dicarboxylphenyl)phthalic acid(H6dccpa) ligand[69] and metal sulfonates.[64,70-72.]

Generally, ligands bearing nitrogen (e.g., pyridine-based ligands) produce very stable MOFs. Hence, ligands containing primary amines produce much fewer stable frameworks shown because primary amines exhibit poorer donor ability towards metal centres. The metal-N bond is relatively labile, especially when the pyridine-based ligands are used.[73] However, the degree of lability is highly dependent on the metal ions used. As a result of which, the rearrangement of the networks is highly probable which can consequently result in the formation of unexpected frameworks in a phenomenon termed as ‘’supramolecular isomerism’’.[74,75]

Unlike their carboxylate counterparts, Pyridyl ligands are neutral, and once coordinated to a cationic metal centre, the resultant network retains its positive charge(s), which must be balanced by counter ions, which occupy the pores of the framework. This can be disadvantageous if such material is used for gas adsorption studies. MOFs constructed from N-donor linkers have been found appropriate for applications in diverse fields of science, such as catalysis, molecular sieving, gas/solvent storage, catalysis, capturing priority pollutants, and magnetism. Interestingly, a novel metal−organic material (MOM) platform of formula $[M(bpe)_2(M'O_4)]$ (M = Co or Ni; bpe = 1,2-bis(4-pyridyl)ethene; M′ = Mo or Cr) were synthesized and assessed for gas sorption applications. $[Ni\text{-}(bpe)_2(MoO_4)]$, MOOFOUR-1-Ni, and its chromate analogue, CROFOUR-1-Ni, exhibit high CO_2 affinity and selectivity, especially at low loading. This behaviour was attributed to exceptionally high isosteric heats of adsorption (Qst) of CO_2 in MOOFOUR-1-Ni and CROFOUR-1-Ni of ∼56 and ∼50 kJ/mol, respectively, at zero loading.[76]

1.2.6. Methods of crystallization

Conventional solvothermal synthesis is a simple and easy-to-understand conventional method used in synthesizing MOF. It involves combining a metal salt with an organic linker in a high boiling point solvent (for instance, DEF, DMF, or DMSO) in a screw-top vial, ‘’which is heated to induce the release of a base by thermal decomposition, thus initiating self-assembly, although many alternative protocols have been successfully developed’’.[35] The mixture is usually heated in an oven or on a hot plate

in a fume hood and equipped with a bath of non-flammable silicone-based oil (not mineral oil), typically for 12 to 72 hours. Common physicochemical parameters that can be altered include reagent concentration, reaction temperature, nature of the precursors used, time, pH and solvent. These parameters determine the metal-organic framework material's crystal size, topology and phase purity. The organic linker and metal precursor should be soluble, especially when the mixture reaches the reaction target temperature.[35] By design, care must be taken in choosing and selecting all parameters because MOF synthesis is dynamic and may be very sensitive to small variations within the reaction mixture.

The choice of the metal source is very important to the crystallization process. For instance, a metal chloride (MClx) combined with a multitopic carboxylic acid linker will generate a stoichiometric amount of HCl. This strong acid can inhibit crystal growth and dissolve the MOF during the formation process. However, a mild metal-bearing compound being used is metal acetylacetonate (M(acac)x), which produces acetylacetone as a by-product (pKa ≈ 9 in water), which should not disrupt crystal growth.[35,64]

Planning MOF's synthesis entails the selection of the reaction vessel. When choosing the reaction vessel (mostly a screw-top vial), factors to be critically considered include the reaction scale, target temperature, and solvent volume required. The reactant and reaction environment should be controlled so sufficient headspace can accommodate potential pressure build-up.[35,64]

The influence of acidic or basic modulators has been widely reported in MOF synthesis. Studies show that the chemical nature of the modulator will dictate the physical properties of the resulting modulated MOF.[77] Brozek *et al*.[78] have carried out a comprehensive analysis on the self-assembly of nanoscale MOFs, evaluating a number of factors that influence particle size, including the amount of modulator added to syntheses. Studies suggested that by the addition of small amounts of acidic modulators (lower pH), particle size decreases; when the modulator ratio increases, the additional proton content will prohibit linker deprotonation, thus creating excessive coordination competition with the linker for the metal site, which will consequently result in an increase in particle size.[78-80]

Attempting the control of MOF particle size requires the knowledge of the pKa of the modulator relative to that of the linker in use.[78] This is because the conjugate basicity of the deprotonated carboxylate modulator will mediate the level of coordinative competition. It is expected that modulators possessing pK_a values most exactly like those of the linkers will enable the growth of large particles and single crystals. This explains why the widespread weak organic acids (non-structural, monotopic linkers), such as acetic acid (pK_a = 4.76) and benzoic acid (pK_a = 4.20), have been successfully used in the isolation of single crystals of MOFs linked by 1,4-BDC (first pK = 4.82). For instance, ''UiO-66 and its isoreticular analogues modulated with benzoic acid''. [80-82]

Zhang *et al*.[80] in figure 1.8 attempted to explain the dual roles of pH control and coordination modulation in MOF particle size control.

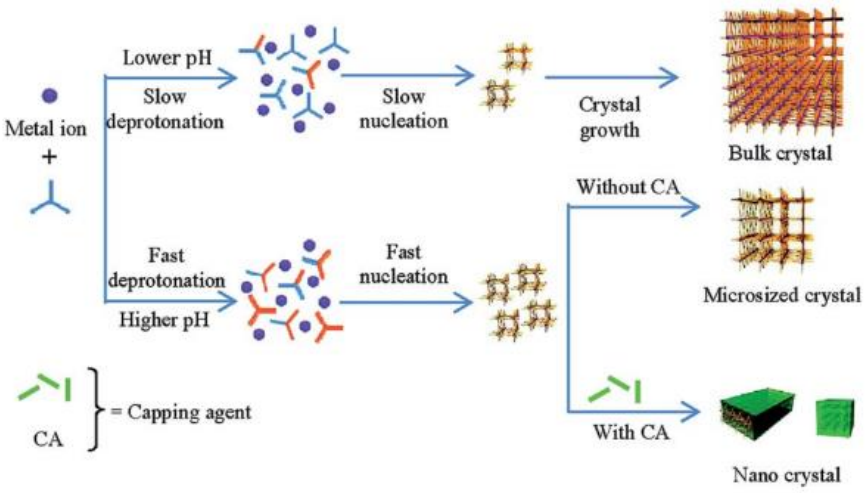


Figure 1.8: Mechanisms for dual roles of pH control and coordination modulation in MOF particle size control as proposed by Zhang *et al*.[80]

Modulated synthesis helps to exercise control over the self-assembly of MOFs and create materials with desired properties.[35] These physical properties need to be controlled to ensure that MOFs are systematically optimized and improved for particular potential future applications.[79] In the opinion of Forgan, 2020,[79] coordination modulation does not ''only tune the physical properties of previously known MOFs, but also aids the enhancement, promotion and formation of new phases.''[79] The requirement for a modulator is based on the strength of the metal-ligand bond and its effect on the MOF synthesis. For instance, if the metal−ligand bonds are very strong, a modulator can help prevent the rapid precipitation of amorphous material.[79,83-85]

Over time, the incorporation of modulators into MOF synthesis has aided the control of particle size, phase selection and other multiple physical properties. It has also enhanced the production of single crystals and defects and phase control in complex MOF systems. Figure 1.9 shows the range of effects coordination modulators can have when incorporated into MOF synthesis.[79]

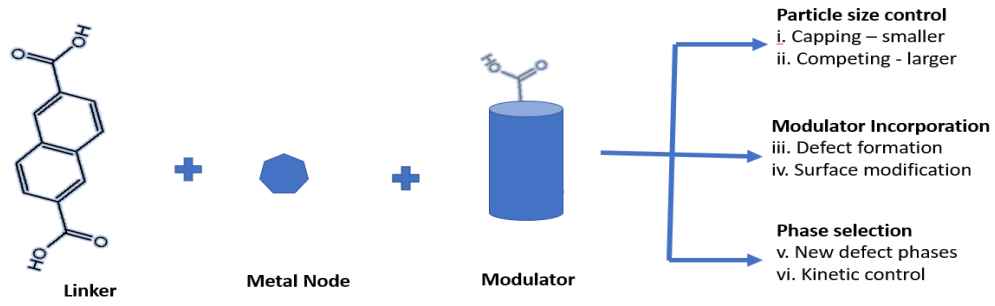


Figure 1.9: Schematic of coordination modulation, with various potential outcomes. Note that these can occur concurrently; for example, (i) aligns with (iv), (iii) can align with (v), and (ii) can align with (vi).[79]

The influence of coordination modulators also reflected in MOFs' selection phase (morphology). There are several metal-ligand combinations through which multiple framework structures can be synthesized. Phase selection from complex mixtures can be made possible either by ‘’pre-organizing particular discrete metal clusters or by controlling the kinetics of self-assembly through competition for both metal ions and protons’’.[79] While studying the Cr(III) 1,4-BDC system, Liu *et al*.[87] deduced that by the introduction of varied amount of benzoic acid modulator to hydrothermal syntheses, two MOF phases, MIL-88B(Cr) and MIL-101(Cr) were isolated as shown in Figure: 1.10 below.

Unmodulated syntheses resulted in the formation of MIL-101(Cr), which is expected to be the kinetic product of this metal–ligand system, and the addition of up to 3 equivalents of benzoic acid to syntheses steadily reduced particle size while enhancing porosity. However, on the addition of 5 equivalents of benzoic acid, MIL-88B(Cr) (figure 1.10 right, hexagonal rods, scale bar 3 mm) was synthesized possessing the same metal cluster (SBU) and overall composition of MIL-101(Cr) (figure 1.10 left, octahedra, scale bar 500 nm) but a denser structure, appears in a mixture of the two phases. It was reported that 10 benzoic acid equivalents only yielded MIL-88B(Cr), the thermodynamic product.[79,87] This research indicated that

modulation affected the kinetics of self-assembly. The work suggested ‘’that coordination modulation can select for the thermodynamic product by competing with ligands for metal ion and proton, effectively slowing the self-assembly process’’.[79,87]

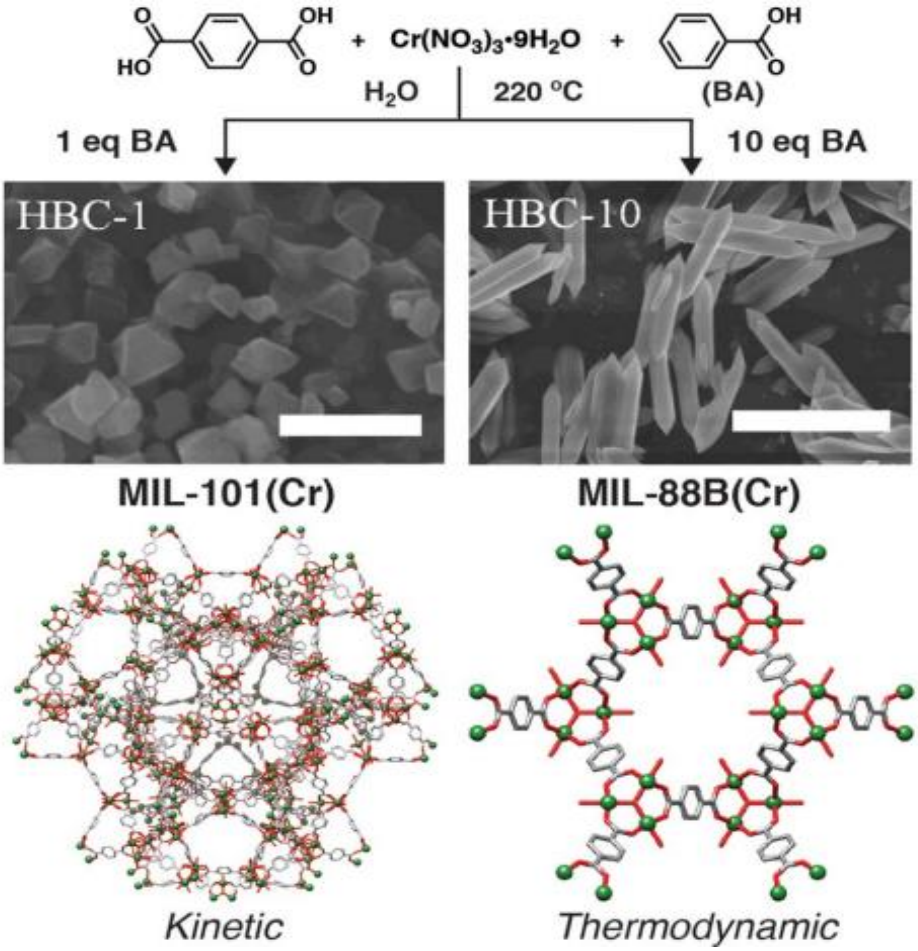


Figure 1.10: Schematic of benzoic acid (BA) modulated hydrothermal syntheses of Cr(III) MOFs linked by 1,4-BDC, displaying a selection of the thermodynamic MIL-88B(Cr) phase (right, hexagonal rods, scale bar 3 mm) over the kinetic MIL-101(Cr) phase (left, octahedra, scale bar 500 nm) as the modulator content in syntheses increases.[79,87]

Microwave-assisted synthesis of zirconium (Zr) based metal-organic frameworks (MOFs) were performed, and the yield and porous property of UiO-67 was optimized by varying the quantity of the modulator (benzoic acid, BenAc and hydrochloric acid, HCl), reaction time and temperature. It was found that (i) an increase in the amount of modulator enhanced the specific surface area and pore volume of UiO-67 due to the promotion of linker deficiency, and (ii) the presence of modulators influenced the number of nuclei (and hence the crystal size) and nucleation time (and hence the

yield). In addition, UiO-67 MOFs from different synthesis methods (i.e. the microwave-assisted and solvothermal method) were evaluated using single-component (CO_2 and CH_4) adsorption, showing comparable gas uptakes.[88-90]

1.2.7. Electrochemical Synthesis

The electrochemical synthesis of MOFs was first reported in 2005. The benefit of this method is that it does not require the inclusion of metal salts in the MOF reaction.[91-93] Therefore, unwanted anions (such as chloride, perchlorate, nitrate, etc.) are excluded, which enhances continuous industrial-scale production of MOF crystals, avoiding the challenges associated with removing anions. The metal ions are continuously injected through anodic dissolution into the reaction medium, which consists of the dissolved organic linker molecules and a conducting salt. [91-93] The use of protic solvents is required to prevent metal deposition on the cathode; however, Hydrogen formation occurred. Industrial application of electrochemical synthesis helps in the possibility to operate a continuous process and get a higher solids content than the usual batch reactions.

Cu- and Zn-based MOFs were obtained successfully through electrochemical synthesis. .[94] In this study, anode materials (Zn, Cu, Mg, Co) and linkers [H_2BDC, 1,3,5-H_3BTC, H_2BDC $(OH)_2$ and 1,2,3-H_3BTC] were reacted and several successful upscaling of synthesis experiments achieved. Four Cu- or Zn-containing compounds with high porosity were obtained from these combinations. Example of MOF formed include HKUST-1.[94] (Figure 1.11). There might be some differences in the quality of products obtained during characterization studies between different methods. For instance, a comparative study of HKUST-1 synthesis by solvothermal and electrochemical synthesis was carried out. The analysis of results from TGA experiments, elemental analyses, and sorption experiments showed that the inferior quality HKUST-1 was obtained using electrochemical synthesis. However, the HKUST-1 gotten from both methods produced same structure as confirmed by PXRD data.[91-94]

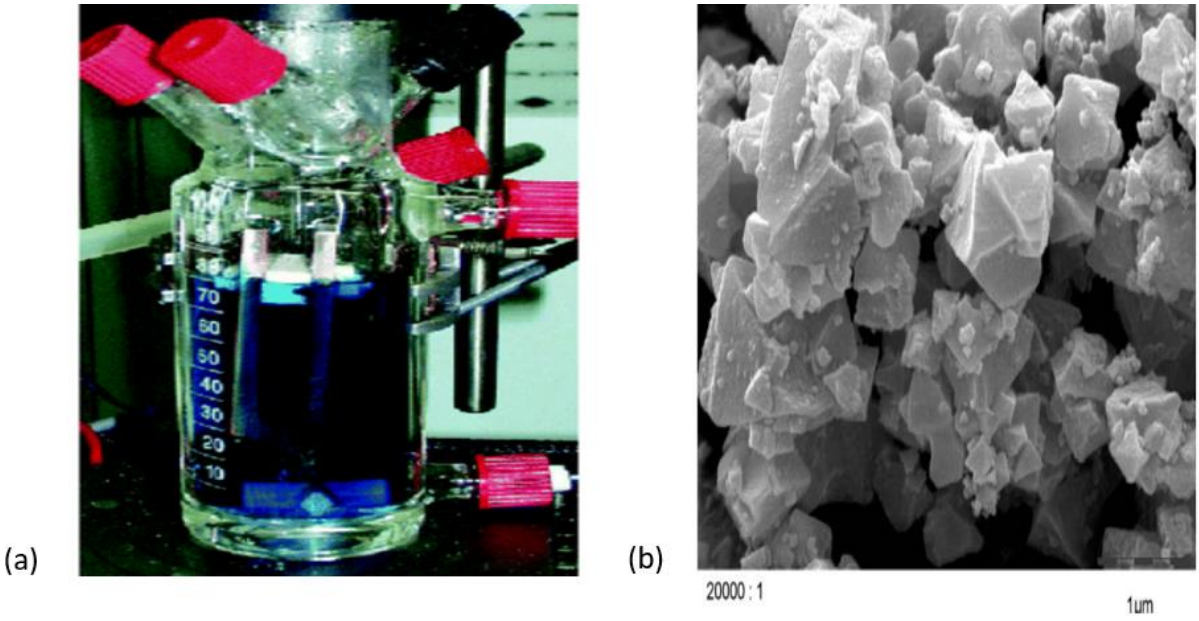


Figure 1.11: Experimental Setup for electrochemical synthesis of MOF HKUST-1 with Cu-plates as electrode material (a) and SEM image of the product (b) (magnification, x20 000).[94]

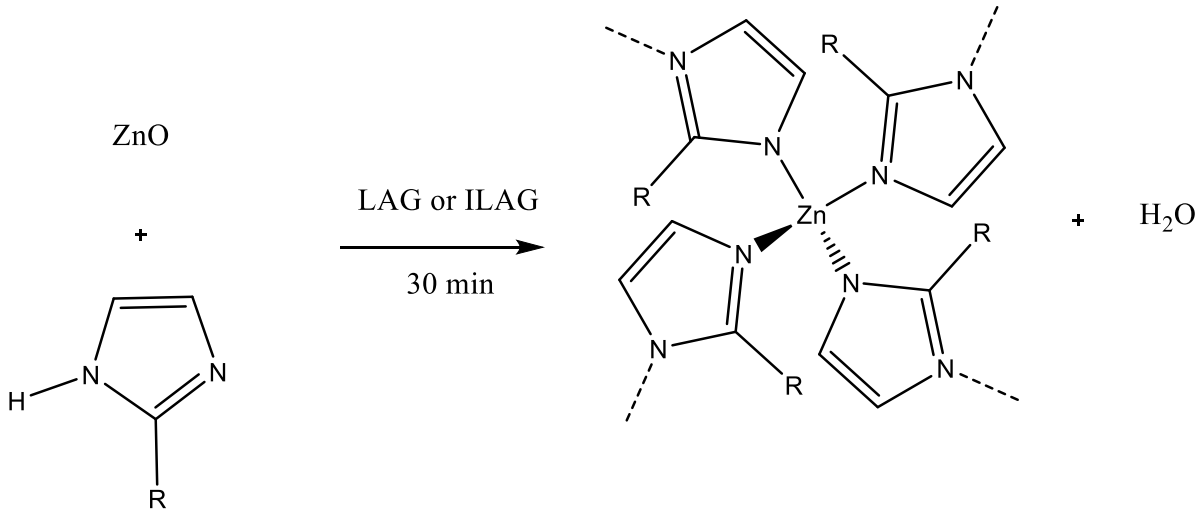
1.2.8 Mechanochemical Synthesis

In mechanochemical synthesis, mechanical force can induce many chemical reactions, which involve the mechanical breakage of intramolecular bonds followed by a chemical transformation. [95,96] Solving waste disposal, cost, and environmental issues, mechanically activated MOF synthesis can be executed at room temperature under solvent-free conditions; organic solvents are avoided.[97]

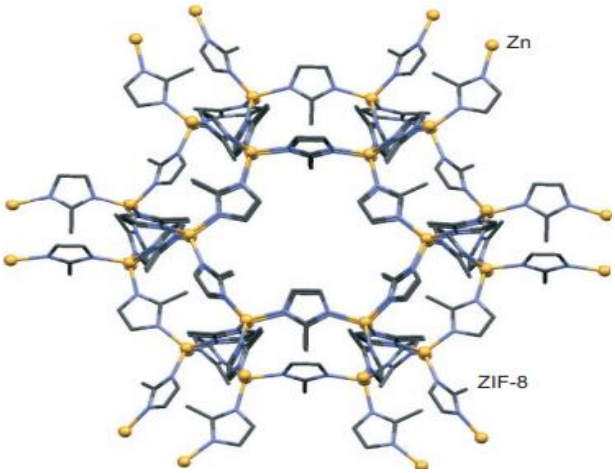
In addition, metal oxides can be used as a starting material instead of metal salts, thus leaving water as the only side product. For instance, ZnO was suitable for synthesising pillared layered MOFs and ZIFs.[98-100] In contrast, metal oxides are rarely used in solvent-based reactions due to their low solubility. The first studies were performed under solvent-free conditions.[101-103] Presently, no general theory can explain the physicochemical processes that occur in mechanochemical reactions. The most common approaches, so far, are the hot-spot model and the magma ± plasma model.[104,105]

Recently, liquid-assisted grinding (LAG), which involves adding small amounts of solvents, has been shown to be effective[101-103,] enhancing the acceleration of mechanochemical reactions, possibly due to increased mobility of the reactants on the molecular level.[35] In addition, the presence of the liquid can exert structure-directing

properties.[100] In a recent report, LAG was modified to ion- and liquid-assisted grinding (ILAG), this was demonstrated to be highly efficient for the selective construction of pillared layered MOFs, and it was shown that the ions, as well as solvents, exert a structure-directing effect.[100] Friscic *et al*.[106] have demonstrated in Figure 1.12 that by varying the solvent added in a LAG process, one-dimensional, two-dimensional and three-dimensional coordination polymers could be obtained from the same reaction mixture.



(a)



(b)

Figure 1.12 (a) The reactions carried out by milling imidazole derivatives as ligand and metal oxide in the presence of catalytic amounts of liquid (LAG) or catalytic amounts of liquid together with an ionic additive (ILAG). (b) Part of the structure of one of the products, ZIF-8.[110]

In Figure 1.12 Friscic and co-workers synthesized MOFs from reactions by grinding, LAG with ethanol (EtOH) or N, N -dimethylformamide (DMF) as additives, and ILAG using EtOH or DMF as additives in the presence of ammonium nitrate NH_4NO_3, ammonium methanesulfonate $NH_4CH_3SO_3$ or ammonium sulphate $(NH_4)_2SO_4$. The ligands used were imidazole, 2-methylimidazole or 2-ethylimidazole.[110]

1.2.9 Sonochemical Synthesis

Sonochemical Synthesis of MOF was primarily developed to achieve a room-temperature synthesis with high energy efficiency and environmentally friendliness. Sonochemistry is a branch of chemistry that employs the application of intensive ultrasonic radiation (20 kHz–10 MHz) to effect chemical change in molecules. Ultrasound generates chemical or physical changes because of a cavitation process comprising formation, growth and speedy collapse of bubbles in a liquid, creating local hot spots of a short lifetime with high pressure and temperature. These extreme conditions stimulate chemical reactions by the instantaneous formation of excess crystallization nuclei. Compared with hydrothermal synthesis, this technique yielded reduced crystallization time and homogeneous nucleation centres.[107] MOF-5 has been successfully synthesised using sonochemical irradiation in 1-methyl-2-pyrrolidinone. The method produced crystals between 5 and 25 μm in 30 min, similar to MOF-5 synthesized using either solvothermal or microwave methods.[107]

Likewise, Boukli-Hacene *et al*,[108] reported the successful sonochemical synthesis of Zr-fumaric-based MOF having a crystallization time of 45 min. X-ray powder diffraction (XRPD) was used to identify the atomic and molecular structures of the as-synthesized MOF-801. The diffractogram was confirmed to be the same as reported in previous studies [109-111,] with the main peaks situated at 2θ equal to 8.77, 10.09, and 30.1, confirming the successful synthesis of the Zr-fum MOF.[108] The studies were conducted using a different setup: ultrasonic cleaning baths with lower power intensities.

Results of the sonochemical synthesis of MOFs were mostly affirmed with others obtained by mechanochemical, MW-assisted, electrochemical, and other conventional syntheses. Reported examples showed that only known MOFs, MOF-5, MOF-177, and HKUST-1 structures, have been sonochemically synthesized under mild conditions (at room temperature). Jiang *et al*.[112] 2008 reported the first sonochemical synthesized Zn carboxylates, $[Zn_3(BTC)_2]$[112] MOFs from the reaction of an aqueous solution of zinc acetate and H_3BTC in a mixture of ethanol and water at room

temperature in an ultrasonic bath. The only parameter that varied was the reaction time. Sonication time and power level of the sonicator strongly influenced the product properties. The optimization of these parameters led to high-quality crystals matching the highest reported surface area S_{BET} values for MOF-177.[112]

1.2.10 Microwave-assisted synthesis

Microwave irradiation has been used as an energy source in synthetic–organic chemistry. [113-115] Many reactions have been completed using microwave-assisted synthesis; these involve many solid-solid reactions and solution-based syntheses, MOFs,[115]

An interaction exists between the electromagnetic waves and mobile electric charges for microwave-assisted synthesis to occur. The interaction exists in polar solvent molecules/ions in a solution or electrons/ions in a solid. In the solid, an electric current is formed, and heating is due to the electric resistance of the solid. In solution, polar molecules try to align themselves in an electromagnetic field and an oscillating field so that the molecules change their orientations permanently. Thus, applying the appropriate frequency, a collision between the molecules will take place, which leads to an increase in kinetic energy, i.e., temperature, of the system.[113-115]

Due to the direct interaction of the radiation with the solution/reactants, MW-assisted heating presents a very energy-efficient heating method. Thus, high heating rates and homogeneous heating throughout the sample are possible. Attention must be paid to the choice of appropriate solvents and selective energy input since starting materials may interact strongly with the MW radiation. Microwave ovens suited for materials syntheses allow one to monitor temperature and pressure during the reaction and thus allow more precise control of reaction conditions.[113-115]

Employing MW-assisted MOF syntheses usually involves direct heating of solvents, and higher nucleation rates were observed in most cases. It helps to achieve the acceleration of crystallization and synthesis of nanoscale products. The products formed also possess improved purity compared to other methods. Also, selective synthesis of polymorphs has been enabled using this method. [113-115]

By design, MW-assisted synthesis of MOFs has often been carried out at a temperature above 100 ^{o}C, with reaction times rarely exceeding 1 h. In a few works of literature, process parameters such as solvent, irradiation time, reaction temperature,

power level, the molar ratio of the reactants, reactant concentration and others were varied to adjust the reaction conditions. Heating with MW irradiation enhances the more rapid synthesis of smaller crystals than CE heating.[113-115]

Lots of metal (III) carboxylate-based MOFs (M = Fe, Al, Cr, V, Ce) have been prepared by the MW-assisted synthesis route. The first MW synthesis of MOFs studied, Cr-MIL-100, was synthesized in 4 h at 220 ^{o}C under MW irradiation with 44% yield, [116] which is comparable with that of CE synthesis.[116-118] Another interesting exploit of MW-assisted synthesis of nanoscale Cr-MIL-101 is explained in two works of literature. [116-118]

1.2.11. Purification and activation Strategies

The synthesis of MOFs comes with impurities from solvent molecules and excess organic linkers. The solvent molecules are usually trapped in the pores of the framework. Therefore, MOFs obtained after each synthesis must be purified of excess linkers (as we found in Cr-MIL-101)[119] and solvent molecules trapped to attain the goal of the permanent porosity and high surface areas expected of many framework structures for potential industrial applications. The process of removing entrapped solvent molecules is termed activation.[119]

Purity of the MOF material must be achieved, especially in applications desiring highly pure materials. The negative effects of impurities in catalysis are harmful because impurities can affect overall catalytic activity as well as lowering of MOFs sorption capacity.[120,121] Purification of a MOF reaction, where a mixed organic solvent system was used, was achieved by using differences in density to enable the separation of a mixture of catenated and non-catenated MOF phases.[121] Other control measures for catenation include temperature adjustment,[123] concentration,[122] solvent-assisted linker exchange (SALE)[120,124] use of templating solvents[124,125,] to mention a few. The use of X-ray powder diffraction aids in the detection of crystalline impurities, while amorphous by-products can be detected in thermogravimetric or elemental analysis. To design the right purification and activation process, MOFs' chemical and thermal stability must be examined.[120]

MOF activation aims to attain materials with high surface area and porosity. The process must be carefully selected to avoid a structural collapse resulting from strong host-guest interaction, especially if high temperatures treatment is required.[127] For

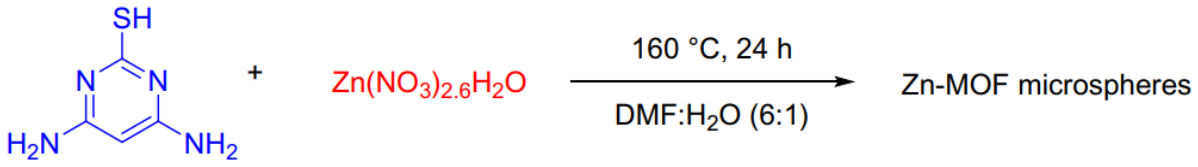
instance, effective activation of Cr-MIL-53[124] and Al-MIL-53[125] used high temperature during which unreacted ligand was expelled by heating in air at 300°C. However, solvent exchange methods have been successfully applied for some less stable MOF materials. In this case, the reaction solvent molecules will be first exchanged with more volatile compounds like chloroform, methanol or dichloromethane[126], which can be eliminated without additional thermal treatment.

1.3 Application of MOFs in catalysis, gas storage, organic electronic and photovoltaic devices

1.3.1 Catalysis

MOFs have found extensive application in catalysis due to a combination of features such as high porosity, high surface area, desired morphology, active metal sites, stability and controllable pore size.[128] The catalytic synthesis of diverse organic and bioorganic molecules through organic transformations by MOFs has been reported in several kinds of literature.[129-132] Typically, MOFs are thermally decomposed to form metallic nanoparticles dispersed through carbon and/or metal oxide frameworks. The resulting carbon-based materials have been used as catalysts for different kinds of reactions such as CO_2 conversion, CO_2 reduction, and oxygen evolution reaction (OER) to mention a few.[133-136]

Mohammed *et al*.[137] reported a ‘’heterogeneous catalyst (Figure 1.13) which was a three-dimensional walnut-like Zn-based MOF microsphere system designed and synthesized through hydrothermal reaction of zinc salt with 4,6-diamino-2-pyrimidinethiol as a tridentate ligand.[137]



4,6-diamino-2-pyrimidinethiol Zn Source MOF

Figure 1.13: The synthesis of Zn-MOF microspheres (a heterogenous catalyst).[137]

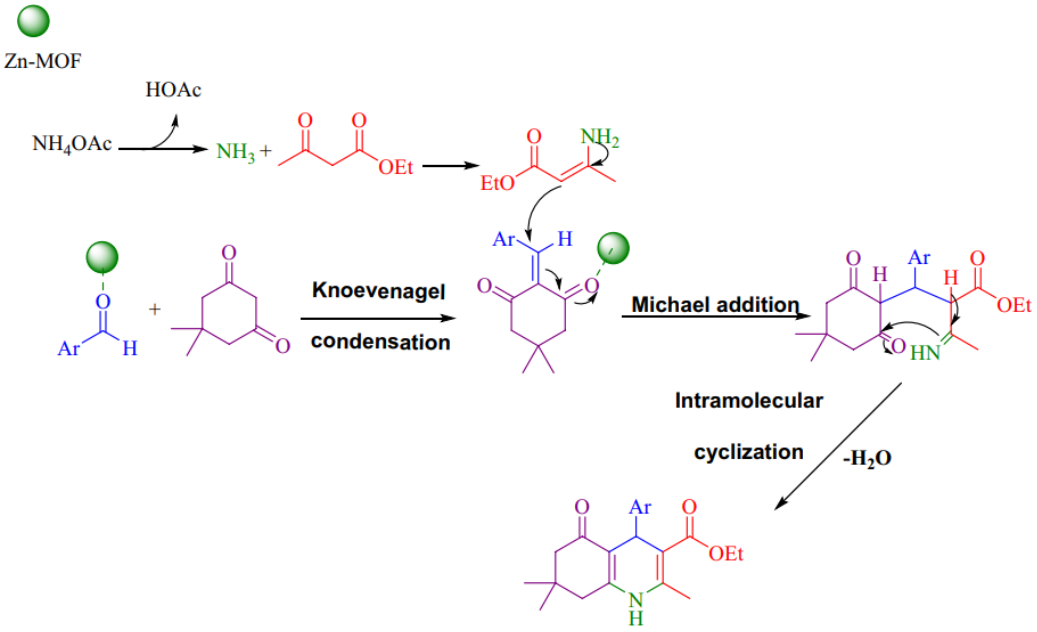


Figure 1.14: Proposed mechanism for the synthesis of polyhydroquinolines in the presence of nanoporous Zn-MOF microspheres.[137]

In Figure 1.14, the Zn-MOF microspheres were employed in the Hantzsch reaction (an asymmetric reaction of an aldehyde, two components of β-keto esters, and a nitrogen donor, which generates chiral dihydropyridines) for the selective synthesis of asymmetric polyhydroquinolines, used as useful precursors to many compounds of biological and pharmaceutical applications.[138,139] After using various aromatic aldehydes, selective synthesis with good yields, short reaction time, a low limit of steric hindrance and electronic effects were reported.[137]

Additionally, mixed metal MOF materials have found many new applications in catalysis. Recent developments have shown MOF's utility as a catalyst or support for carbon capture and CO_2 conversion. Amal *et al*.[140] and co-workers reported using NiMg-MOF-74 as a template to disperse small Ni nanoclusters throughout the parent MOF. By manipulating the difference in Ni-O and Mg-O coordination bond strength, Ni^{2+} was selectively reduced to form highly distributed Ni nanoclusters constrained by the parent MOF pore diameter, but Mg^{2+} remained coordinated in the framework. To induce CO_2 adsorption capacity and hydrogenation selectivity, the ratio of Ni to Mg in the parent MOF was modified to achieve accessible surface area, and crystallinity was tuned upon thermal treatment at 350 ^{o}C. The resulting Ni nanoclusters proved to be

an active catalyst for CO_2 methanation. Also, by preserving a segment of the Mg^{2+}-containing MOF framework, the composite system retained a portion of its CO_2 adsorption capacity while also maintaining catalytic activity. The approach effectively demonstrates the potential of mixed metal MOFs to bridge the gap between carbon capture and CO_2 utilization.[140]

Zurrer *et al*.[140] in Figure 1.15 showed how the catalyst can aid pollution control because the conversion of CO_2 to other gases such as methane (CH_4), carbon monoxide (CO), formic acid (HCOOH), and methanol (CH_3OH) of immense industrial usage. For example, CH_4 is a component in liquefied natural gas and is also used as feedstock for H_2 production. CO_2 conversion also helps to limit the rise in atmospheric CO_2 concentration, a major cause of the greenhouse effect.[140]

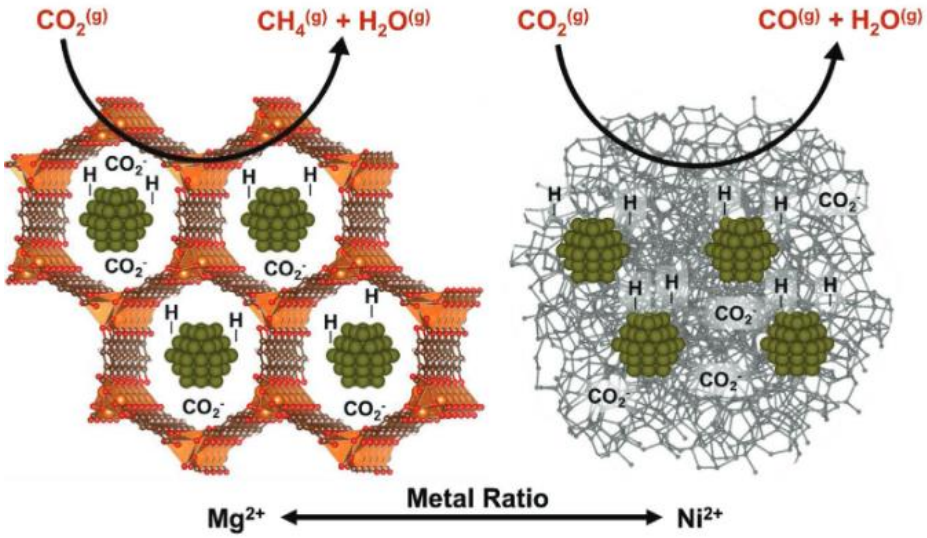


Figure 1.15: Qualitative CO_2 hydrogenation reaction pathway involving the reverse water–gas shift and Sabatier reactions dictated by the resulting support material.[140]

Other examples of MOFs used in catalysis include CPO-27-Mn for the cyanosilylation of aldehydes with trimethylsilylcyanide,[141] MIL-100(ScFe),[142] Encapsulated palladium nanoparticles in Pd@MIL-101,[143] a bifunctional Lewis acid/hydrogenation catalyst was reported as successful material for menthol synthesis tandem reaction.[144] According to Cirujano et al.,[144] Pd@MIL-101 material contains coordinatively unsaturated Cr^{3+} Lewis acid sites and encapsulated Pd nanoparticles as the catalyst for the one-pot two-step transformation of citronellal into menthol. This study showed the presence in Pd@MIL-101 of a fraction of Pd^{2+}, not completely reduced during the hydrogenation

of the palladium precursor, which can enhance the acid-catalyzed citronellal cyclization described in Figure 1.16 below. The second step of the tandem reaction to convert citronellal to menthol entails hydrogenating the isopulegol synthesized in the previous step. Complete citronellal conversion and an overall yield of the desired menthol of 74% were achieved after 18 h.[144]

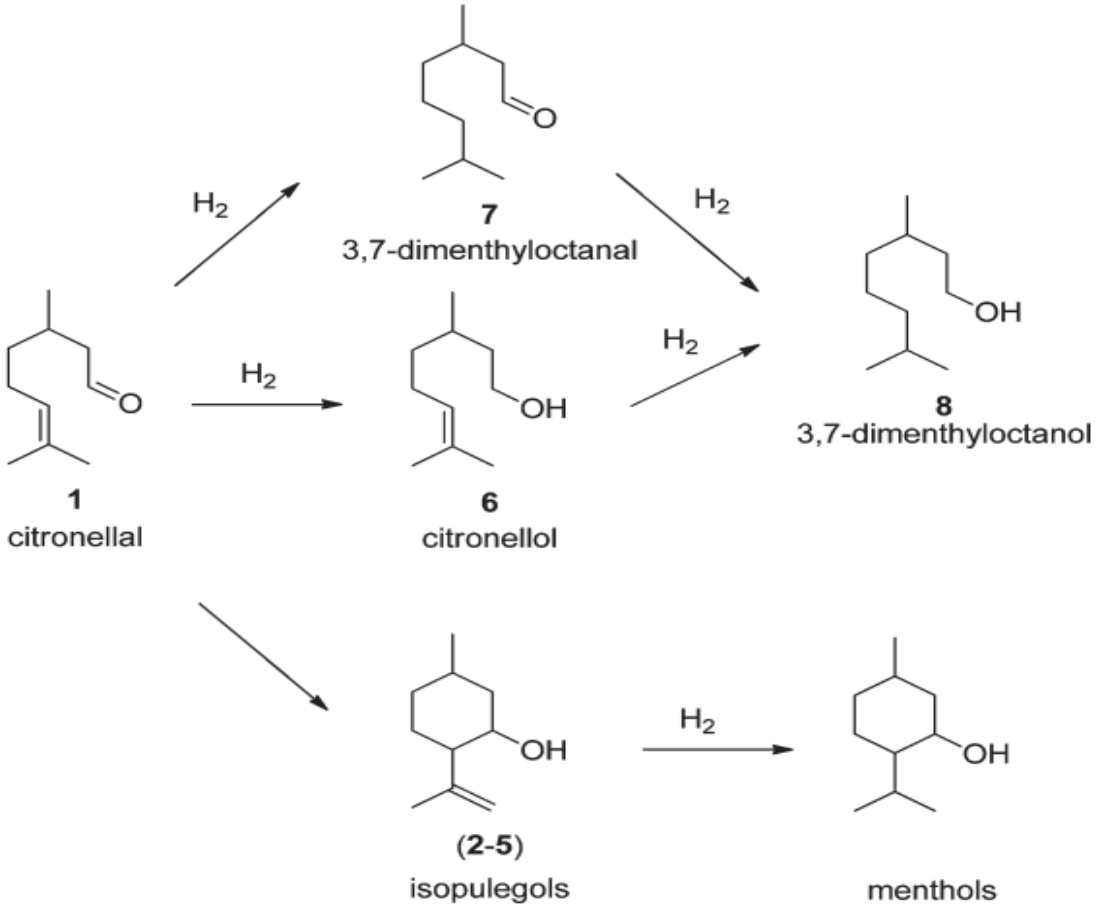


Figure 1.16: The isomerization of citronellal to isopulegol and tandem isomerization/hydrogenation of citronellal to menthol.[144]

1.3.2 Gas Adsorption

Growing advances in the science and technology of MOFs for gas storage and separation are eliciting applications in various fields, such as industrial production, environmental management and energy utilization. MOFs can either be employed as adsorbents or membrane materials in most applications. The gas separability by adsorbent relies on differences in interaction between gas species and frameworks and the consequent selective adsorption of the target gas.[145] The interest in gas

storage and separation is indispensable in most human endeavours. For instance, carbon dioxide separation is essential for mitigating the greenhouse effect; hydrogen and methane storage are important for delivering clean energy.[145]

Likewise, in pollution control and industrial chemical manufacturing, separating and storing notable toxic gases, such as ammonia and carbon monoxide, are the feedstock of immense economic value. Porous materials (silica, activated carbons and zeolites) have been applied in various industrial applications needing alternative raw materials.[146] The physicochemical properties like large surface area, high porosity, tuneable structure, and adjustable functionality are structural features of MOFs, enhancing their application for gas storage and separation.[147-149]

1.3.2.1 CO_2 Adsorption Applications

Metal-organic framework potential in CO_2 adsorption is gaining lots of attention. Zaworotko *et al*.[150] reported a novel metal−organic material (MOM) platform of formula $[M(bpe)_2(M'O_4)]$ (M = Co or Ni; bpe = trans-1,2-bis(4-pyridyl)ethene; M′ = Mo or Cr) synthesized and assessed for gas sorption applications. $[Ni\text{-}(bpe)_2(MoO_4)]$, MOOFOUR-1-Ni, and its chromate analogue, CROFOUR-1-Ni, exhibited high CO_2 affinity and selectivity, especially at low loading. Also observed was an exceptionally high isosteric heat of adsorption (Qst) of CO_2 in MOOFOUR-1-Ni and CROFOUR-1-Ni of about 56 and 50 kJ/mol$^{-1,}$ respectively, at zero loading.[150] This behaviour was attributed to strong quadrupole−quadrupole interactions between CO_2 and MoO_4^{2-} (MOOFOUR-1-Ni) and CrO_4^{2-} (CROFOUR-1-Ni) binding sites.[150]

1.3.2.2 Hydrogen Adsorption

Hydrogen storage appears to be one of the main applications of MOFs. Hydrogen possesses large gravimetric heat of combustion (120 MJkg^{-1}), which positions it as an ideal alternative energy source and could significantly mitigate the environmental problems caused by fossil fuels. However, its low density of 0.08 kg m-3 in the gaseous state renders storage at ambient conditions very problematic, limiting its potential as fuel for industrial applications. The use of MOFs for storage functions are influenced by many other factors which include possession of very high surface area, functionalized polar groups, open metal centres and specific weak interactions.[151]

Efforts to improve the hydrogen uptake have been done by tuning the pore size, insertions of metal nanoparticles, creating extra unsaturated metal sites and by linker modification.[40] Judging from theoretical computation studies it was envisaged that the inclusion of alkali metals such as Li, K, Na (as dopants) could have improved H_2 uptake capacity[107] because of their high affinity for H_2. Long *et al*.[152] synthesized a series of the mixed-cation version of the $Mn_3[(Mn_4Cl)_3(BTT)_8(CH_3OH)_{10}]_2$ for H_2 adsorption.[152] For a systematic tuning of the H_2 adsorption affinity, the cationic guest Mn^{2+} was partially substituted with Li^+, Cu^+, Fe^{2+}, Co^{2+}, Ni^{2+}, Cu^{2+}, and Zn^{2+} ions. All the materials showed relatively high H_2 uptakes ranging from 2.00 to 2.29 wt% at 77 K and 900 Torr.[152]

Additionally, Arrozi *et al*.[153] reported that HKUST-1 can be ex-situ modified with magnesium(II) ions at 3, 5, and 10 wt% to serve as additional binding sites for hydrogen sorption enhancement. X-ray diffraction, FTIR and SEM analysis validated the stability of the structure and morphology of HKUST-1 after it was doped with Mg^{2+}. Nitrogen sorption isotherms revealed that before and after modification with Mg^{2+}, the materials were classified as microporous, and the surface area was raised substantially from 713.283 to 1200.211 m^2/g. It was concluded that the presence of Mg^{2+} in the HKUST-1 influenced its hydrogen sorption capacity up to 0.292 wt% at 1.2 bar under a temperature of 30°C and 0.48 wt% at 80°C (1.4 bar). MOF 5,[154]. MOF 177,[155] Ni-MOF-74,[156] Co-MOF-74,[156] and NOTT-140,[157] to mention a few, are other potential MOFs reported for hydrogen storage.

1.3.2.3 Sensing

Sensing is relevant to biological systems for small molecule and toxic analyte detection, thus demanding extensive development of advanced probes.[40] Research interest in MOF is growing for sensing technology because optical sensors are known for their high sensitivity, fast response and selectivity.

MOFs possess exceptional properties such as ease of post-synthetic modification, high tuneable porosity, and distinct pores. This aids the integration of additional functional units to make MOFs applicable to sensing technologies. Sensing properties are exhibited because the analyte and MOF's interaction usually results in a change in MOF's structure, which eventually leads to the alteration of the intrinsic physicochemical properties of the MOF which is then transduced into a measurable

signal. In recent developments, MOFs and linkers are being functionalized to develop highly selective probes. For instance, the Nitrogen donor MOFs have demonstrated flexibility and ability to incorporate guests, thus enhancing the framework analyte interaction required to maximize response and sensitivity.[158]

The source of luminescence in MOFs is due to a combination of several electronic transitions, the ability to tune electronic properties and pore chemistry. MOF applications, studies, development, and scope have covered the sensing of toxic analytes, anions, oxygen, VOCs, and industrial feedstock gases. Zhang *et al*.[159] ''developed a series of oxygen sensors, namely MAF-4@pyrene or ZIF-8@pyrene, with the formula [$Zn(mim)_2$] (where mim = 2-methylimidazole) and consists of two kinds of cavities: larger cavity (d ~11.4 Å) and smaller cavity (d ~ 3.3 Å)''.[159]

Lanthanide series containing luminescent MOFs were studied for sensing applications.[160] Metal ions of the lanthanide series combined with strongly absorbing ligands were used to prepare luminescent MOFs because light emission accompanies electronic transitions from d to f shells.[160,161] The luminescent metal ions include Tb(III), Eu(III), Dy(III), Sm, Nd(III), Gd(III), Er(III) and Yb(III). The strong absorption, emission and electronic transition occur due to organic linkers possessing significant conjugation via an extended π-system.[107] The electronic transitions usually only observed in organic ligands are π–π* and n–π*. Chen *et al*.[161] tuned the luminescent properties of MOFs by generating a series of mixed-metal (Tb^{3+}, Eu^{3+}) MOFs.[160] In this research, a source of Eu^{3+} was doped into a $[Tb_2(dmbdc)_3]_n$ (2,5-dimethoxy-1,4-benzenedicarboxylate) framework to synthesize mixed-lanthanide MOFs, $Eu_{0.0069}Tb_{0.9931}$-dmbdc compound which exhibited temperature-dependent luminescence colours turning from green-yellow to red upon heating from 10 to 300 K[160] as shown in Figure 1.17.

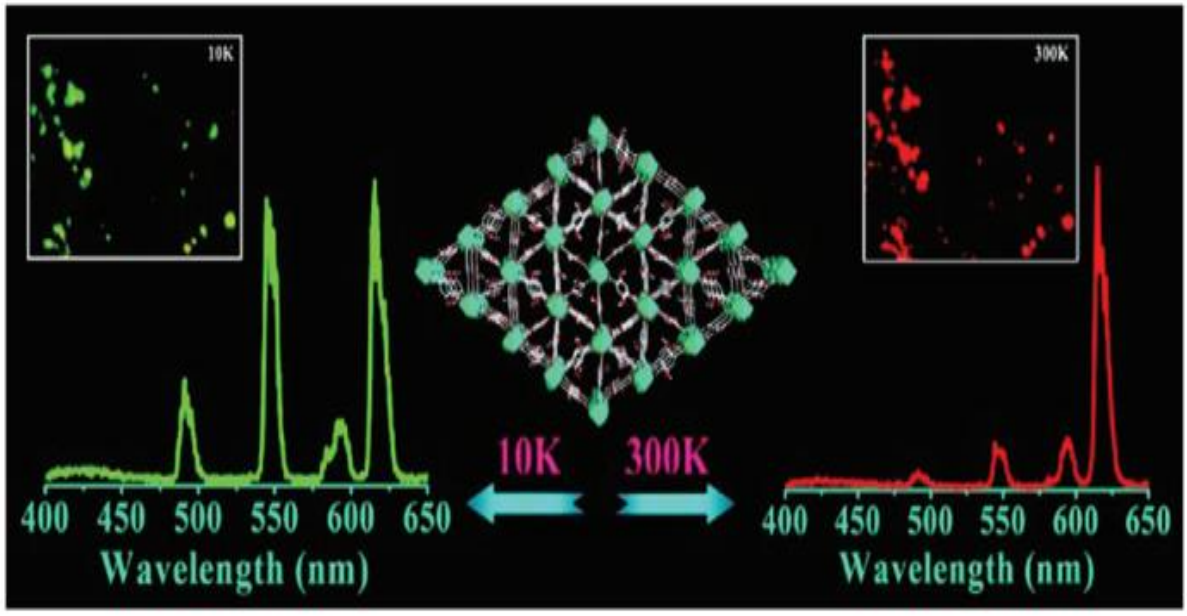


Figure 1.17: Snapshots of the structure, luminescence and emission spectra of the $Eu_{0.0069}Tb_{0.9931}$-dmbdc MOF at 10 and 300 K upon excitation at 312 nm.[161]

To further explore the applications of mixed–Lanthanide MOFs, Chen *et al*.[161,162] incorporated a new organic ligand with a higher triplet state energy (H_2pia = 5-(pyridin-4-yl) isophthalic acid) to form luminescent $Tb_{0.9}Eu_{0.1}$PIA thermometers which demonstrated a much higher relative sensitivity of 3.53% K^{-1}, higher than all other kinds of luminescent thermometers. Carlos et al.163 also developed a luminescent nanothermometer to measure the physiological temperatures in biological applications. The $Tb_{0.99}Eu_{0.01}$-(BDC)1.5(H_2O)$_2$ MM-MOF was used as a temperature sensor in the physiological range (300–320 K), with high sensitivities in both water media and as a solid probe. Additionally, Qian *et al*.[164] designed a NdYb-MOF for temperature sensing in the range of 293 K to 313 K under laser pumping. Additionally, luminescent MOFs were designed as turn-off or turn-on sensors for organic molecules, particularly nitroaromatic explosives. Huang .[165] reported the application of a $Tb_{0.01}Gd_{0.99}$L MM-MOF (H_4L = [1,1’ :4’ ,1’’-terphenyl]-2’ ,4,4’’,5’ -tetracarboxylic acid) for the detection of picric acid.

Anion recognition is a crucial area of investigation playing a pivotal role especially in the biological and chemical processes. Dong et al.166 synthesized a cationic porous fluorene-based MOF to explore the domain of MOFs for anion recognition. The

molecular formula of the compound was found as ($[CuL_2(H_2O)_{0.5}](NO_3)_2.3.25(CH_2Cl_2).(CH_3OH).0.5H_2O$) where L = 4,40 -(9,9-dibutyl.9H-fluorene-2,7-diyl)dipyridine.[166]. The MOF was a one-dimensional channel with nitrate anions aligning through the channel. The anion exchange ability of the MOF was investigated by immersing the desolvated framework in the aqueous solution of NaCl, KBr, KI, KSCN and NaN_3. The successful anionic exchange was associated with developing a rapid, visible colourimetric transition. The inclusion of anions in the framework was monitored by FT-IR analysis, displaying characteristic peaks for both nitrate and each anion. A partial exchange of anions was observed.[166]

Dong *et al*.[167] also synthesized Cu(I) based MOF viz. [H_2O. $Cu_2(L)_2I_2$; wherein L = 1-benzimidazolyl-3,5-bis(4-pyridyl)benzene] for detection of small polar aliphatic volatile organic compounds.[167] With the aid of single crystal X-ray diffraction. The interaction site of the MOF was probed, thus enabling the detection of the MeOH, EtOH, n-propanol, CH_2Cl_2, $CHCl_3$ and the hydrogen bonding interaction existing between host–guest.[167]

1.4 Aims and objectives

The inclusion of alkali metal ions into an adsorbent is a strategy to improve gas affinity and the corresponding gas sorption performance of MOF materials.[168] Many theoretical computational studies have justified the impact of alkali metal incorporation on MOF adsorptive performance.[169-171] However, only a few MOFs featuring alkaline metal sites exhibit open porous structures due to the competing role of alkaline ions in the coordination assembly process of MOFs and the uncertainty of their coordination geometry. Consequently, the influence of alkali metal incorporation into MOF materials on the adsorption of N_2, CH_4, H_2 and CO_2 capture has been relatively less investigated.[168,169,172]

This research primarily aims at synthesizing and characterising novel self-assembled metal-organic frameworks by direct solvothermal synthesis. Solvothermal methods were employed for bimetallic metal-organic framework from zinc, lanthanum and alkali metal (potassium and lithium) using carboxylate linkers as organic linkers.

Chapter 2 explains the characterization methods used to analyse our samples in these studies. Chapter 3 will focus on the synthesis and characterization of zinc/alkali-metal organic framework with zinc-potassium and zinc-lithium MOF system in focus, and

chapter 4 explains the gas adsorption and separation studies of zinc-potassium and zinc-lithium MOF system synthesized in chapter 3. Chapter 5 discusses the synthesis, characterization, and gas adsorption properties of lanthanum/alkali metal-organic frameworks with lanthanum-potassium and lanthanum-lithium MOF systems in focus. The last chapter, six, compiles the studies' conclusions in chapters 1 to 5.

1.5 References

1. L. Chen, H. Wang, C. Li and Q. Xu, *Chem. Sci.,* 2020, **11**, 5369.

2. S. Kitagawa, R. Kitaura and S. I. Noro, *Angew. Chem., Int. Ed.,* 2004, **43**, 2334–2375.

3. H. Furukawa, K. E. Cordova, M. O'Keeffe and O. M. Yaghi, *Science,* 2013, **341**, 974–986.

4. S. J. Dalgarno , P. K. Thallapally, L. J. Barbour and J. L. Atwood, *Chem. Soc. Rev.,* 2007, **36(2)**, 236–245.

5. O. Shekhah, J. Liu, R. A. Fischer and C. Wöll, *Chem. Soc. Rev.,* 2011,**40**, 1081-1106.

6. H. K. Chae, D. Y. Siberio-Pérez, J. Kim, Y. Go, M. Eddaoudi, A. J. Matzger, M. O'Keeffe and O. M. Yaghi, *Nature,* 2004, **427,** 523–527.

7. A. J. Howarth, A. W. Peters, N. A. Vermeulen, T. C. Wang, J. T. Hupp and O. K. Farha, *Chem. Mater.,* 2017, **29**, 26−39.

8. E. A. Tomic, *J. Appl. Polym.,* Sci. 1965, **9**, 3745−3752.

9. H. F. Hoskins and R. Robson, *J. Am. Chem. Soc.*, 1990, **112**, 1546−1554.

10. O. M. Yaghi and Li, H. Li, *J. Am. Chem. Soc.*, 1995, **117**, 10401−10402.

11. M. Kondo, T. Yoshitomi, H. Matsuzaka, S. Kitagawa and K. Seki, *Angew. Chem., Int. Ed. Engl.*, 1997, **36**, 1725−1727.

12. H. Li, M. Eddaoudi, M. O'Keeffe and O. M. Yaghi, *Nature,* 1999, **402**, 276−279.

13. G. Ferey, C. Mellot-Draznieks, C. Serre, F. Millange, J. Dutour,´ S. Surble and I. Margiolaki, *Science*, 2005, **309**, 2040−2042.

14. H. Furukawa, Y. B. Go, N. Ko, Y. K. Park, F. J. Uribe-Romo, J. Kim, M. O'Keeffe and O. M, Yaghi, *Inorg. Chem.,* 2011, **50**, 9147−9152.

15. H. Furukawa, N. Ko, Y. B. Go, N. Aratani, S. B. Choi, E. Choi, A. O. Yazaydin, R. Q. Snurr, M. O'Keeffe, J. Kim and O. M. Yaghi, O. M, *Science*, 2010, **329**, 424−428.

16. K. Koh, A. G. Wong-Foy and A. J. Matzger, *J. Am. Chem. Soc.*, 2009, **131**, 4184−4185.

17. J. R. Li, R. J. Kuppler and H. C. Zhou, *Chem. Soc. Rev.,* 2009, **38**, 1477−1504.

18. J. Lee, O. K. Farha, J. Roberts, K. A. Scheidt, S. T. Nguyen and J. T. Hupp, *Chem. Soc. Rev.*, 2009, **38**, 1450−1459.

19. J. M. Falkowski, S. Liu and W. Lin, *Isr. J. Chem.* 2012, **52**, 591−603.

20. J. Gascon, A. Corma, F. Kapteijn and F. X. Llabres I Xamena, *ACS Catal.* 2014, **4**, 361−378.

21. T. M. McDonald, J. A. Mason, X. Kong, E. D. Bloch, D. Gygi, A. Dani, V. Crocella, F. Giordanino, S. O. Odoh, W. S. Drisdell, B. Vlaisavljevich, A. L. Dzubak, R. Poloni, S. K. Schnell, N. Planas, K. Lee, T. Pascal, L. F. Wan, D. Prendergast, J. B. Neaton, B. Smit, J. B. Kortright, L. Gagliardi, S. Bordiga, J. A. Reimer and J. R. Long, *Nature,* 2015, **519**, 303−308.

22. J. B. DeCoste and G. W. Peterson, *Chem. Rev.,* 2014, **114**, 5695−727.

23. A. J. Howarth, Y. Liu, J. T. Hupp and O. K. Farha, *CrystEngComm*, 2015, **17**, 7245−7253.

24. P. Nugent, Y. Belmabkhout, S. D. Burd, A. J. Cairns, R. Luebke, K. Forrest, T. Pham, S. Ma, B. Space, L. Wojtas, M. Eddaoudi and M. J. Zaworotko, *Nature*, 2013, **495**, 80−84.

25 X. Cui, K. Chen, H. Xing, Q. Yang, R. Krishna, Z. Bao, H. Wu, W. Zhou, X. Dong, Y. Han, B. Li, Q. Ren, M. J. Zaworotko and B. Chen, *Science*, 2016, **353**, 141−144.

26. P. Horcajada, C. Serre, M. Vallet-Regí, M. Sebban, F. Taulelle and G. Ferey, *Angew. Chem., Int. Ed.*, 2006, **45**, 5974−5978.

27. R. C. Huxford, J. D. Rocca and W. Lin, *Curr. Opin. Chem. Biol.* 2010, **14**, 262−268.

28. D. E. Williams and N. B. Shustova, *Chem. Eur. J.*, 2015, **21**, 15474−15479.

29. L. E. Kreno, K. Leong, O. K. Farha, M. Allendorf, R. P. Van Duyne and J. T. Hupp, *Chem. Rev.* 2012, **112**, 1105−1125.

30. Z. Hu, B. J. Deibert and J. Li, *Chem. Soc. Rev.*, 2014, **43**, 5815−5840.

31. L. Sun, M. G. Campbell and M. Dinca, *Angew. Chem., Int. Ed.* 2016, **55**, 3566−3579.

32. J. E. Mondloch, M. J. Katz, W. C. Isley, P. Ghosh, P. Liao, W. Bury, G. W. Wagner, M. G. Hall, J. B. DeCoste, G. W. Peterson, R. Q. Snurr, C. J. Cramer, J. T. Hupp and O. K. Farha, *Nat. Mater.* 2015, **14**, 512−516.

33. S. Y. Moon, Y. Liu, J. T. Hupp and O. K. Farha, *Angew. Chem., Int. Ed.* 2015, **54**, 6795−6799.

34. X. Zhao, X. Bu, T. Wu, S. T. Zheng, L. Wang and P. Feng, *Nat. Commun.* 2013, **4**, 2344.

35. N. Stock and S. Biswas, *Chem. Rev.,* 2012, **112**, 933–969.

36. J. Jiang, Y. Zhao and O. M. Yaghi, *J. Am. Chem. Soc.,* 2016, **138**, 3255−3265.

37 O. Karagiaridi, W. Bury, J. E. Mondloch, J. T. Hupp and O. K. Farha, *Angew. Chem.,* Int. Ed. 2014, **53**, 4530−4540.

38. M. Lalonde, W. Bury, O. Karagiaridi, Z. Brown, J. T. Hupp, and O. K. Farha, *J. Mater. Chem. A*, 2013, **1**, 5453−5468.

39. C. K. Brozek and M. Dinca, *Chem. Soc. Rev.* 2014, **43**, 5456−5467.

40. S. Abednatanzi, P. G. Derakhshandeh, H. Depauw, F. Coudert, H. Vrielinck, P. Van Der Voort and K. Leus, *Chem. Soc. Rev*., 2019, **48**, 2535—2565.

41. N. Li, J. Xu, R. Feng, T. L. Hu and X. H. Bu, *Chem. Commun*., 2016, **52**, 8501–8513.

42. V. Colombo, S. Galli, H. J. Choi, G. D. Han, A. Maspero, G. Palmisano, N. Masciocchi and J. R. Long, *Chem. Sci*., 2011, **2**, 1311–1319.

43. R. K. Hocking and T. W. Hambley, *Inorg. Chem.*, 2003, **42**, 2833–2835.

44. V. M. Goldschmidt, *Trans. Faraday Soc.*, 1929, **25**, 253–283.

45. L. Pauling, *J. Am. Chem. Soc.*, 1927, **49**, 765–790.

46. A. K. Cheetham, G. Kieslich and H. H. M. Yeung, *Acc. Chem. Res.,* 2018, **51**, 659–667.

47. F. Nuar, T. Devic, H. Chevreau, N. Guillou, E. Gibson, G. Clet, M. Daturi, A. Vimont, J. M. Greneche, M. I. Breeze, R. I. Walton, P. L. Llewellyne and C. Serre, *Chem. Commun*., 2012, **48**, 10237–10239.

48. S. Wongsakulphasatch, F. Nouar, J. Rodriguez, L. Scott, C. Le Guillouzer, T. Devic, P. Horcajada, J. M. Greneche, P. L. Llewellyn, A. Vimont, G. Clet, M. Daturi and C. Serre, *Chem. Commun.,* 2015, **51**, 10194–10197.

49. Y. Jiao, C. R. Morelock, N. C. Burtch, W. P. Mounfield, J. T. Hungerford and K. S. Walton, *Ind. Eng. Chem. Res.*, 2015, **54**, 12408–12414.

50. L. J. Wang, H. X. Deng, H. Furukawa, F. Gandara, K. E. Cordova, D. Peri and O. M. Yaghi, *Inorg. Chem*., 2014, **53**, 5881–5883.

51. X. Song, S. Jeong, D. Kim and M. S. Lah, *CrystEngComm,* 2012, **14**, 5753–5756.

52. H. H. Fei, J. F. Cahill, K. A. Prather and S. M. Cohen, *Inorg. Chem*., 2013, **52**, 4011–4016.

53. J. P. Tu, X. L. Zeng, F. J. Xu, X. Wu, Y. F. Tian, X. D. Hou and Z. Long, *Chem Commun.*, 2017, **53**, 3361-3364.

54. X. Song, S. Jeong, D. Kim and M. S. Lah, *CrystEngComm,* 2012, **14**, 5753–5756.

55. S. Das, H. Kim and K. Kim, *J. Am. Chem. Soc.,* 2009, **131**, 3814–3815.

56. C. K. Brozek and M. Dinca, *J. Am. Chem. Soc.*, 2013, **135**, 12886–12891.

57. E. García-Pérez, J. Gascón, V. Morales-Flórez, J. M. Castillo, F. Kapteijn and S. Calero, *Langmuir*, 2009, 25, **3**, 1725-1731.

58. X. Kong, E. Scott, W. Ding, J. A. Mason, J. R. Long and J. A. Reimer, *J Am Chem Soc*., 2012, 134, **35**, 14341-4.

59. H. Furukawa, M. A. Miller and O. M. Yaghi, *J. Mater. Chem*., 2007, **17**, 3197.

60 J. Tao, M. L. Tong and X. M. Chen, *J.Chem. Soc. Dalton Trans.,* 2000, 3669-3674.

61. O. M. Yaghi, C. E. Davis, G. Li and H. Li, *J. Am. Chem. Soc.,* 1997, **119**, 2861-2868.

62. R. L. Rardin, W. B. Tolman and S. J. Lippard, *New J. Chem.,* 1991, **15**, 417.

63. H. K. Fun, S. S. S. Raj, R. G. Xiong, J. L. Zuo, Z. Yu and X. Z. You, *J. Chem. Soc., Dalton Trans.,* 1999, 1915.

64. A. V. Desai, S. Sharma. S. Let and S. K. Ghosh, *Coord. Chem. Rev*., 2019, **395**, 146–192.

65. A. Phan, C. J. Doonan, F. J. Uribe-Romo, C. B. Knobler, M. O'Keeffe and O. M. Yaghi, *Acc. Chem. Res.,* 2010, **43**, 58–67.

66. S. Horike, S. Shimomura and S. Kitagawa, *Nat. Chem.,* 2009, **1**, 695–704.

67. B. Manna, A. V. Desai and S. K. Ghosh, *Dalton Trans.,* 2016, **45**, 4060–4072.

68. N. V. Izarova, M. N. Sokolov, A. Rothenberger, L. Ponikiewski, D. Fenske and V.P. Fedin, *Comptes Rendus Chim*., 2005, **8**, 1005–1010.

69. Y. P. Wu, X.-Q. Wu, J. F. Wang, J. Zhao, W. W. Dong, D. S. Li and Q. C. Zhang, *Cryst. Growth Des.*, 2016, **16**, 2309–2316.

70. J. Zhao, W. W. Dong, Y. P. Wu, Y. N. Wang, C. Wang, D.-S. Li and Q.-C. Zhang, *J. Mater. Chem.,* A., 2015, **3**, 6962–6969.

71. G. Zhang, G. Wei, Z. Liu, S. R. J. Oliver and H. Fei, *Chem. Mater*., 2016, **28**, 6276– 6281.

72. G. Zhang, H. Yang and H. Fei, *ACS Catal.,* 2018, **8,** 2519–2525.

73. P. Z. Moghadam, A. Li, X. W. Liu, R. Bueno-Perez, S. D. Wang, S. B. Wiggin, P. A. Wood and D. Fairen-Jimenez*, Chem. Sci.*, 2020, **11**, 8373 —8387.

74. L. Carlucci, G. Ciani, D. M. Proserpio and F. Porta, *CrystEngComm.,* 2006, **8**, 696-706.

75. Y. Q. Tian, Z. X. Chen, L. H. Weng, H. B. Guo, S. Gao and D. Y. Zhao, *Inorg. Chem.*, 2004, **43**, 4631–4635.

76. M. H. Mohamed, S. K. Elsaidi, L. Wojtas, T. Pham, K. A. Forrest, B. Tudor, B. Space and M. J. Zaworotko, *J. Am. Chem. Soc.* 2012, **134**, 19556–19559.

77. H. Guo, Y. Zhu, S. Wang, S. Su, L. Zhou and H. Zhang, *Chem. Mater*., 2012, **24**, 444–450.

78. C. R. Marshall, S. A. Staudhammer and C. K. Brozek, *Chem. Sci.*, 2019, **10**, 9396–9408.

79. R. S. Forgan, *Chem. Sci.,* 2020, **11**, 4546–4562.

80. H. Guo, Y. Zhu, S. Wang, S. Su, L. Zhou and H. Zhang, *Chem. Mater*., 2012, **24**, 444–450.

81. A. Schaate, P. Roy, A. Godt, J. Lippke, F. Waltz, M. Wiebcke and P. Behrens, *Chem.–Eur. J*., 2011, **17**, 6643–6651.

82. S. Øien, D. Wragg, H. Reinsch, S. Svelle, S. Bordiga, C. Lamberti and K. P. Lillerud, *Cryst. Growth Des.,* 2014, **14**, 5370–5372.

83. H. Xu, S. Sommer, N. L. N. Broge, J. Gao and B. B. Iversen, *Chem.–Eur. J.*, 2019, **25**, 2051–2058.

84. R. J. Marshall, C. L. Hobday, C. F. Murphie, S. L. Griffin, C. A. Morrison, S. A. Moggach and R. S. Forgan, *J. Mater. Chem. A*, 2016, **4**, 6955–6963.

85. O. V. Gutov, S. Molina, E. C. Escudero-Adán and A. Shafir, *Chem.–Eur. J.*, 2016, **22**, 13582–13587.s

86. C. L. Hobday, R. J. Marshall, C. F. Murphie, J. Sotelo, T. Richards, D. R. Allan, T. Düren, F. X. Coudert, R. S. Forgan, C. A. Morrison, S. A. Moggach and T. D. Bennett, *Angew. Chem., Int. Ed.*, 2016, **55**, 2401–2405.

87. L. Yang, T. Zhao, I. Boldog, C. Janiak, X.-Y. Yang, Q. Li, Y. J. Zhou, Y. Xia, D. W. Lai and Y. J. Liu, *Dalton Trans.*, 2019, **48**, 989–996.

88. J. H. Cavka, S. Jakobsen, U. Olsbye, N. Guillou, C. Lamberti, S. Bordiga and K. P Lillerud, *J. Am. Chem. Soc.,* 2008, **130**, 13850–13851.

89. N. Ko, J. Hong, S. Sung, K. E. Cordova, H. J. Park, J. K. Yang and J. Kim, *Dalton Trans..*2015, **44,** 2047–2051.

90. Z. Hu, M. Khurana, Y.H. Seah, M. Zhang, Z. Guo and D. Zhao, *Chem. Eng. Sci.,* 2015, **124**, 61–69.

91. V. V. Butova, M. A. Soldatov, A. A. Guda, K. A. Lomachenko and C. Lamberti, *Russ. Chem. Rev.,* 2016, **85**, 280-307.

92. C. Dey, T. Kundu, B. P. Biswal, A. Mallick and R. Banerjee, *Acta Cryst.,* 2014, **B70**, 3-10.

93. A. Martinez Joaristi, J. Juan-Alcaniz, P. Serra-Crespo, F. Kapteijn and J. Gascon, *Cryst. Growth Des.,* 2012, **12,** 3489–3498.

94. U. Mueller, M. Schubert, F. Teich, H. Puetter, K. Schierle-Arndt and J. PastreÂ, *J. Mater. Chem.,* 2006, **16,** 626-636.

95. J. F. Fernandez-Bertran, *Pure Appl. Chem.,* 1999, **71**, 581.

96. V. V. Boldyrev and K. J. Tkacova, *Mater. Synth. Proc*., 2000, **8**, 121.

97. A. Lazuen-Garay, A. Pichon and S. L. James, *Chem. Soc. Rev.*, 2007, **36**, 846.

98. T. Friscic and L. Fabian, *CrystEngComm.,* 2009, **11**, 743.

99. W. Yuan, T. Friscic, D. Apperley and S. L. James, *Angew. Chem.*, Int. Ed. 2010, **49**, 3916.

100. T. Friscic, D. G. Reid, I. Halasz, R. S. Stein, R. E. Dinnebier and M. J. Duer, *Angew. Chem.,* Int. Ed. 2010, **49**, 712.

101. T. J. Friscic, *Mater. Chem.,* 2010, **20**, 7599.

102. A. Pichon, A. Lazuen-Garay and S. L. James, *CrystEngComm.,* 2006, **8**, 211.

103. A. Pichon and S. L. James, *CrystEngComm.*, 2008, **10**, 1839.

104. V. V. Butova, M. A. Soldatov, A. A. Guda, K. A. Lomachenko and C. Lamberti, *Russ. Chem. Rev.,* 2016, **85**, 280-307.

105. K. Fujii, A. Lazuen-Garay, J. Hill, E. Sbircea, Z. Pan, M. Xu, D. C. Apperley, S. L. James and K. D. M. Harris, *Chem. Commun.*, 2010, **46**, 7572.

106. T. Friscic, I. Halasz, P. J. Beldon, A. M. Belenguer, F. Adams, S. A. Kimber, V. Honkimaki and R. E. Dinnebier, *Nat. Chem.,* 2013, **5**, 66–73.

107. C. Dey, T. Kundu, B. P. Biswal, A. Mallick and R. Banerjee, *Acta Cryst.,* 2014, **B70**, 3-10.

108. M. Saidi, A. Benomara, M. Mokhtari and L. Boukli-Hacene, *Reac Kinet Mech Cat.*, 2020, **131,** 1009 -1021**.**

109. J. David, G. Trolliard, C. Volkringer, T. Loiseau, O. Masson and A. Maître, *J Alloys Compd*., 2016, **680**, 571–585.

110. G. Wißmann, A. Schaate, S. Lilienthal, I. Bremer, A. M. Schneider and P. Behrens, *Microporous Mesoporous Mater.*, 2012, **152**, 64–70.

111. G. Zahn, H. Albert Schulze, J. Lippke, S. König, U. Sazama, M. Fröba and P. Behrens, *Microporous Mesoporous Mater*., 2015, **203**, 186–194.

112. L. G. Qiu, Z.-Q. Li, Y. Wu, W. Wang, T. Xu and S. Jiang, *Chem. Commun*., 2008, 3642.

113. D. M. P. Mingos and D. R. Baghurst, *Chem. Soc. Rev.,* 1991, **20**, 1.

114. C. O. Kappe, *Chem. Soc. Rev.,* 2008, **37**, 1127.

115. J. Klinowski, F. A. A. Paz and J. Rocha, *J. Dalton Trans.*, 2011, **40**, 321.

116. S. H. Jhung, J. H. Lee and J. S. Chang, *Bull. Korean Chem. Soc.*, 2005, **26**, 880.

117. S. H. Jhung, J. H. Lee, J. W. Yoon, C. Serre, G. Ferey and J. S. Chang, *Adv. Mater.,* 2007, **19**, 121.

118. N. A. Khan, I. J. Kang, H. Y. Seok and S. H. Jhung, *Chem. Eng. J*., 2011, **166**, 1152.

119. G. Ferey, C. Mellot-Draznieks, C. Serre, F. Millange, J. Dutour, S. Surble and I. Margiolaki, *Science,* 2005, **309**, 2040−2042.

120. O. K. Farha and J. T. Hupp, *Acc. Chem. Res.* 2010, **43**, 8, 1166–1175.

121. O. K. Farha, K. L. Mulfort, A. M. Thorsness and J. T. Hupp, *J. Am. Chem. Soc.* 2008, 130, **27**, 8598–8599.

122. M. Eddaoudi, J. Kim, N. Rosi, D. Vodak, J. Wachter, M. O'Keeffe and O. M. Yaghi, *Science* (80-), 2002, **295** (5554), 469–472.

123. J. J. Zhang, L. Wojtas, R. W. Larsen, M. Eddaoudi and M. J. Zaworotko, *J. Am. Chem. Soc.* 2009, 131, **47**, 17040–17041.

124. C. Serre, F. Millange, C. Thouvenot, M. Noguès, G. Marsolier, D. Louër and G. Férey, *J. Am. Chem. Soc.,* 2002, 124, **45**, 13519–13526.

125. T. Loiseau, C. Serre, C. Huguenard, G. Fink, F. Taulelle, M. Henry, T. Bataille and G. Férey, A *Chem. - A Eur. J.,* 2004, 10, **6**, 1373–1382.

126. A. Dauth and J. A. Love, *Dalt. Trans.,* 2012, 41, **26**, 7782.

127. J. E. Mondloch, O. Karagiaridi, O. K. Farha and J. T. Hupp, *CrystEngComm*., 2013, **15**, 9258−9264.

128. S. M. Ramish, A. Ghorbani-Choghamarani and M. Mohammadi*, Scientific Reports,* 2022, **12**, 1479.

129. L. W. Rogowski, J. Ali , X. Zhang, J. N Wilking, H. C. Fu and M. J. Kim, *Nat. Commun.,* 2021, **12,** 1116.

130. Y. Hu, B. Jiang, Y. Weng, Z. Sui, B. Zhao, Y. Chen, L. Liu, Q. Wu, Z. Liang, L. Zhang and Y. Zhang, *Nat. Commun.,* 2020. **11,** 6226.

131. Y. Ding, Y. Yan, H. Wang, X. Wang, T. Hu, S. Tao and G. Li, *ACS Appl. Mater. Interfaces*., 2018, **10**, 41793–41801.

132. Y. Feng, Y. Shao, X. Chen, Y. Zhang, Q. Liu**,** M. He and H. Li**,** *ACS Appl. Energy Mater.,* 2021, **4**, 633–642.

133. X. Wang, H. Xiao, A. Li, Z. Li, S. Liu, Q. Zhang, Y. Gong, L. Zheng, Y. Zhu, C. Chen, D. Wang, Q. Peng, L. Gu, X. Han, J. Li and Y. Li, *J. Am. Chem. Soc.,* 2018, **140**, 15336.

134. X. Zhao, B. Pattengale, D. Fan, Z. Zou, Y. Zhao, J. Du, J. Huang and C. Xu, *ACS Energy Lett.*, 2018, **3**, 2520.

135. F. L. Li, Q. Shao, X. Huang and J. P. Lang, *Angew. Chem. Int. Ed. Engl.*, 2018, **57**, 1888.

136. R. Lippi, S. C. Howard, H. Barron, C. D. Easton, I. C. Madsen, L. J. Waddington, C. Vogt, M. R. Hill, C. J. Sumby, C. J. Doonan and D. F. Kennedy, *J. Mater. Chem.,* 2017, **5**, 12990.

137. S. M. Ramish, A. Ghorbani-Choghamarani and M. Mohammadi*, Scientific Reports,* 2022, **12**, 1479.

138. M. Kazemi and M. Mohammadi, *Appl. Organomet. Chem.,* 2020, **34**, e5400.

139. C. G. Evans and J. E. Gestwicki, *Org. Lett.,* 2009, **11**, 2957–2959.

140. T. Zurrer, K. Wong, J. Horlyck, E. C. Lovell, J. Wright, N. M. Bedford, Z. Han, K. Liang, J. Scott, and R. Amal, *Adv. Funct. Mater.*, 2021, **31**, 2007624.

141. H. F. Yao, Y. Yang, H. Liu, F. G. Xi and E. Q. Gao, *J. Mol. Catal. A Chem*. 2014, 394, 57– 65.

142. L. Mitchell, P. Williamson, B. Ehrlichov, A. E. Anderson, V. R. Seymour, S. E. Ashbrook, N. Acerbi, L. M. Daniels, R. I. Walton and M. L. Clarke, *Chem. - A Eur. J.,* 2014, **20 (51)**, 17185–17197.

143. F. G. Cirujano, and F. X. Llabrés i Xamena, *Dalt. Trans*., 2012, **41(14)**, 4249.

144. D. Jagadeesan, *Appl. Catal. A Gen*., 2016, **511**, 59–77.

145. H. Li, K. Wang, Y. Sun, C. T. Lollar, J. Li and H. Zhou, *Mater. Today*, 2018, 21, **2**, 108 – 121.

146. J. Jiang, H. Furukawa, Y. Zhang and O. M. Yaghi, *J. Am. Chem. Soc.*, 2016, **138,** 10244–10251.

147. M. K. Taylor, T. Runčevski, J. Oktawiec, M. I. Gonzalez, R. L. Siegelman, J. A. Mason, J. Ye, C. M. Brown and J. R. Long, *J. Am. Chem. Soc.,* 2016, **138**, 15019–15026.

148. K. Wang, D. Feng, T. F. Liu, J. Su, S. Yuan, Y. P. Chen, M. Bosch, X. Zou. and H. C. Zhou, *J. Am. Chem. Soc.,* 2014, **136** (40), 13983–13986.

149. J. Jiang, H. Furukawa, Y. Zhang and O. M. Yaghi, *J. Am. Chem. Soc.*, 2016, **138,** 10244–10251.

150. M. H. Mohamed, S. K. Elsaidi, L. Wojtas, T. Pham, K. A. Forrest, B. Tudor, B. Space and M. J. Zaworotko, *J. Am. Chem. Soc.,* 2012, **134**, 19556–19559.

151. J. A. Villajos, G. Orcajo, C. Martos, J. A. Botas, J. Villacanas and G. Calleja, *Int. J. Hydrogen Energy,* 2015, **40**, 5346–5352.

152. M. Dinca and J. R. Long, *J. Am. Chem. Soc.,* 2007, **129**, 11172–11176.

153. W. W. Lestari, D. Ni'maturrohmah R. Putra, H. Suwarno and U. S. F. Arrozi, *IOP Conf. Ser.: Mater. Sci. Eng.*, 2019, **509**, 012152.

154. S. S. Kaye, A. Dailly, O. M. Yaghi and J. R. Long, *J. Am. Chem. Soc.,* 2007, 129, **46**, 14176-14177.

155. A. G. Wong-Foy, A. J. Matzger and O. M. Yaghi, *J. Am. Chem. Soc.*, 2006, **128**, 3494– 3495.

156. J. A. Villajos, G. Orcajo, C. Martos, J. A. Botas, J. Villacanas and G. Calleja, *Int. J. Hydrogen Energy*., 2015, **40**, 5346–5352.

157. C. Tan, S. Yang, X. Lin, A. J. Blake, W. Lewis, N. R. Champness and M. Schröder. *Chem. Commun.,* 2011, **47**, 4487-4489.

158. W. P. Lustig, S. Mukherjee, N. D. Rudd, A. V. Desai, J. Li and S. K. *Ghosh, Chem. Soc. Rev.,* 2017, **46,** 3242–3285.

159. J. W. Ye, H. L. Zhou, S. Y. Liu, X. N. Cheng, R. B. Lin, X. L. Qi, J. P. Zhang and X. M. Chen, *Chem. Mater.*, 2015, **27,** 8255–8260.

160. M. L. Reddy and S. Sivakumar, *Dalton Trans*., 2013, **42**, 2663–2678.

161. Y. Cui, H. Xu, Y. Yue, Z. Guo, J. Yu, Z. Chen, J. Gao, Y. Yang, G. Qian and B. Chen, *J. Am. Chem. Soc*., 2012, **134**, 3979–3982.

162. X. T. Rao, T. Song, J. K. Gao, Y. J. Cui, Y. Yang, C. D. Wu, B. L. Chen and G. D. Qian, *J. Am. Chem. Soc.,* 2013, **135**, 15559–15564.

163. A. Cadiau, C. D. S. Brites, P. M. F. J. Costa, R. A. S. Ferreira, J. Rocha and L. D. Carlos, *ACS Nano*, 2013, **7**, 7213–7218.

164. X. S. Lian, D. Zhao, Y. J. Cui, Y. Yang and G. D. Qian, *Chem. Commun.,* 2015, **51**, 17676–17679.

165. L. Li, J. H. Cheng, Z. P. Liu, L. Song, Y. J. You, X. H. Zhou and W. Huang, *ACS Appl. Mater. Interfaces,* 2018, **10**, 44109–44115.

166. J. P. Ma, Y. Yu and Y. B. Dong, *Chem. Commun*., 2012, **48,** 2946–2948.

167. Y. Lu, J. P. Ma, C. W. Zhao, J. Yang, X. M. Zhang, Q. K. Liu and Y. B. Dong, *Inorg. Chem.,* 2015, **54,** 11590–11592.

168. N. Li, Z. Chang, H. Huang, R. Feng, W. He, M. Zhong, D. G. Madden, M. J. Zaworotko and X. Bu, *Small,* 2019, **15**, 1900426.

169. M. Almasi, A. Sharma and T. Zelenka, *Inorganica Chimica Acta*, 2021, **526**, 120505.

170 R. Babarao, R and J.W. Jiang, *Langmuir*, 2008, **24**, 6270–6278.

171. Z. H. Xiang, Z. Hu, D. P. Cao, W. T. Yang, J. M. Lu, B. Y. Han and W. Wang, *Angew. Chem. Int. Edit.*, 2011, **50**, 491–494.

172. L. Song, C. Xue, H. Xia, S. Qiu, L. Sun and H. Chen, *Materials,* 2019, **12**, 844.

Chapter 2: Characterization Techniques

2.0. Reagents and Purification

All chemicals and dry solvents were sourced from Fluorochem, Alfa Aesar, Fisher Scientific, Sigma-Aldrich, or VWR International and used without further purification. Column chromatography was performed on silica gel 60A. Zinc nitrate and Lanthanum nitrate were purchased from Sigma-Aldrich and used as received. Anhydrous dichloromethane was purchased from Sigma-Aldrich (Fluka) and stored in a nitrogen atmosphere over 4 Å molecular sieves. Potassium tert butoxide and lithium-tert butoxide were purchased from Aldrich and used as received. The glassware used was flame-dried under vacuum and backfilled with dinitrogen. FTO glass slides were purchased from Sigma-Aldrich and washed using Alconox solution and rinsed with acetone and ethanol before use.

2.1 General Synthesis of Mixed-Metal Metal-Organic Framework

In this report, all MOF synthesis reactions were accomplished using the hydrothermal or solvothermal method, which involves the use of Teflon-lined autoclaves supplied by Parr Instrument Company. The 23 mL autoclave and a 40 mL autoclave were used in this work. Chemicals were purchased from commercial suppliers; Sigma Aldrich, VWR, Acros, and BDH chemicals. Typical MOF synthesis involves, a metal source (lanthanum nitrate or zinc nitrate, $Zn(NO_3)_2 \cdot 6H_2O$, Lithium *tert*-butoxide, potassium *tert*-butoxide) which is mixed with the organic linkers which are generally in the form of a carboxylic acid, in a solvent (DMF = N, N´- dimethylformamide) or a mixture of solvents, where the solvent controls the solubility, and therefore the availability of the organic linker during the crystallization. The MOF reactants were homogenized through 15 minutes of sonication before they were transferred into a Teflon-lined autoclave and solvothermal treated with different synthesis parameters, including temperature and heating times. After heating, the autoclaves are cooled under temperature control, and the mixtures are filtered and washed with solvent fresh DMF in solvent exchange with chloroform and finally with methanol. Then, the materials were dried overnight on a Schlenk line under nitrogen at 60 ^{o}C. The first characterization of the resulting single crystal was initially performed by Single Crystal X-ray diffraction (SCXRD); after drying and grinding, many other characterization

methods included SCXRD, PXRD, SEM/EDX, elemental analysis (CHN) and TGA prior to gas adsorption experiments.[1-4]

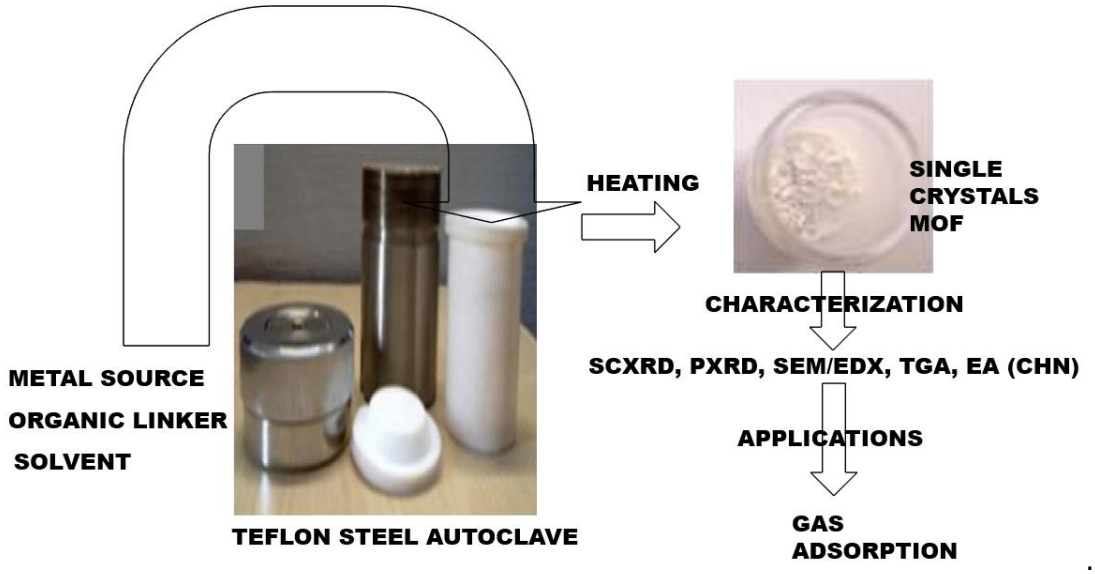


Figure 2.1: Summary of Synthesis Set–up and Characterisation techniques employed for MOFs in this thesis.

2.2. X-ray Diffraction (XRD)

Single crystal X-ray diffraction experiments were performed on an Oxford Diffraction SuperNova CCD area detector diffractometer at 120 K using monochromated Cu Kα radiation (λ = 1.54184 Å); on Agilent GV1000 AtlasS2 or TitanS2 CCD area detector diffractometers at 120 K using monochromated CuKα radiation (λ = 1.54184 Å); or at the UK Diamond Light Source I19-1 3- circle diffractometer4 (λ = 0.6889 Å). Absorption corrections were applied using analytical numerical methods using CrysAlisPro software.[5] Using Olex-2,[6] the structures were solved by direct methods using ShelXT7 and refined with ShelXL[8] using a least squares method. All hydrogen atoms were placed in geometrically calculated positions; non-hydrogen atoms were refined with anisotropic displacement parameters. Dr. Stephen Argent performed CIF checks. In specific cases, geometric restraints were applied. Details of crystal data can be found in the appendix section.

The powder x-ray diffraction (PXRD) data were obtained using a PANalytical MPD diffractometer equipped with a Cu anode X-ray tube, Kα1 monochromator (λ = 1.54184 Å). The recorded PXRD patterns were compared to those simulated from the crystallographic information files (CIFs) utilizing Mercury software. However, this

comparison cannot be relied upon because it cannot represent the bulk of the sample. Only one well-diffracting crystal is used to obtain the material's structure using SCXRD.

2.3 Scanning Electron Microscopy with Energy Dispersive X-Ray Analysis (EDX)

SEM images were acquired using a JEOL 7100F field emission gun scanning electron microscope. Samples were prepared on 10 mm aluminium with an adhesive carbon tab and coated with 8 nm layer of Iridium using a QUORUM QISOT ES coater. Imaging was conducted at a working distance of 10 mm and an electron gun accelerating potential of 15 kV.

2.4 Elemental Analysis (EA)

Chemical Elemental Analysis (CHN) is an analytical technique applied to determine the organic content of a material. The analysis determines the percentage weight of carbon (C), hydrogen (H) and nitrogen (N) using an automated elemental analyzer, which enables the determination of the C, H and N content of the MOF sample to an accuracy of 0.3%. This technique is executed by combustion or burning the sample in excess oxygen to form carbon dioxide, water and nitric oxide, which can be isolated and each element's weight percentage (wt %) calculated. Elemental analysis determined the relative amount of C, H, and N in the synthesized mixed metal metal-organic framework materials. Elemental analyses were performed by **CHN Elemental Microanalysis**, School of Chemistry, University of Nottingham, Nottingham, UK.

2.5 Infrared Spectroscopy (FTIR)

The Attenuated Total Reflectance Fourier Transformed Infrared (ATR-FTIR) spectra were obtained between 400-4000 cm^{-1} using a Bruker Tensor 27 spectrometer with an ATR attachment.

2.6. Gas Adsorption

Gas adsorption is an experimental method utilized to study surface properties, it is largely utilized to ascertain the pore volume, specific surface area and pore size distribution in porous materials.[1,2] Adsorption is defined as the concentration of gas molecules near the surface of a solid material. In chemistry, the adsorbed gas is termed an adsorbate and the solid on which adsorption takes place is known as the adsorbent.[1-3] Based on the nature and strength of interaction between adsorbate and

adsorbent, adsorption is categorized into chemisorption and physisorption. Chemisorption involves the formation of bonds, while in physisorption, only dispersive, dipole-charge and quadrupole interactions are involved. From the account of the literature, measurements are commonly taken at 298 K (25 ^{o}C) for H_2, CO_2, and CH_4, while 77 K (-196) and 273 K (0 ^{o}C) are also typical for H_2 and CO_2, respectively.[4-8]

A series of isotherms at various temperatures for a given adsorbate-sample pair are also reported to allow the determination of isosteric heats of adsorption Q_{st}.[9] For N_2, adsorption isotherms are usually measured at 77 K (-196 ℃), where interactions like those involved in the liquefaction of N_2 are involved. Physisorption involves physical adsorption comprising weak van der Waals forces between a gas molecule and solid adsorbent on contact. On the other hand, chemisorption involves stronger chemical attractive forces existing between the exposed surface of the solid and the gas molecules.

The external surface and the internal surface of the pores make up the surface area of the solid. However, because of the weak interaction (bonds) existing between gas molecules and the surface (<15 kJmol^{-1}), physical adsorption can be considered a reversible phenomenon that allows regeneration of the adsorbent and recovery of the adsorbates by decreasing pressure or increasing temperature.[4] Gas physisorption is generally nonselective, thus filling the surface layer by layer based on the available solid surface and the relative pressure. Adsorption isotherms represent mathematical models that describe the adsorption properties and interaction between the adsorbate and adsorbent at specific temperatures and pressures. Qualitative structural information can be extracted from the shape of a gas adsorption isotherm.[3]

Figure 2.2 shows the IUPAC classification of the sorption isotherms[1,3.] The six types of isotherms are described as follows:[1-3]

Type I isotherm is typical of monolayer chemisorption or physisorption on microporous materials solids. Usually, high adsorption at low relative pressure is recorded here due to the narrow pore width and the high adsorption potential so that micropore filling with increasing pressure and the absorbed amount approaches a limiting value as $P/P_o \rightarrow 1$. This is a common adsorption pattern in molecular sieves, zeolite and some activated carbon.

Type II isotherm describes the standard form of the isotherm on a non-porous or microporous material with strong adsorbate-adsorbent interaction, where unrestricted monolayer-multilayer adsorption can happen. Point B in this type of isotherm indicates the stage at which the monolayer coverage is completed then the multilayer adsorption occurs.

Type III isotherms are uncommon and show adsorption on non-porous or microporous adsorbents with relatively weak adsorbate-adsorbent interactions, but a stronger lateral interaction exists between adsorbed molecules, which then consequently clustered around the most favourable sites on the surface of a nonporous-or-macroporous-solid. The reversible Type III isotherm is convex to the P/P_o (x-axis) over its entire range.

Types IV and V adsorption isotherms are normally exhibited by mesoporous materials with pore diameters ranging between 2-50 nm. Examples of mesoporous adsorbents exhibiting Type IV isotherms include oxide gels, mesoporous molecular sieves, and industrial adsorbents. Characteristically, adsorption on mesoporous solids proceeds via multilayer adsorption followed by capillary condensation, making Type IV and V isotherms. Distinguishing features of the Type IV isotherm are its hysteresis loop, which is associated with capillary condensation taking place in mesopores, and the limiting uptake over a range of high P/P_0.[3] The initial part of the type IV isotherm can be attributed to mono-layer adsorption like that observed in isotherm type II, whereas in the type V isotherm the initial part is related to weak interaction between the adsorbent and adsorbate as in the case of type III isotherm. Type V isotherms have been recorded for water adsorption on hydrophobic microporous and mesoporous adsorbents.

Type VI describes the step-by-step multilayer adsorption on a uniform, non-porous surface. The step height shows the ability of each adsorbed layer, while the temperature and the environmental system dictate the sharpness of the step. The pattern is seen in some materials with relatively strong fluid-wall forces and usually occurs at a temperature very close to the melting point for the adsorbed gas. It can also be observed for MOFs that contain cages of different sizes. Type VI isotherms were recorded for krypton on graphitized carbons.[10-14]

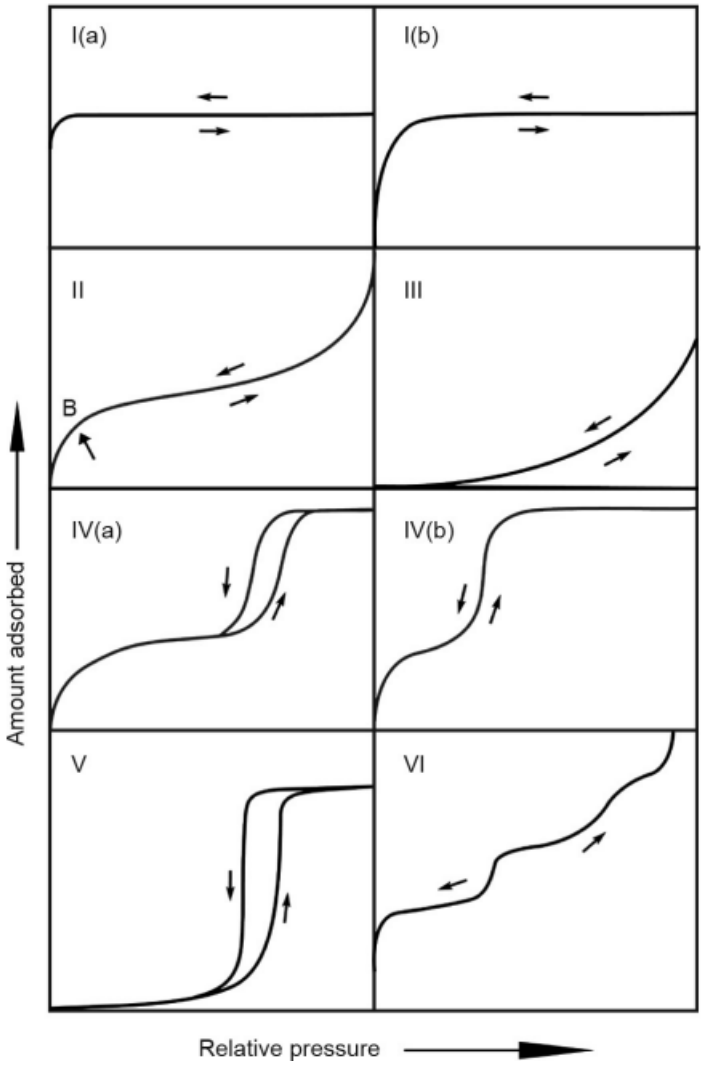


Figure 2.2: IUPAC Classification of physisorption isotherms. B represents monolayer formation.[1,3]

2.7 Determination of Surface Area and Porosity

The specific surface area analyzed through adsorption using the Brunauer, Emmett, and Teller (BET) isotherm was performed with a Quadrasorb SI (Quantachrome Instruments). Leo Blankenship, University of Nottingham, and Dr. David Madden of the University of Cambridge supplied all gas adsorption experimental data.

2.8 An Ideal Adsorbed Solution Theory (IAST) Method for Gas Separation Study

The adsorption selectivity, S_{ads}, is defined for separating a binary mixture of species 1 and 2 where q_1, q_2 and p_1, p_2 represent the amount of adsorbed and partial pressure of 'i' species in a binary gas mixture. In many CO_2 separation applications, the pressures P_1 and P_2 encountered are high, in the 1–10 MPa range, and

thermodynamic non-idealities are non-negligible. Therefore, we determined the binary mixture adsorption selectivities for the different MOFs at 298 K. In these calculations, the partial pressures of CO_2 and CH_4, CO_2 and N_2, CO_2 and H_2 are considered equal, that is, P_1=P_2.

Using the pure component isotherm fits, the adsorption selectivities defined by

$$S_{ads} = \frac{q_1/q_2}{P_1/P_2} \qquad \text{Equation (1)}$$

were determined using the Ideal Adsorbed Solution Theory (IAST) of Myers and Prausnitz.[15] The accuracy of the IAST calculations for estimating the component loadings for several binary mixtures in a wide variety of zeolites and MOFs has been well established by comparison with the Configurational-Biast Monte Carlo simulations of mixture adsorption.[15,16]

2.9 Isosteric heat of adsorption, Q_{st}

The isosteric heat of adsorption is the difference between the gaseous phase's molar enthalpy and the adsorbed phase's differential enthalpy.[17] Also, the heat of adsorption can be considered as the release of the kinetic energy from the molecules of the bulk phase being adsorbed onto the surfaces of the adsorbent.,[17,18] Isosteric heat of adsorption (Q_{st}) stands to be one of the properties required for the characterization and optimization of the adsorption process. It has been used for characterizing the surface of adsorbents.[19,20] An adsorbent is homogeneous and possesses a linear relationship if its isosteric heat of adsorption, Q_{st} is independent of the amount of adsorbate it adsorbs as shown in figure (2.3). However, heterogeneity of the adsorbent occurs if its Q_{st} varies with the amount of adsorbate adsorbed.[20] The surface area of MOF has an enormous effect on the isosteric heat of adsorption. A report by Kushwaha et al.[21] showed that increasing the Isosteric heat of adsorption for MOFs with large surface area results in higher hydrogen storage capacity.[21]

Kushwaha et al.[21] used Q_{st} to identify the adsorption mechanism of adsorbent further, and their study observed that the isosteric heat of adsorption (Q_{st}) for the adsorption of malachite green onto treated ice husk was chemisorption as Isosteric heat of adsorption (Q_{st}) found in their investigation was between 78 and 89 kJ·mol^{-1}.[21,22]

Bae and Snurr[20] defined the Isosteric heat of adsorption, $Q_{st,}$ as ‘’the ratio of the extremely small change in the adsorbate enthalpy to the infinitesimal change in the quantity adsorbed under constant temperature and pressure.[24,25] It is also defined as the heat of adsorption determined at constant surface coverage (q). Surface coverage is defined as:

$$\theta = \frac{q}{q_m} \qquad \text{Equation (2)}$$

Where ‘’q [mmol g^{-1}] – the amount of adsorbed CO_2 at given temperature and equilibrium pressure p; q_m [mmol g^{-1}] – the maximum amount of adsorbed CO_2 at given temperature’’.[19] The isosteric heat of adsorption was calculated using the Clausius–Clapeyron Equation (3)

$$Q_{st=-R\left(\frac{\partial \ln(p)}{\partial\left(\frac{1}{T}\right)}\right)_{\theta}} \qquad \text{Equation (3)}$$

Q_{st} is the isosteric heat of adsorption, R is the universal gas constant (8.314 J/mol/K), T (T_1 = 298 K; T_2 = 273 K) is the adsorption temperature, and P is the adsorption pressure.[26]

There are always variations in the isosteric heat of adsorption, $Q_{st;}$ hence, to estimate the isosteric heat for various adsorbent and adsorbate two pairs, Clasius-Clayperon and Van't Hoff equations are readily employed. The first assumption of these equations is that the adsorbed phase volume will be negligible compared to the gaseous phase and behave as an ideal gas. [1,26]

Isosteric heat of adsorption is a vital thermodynamic quantity in assessing the energy associated with the adsorption systems. A good understanding of the isosteric heat involved during sorption (adsorption and desorption) processes is required to obtain an excellent and cost-beneficial adsorption system design.[15,27] Several adsorbents plus adsorbate pairs have been effectively applied in a broad range of laboratory, industrial and commercial applications, starting from HVAC (cooling, refrigeration and dehumidification)[28-33] energy storage[18-35] separation for environmental control[18] and desalination.[36] Advancements in developing customized adsorbents for a typical adsorbate require precise estimation of the energy involved at a particular amount of adsorption.

From the thermodynamic perspective, the heat of adsorption is determined using the phase information at the specified temperature, pressure and concentration or the amount adsorbed. In adsorption applications, some critical complex factors need to be considered. These involve factors such as a large database and combinations of adsorbent plus adsorbate pairs, wide operating pressures (from sub-atmospheric to supercritical), and temperatures (spanning from cryogenic to several tens of Celsius). [28-33] Therefore, isosteric heat can be categorized into three types with respect to the amount adsorbed or uptake. [28-33,44]

These types of isosteric heat of adsorption are usually described by typical curves[28,-33,37,44] whereby $Q_{st,}$ isosteric heat is (a) constant value irrespective of the uptake, (b) decreasing with increasing uptake, and (c) increasing with higher uptake. [28,-33,37,44]

(1) constant Q_{st} value irrespective of the uptake (Figures 2.3 and 2.4a)

Constant isosteric heat is usually associated with the adsorption of certain adsorbates onto an energetically homogenous adsorbent. Therefore almost linear relationship exists between isosteric heat and uptake. For instance, Sun et al.[38] reported the isosteric heat of H_2 adsorption (figure 2.3) of a two-fold interpenetrated Zn-MOF [(UPC-501, UPC = China University of Petroleum (East China)] based on $Zn_4O(COO)_6$ SBUs and an imidazole-functionalized ligand, 4,4′,4″-(1H-imidazole-2,4,5-triyl) tribenzoic acid (H_3ITTA). The Q_{st} of UPC-501[38] was 5.29 kJ mol^{-1} at lower coverage (Figure 2.3), which can be compared with those of other Zn_4O-based MOFs.[39] The Q_{st} is almost constant as the H_2 loading increases, indicating the homogeneity of the H_2 adsorption sites in UPC-501. The relatively stable and low Q_{st} values reflect the nature of the lack of open metal sites in UPC-501.[38]

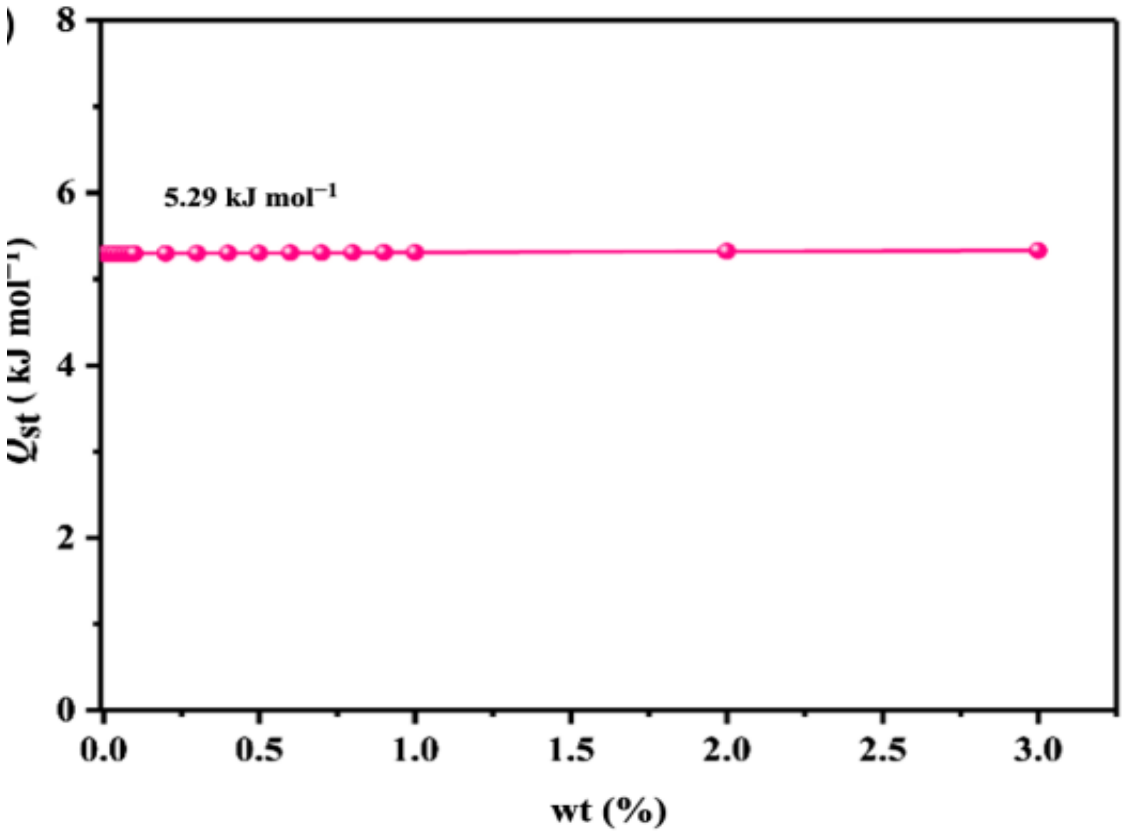


Figure 2.3: The Q_{st} of UPC-501 for H_2. ADS, adsorption; DES, desorption.[38]

(2) decreasing Q_{st} value with increasing uptake, As shown in (figure 2.4b), in which we have some adsorbent - adsorbate pairs, isosteric heat reduces at higher uptake or loading due to the variability in energetic heterogeneity and weaker bonding at multi-layer adsorption. [28-33,37]

(3) increasing Q_{st} value with higher uptake- when the Q_{st} rises slowly with loading, this means that the lateral interactions between adsorbate (e.g., CO_2) molecules are stronger than the adsorbate-adsorbent interactions at higher uptake.[28-33,40,41] A1PO-34[42] curve also exhibits this Q_{st} pattern property as shown in figure 2.5.[42]

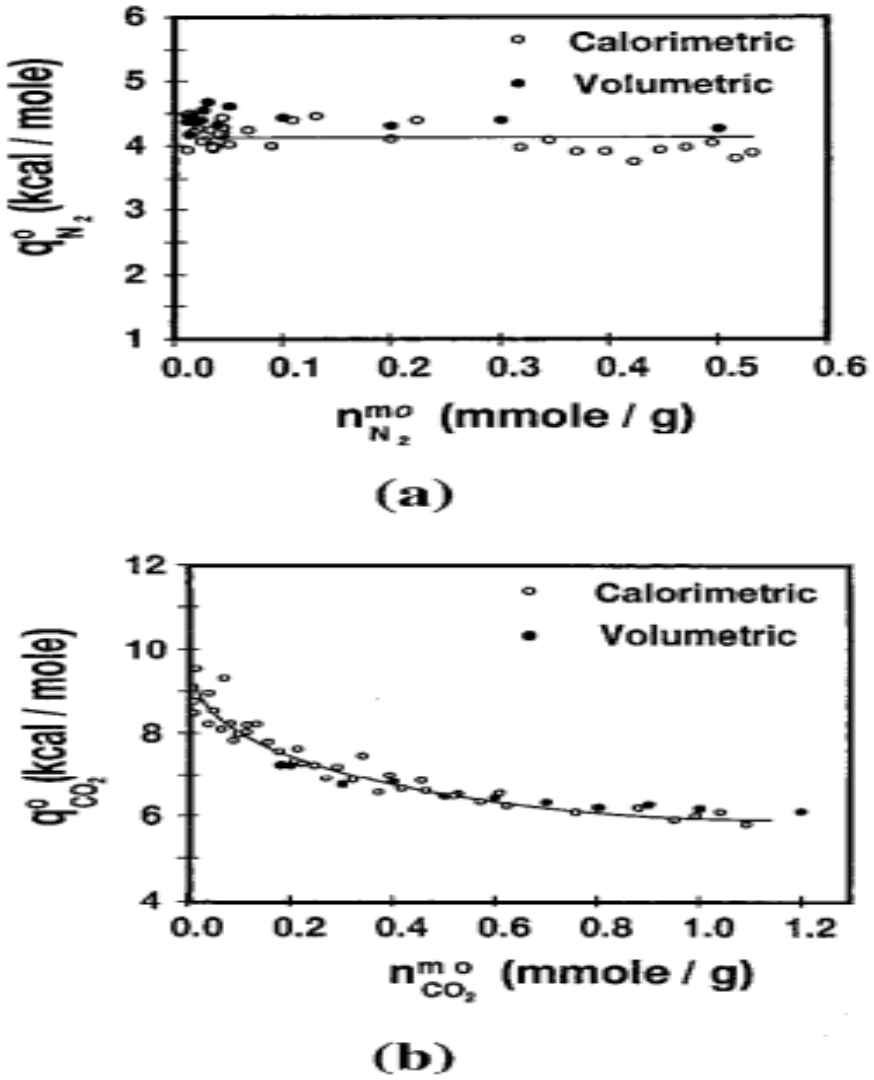


Figure 2.4: The Isosteric heats of adsorption of (a) pure N_2 and (b) pure CO_2 on the pelletized silicalite sample determined by calorimetry (open circles) and by volumetric adsorption apparatus (closed circles).[43]

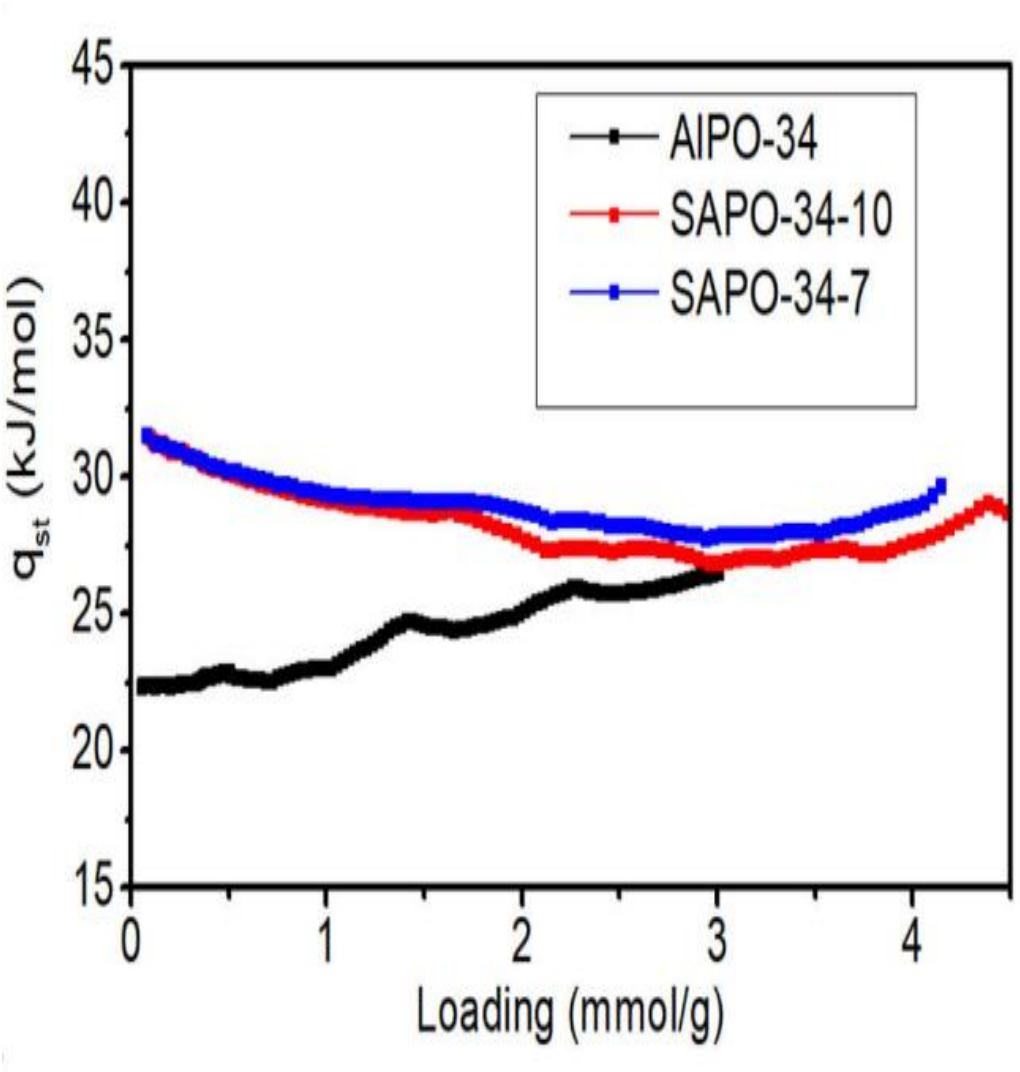


Figure 2.5: CO_2 Isosteric heat of adsorption depending on the loading on aluminophosphate (AlPO) and silicoaluminophosphate (SAPO) molecular sieves.[42]

Different reviews identified methods for isosteric heat of adsorption measurement; these include the Clasius-Clayperon type equation, the use of gas fugacity, and calorimetry experiments at sub-atmospheric pressures. However, a review of different methods for measuring isosteric heat of adsorption indicates that there is an agreement between the Clasius-Clayperon type equation and the calorimetry experiments at sub-atmospheric pressures; however, they concluded that an average difference of about 2.0 kJ/mol remains unaccounted even for low-pressure adsorption processes.[17] Therefore, the Clasius-Clayperon type equation was employed in this study for the measurement of isosteric heat of adsorption,

2.10 Thermogravimetry Analysis (TGA)

The thermal stability of MOFs can be studied using thermogravimetric analysis (TGA). TGA measures the mass of the analysed sample as a function of temperature. During typical thermogravimetric analysis, the MOF sample is steadily heated to high temperature (usually between 500 and 800 ^{o}C) under conditions which could be either atmospheric oxygen (air) or inert conditions (argon). The complicated structure and the presence of several building blocks in the as-synthesized material are reflected on the TG curve by a multi-stage thermal decomposition.[45] The series of resulting curves correspond to the loss of solvent molecules and organic linkers, indicating the MOF's overall stability. For instance, Figure 2.6 is a typical TGA plot of as-synthesized and ion-exchanged samples, Zn BTC Li^+, Zn BTC Na^+, Zn BTC K^+, Zn BTC Rb^+ and Zn BTC Cs^+ and Zn BTC DMA^+ measured in an air atmosphere and temperature range of 30–600 ◦C. The TGA experiments were performed on TGA Q500 V20.13 Build 39 under an air and argon atmosphere from 0 to 1000 ^{o}C with a ramp of 10 ^{o}C/min and argon flow rate of 60 mL/min.

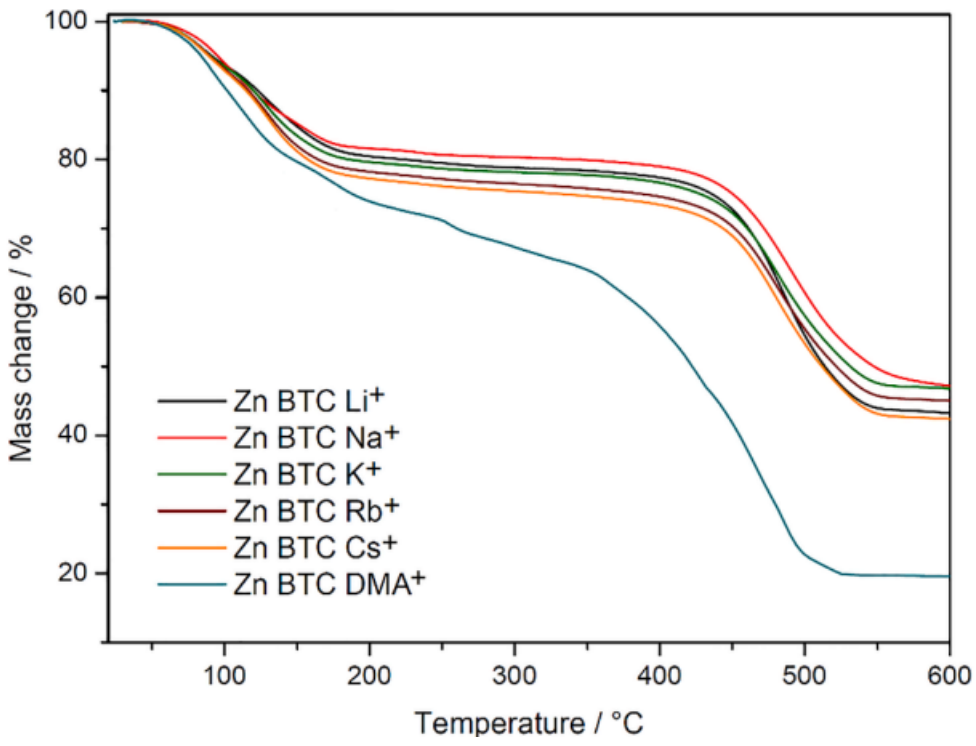


Figure 2.6: TG curves of as-synthesized and ion-exchanged samples measured in an air atmosphere and temperature range of 30–600 ◦C.[45]

Multiple techniques are to be used for the structural elucidation of MOFs. Other methods used in addition to other characterization methods include infrared (IR) spectroscopy, elemental analysis (for C, H, N, Metal, etc. quantification), nuclear magnetic resonance (NMR) spectroscopy, extended X-ray absorption fine-structure (EXAFS), scanning electron microscopy (SEM), X-ray absorption near-edge structure (XANES), etc.

2.11 References

1. M. Thommes, K. Kaneko, A. V. Neimark, J. P. Olivier, F. Rodriguez-Reinoso, J. Rouquerol and K. S. W. Sing*, Pure Appl. Chem.*, 2015; **87(9-10),** 1051–1069.

2. S. Braunauer, P. H. Emmett and E. Teller, *J. Am. Chem. Soc*., 1938, **60**, 309.

3. M. Kruk and M. Jaroniec, *Chem. Mater***.**, 2001, **13**, 3169-3183.

4. L. S. Blankenship and R. Mokaya, *Mater. Adv.,* 2022, **3,** 1905.

5. M. De la Casa-Lillo, F. Lamari-Darkrim, D. Cazorla-Amoros and A. Linares-Solano, *J. Phys. Chem. B.,* 2002, **106**, 10930–10934.

6. M. Sevilla and R. Mokaya, *Energy Environ. Sci.,* 2014, **7**, 1250–1280.

7. Q. Wang, J. Luo, Z. Zhong and A. Borgna, *Energy Environ. Sci.,* 2011, **4**, 42–55.

8. S. S. Samantaray, S. R. Mangisetti and S. Ramaprabhu, *J. Alloys Compd.,* 2019, **789**, 800–804.

9. J. B. Condon, Surface Area and Porosity Determination by Physisorption Measurements and Theory, 2006, ch. 2, pp. 29–53.

10. H. L. McDermot and B. E. Lawton, *Can. J. Chem.* 1959, 37.

11. S. Lowell and J. E. Shields, Powder Surface area and porosity, Springer, USA, 3 edition edn., 1991.

12. S. Braunauer, P. H. Emmett and E. Teller, *J. Am. Chem. Soc.,* 1938, **60**, 309.

13. R. L. Grob and E. F. Barry, *WileyBlackwell*, USA, 2004.

14. J. Kenkel, *Analytical Chemistry for Technicians*, CRC Press, USA, Third Edition edn., 2003.

15. A. L. Myers and J. M. Prausnitz, *AIChE J.,* 1965, **11**, 121–130.

16. R. Krishna and J. M. Van Baten, *Phys. Chem. Chem. Phys., 2011,* **13**, 10593–10616.

17. D. Shen, M. Bülow, F. Siperstein, M. Engelhard and A.L. Myers, *Adsorption*, 2000, **6**, 275.

18. S. Sircar, *Ind. Eng. Chem. Res.*, 2006, **45**, 5435.

19 W. Kukulka, K. Cendrowski, B. Michalkiewicz and E. Mijowska, *RSC Adv*., 2019, **9**, 18527–18537.

20. Y. S. Bae and R.Q. Snurr, *Microporous and Mesoporous Mater.*, 2010, **132**, 300-303.

21. S. Chowdhury, R. Mishra, P. Saha and P. Kushwaha, *Desalination,* 2011, **265**, 159-168.

22. M. Horsfall and I. A. Spiff, *J. Sci. Ind. Res.,* 2005, **64**, 613-620.

23. V. K. Gupta, *Ind. Eng. Chem. Res.,* 1998, **37**, 192-202.

24. A. N. Ebelegi, N. Ayawei and D. Wankasi, *Open J. Phys. Chem*., 2020, **10**, 166-182.

25. L. Lei, Y. Cheng, C. Chen, M. Kosari, Z. Jiang and C. He, *J. Colloid Interface Sci.*, 2022, **612,** 132–145.

26. D. G. Hartzog and S. Sircar, *Adsorption, 1995,* **1**, 133.

27. Y. Aristov, G. Restuccia, G. Cacciola and V. Parmon, *Appl. Therm. Eng.*, 2002, **22**, 191.

28. A. Chakraborty, B. B. Saha, S. Koyama and K. C. Ng, *Appl. Phys. Lett.*, 2007, **90**.

29. H. T. Chua, K. C. Ng, A. Malek, T. Kashiwagi, A. Akisawa and B. B. Saha, *Int. J. Refrig*., 2008, **31**, 536.

30. S. K. Henninger, H. A. Habib and C. Janiak, *J. Am. Chem. Soc.*, 2009, **131**, 2776.

31. M. Z. I. Z. I. Khan, K. C. A. C. A. Alam, B. B. B. Saha, Y. Hamamoto, A. Akisawa and T. Kashiwagi, *Int. J. Therm. Sci.*, 2006, **45**, 511.

32. A. Myat, K. Thu, Y.D. Kim, B. B. Saha and K. Choon Ng, *Energy*, 2012, **46**, 493.

33. A. Chakraborty, K. C. Leong, K. Thu, B. B. Saha and K. C. Ng, *Appl. Phys. Lett*., 2011, **98**, 221910.

34. J. Sun, T. D. Jarvi, L. F. Conopask, S. Satyapal, M. J. Rood and M. Rostam-Abadi, *Energy & Fuels*, 2001, **15**, 1241.

35. N. Bimbo, V. P. Ting, A. Hruzewicz-Kolodziejczyk and T. J. Mays, *Faraday Discuss., 2011,* **151**, 59.

36. S. Mitra, P. Kumar, K. Srinivasan and P. Dutta, *Int. J. Refrig.*, 2015, **58**, 186.

37. A. Chakraborty, B. B. Saha, K. C. Ng, S. Koyama and K. Srinivasan, *Langmuir.,* 2009, **25**, 2204.

38. F. Li, C. Liu, D. Yuan, F. Dai, R. Wang, Z. Wang, X. Lu and D. Sun, *CCS Chem.* 2022, **4**, 832–837.

39. H. Furukawa, N. Ko, Y. B. Go, N. Aratani, S. B. Choi, E. Choi, A. O. Yazaydin, R. Q. Snurr, M. O'Keeffe, J. Kim and O. M. Yaghi, *Science,* 2010, **329**, 424–428.

40. S. Sircar, and A. Myers, Gas separation by zeolites," in Handbook of Zeolite Science and Technology, eds S. M. Auerbach, K. A. Carrado and P. K. Dutta (New York-Basel: Marcel-Dekker), 2003, 1062–1103.

41. A. Chakraborty, B. B. Saha, S. Koyama and K. C. Ng, *Appl. Phys. Lett.,* 2006, **89**.

42. E. Pérez-Botella, R. Martínez-Franco, N. González-Camuñas, Á. Cantín, M. Palomino, M. Moliner, S. Valencia and F. Rey, *Front. Chem.*, 2000, **8**, 588712.

43. S. Sircar, R. Mohr, C. Ristic and M. B. Rao, *J. Phys. Chem., B.,* 1999, **103**, 6539-6546.

44. K. Thu, S. Mitra and B. B. Saha, Theoretical development on the isosteric heat of adsorption and experimental confirmation, https://export.arxiv.org/ftp/arxiv/papers/1709/1709.01723.pdf, accessed 22nd July, 2022.

45. M. Almasi, A. Sharma and T. Zelenka, *Inorganica Chimica Acta*, 2021, **526**, 120505.

Chapter 3: Synthesis of Zinc/Alkali Metal-Organic Frameworks

3.0 Introduction

The effects of diverse metal nodes in the crystal engineering of MOFs have been reported in various applications. Enormous chemical and structural diversity have been enhanced, thus widening the scope of reported applications, including gas storage,[1] carbon capture, electronics, separation and catalytic reactions[1] such as epoxidation,[2] oxidation,[3] condensation,[4] esterification,[5] and hydroxylation.[6] The development of heterometallic MOF catalysts is of unique interest because incorporating two or more kinds of metal atoms can result in improved activity and selectivity or different reactivity of MOFs catalysts.[1-4] In 2017, Peedikakkal et al.[1] investigated the catalytic activities of the M–Zn–BTC (BTC=1,3,5-benzenetricarboxylate) in the oxidation of toluene and cycloalkanes using hydrogen peroxide as oxidant. The presence of Fe as the second metal to the node in Fe–Zn–BTC MOFs improved the toluene conversion from 22 to 70%. Also, the selectivity for the formation of benzaldehyde improved from 22 to 57%. The catalysts show improved activity and selectivity for toluene oxidation relative to unmodified ZnBTC MOF.[1]

The heterometallic mixed-metal approach in MOFs allows for the incorporation of two or more different metals into the same framework to form solid-solution-like mixed-metal MOFs,[7] This offers MOFs with an additional degree of structural complexity, resulting in new functionalities because their properties are dependent on the incorporated metal atoms. For instance, Sun et al.[8] demonstrated that the Ti moiety in the mixed-metal NH_2−UIO-66(Zr/Ti) acted as an electron mediator, facilitating the linker-to-metal charge transfer required for improved photocatalytic performance.[8] The introduction of reduced-metal cations such as Ti(II) and Fe(II) into the MOF-5 framework enabled redox reactivity to inert MOF-5.[9]

Reported synthetic methods involving hydrothermal and post-synthetic exchange (PSE) for metal ion or transmetallation has been utilized as synthesis method for MM-MOFs.[1] The method involves substituting some or all metal nodes in a preformed MOF with another metal ion.[1] Peedikakkal et al.[1] synthesized MM-MOFs denoted as M–Zn–BTC, where M = Cu(II), Co(II) and Fe(II) using post-synthetic exchange (PSE) method and the catalytic performance of these materials was investigated for the oxidation of

toluene and cycloalkanes in the presence of hydrogen peroxide as oxidant. MM-MOFs for Cu–Zn–BTC and Cu–Ru–BTC have been reported.[10-12]

Previous studies showed that the mixed-metal MOFs exhibited properties superior to their parent MOFs induce new functionalities because of the introduction of the second metal ions depending on individual physico-chemical properties of the participating metals. The substitution of Zr with Ti in NH_2−Uio-66(Zr) improved its adsorption capacity toward CO_2.[13] Also, Co-substitution induces aerobic oxidation of cyclohexene over inactive Ni-MOF-74.[13] Sun et al.[8] 2015 confirmed that the mixed-metal Co/Ni-MOF-74 showed superior catalytic performance, compared with pure Co-MOF-74 containing a similar amount of Co^{2+}, because Co^{2+} was favourably substituted at positions more accessible to the substrates this enables the inert Ni-MOF-74 to show catalytic activity for cyclohexene oxidation.[8]

The inclusion of alkali metal ions into an adsorbent is a strategy to improve gas affinity and the gas sorption performance of the MOF materials. Many theoretical computational studies have explained the impact of alkali metal incorporation into MOF.[14,15,16] However, only a few MOFs featuring alkaline metal sites exhibit open porous structures due to the competing role of alkaline ions in the coordination assembly process of MOFs and the uncertainty of their coordination geometry.[14]

Consequently, the influence of alkali metal incorporation into MOF materials on the adsorption of N_2, CH_4, H_2 and CO_2 capture has been relatively less investigated. Many successful incorporation of alkali metal ions into MOFs were possible using ion-exchange synthesis. Almasi et al.[17] reported the gas adsorptive performance of as-synthesized and ion-exchanged samples, Zn BTC Li^+, Zn BTC Na^+, Zn BTC K^+, Zn BTC Rb^+ and Zn BTC Cs^+ and Zn BTC DMA^+. Nitrogen adsorption has shown that the pores of the materials are filled with exchanged ions and corresponding metal nitrates. Hydrogen adsorption showed that ion-exchanged samples Zn BTC Rb^+ and Zn BTC Cs^+ could adsorb this gas, with the maximum sorption capacity of 0.15 wt% H2 at 77 K and 1 atm.[17]

In addition, the synthesis of two crystalline porous MOFs, $[Zn_3Na_2O(BTC)_2(DMF)_2](DMF)(H_2O)$ and $[Zn_2K_3(BTC)_2(HCOO)(DMF)_3](DMF)_3(H_2O)_2$ from the solvothermal reactions of $Zn(NO_3)_2.6H_2O$ and alkali (Na, K) chloride with the trigonal-planar ligand benzene-1,3,5-tribenzoic acid H_3BTC., (DMF = N,N,-

dimethyformamide) help to further explain the stability of Zinc-based MM MOF.[18] These two MOFs exhibit similar alkali-bridged 2-fold interpenetrated, (3,6)- connected nets with distinct metal clusters as molecular building blocks (MBBs). The zinc/sodium mixed cluster resulted in an alkali–bridged interpenetration that fosters a decrease in the density of the framework, accounting for their permanent porosity, high thermal stability and moisture stability compared to the earlier described Zn_4O cluster.[19]

The influence of different metal doping on the gas adsorption performance of MOFs via a grand canonical Monte Carlo (GCMC) simulation.[20] was further investigated. It was found that CO_2 preferentially adsorbs at the alkali metal doping position, thus increasing the carbon dioxide adsorption capacity. This position was further supported by theoretical computational studies by Babarao et al.[15] and Xiang et al.[16,21]

Song et al.[21] solvothermal synthesized and studied a series of the titanium-based, metal–organic framework (MOF) materials, xM@NH2-MIL125(Ti) (where x, is the alkali metal loading percentage during the synthesis; M = Li, Na, K). The variation of the alkali metal loading results in substantial differences in the CO_2 adsorption. They agreed that introducing alkali metals pointedly affects CO_2 adsorption in two ways. Firstly, it impacts the crystal growth rate of MOFs, yielding different morphology and size of crystals, thus leading to differences in specific surface area and pore size, with a significant impact on CO_2 adsorption.[21] Secondly, the alkali metals, existing in the final framework after a series of solvent-exchanging treatments, influence the CO_2 adsorption due to the increased specific surface area and alkali metal coordination.[21]

In the present work, we report the synthesis of a new bimetallic Zn(II) and K(I), and Li(I), Zinc/Alkali metal-organic frameworks (ZnKMOF) and (ZnLiMOF), respectively. The study aims to study the physicochemical properties and potential applications of hybrid mixed valent MOFs. Potassium *tert*-butoxide, and lithium *tert*-butoxide, were used as sources of potassium and Lithium in this study. We now report the synthesis and characterization of new bimetallic, transition metal - alkali metal-based MOFs composed of divalent Zn and monovalent K ion (ZnKMOF), Li ions (ZnLiMOF) linked with 1,3,5-tris(4-carboxyphenyl)benzene (BTB), benzene-1,4-dicarboxylic acid (1,4-BDC), and 2,6-naphthalenedicarboxylic acid (2,6-NDC) using solvothermal methods at temperatures 120 °C and 170 °C. We further investigated the effects of monovalent alkali cations, K^+ and Li^+ on CO_2, N_2, H_2, O_2 and CH_4 adsorption in ZnK and ZnLi MOF

systems exhaustively. It is very important to note that attempts at synthesising some other combinations, such as Cu/K, Ni/K**,** Cr/K, Co/K, Co/Li, Ni/Li, Cu/K, Cd/K, Zn/Na failed during the several stages of this research.

3.1 Experimental

3.1.1 Reagents

Chemicals and solvents were purchased from Alfa Aesar, Fluorochem, Sigma-Aldrich, and VWR 1293 and used without further purification. Diffraction data were collected on a Rigaku model. Data for ZNOABT (ZnKBDC), ZNOABZ3 (ZnKNDC), ZNOACD2 (ZnKBTB) (ZNOACJ) ZnLiBDC and (ZNOACI) ZnLiNDC, were collected on Oxford SuperNova diffractometers with Atlas S2 detectors using Cu (Kα: 1.54184 Å) radiation at 293 K, 120 K 120.0 K respectively and processed through CrysAlis software and at Diamond Light source Cambridge.

3.2 Synthesis of Mixed-Metal Organic Frameworks ZnKBDC

3.2.1 Synthesis of ZnKBDC MOF

A mixture of zinc nitrate hexahydrate (200 mg, 0.67 mmol), benzene-1,4-dicarboxylic acid (57 mg, 0.34 mmol), potassium *tert*-butoxide (115 mg, 1.02 mmol) and DMF (6 mL) was sonicated for 30 mins. The reaction mixture was heated at 120 °C for 72 h in a 23 mL Teflon Stainless Steel lined autoclave vessel as described in Figure 3.1(iii). Colourless crystals together with a white microcrystalline solid were obtained; the crystals were separated manually from the bulk product, being suitable for single crystal X-ray diffraction (SCXRD). The same reaction was repeated at 170 °C. The mixture was cooled at a rate of 0.2 °C min^{-1} to room temperature. Hexagonal-shaped crystals were formed and isolated by washing with DMF (4 x 2 ml) and drying overnight in the air (5 mg, 32% based on $Zn(NO_3)_2 \cdot 6H_2O$). The bulk product was identified as $[ZnK(BDC)_{1.5}.DMF].2H_2O$ $\{ZnKC_{14.4}H_{12}O_9N_{0.7}\}_n$ by SCXRD. Yield: 30%. Elemental analysis (exp %): C: 38.62; H: 2.40; N: 2.17; (calc %): C: 39.01; H: 2.73; N: 2.21.

Please note that to synthesize ZnLiBDC MOF, potassium tert-butoxide was substituted with lithium tert-butoxide, using the same stoichiometric ratio.

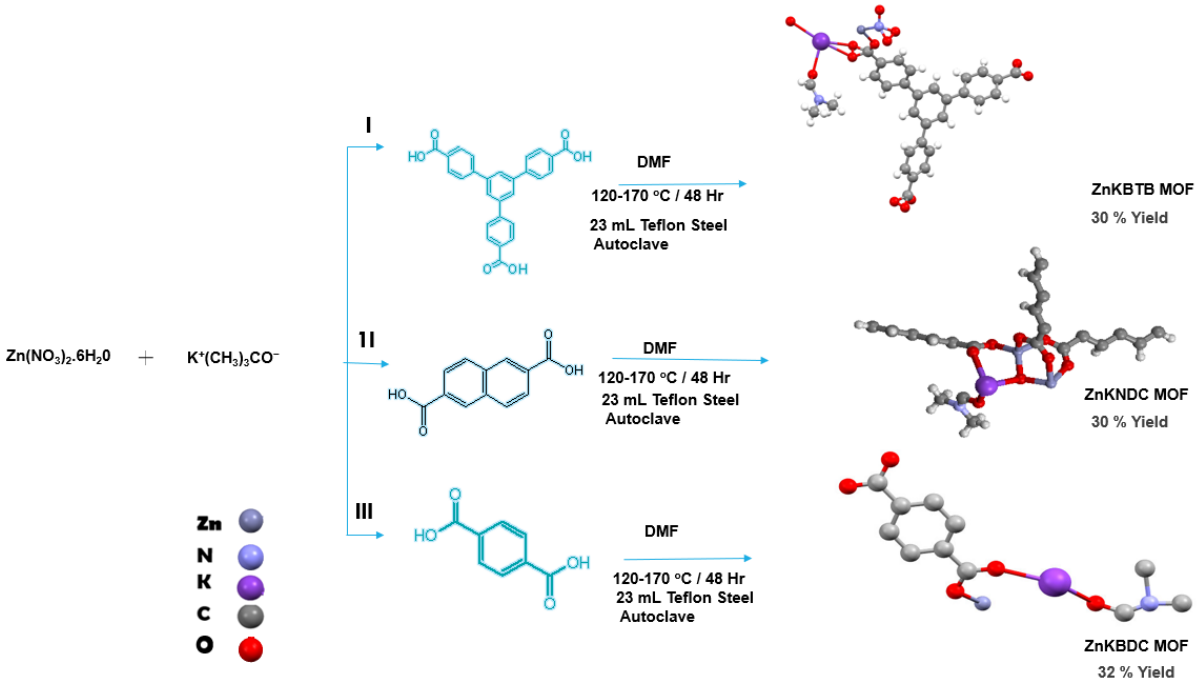


Figure 3.1 Synthesis of (i) ZnKBTB (ii) ZnKNDC (iii) ZnKBDC MOF under same reaction conditions.

3.2.2 Synthesis of ZnKNDC MOF

Zinc nitrate hexahydrate (200 mg, 0.67 mmol), 2,6-naphthalenedicarboxylic acid (73 mg, 9 mmol) potassium *tert*-butoxide (113 mg, 1.02 mmol) and DMF (6 mL) was sonicated for 30 mins. The reaction mixture was heated at 120 °C for 72 h in a 23 mL Teflon Stainless Steel lined autoclave vessel as described in Figure 3.1(ii). Colourless crystals together with a white microcrystalline solid were obtained; the crystals were separated manually from the bulk product, being suitable for SCXRD. The same reaction was repeated at 170 °C. The mixture was cooled at a rate of 0.2 °C min^{-1} to room temperature. Block-shaped crystals were formed and isolated by washing with DMF (4 x 2 ml) and drying overnight in air (5 mg, 32% based on 2,6-NDC). The bulk product was identified as $[Zn_2K(NDC)_{2.5}.DMF].3DMF$ $\{Zn_2KC_{42}H_{48}O_{10}N_{4.4}\}_n$ by single crystal X-ray diffraction. Yield: 30%. Elemental analysis (exp %): C: 53.57; H: 4.92; N: 6.16; (calc %): C: 53.42; H: 5.12; N: 6.53.

Please note that to synthesize ZnLiNDC MOF, potassium tert-butoxide was substituted with lithium tert-butoxide, using the same stoichiometric ratio.

3.2.3 Synthesis of ZnKBTB MOF

The standard material 40% MM-MOF was synthesized as follows: Zinc nitrate hexahydrate (200 mg, 0.67 mmol), 1,3,5-Tris(4-carboxyphenyl)benzene (147 mg, 0.34 mmol) potassium *tert*-butoxide (113 mg, 1.02 mmol) and DMF (6 mL) was sonicated for 30 mins. The reaction mixture was heated at 120 °C for 72 h in a 23 mL Teflon Stainless Steel lined autoclave vessel as described in figure 3.1(i). Colourless crystals together with a white microcrystalline solid were obtained; the crystals were separated manually from the bulk product, being suitable for SCXRD. The same reaction was repeated at 170 °C. The mixture was cooled at a rate of 0.2 °C min^{-1} to room temperature. Block-shaped crystals were formed and isolated by washing with DMF (4 x 2 ml) and drying overnight in air (5 mg, 32% based on H_3BTB). The bulk product was identified as $[KZn_4O(BTB)O_4NO_3.DMF].DMF$ $\{C_{33}H_{27.5}Zn_{3.5}N_{1.5}KO_{15.5}\}_n$ by single crystal X-ray diffraction. Yield: 30%. Elemental analysis (exp %): C: 41.24, H: 2.39, N: 1.89; (calc %): C: 41.24; H: 2.88; N: 2.19.

Please note that to synthesize ZnLiBTB MOF, potassium tert-butoxide was substituted with lithium tert-butoxide using the same stoichiometric ratio.

3.3 XRD Analysis

A crystal of ZnKBDC, ZnKNDC and ZnKBTB MOFs were selected and maintained at 120 K during data collection on a single crystal X-ray diffractometer. Using Olex-2, [22] the structure was solved with the SHELXT[23] structure solution program using Intrinsic Phasing and refined with the SHELXL[24] refinement package using Least Squares minimisation. The crystal data and refinement parameters are presented in Table 3.1 shows the SCXRD analysis of ZnKBDC, ZnKNDC and ZnKBTB MOF.

The SCXRD analysis of ZnKBDC MOF revealed the formation of an orthorhombic crystal system with an Fdd2 space group having a 3D porous framework. The asymmetric unit as shown in Figure 3.2a, reveals one carboxylate ligand oxygen coordinated to one potassium atom and the second O coordinated Zinc atom. The potassium is coordinated to a molecule of DMF. Each Zn (II) forms coordinate bonds with a slightly distorted tetrahedral coordination with four oxygen atoms from four different BDC ligands. The fourth coordination is satisfied by carboxylate oxygen (O) of another BDC linker (Figure 3.2b). The second metal K(I) is 8-coordinated,

surrounded by four oxygen atoms, one from DMF and three from three BDC ligands in a distorted square antiprismatic geometry. The study of the coordination mode of the BDC ligands in the metal centre (Figure 3.2b) revealed that the BDC ligands acted as a bridging bis-tridentate (μ_3-η^1:η^2) agent whereby one the carboxylate oxygen, -COO- is bonded to Zn (II) ion and K ion (bridging) the other oxygen bonded to one K ion. The Zn-O bond distance are in the range of 1.958(4)-1.994(4) Å and K-O bond lengths are in range of 2.598(4)-3.10(15)8 Å, Zn-K bond lengths are in range of 3.667(12)-3.917(11) Å (see Appendix I for detailed bond distances and bond angles).

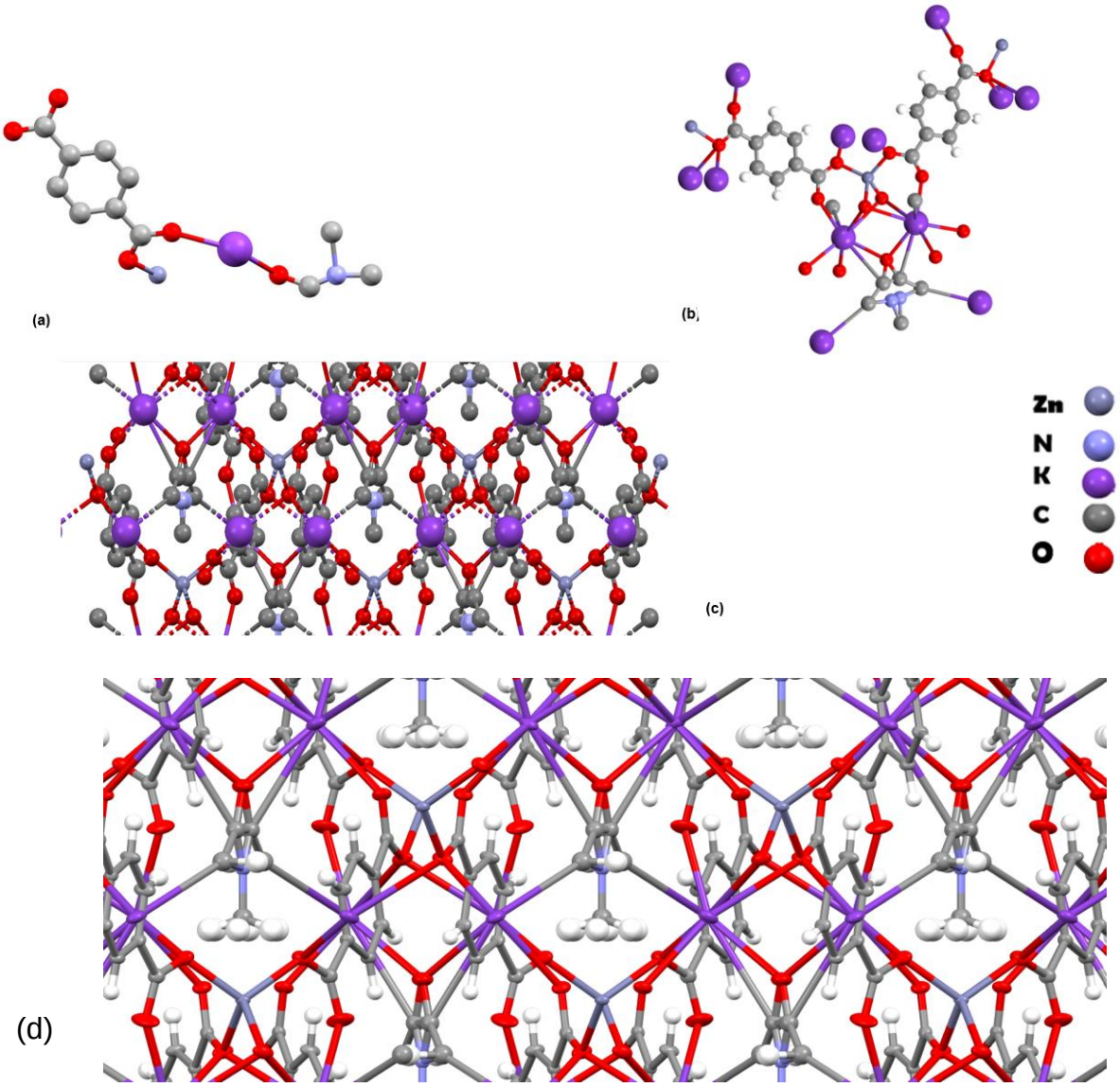


Figure 3.2: (a) 'b' view ZnKBDC MOF Asymmetric unit (b) 'b' view ZnKBDC MOF Autocentre (c) 'a' view ZnKBDC MOF Packed Structure as ascertained via SCXRD, and elemental analysis of ZnKBDC MOF (d)'b' view ZnKBDC showing pore blocking.

Table 3.1 Crystal data and structure refinement for ZnKBDC, ZnKNDC and ZnKBTB MOF.

	ZnKBDC	ZnKNDC	ZnKBTB
Empirical formula	$ZnKC_{14.4}H_{12}O_9N_{0.7}$	$Zn_2KC_{42}H_{48}O_{10}N_{4.4}$	$Zn_{3.5}KC_{33}H_{27.5}N_{1.5}O_{15.5}$
Formula weight	443.33	944.33	961.01
Temperature/K	293(2)	120.00(10)	120.0(2)
Crystal system	Orthorhombic	Triclinic	Monoclinic
Space group	Fdd2	P-1	C2/c
a/Å	10.85030(10)	9.3116(4)	32.0765(15)
b/Å	18.3058(2)	11.7769(6)	7.2813(2)
c/Å	20.9962(2)	12.1179(7)	32.1204(13)
α/°	90	108.833(5)	90
β/°	90	103.929(4)	118.531(6)
γ/°	90	108.030(4)	90
Volume/$Å^3$	4170.34(7)	1106.99(11)	6590.9(6)
Z	2	1	8
$\rho_{calc}g/cm^3$	1.847	1.628	1.393
μ/mm^{-1}	5.768	4.212	2.681
F(000)	2336.0	548.0	2824.0
Crystal size/mm^3	0.251 ×0.095 × 0.051	0.182×0.048 × 0.031	0.191×0.065 × 0.045
Radiation	CuKα (λ = 1.54184)	Cu Kα (λ = 1.54184)	Cu Kα (λ = 1.54184)
2Θ range for data collection/°	10.372 to 145.634	8.328 to 144.938	10.786 to 145.504
Index ranges	-13 ≤ h ≤ 9, -22 ≤ k ≤ 22, -24 ≤ l ≤ 25	-10 ≤ h ≤ 11, -14 ≤ k ≤ 14, -14 ≤ l ≤ 12	-36 ≤ h ≤ 39, -4 ≤ k ≤ 8, -39 ≤ l ≤ 34
Reflections collected	7500	8296	13542
Independent reflections	1969 [R_{int} = 0.0180, R_{sigma} = 0.0155]	4246 [R_{int} = 0.0201, R_{sigma} = 0.0295]	6365 [R_{int} = 0.0213, R_{sigma} = 0.0271]
Data/restraints/parameters	1969/1/156	4246/0/282	6365/3/403
Goodness-of-fit on F^2	1.063	1.117	2.494
Final R indexes [I>=2σ (I)]	R_1 = 0.0355, wR_2 = 0.0945	R_1 = 0.0382, wR_2 = 0.0974	R_1 = 0.1535, wR_2 = 0.4937
Final R indexes [all data]	R_1 = 0.0356, wR_2 = 0.0946	R_1 = 0.0409, wR_2 = 0.0986	R_1 = 0.1575, wR_2 = 0.5002
Largest diff. peak/hole / e $Å^{-3}$	0.40/-0.56	1.20/-0.9	2.14/-1.20
Flack parameter	0.486(5)		

For ZnKNDC, the SCXRD analysis revealed the formation of a triclinic crystal system with a P-1 space group having a 3D porous framework. As shown in Figure 3.3a, the asymmetric unit reveals three half NDC carboxylate ligands, three metal centres involving two crystallographically independent Zn metal centres and a potassium metal centre coordinated to one molecule of DMF distorted symmetry. One Zn coordinated to four carboxylate oxygen, one K and one Zn in a distorted octahedral symmetry, and another Zn tetrahedrally coordinated to four oxygen (three from -COO and a Zn-O-K bridge Oxygen) (Figure 3.3b) ZnKNDC MOF autocentre. K forms coordinate bonds to three carboxylate linkers O and the two Zn metal centres (Figure 3.3 a, b, c). The Zn-O bond distance are in the range of 1.913(2)–2.230(2) Å, K-O bond lengths are in range of 2.673(2)–3.071(2) Å, Zn–Zn is 3.1316(4) Å and Zn-K bond lengths are in range of 3.612(9)-3.929(7) Å (see Appendix II for detailed bond distances and bond angles).

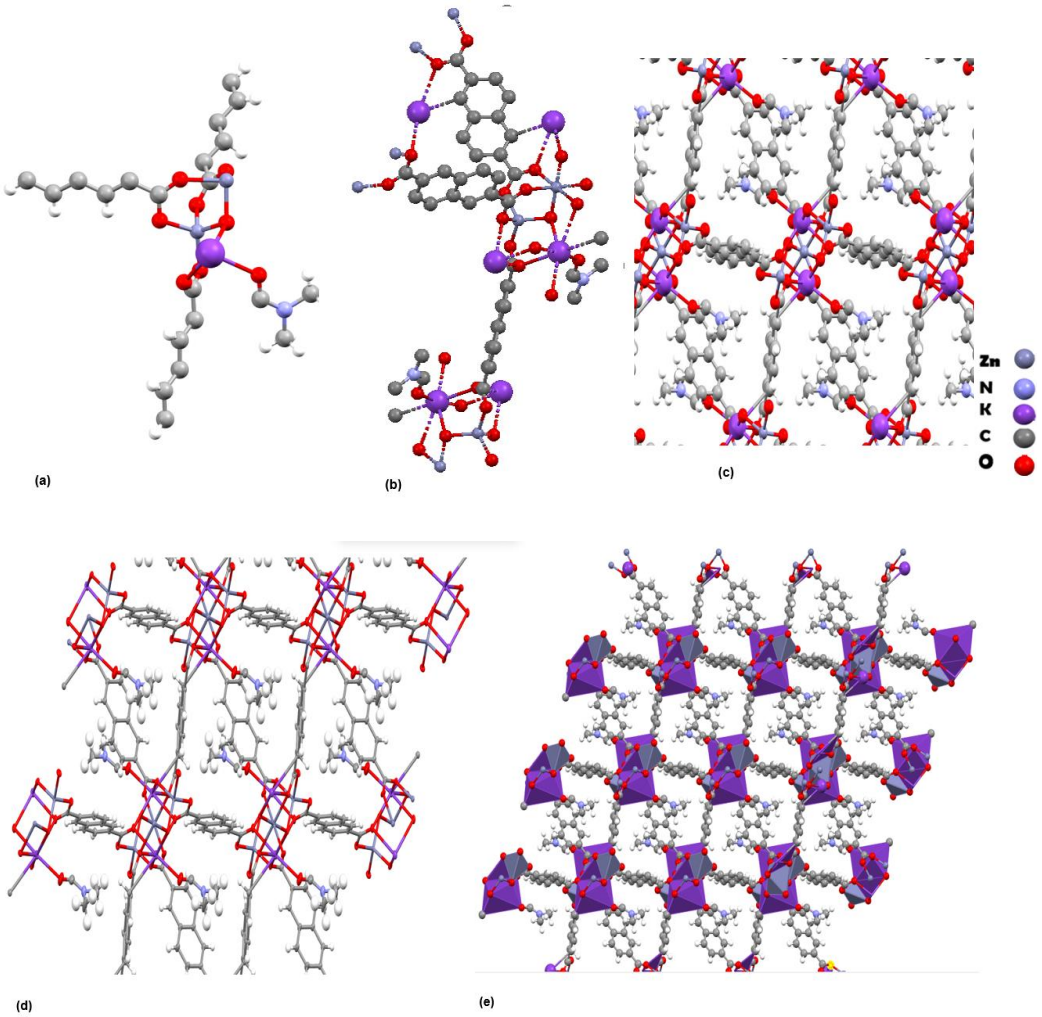


Figure 3.3: SCXRD Structures of ZnKNDC MOF (a) ‘b’ view ZnKNDC MOF

Asymmetric unit (b) ‘b’ view ZnKNDC MOF Autocentre (c) ‘a’ view ZnKNDC MOF Asymmetric unit. (d) The crystal structure of ZnKNDC is viewed along the crystallographic a-axis. (e) Polyhedral Crystal structure of ZnKNDC viewed along the crystallographic b-axis.

Figure 3.3(c-d) shows that each Carboxylates O of NDC ligand binds to Zn and K. Six (6) NDC ligands contribute to the metal centre. Three Zn metals participated in the metal centre, two (2) potassium metal. Each Potassium metal atom, K, is surrounded by six equivalent O-coordinated NDC ligands in the $[M(NDC)_6]$. NDC ligands adopted both bis-tridentate bridging (μ_3-η^1:η^2) and bis-tetradentate (octadentate) (μ_4-η^1:η^3) bridging coordinating mode within the pentanuclear SBU (Figure 3.3b). Therefore, Zn displayed tetrahedral and octahedral coordination geometry by having coordination numbers 4 and 6, while Potassium possesses the coordination numbers 3 and 7 coordinated in a trigonal pyramidal and pentagonal pyramidal geometry, respectively (Figure 3.3b).

The SCXRD analysis of ZnKBTB revealed the formation of a monoclinic crystal system with a C2/c space group with a 2D porous framework, as seen in Table 3.1. The asymmetric unit of ZnKBTB consists of one BTB unit, a terminal nitrate, and one Zn and one K atoms. and a terminal DMF molecule.

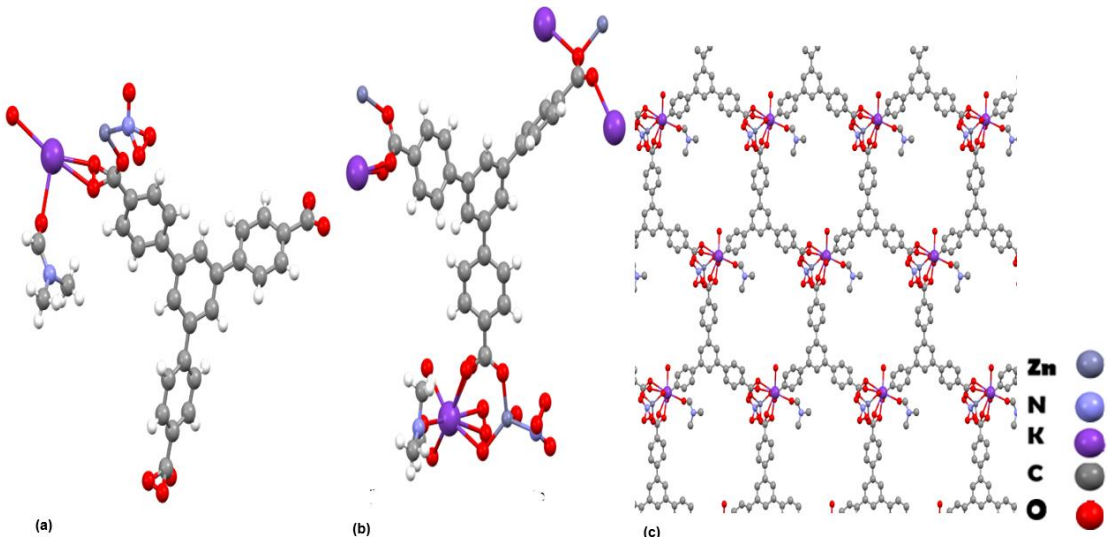


Figure 3.4: SCXRD of ZnKBTB MOF (a) ‘b’ view ZnKBTB MOF Asymmetric unit

(b) ‘b’ view ZnKBTB MOF Auto Centre, coordination environment (c) b’ view ZnKBTB MOF packed unit.

The carbons of the DMF are disordered between two positions. In the polymeric framework, the hexagonal channels propagating along the 'b' crystallographic axis (Figure 3.4c), the nitrate point comes from Zn, which then points to the pore. All the coordinated solvent points into the hexagonal pore, with nitrate coming from Zn, the water (coordinated aquo) ligand is from K, while the DMF is from another K atom. Examining the gas adsorption properties, this geometry helps permit the intermolecular interactions between the CO_2 molecules and the other coordinated solvent (DMF) molecules.[32] The nitrate may leave during the first degradation step of the thermal gravimetric analysis.

A study of the coordination environment of ZnKBTB MOF (Figure 3.4b) shows BTB^{2-} carboxylate O, -COO- ligand adopted two different coordinating modes with Zn and K atoms, which include tridentate bridging (anti-syn-anti, μ_3-η^1:η^2) and bidentate bridging (syn-syn, μ_2-η^1:η^1) mode with the metal ions in the SBU. Therefore, BTB ligand acts as a μ_7-bridge linking three Zn^{2+} and four K^+ ions, in which one carboxylate group adopts two μ_2-η^1:η^1-bridging, and one μ_3-η^1:η^2-bridging mode, respectively (Figure 3.4b). The Zn(II) cation displayed tetrahedral coordination geometry with a coordination number of 4, while the Potassium, K ion possesses the coordination number 8 and was coordinated in a distorted square antiprismatic geometry (see Figure 3.3(b and c)). The Zn-O bond distances are in the range of 1.926(6)–1.952(6) Å, and K-O bond lengths are in the range of 2.588(13) - 2.864(18) Å (See Appendix III for detailed bond distances and bond angles).

3.3.1 PXRD Analysis

Powder XRD patterns (Figures 3.5 and 3.6) for the ZnKMOFs were obtained using monochromatic high-intensity (λ= 0.1541874 nm) CuKα radiation. The powder XRD pattern obtained agrees with the simulated pattern (from the crystallographic information files (CIFs) utilizing Mercury software) and the high crystallinity of the ZnKBDC, ZnKNDC and ZnKBTB MOF systems (Figure 3.5 (a, b and Figure 3.6 respectively). For ZnKBDC MOF, the prominent metallic peaks at the 2θ values at 7.8°, 10.6°, 12.5°, 16.3°, 17.1°, 18.1°, 21.7°, 29.1°, 31.3° and 36.0°. The 2θ values shown show some similarities with BDC-based MOFs, such as the monometallic, ZnBDC MOF named Zn-MOF-1 and Zn-MOF-2 synthesized at room temperature and microwave synthesis, respectively, as reported by Omkaramurthy *et al*.[25] For ZnKNDC

MOF in Figure 3.5b the prominent peak positions were at the 2θ values at 7.1°, 7.8, 14.9°, 15.1°, 19.2°, 22.5°, 24.1°, 27.1°, 29.8°, 36.1° and 37.4°. The coordination of Zinc metal with the BDC and NDC ligands to form ZnKBDC and ZnKNDC MOF can be confirmed. The PXRD pattern shows less noise and extra peaks, indicating that the synthesized are pure and pure in phase. The theoretical (simulated) PXRD pattern calculated from the single-crystal XRD data agrees with the experimental pattern, confirming that the product is pure–phased and highly crystalline.[25]

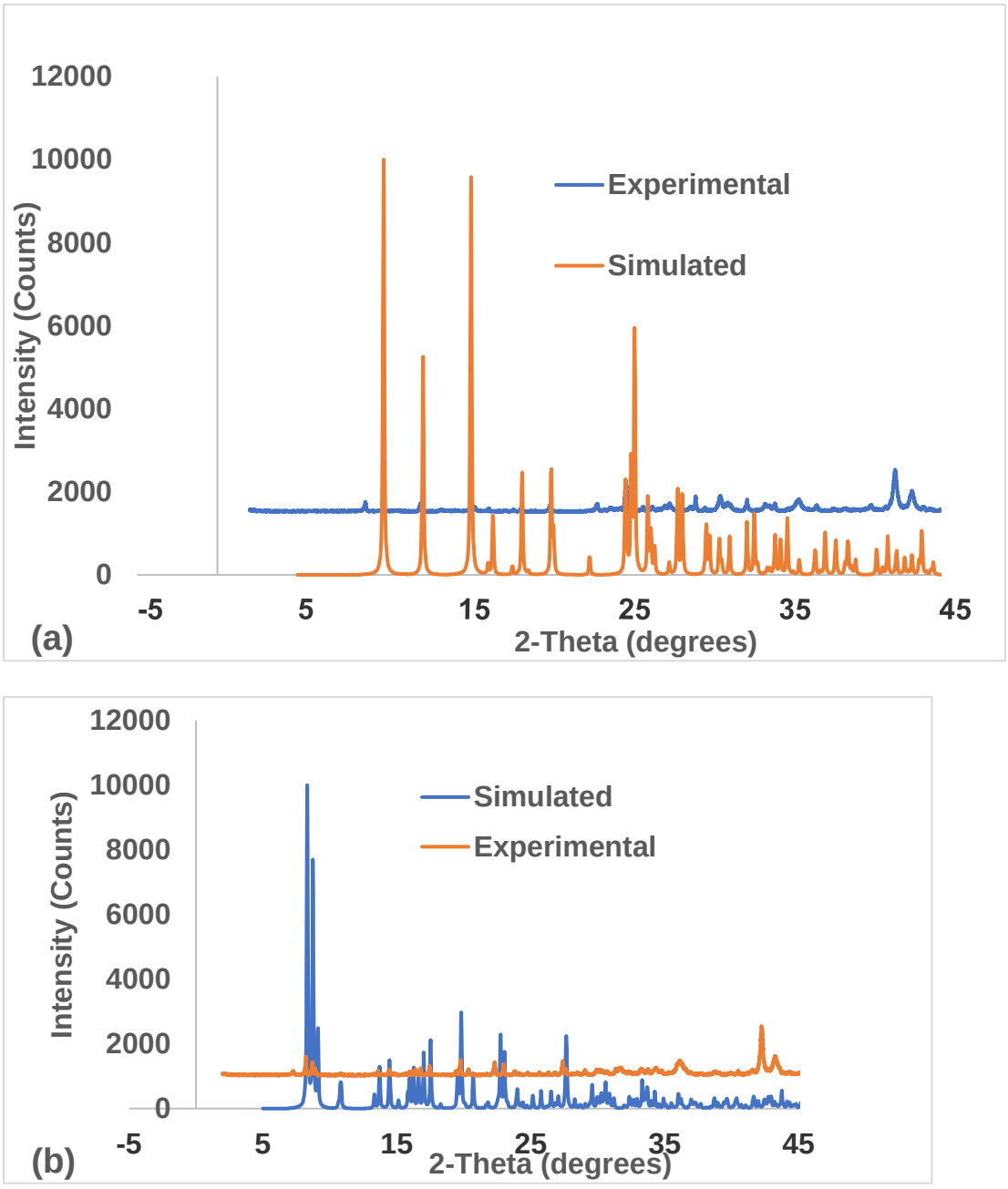


Figure 3.5: PXRD patterns for (a) ZnKBDC (b) ZnKNDC and (c) ZnKBTB MOFs.

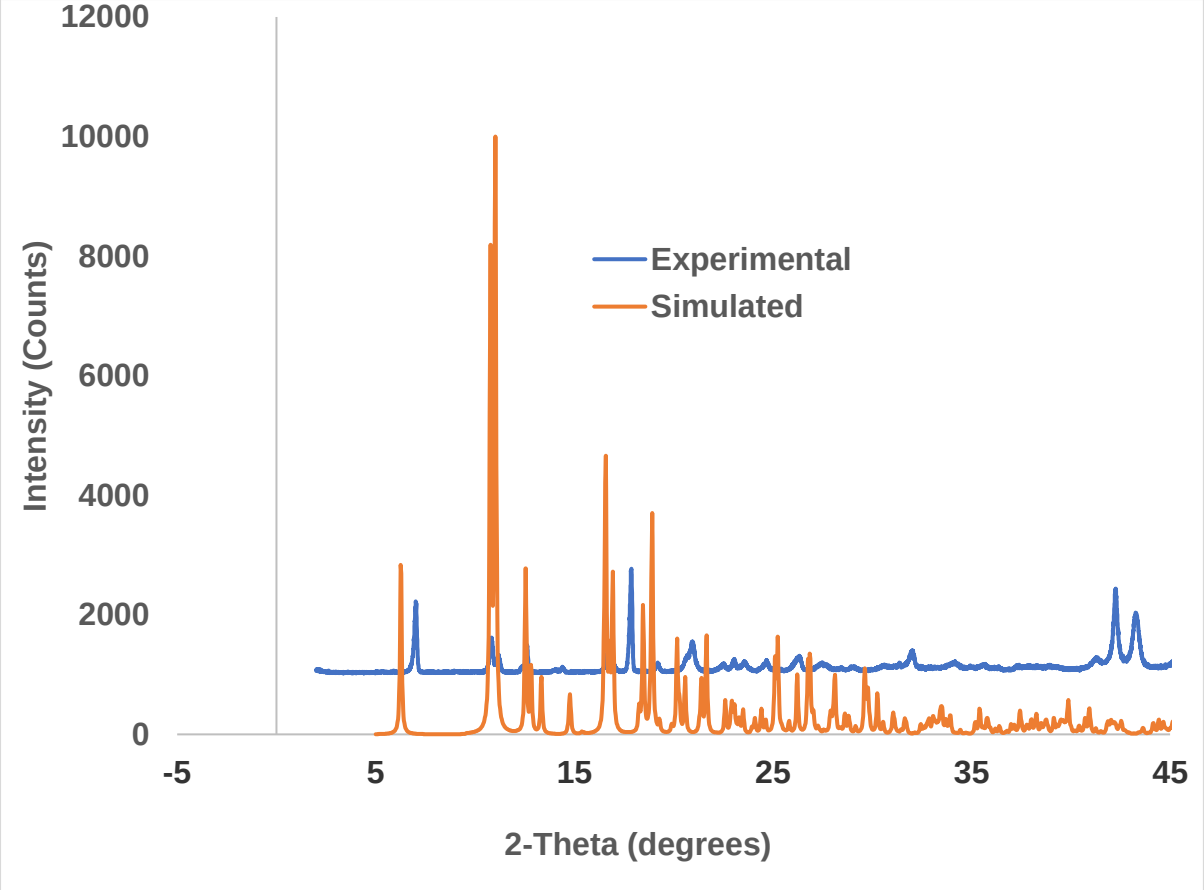


Figure 3.5: PXRD patterns for (a) ZnKBDC (b) ZnKNDC and (c) ZnKBTB MOFs.

The Powder XRD patterns for ZnKBTB MOF have been performed and shown in Figure 3.5c to confirm the crystalline nature of ZnKBTB. The powder XRD pattern obtained agrees with the simulated pattern. The appearance of a peak at 2θ = 6.5°, 11.2°, 12.2°, 17.6°, 20.1°, 22.5°, 25.1°, 31.2° further shows some similarity with 2θ = 5.6°, 10.1° and 2θ = 20.3°corresponding to the MOF-177 (ZnBTB) to the crystalline plane which is in agreement with the published literature.[26,27,28] We observed the strongest peak at higher 2θ = 6.5° and 2θ = 17.6° than the already published XRD patterns of MOF-177 probably due to the presence of K in the coordination.

3.3.2 TGA Analysis

Figure 3.6(a, b and c) shows the TGA curve of ZnKBDC, ZnKBTB and ZnKNDC MOF, respectively. The TGA thermogram was recorded in air, 30-700 °C (heating rate 10 °C/min) of ZnKBDC, ZnKNDC and ZnKBTB MOFs (Figure 3.3). All three MOF samples showed similar properties in air and nitrogen. In all cases, there were three degradation steps. The first degradation step most likely corresponds to the loss of occluded solvent molecules; the second step corresponds to the ligand decomposition

and, therefore, MOF structural damage and the final decomposition leads to the formation of oxides of Zn and K.

For sample ZnKBDC (Figure 3.6a), the 2.2 % weight loss in the temperature range of 20–110 °C is assigned to the H_2O desorption, another weight loss of 11.4% in the range of 100–400 °C was assigned to DMF desorption. The rather sharp weight loss of the sample took place after 415 °C, corresponding to the structural decomposition to ZnO. The weight loss for the ZnKBDC upon decomposition to oxides of K and Zn, e.g. ZnO is 40.5 %, which is low and may be attributed to trapped species. Based on the formula, the calculated C and H percentage is C: 39.01% and 2.73%, consistent with the elemental analysis result C: 38.62 %; H: 2.40%.

For the sample ZnKNDC (Figure 3.6c), the 2% weight loss in the temperature range of 20–100 °C is assigned to the H_2O desorption, another weight loss of 11.0% in the range of 100–400 °C was assigned to DMF desorption. The rather sharp weight loss of the sample took place after 373 °C, corresponding to the structural decomposition to ZnO. The weight loss for the ZnKNDC upon decomposition to oxides of K and Zn like ZnO is 41.1%, which is low and may be attributed to trapped species. Based on the formula, the calculated C and H percentage is 53.42% and 5.12%, consistent with the elemental analysis result C: 53.57%; H: 4.92%.

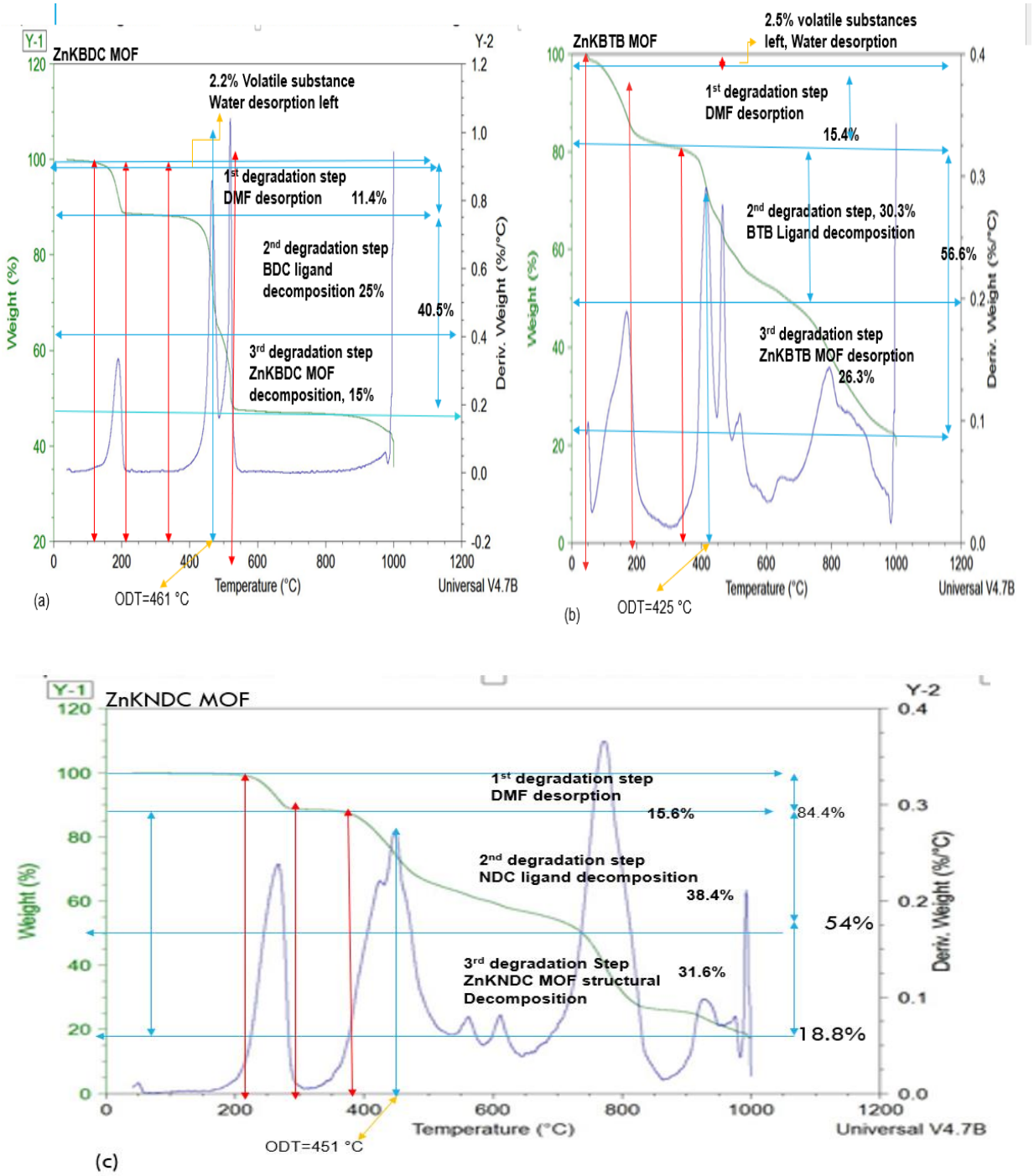


Figure 3.6: Thermogravimetric analysis (TGA) profiles for (a) ZnKBDC, (b) ZnKBTB, (c) ZnKNDC MOFs under air atmosphere.

The TGA thermogram of sample ZnKBTB (Figure 3.6b) shows the 2.5% weight loss in the temperature range 20–100 °C is assigned to the H_2O desorption, another weight loss of 12.0% in the range of 100–400 °C was assigned to DMF desorption. The sharp weight loss of the sample took place after 380 °C, corresponding to the ZnKBTB MOF decomposition to ZnO. The weight loss for the ZnKBTB upon decomposition to oxides

of Zn and K, such as ZnO is 56.6%, which is low and may be attributed to trapped species. Based on the formula, the calculated C and H percentage is 41.24% and 2.88%, consistent with the elemental analysis result C: 41.24%; H: 2.39%.

3.3.3 Scanning Electron Microscopy (SEM)/ Energy Dispersive X-Ray Analysis (EDX)

SEM micrographs (Figure 3.7a) of MOF formed at 120 °C – 170 °C show the formation of crystalline materials, as expected. ZnKBDC occurrence was observed to be a regular hexagonal-shaped crystal with sizes of a few microns.

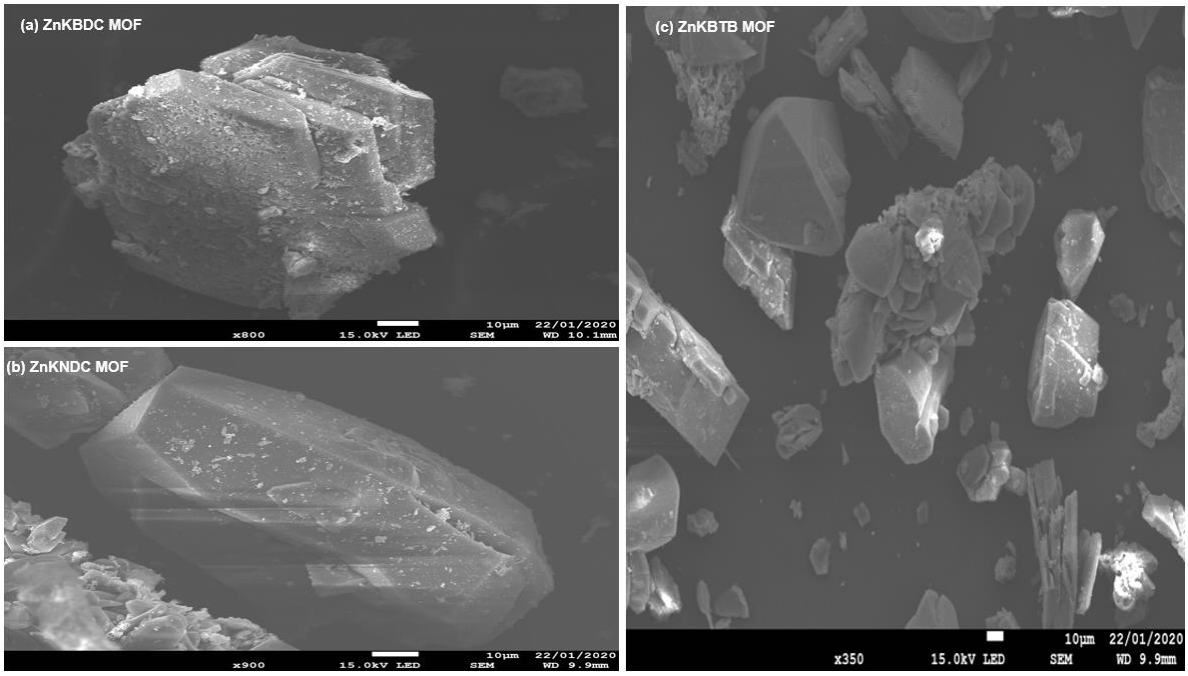
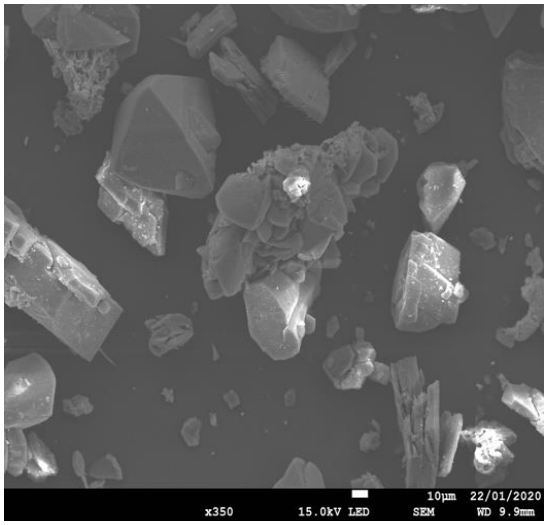
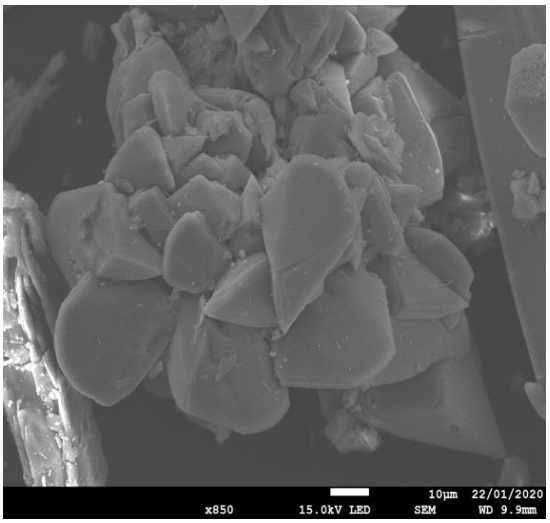


Figure 3.7: SEM images for single crystals of (a) ZnKBDC, (b) ZnKNDC, and (c) ZnKBTB MOFs at different magnifications.

Figure 3.7b is scanning electron micrographs, SEM micrographs of ZnKNDC MOF formed at 120 °C – 170 °C show the formation of crystalline materials as expected. ZnKNDC was observed to be a regular hexagonal prism-shaped columnar crystal with sizes of a few microns (about 10 µm in size). Additionally, SEM micrographs (Figures 3.7a and 3.7b) show the formation of crystalline materials as expected. ZnKBTB occurrence was observed to be a polyhedral Square pyramidal crystal with sizes of a few microns (Figures 3.7c and 3.8).



(a)


(b)

Figure 3.8: SEM Images of ZnKBTB MOF synthesized at 170 ^{o}C.

Figure 3.9 is the SEM / EDX Spectrum of ZnKBDC, ZnKNDC and ZnKBTB respectively. As expected, MOFs confirmed the presence of Zn, K, C, and O in all our samples.

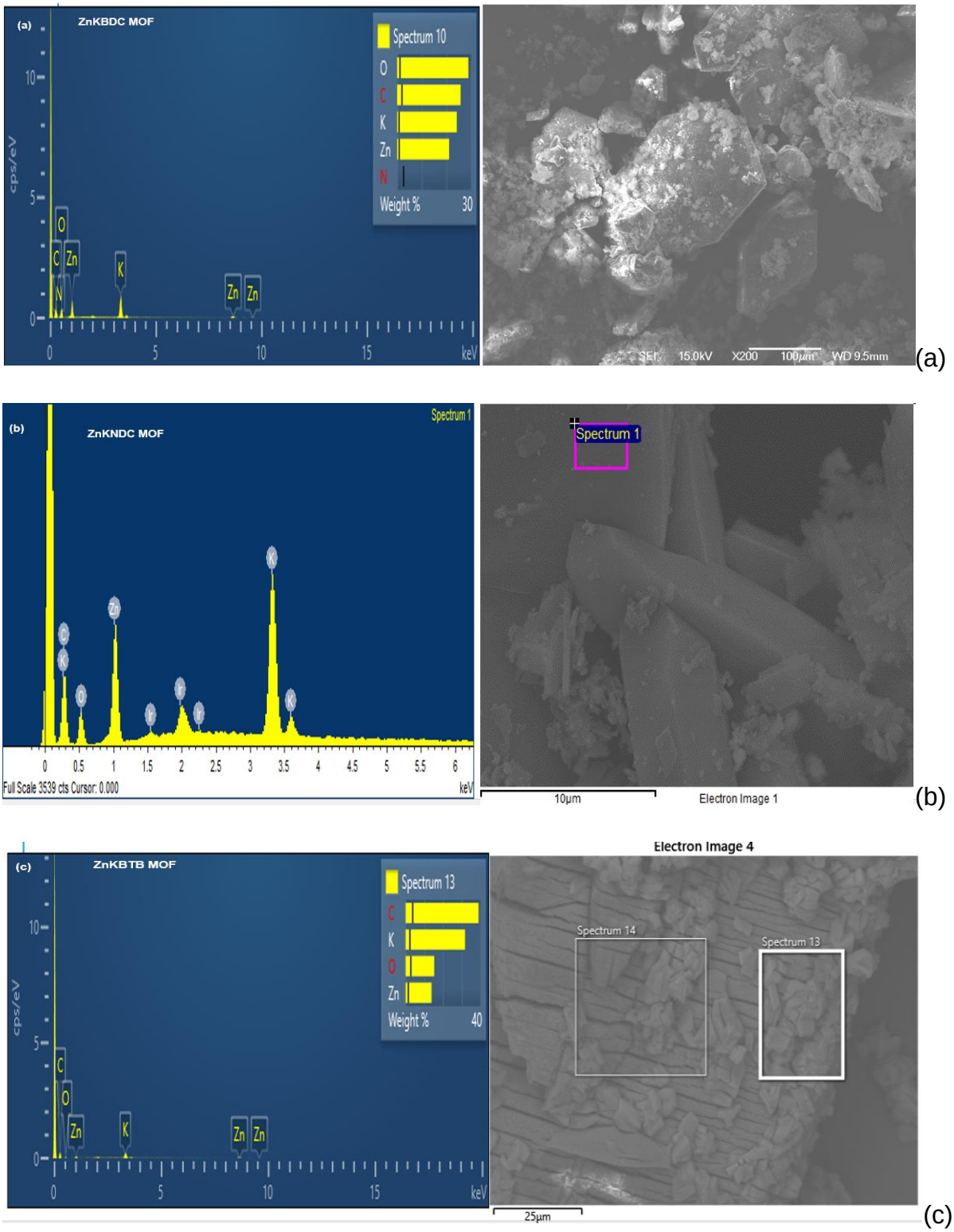


Figure 3.9: SEM/EDX spectrum of (a) ZnKBDC (b) ZnKNDC (c) ZnKBTB MOFs at 120 °C confirming presence of Zn, K C, and O in ZnKNDC MOF**.**

3.4 FTIR spectroscopy

FTIR spectroscopy was measured throughout the region at wavenumbers of 400-4000 cm-1 (mid-infrared) to identify the functional group of the mixed metal MOFs. As shown

in Figures 3.10, 3.11 and 3.12, two strong peaks were observed at 1364 cm^{-1} and 1401 cm^{-1}, indicating both symmetric and asymmetric vibrations of C=O, respectively. The 1602–1560 cm-1 and 1402–1364 cm-1 peaks may be attributed to bridging and chelating carboxyl groups.[12]

Moreover, a strong peak at 1554 cm^{-1} showed the complex interaction of the C=O with metals Zn and K. The vibration C=O stretching mode of DMF shifted to the lower wavenumbers (1660 cm^{-1}) relative to the free amide value (1680 cm^{-1}), showing that the ligations of all DMF molecules with their carbonyl groups were successfully formed. Generally, the absorption band was absent in the region of 1700 cm-1, indicating that carboxylic groups in the dicarboxylic ligand were completely deprotonated. This indicated that the carboxylate groups of the BTB are coordinated to metal ion nodes. The absence of the O-H stretching vibrations from water molecules (two peaks, sharp peak and broad peak, at 3460 cm^{-1} and 3220 cm^{-1}, respectively) shows the absence of water molecules in the frameworks.[29,30]

Comparison of FTIR-ATR spectra for MOFs at 120^{o}C and 170^{o}C starting materials 2,6 Naphthalene dicarboxylic acid [NDC] Terephthalic acid [H_2BDC], potassium tert butoxide (blue curve) materials. We conclude that The FTIR-ATR spectra of MOFs synthesized at 120^{o}C and 170^{o}C materials closely resemble each other. No trace of starting materials, potassium tert butoxide and H_2BDC was observed in the as-synthesized products.

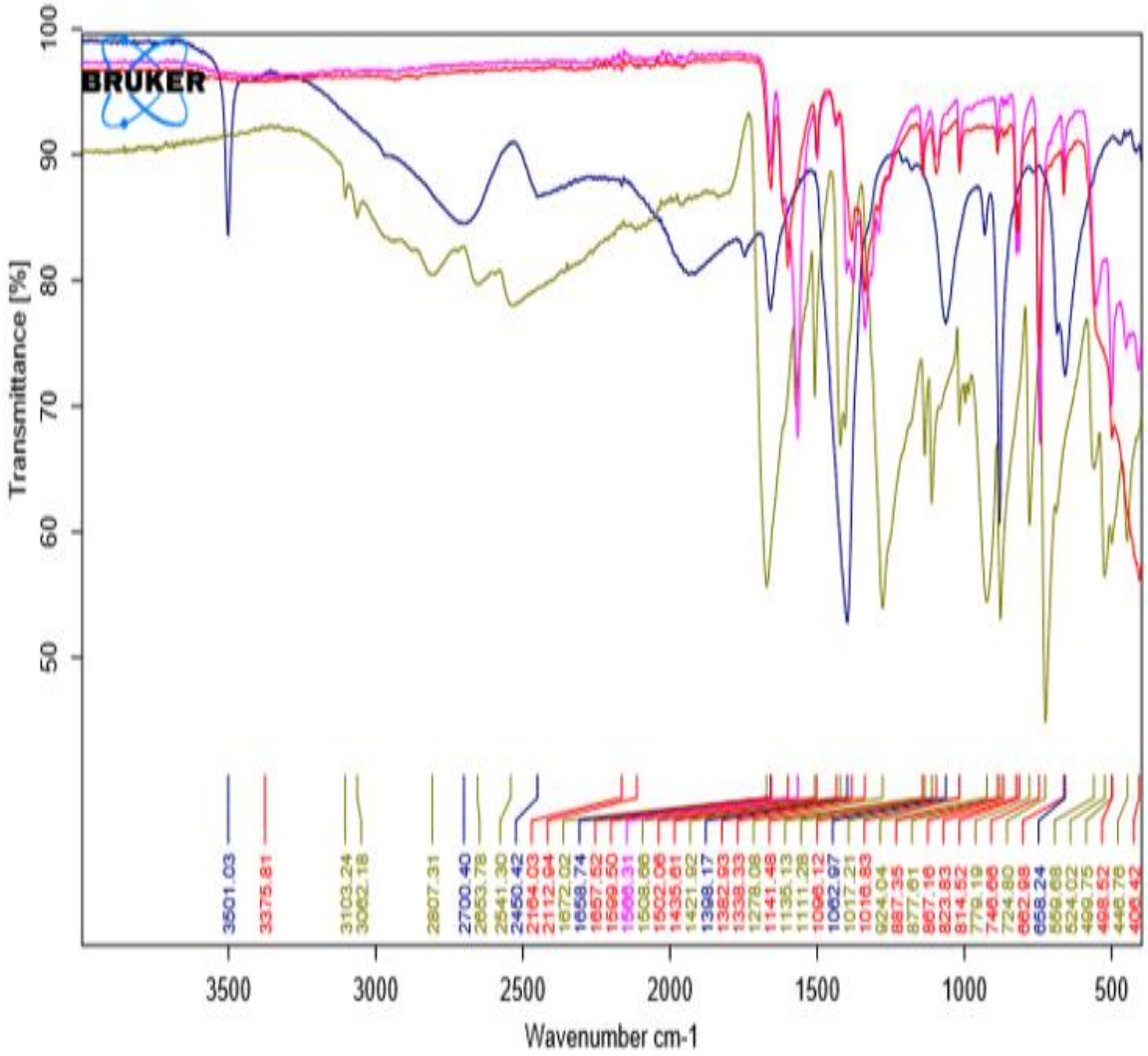


Figure 3.10: FTIR-ATR spectra for (a) ZnKBDC MOF synthesized at 120^{o}C (red curve), (b) ZnKBDC MOF synthesized at 170^{o}C (pink curve), (c) Terephthalic acid, H_2BDC (brownish green curve) and (d) potassium tert butoxide (blue curve).

Comparison of FTIR-ATR spectra (top-to-bottom) are in Figure 3.10 for ZnKBDC MOF synthesized at 120^{o}C (red curve), ZnKBDC MOF synthesized at 170^{o}C (pink curve), [Terephthalic acid, H_2BDC] (grey curve), potassium tert butoxide (blue curve) materials. The FTIR-ATR spectra of the ZnKBDC MOF synthesised at 120^{o}C and ZnKBDC MOF at 170^{o}C materials closely resemble each other. No trace of starting materials, potassium *tert*-butoxide and H_2BDC was observed in the as-synthesized products.

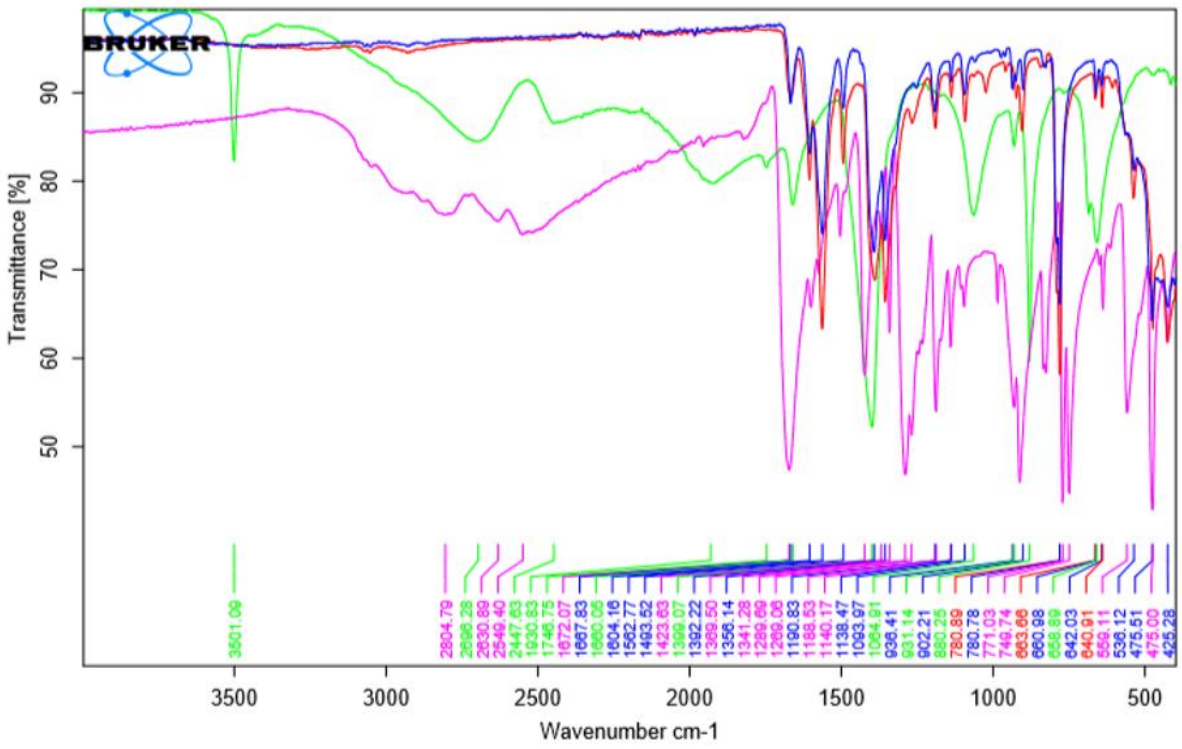


Figure 3.11: FTIR-ATR spectra for (a) ZnKNDC MOF synthesized at 120^{o}C (blue curve) (b) ZnKNDC MOF synthesized at 170^{o}C (red curve) (c) Naphthalene 2, 5 - dicarboxylic acid, 2,5-NDC (pink curve) and (d) potassium tert butoxide (green curve)

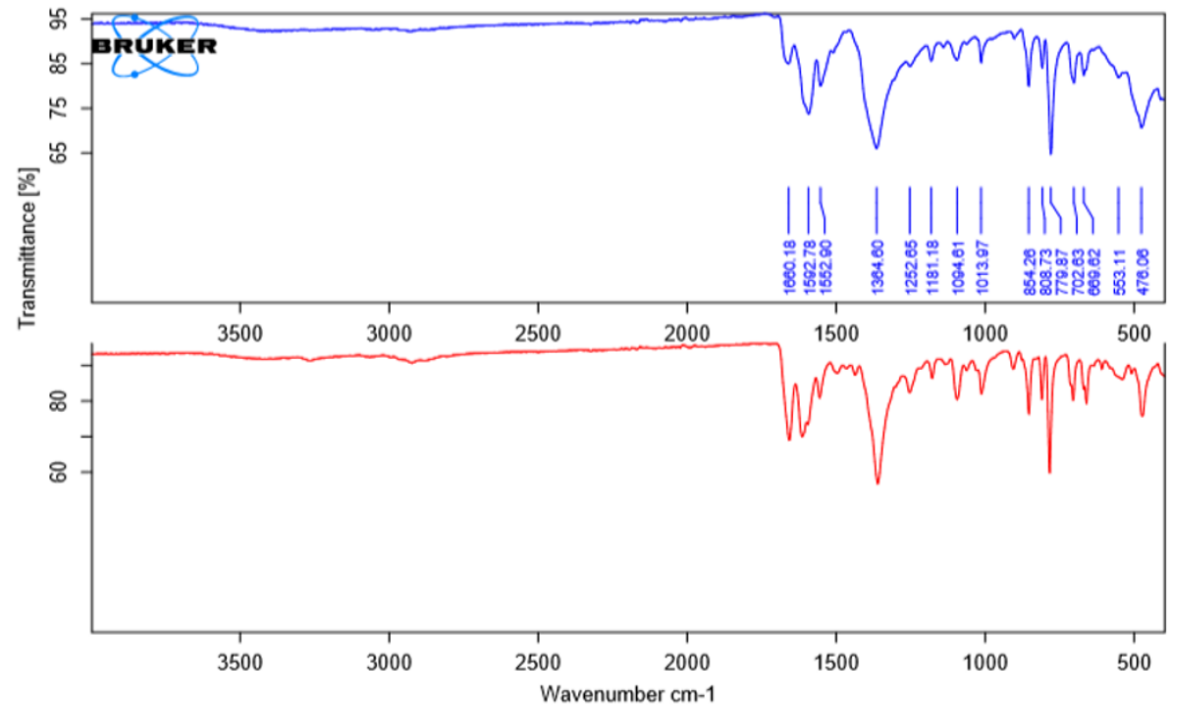


Figure 3.12. FTIR spectra of ZnKBTB MOFs at 120 °C (blue) and 170 °C (red colour curve).

3.5 Zinc Lithium MOF System

In synthesising the Zinc-Lithium systems, we follow the same procedures and stoichiometry as in sections 3.2.1, 3.2.2, 3.2.3 for the synthesis of ZnLiBDC, ZnLiNDC and ZnLiBTB MOF. The main difference is the substitution of $K^{+}(CH_3)_3CO^{-}$ potassium tert butoxide with lithium tert butoxide, $Li^{+}(CH_3)_3CO^{-}$ in the reaction medium. The single crystal PXRD of ZnLiNDC and ZnLiBDC are shown in the asymmetric unit in Figure 3.13.

Table 3.2 shows the crystal data for ZnLiBDC and ZnLiNDC MOFs. The asymmetric unit of ZnLiBDC MOF in Figure 3.13a consists of three BDC, two Li and two Zinc atoms. Each zinc is coordinated to 2 oxygen, each of which is from different BDC units. Each Li is also coordinated with two oxygens from different BDC units. While the Zn is coordinated to a terminal nitrate ion, the Li is coordinated to a DMF molecule. Three (3) occluded DMF molecules were successfully modelled, where 1.75 disordered DMF units were found using an Olex 2 solvent mask.[23-24] A solvent mask was calculated using PLATOON SQUEEZE, and 286 electrons were found in a volume of 1294 $Å^3$ in 1 void per unit cell. This is consistent with the presence of $1.75[C_3H_7NO]$ per asymmetric unit, accounting for 280 electrons per unit cell. (formula $C_{57.5}\ H_{45}\ Li_{2.5}\ O_{30}\ Zn_{2.5}\ N_{0.25}$, Moiety $=C_{30}\ H_{23}\ Li_2\ N_4\ O_{19.5}\ Zn_2$, $C_{2.25}\ N\ O_{0.5}$, $C_{1.667}\ N\ O_{0.333}$, $C_3\ H_8\ N\ O$, $C_{2.5}\ H_{6.5}\ N\ O$, $1.75[C_3H_7NO]$)

The study of the coordination environment of the metal centre and grown structure (Figures 3.13c and 3.13d) reveals that both the Li and Zn had a coordination number of 4 with a distorted tetrahedral geometry such that each Zn is N-coordinated to a terminal nitrate and two oxygens, O from three different carboxylate BDC units. Similar coordination is seen for the Li, except there is a terminal DMF instead of the nitrate. This two-dimensional structure is due to terminal nitrate and DMF, which prevented it from growing in the third direction, as shown in Figure 3.13b.

For clarity, the packed structure (Figure 3.13d) is viewed along the crystallographic (a) and (b) directions showing hexagonal pores. The oxygen at the nitrate has high thermal motion; hence, there is probability of a whole disorder of the whole moiety.`

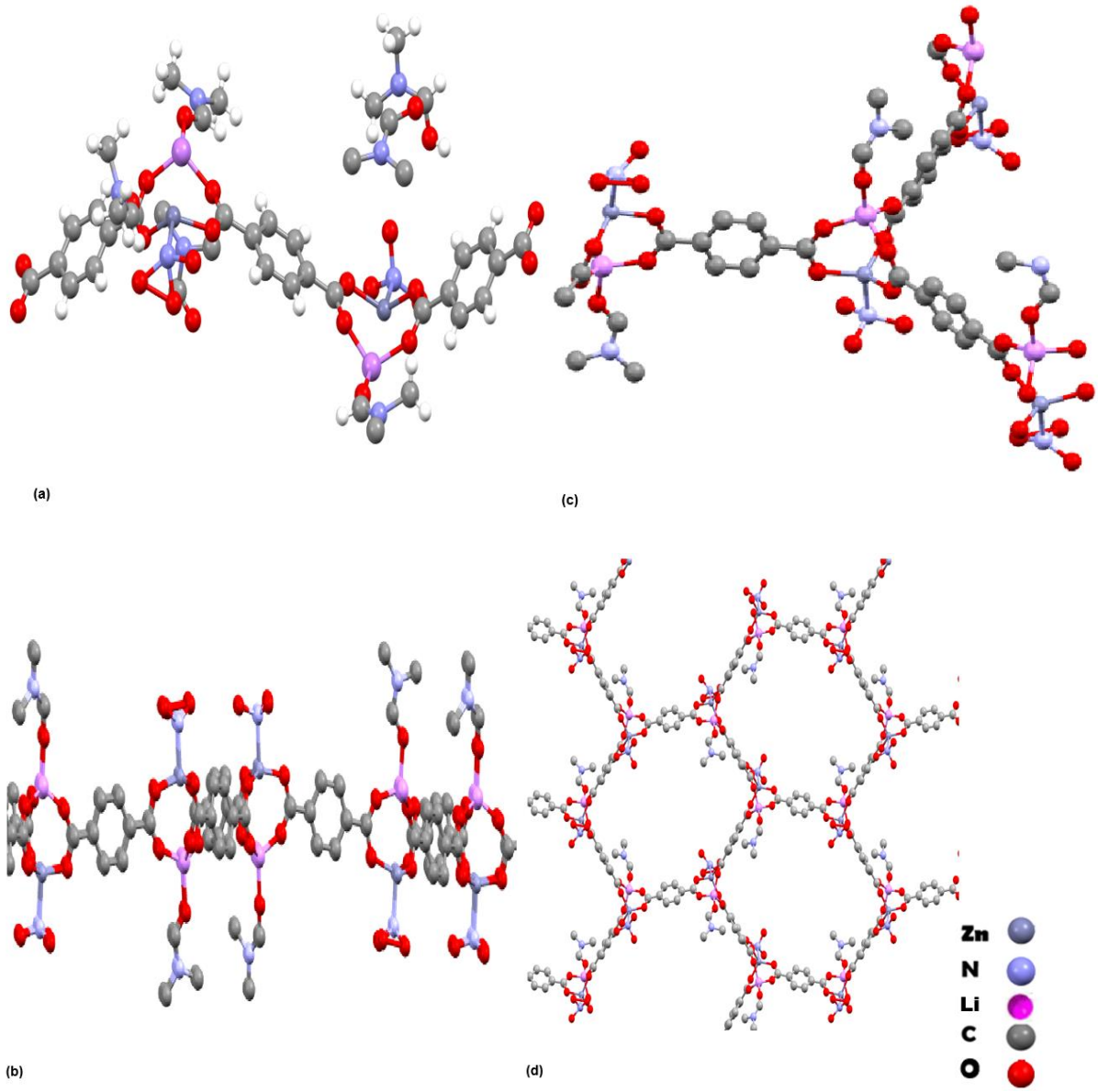


Figure 3.13: (a) ‘b’ view of ZnLiBDC MOF Asymmetric unit and (b) ‘b’ view of the 2D structure of ZnLiBDC MOF (c) ‘b’ view of the repeated centre unit of ZnLiBDC MOF grown structure (d) ‘b’ view of ZnLiBDC MOF packed unit (grey = C, light blue = Zinc, magenta = Li, red = O, blue = N, H = light grey; hydrogen atoms have been removed for clarity).

The Zn-O bond distance are in the range of 1.926(5)–1.947(5) Å, Li-O bond lengths are in range of 1.858(17)–1.953(13) Å, Zn–N in the range 2.047(8)–2.086(7) Å and Zn-Li bond lengths are in range of 3.183(2)-3.247(16) Å (see Appendix IV for detailed bond distances and bond angles). Viewing along the b-axis reveals the terminal nitrate and DMF units. As a two–dimensional structure, it can favour conductivity study measurement as the next research objective for the ZnLiBDC MOF.

Table 3.2 Crystal data and structure refinement for ZnLiBDC and ZnLiNDC MOF.

	ZnLiBDC	**ZnLiNDC**
Empirical formula	$C_{57.5}H_{45}Li_{2.5}O_{30}Zn_{2.5}N_{0.25}$	$C_{94}H_{94}Li_{21.5}N_{11.5}O_{29.5}Zn_4$
Formula weight	1400.21	2267.49
Temperature/K	120.00(10)	293(2)
Crystal system	Monoclinic	Triclinic
Space group	$P2_1/c$	P-1
a/Å	13.6472(10)	11.3072(3)
b/Å	32.6055(14)	12.5141(3)
c/Å	15.6947(9)	21.1700(4)
α/°	90	89.326(2)
β/°	106.436(7)	83.765(2)
γ/°	90	72.705(2)
Volume/Å^3	6698.3(7)	2842.52(12)
Z	4	1
ρ_{calc}g/cm^3	1.388	1.325
μ/mm^{-1}	1.798	1.574
F(000)	2857.0	1159.0
Crystal size/mm^3	0.208 × 0.111 × 0.075	0.182×0.048 × 0.031
Radiation	Cu Kα (λ = 1.54184)	CuKα (λ = 1.54184)
2Θ range for data collection/°	7.278 to 154.67	7.4 to 146.468
Index ranges	-15 ≤ h ≤ 16, -39 ≤ k ≤ 40, -16 ≤ l ≤ 19	-13 ≤ h ≤ 14, -15 ≤ k ≤ 15, -26 ≤ l ≤ 26
Reflections collected	49656	47529
Independent reflections	13181 [R_{int} = 0.1084, R_{sigma} = 0.0891]	11205 [R_{int} = 0.0251, R_{sigma} = 0.0229]
Data/restraints/parameters	13181/60/711	11205/57/668
Goodness-of-fit on F^2	1.361	1.032
Final R indexes [I>=2σ (I)]	R_1 = 0.1403, wR_2 = 0.3691	R_1 = 0.0596, wR_2 = 0.1539
Final R indexes [all data]	R_1 = 0.1757, wR_2 = 0.4217	R_1 = 0.0627, wR_2 = 0.1570
Largest diff. peak/hole / e Å^{-3}	1.06/-1.30	1.89/-0.83

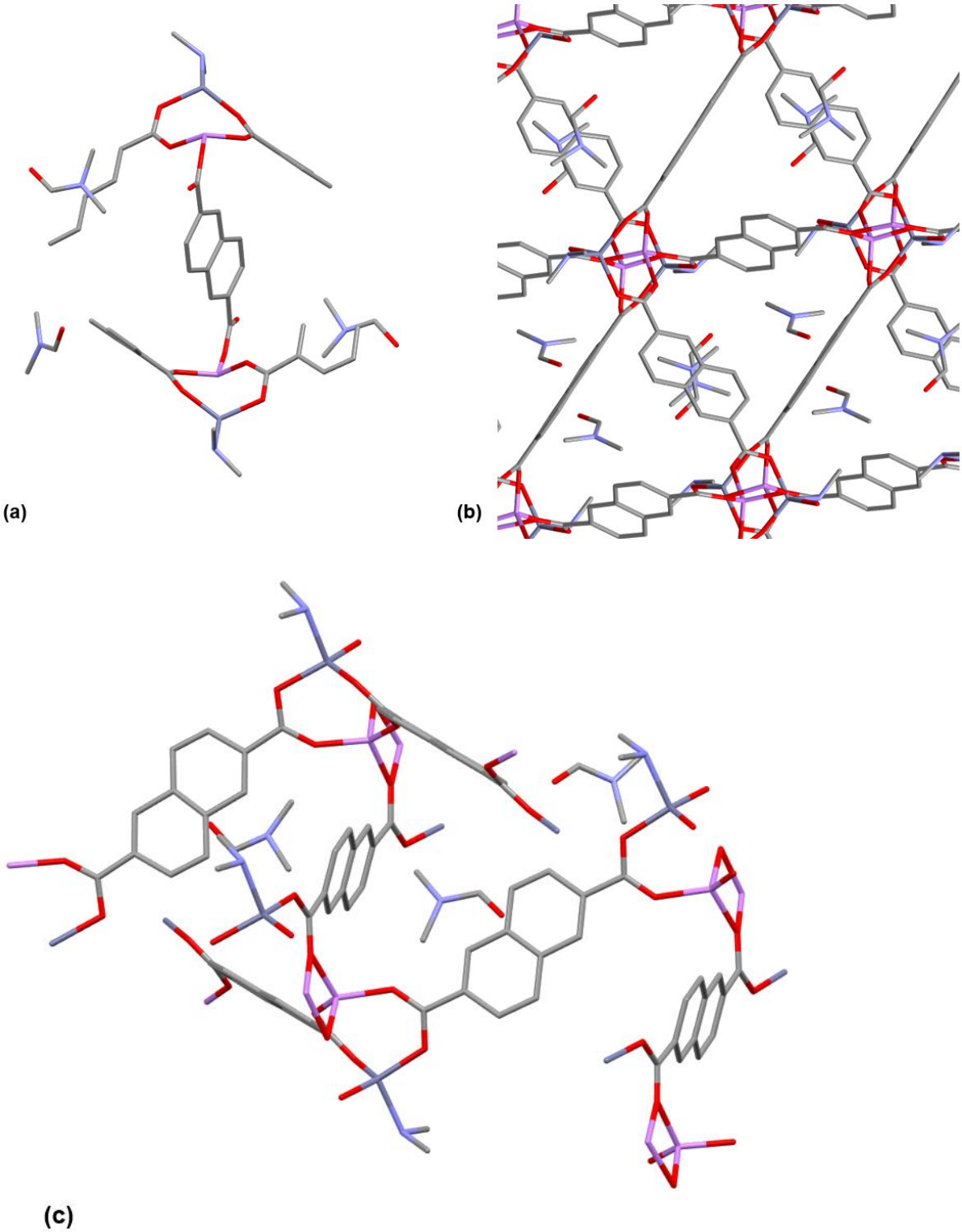


Figure 3.15: Stick representation of (a) Asymmetric units and (b) Packed Unit of ZnLiNDC MOF viewed along 'b' crystallographic axis. (c) 'b' view ZnLiNDC MOF Autocentre showing -COO- coordination modes (grey = C, light blue = Zinc, magenta = Li, red = O, blue = N, H = light grey; hydrogen atoms have been removed for clarity).

The SCXRD analysis of ZnLiNDC MOF revealed the formation of a triclinic crystal system with a P-1 space group with a 2D porous framework. There are two coordination modes observed. First, four of the six $(NDC)^{2-}$ were linked by Zn(II) and Li ions where each of the central NDC –COO− group acted as a bis-monodentate ligand to Li-ion, while the other four acted as a bridging bidentate agent whereby one oxygen is bonded to Zn (II) ion and the other oxygen bonded to Li-ion (Figure 3.15a). Therefore, Zn(II) and Li-ion are N- and O-coordinated tetrahedrally. The asymmetric unit consists of three molecules of successfully modelled DMF, with one unit of DMF being disordered found using Olex 2 solvent mask,[22-24] one full NDC ligand, four halves of NDC ligands, two Zn and two Li atoms. Three DMF molecules were correctly modelled; the other was squeezed out due to disorderliness.

The Zn-O bond distance are in the range of 1.942(2)–1.968(2) Å, Li-O bond lengths are in range of 1.873(5)–1.972(5) Å, Zn–N in the range 2.037(3)–2.048(3) Å and Zn-Li bond lengths are in range of 3.113(5)–3.147(5) Å (see Appendix V for detailed bond distances and bond angles). The two Zn atoms are each attached to a molecule of dimethyl amine, suspected to be a product of hydrolysis of DMF in the presence of base lithium tert butoxide at elevated temperature (near DMF boiling temperature 153 ^{o}C). Therefore, DMF undergoes decarbonylation and degrades to the secondary amine, dimethylamine (DMA) and formic acid (FA) (Figure 3.16).

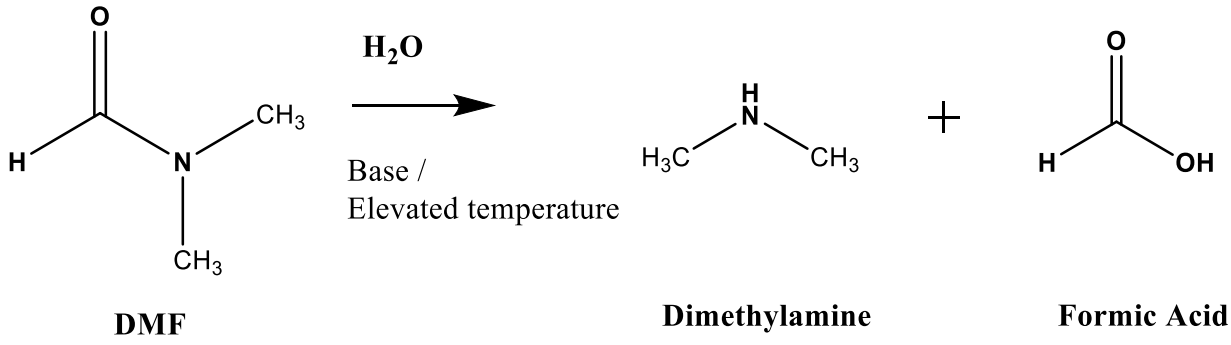


Figure 3.16: Scheme for the hydrolysis of dimethylformamide (DMF) to dimethylamine (DMA) and formic acid (FA).[31]

A solvent mask was calculated, and 86 electrons were found in a volume of 361 $Å^3$ in 2 voids per unit cell. This is consistent with the presence of $2[C_3H_7NO]$ per Asymmetric Unit, which accounts for 80 electrons per unit cell. Chemical formula, C_{94} H_{94} $Li_{21.5}$ $N_{11.5}$ $O_{29.5}$ Zn_4, Moiety = C_{80} H_{64} Li_4 N_4 O_{24} Zn_4, 6(C_3 H_7 N O), 2[C_3H_7NO]

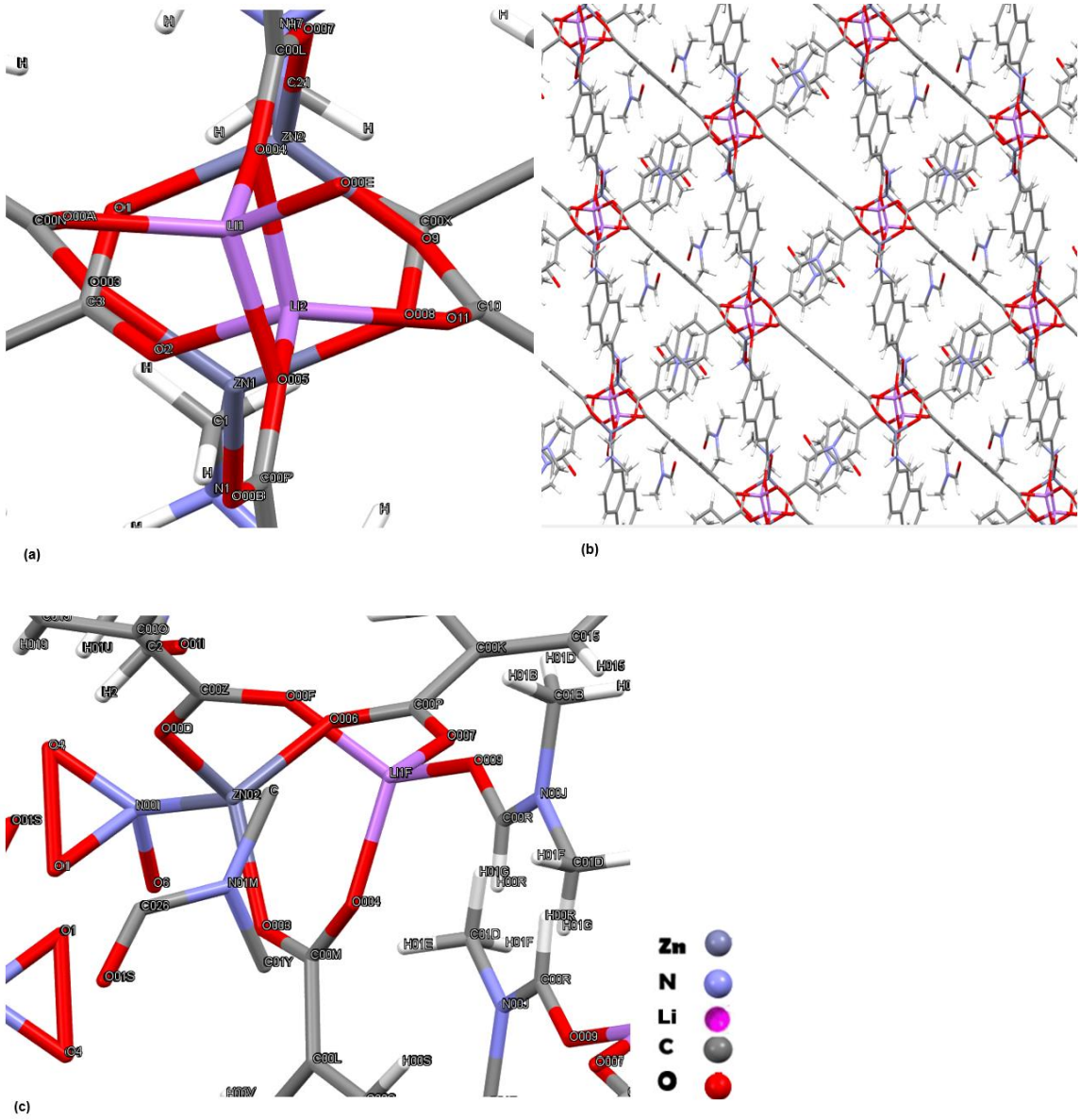


Figure 3.17: Coordination Environment of (a) ZnLiNDC and (b) ZnLiNDC MOF packed structure viewed along ‘b’ crystallographic axis and (c) ZnLiBDC MOF viewed along ‘a’ axis (grey = C, light blue = Zinc, magenta = Li, red = O, blue = N, H = light grey (hydrogen atoms have been removed for clarity).

Figure 3.17 shows the coordination environment of Zn and Li. Zn metal coordinates DMA, Zn-N bond. In Zn-O, Zn coordinates with carboxylate Oxygen from three different NDC ligands. Li-O forms a rectangular cage formed by two Li(I) metal ions, and each O-coordinated to four carboxylate Oxygen, O from four different NDC ligands. Also, Figure 3.17c shows there was no Zn–Li bond, Li O-coordinated (Li-O) to one terminal DMF molecule and three (3) Oxygen atoms of the carboxylate from three different BDC ligands. The Zn metal N-coordinates (Zn-N) to a terminal nitrate.

It also coordinates to three (3) Oxygen atoms of the carboxylate from three different BDC ligands.

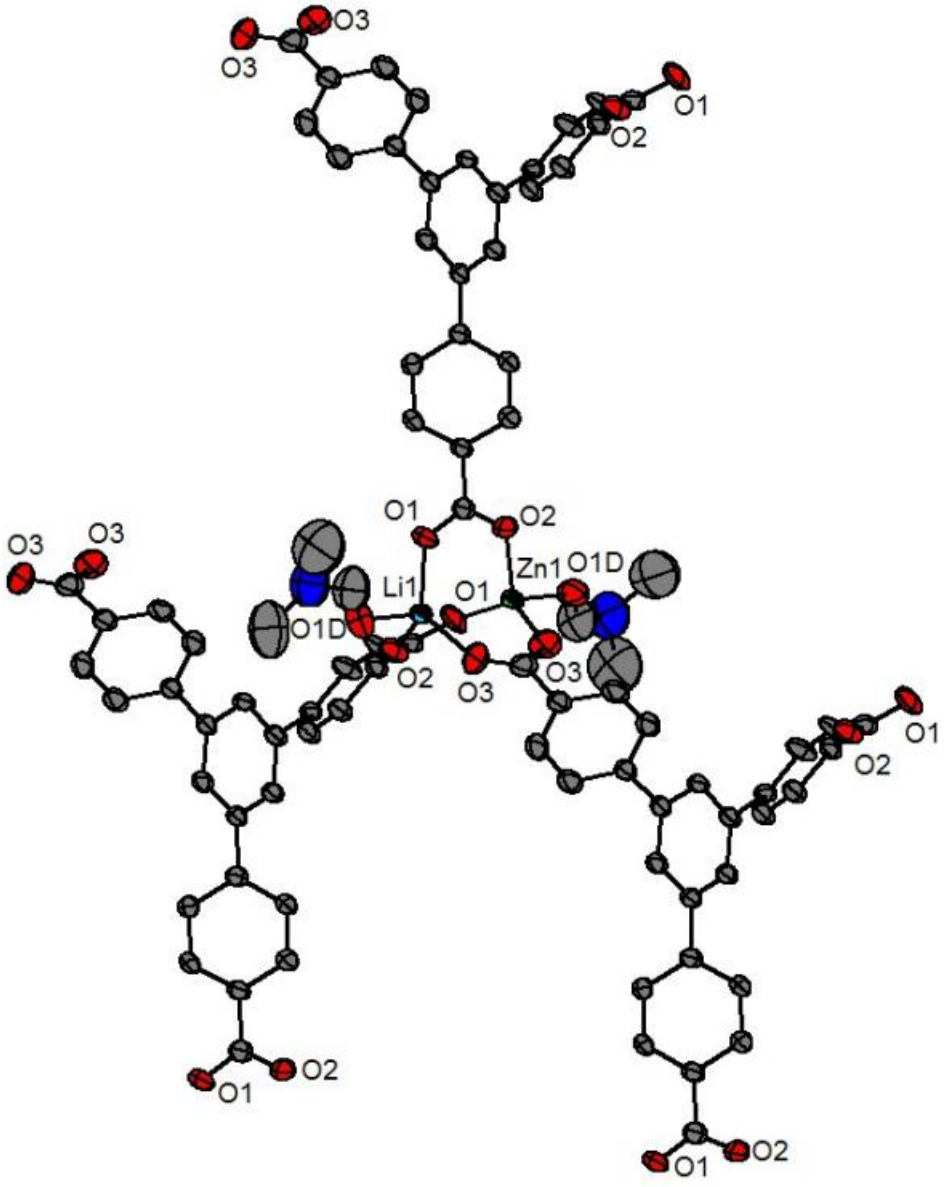


Figure 3.20: Ellipsoid model representation in ZnLiBTB MOF (ellipsoids are at the 50% probability level; hydrogen atoms are removed for clarity; Li cations -blue balls, Co – pink, Zn – green).[32]

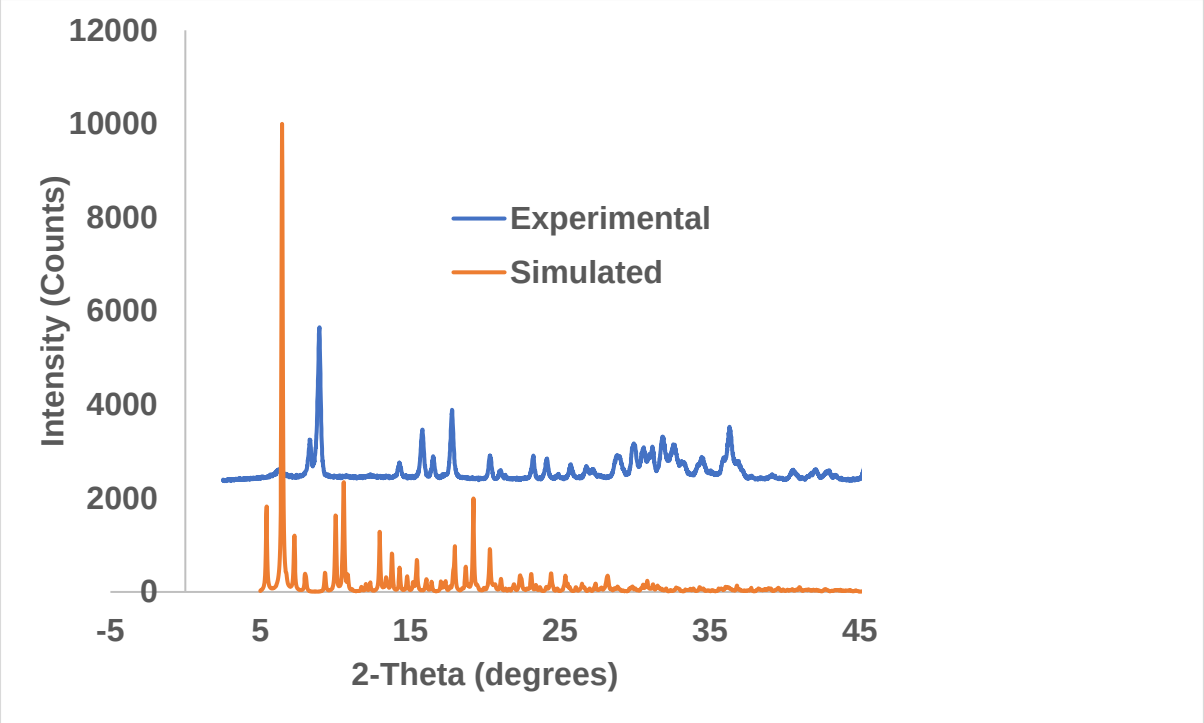
The single crystals structure of ZnLiBTB synthesized in section 3.2.3 was found to be the same product bearing the same unit cell single crystal XRD as $[LiZn(BTB)(DMF)_2]\cdot 2DMF\cdot H_2O$ synthesized and published by Sapianik et al. in 2019.[32] While we utilised direct synthesis procedure involving the heating of Zinc nitrate hexahydrate, 1,3,5-Tris(4-carboxyphenyl)benzene with Lithium tert butoxide in DMF

as described in section 3.2.3. Sapianik and co-worker prepared $[LiZn(BTB)(DMF)_2]\cdot 2DMF\cdot H_2O$ by the substitution of pivalate ligands in $[Li_2Zn_2(piv)_6(py)_2]$ with tricarboxylate bridges (BTB^{3-}). The heterometallic pivalate complex $[Li_2Zn_2(piv)_6]$ possesses a tetranuclear core which consists of two fused dinuclear units $\{LiZn(piv)_3\}$ via lateral Li–O coordination interactions. In this method, the Zinc/Lithium pivalate complex served as the starting complex $[Li_2Zn_2(piv)_6(py)_2]$ as well as the source of the secondary building unit where piv = pivalate anion and py = pyridine as previously synthesised and reported by Sapianik and co-worker in 2017.[33] The Zinc/Lithium pivalate complex was heated with 1,3,5-tris(4-carboxyphenyl)benzene (H_3BTB) in DMF/CH_3CN to effect the substitution reaction.[32]

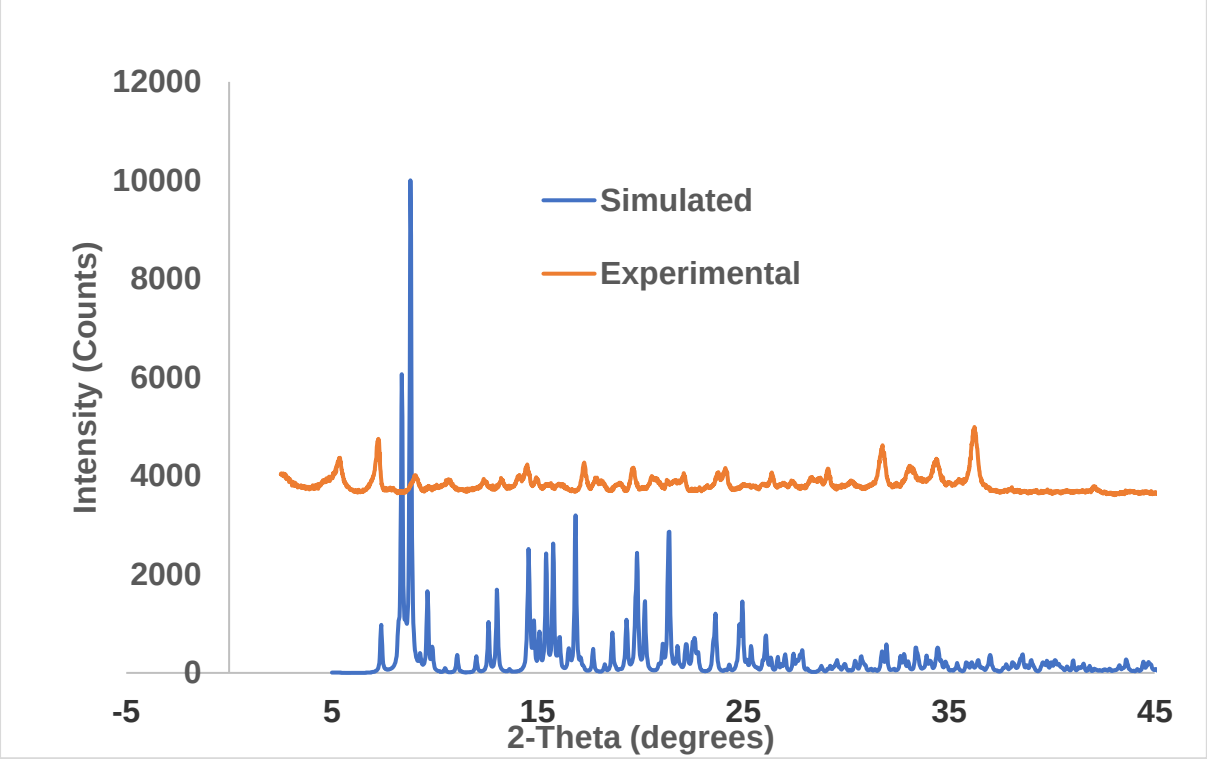
ZnLiBTB MOF crystallizes in monoclinic space group *I*2/a. In this structure, Li and Zn cations are disordering over two positions with 50% occupancy. Figure 3.20 shows each Li/Zn ion coordinates the O atom of the DMF molecule and three O atoms of three carboxylate groups, thus adopting distorted tetrahedral coordination (Li/Zn–O 1.898(3)−2.016(3) Å) as earlier observed in ZnLiBDC and ZnLiNDC MOFs. ZnLiBTB is based on the bimetallic tricarboxylate paddlewheel {LiZn} unit of both Li and Zn. Cations merged between two positions. The Li/Zn–O metal-ligand distances are in the range 1.898(3)−2.016(3) Å.[31]

3.6 PXRD Analysis of ZnLiBDC and ZnLiNDC

The powder XRD pattern obtained agrees with the simulated pattern, and the high crystallinity of the ZnLiNDC and ZnLiBDC MOF system was confirmed with expected peaks of high intensity around 2Θ=10 as shown in the PXRD pattern in Figure 3.14 and SEM/EDX in figure 3.4.3. For ZnLiNDC, the peak is consistent with the peak position found in the MOF with the same NDC ligand, where characteristic peaks with high intensity were observed at 2Θ = 5.32. 7.26 °. 9.07 °, 10.06 °, 12.37 °, 14.49, 17.23 ° and 19.60 °, while for ZnLiBDC, characteristic peaks with high intensity were observed at 2Θ=6.30 °, 8.32 °, 8.94 °, 14.30 °,15.83 °, 17.80 °.



(a)



(b)

Figure 3.14: PXRD Pattern of ZnLiBDC and ZnLiNDC MOF.

3.7 SEM/EDX Analysis of ZnLiMOF

The morphology and sizes of particles corresponding to ZnLIBDC and ZnLiNDC MOFs are described in Figures 3.18 and 3.19 using scanning electron microscopy (SEM). ZnLIBDC and ZnLiNDC MOF morphology consist of colourless rectangular prism particles and rectangular flat sheets with sizes of 8-10 μm (Figures 3.18 and 3.19, respectively) arranged randomly. The crystals were surrounded by whitish microcrystalline nano-threads (Figures 3.18, 3.19b and 3.19c)). Further, the elemental analyses of respective MOFs are carried out using an SEM-coupled EDX spectroscopy measurement, as shown in Figures 3.18 and 3.19.[34]

While potassium, K ion was detected in SEM/EDX spectrum of ZnKMOF as seen in Figure 3.9. It is important to state that Li is not detected with our instrument detector (Figures 3.18 and 3.19) because Li (with atomic number = 3), as a light element, possess very weak intensity of the characteristic peak as was earlier observed in EDX analysis of Li Doped MIL-101-(Cr) MOF.[34] Also, it was reported that EDX measurement could not be a good method for lighter compounds (e.g., C, O, Na, and Zn).[35,36] Therefore, EDX could not show the presence of Lithium in the ZnLiBDC and ZnLiNDC MOF and could not be detected as shown in Figure 3.18.

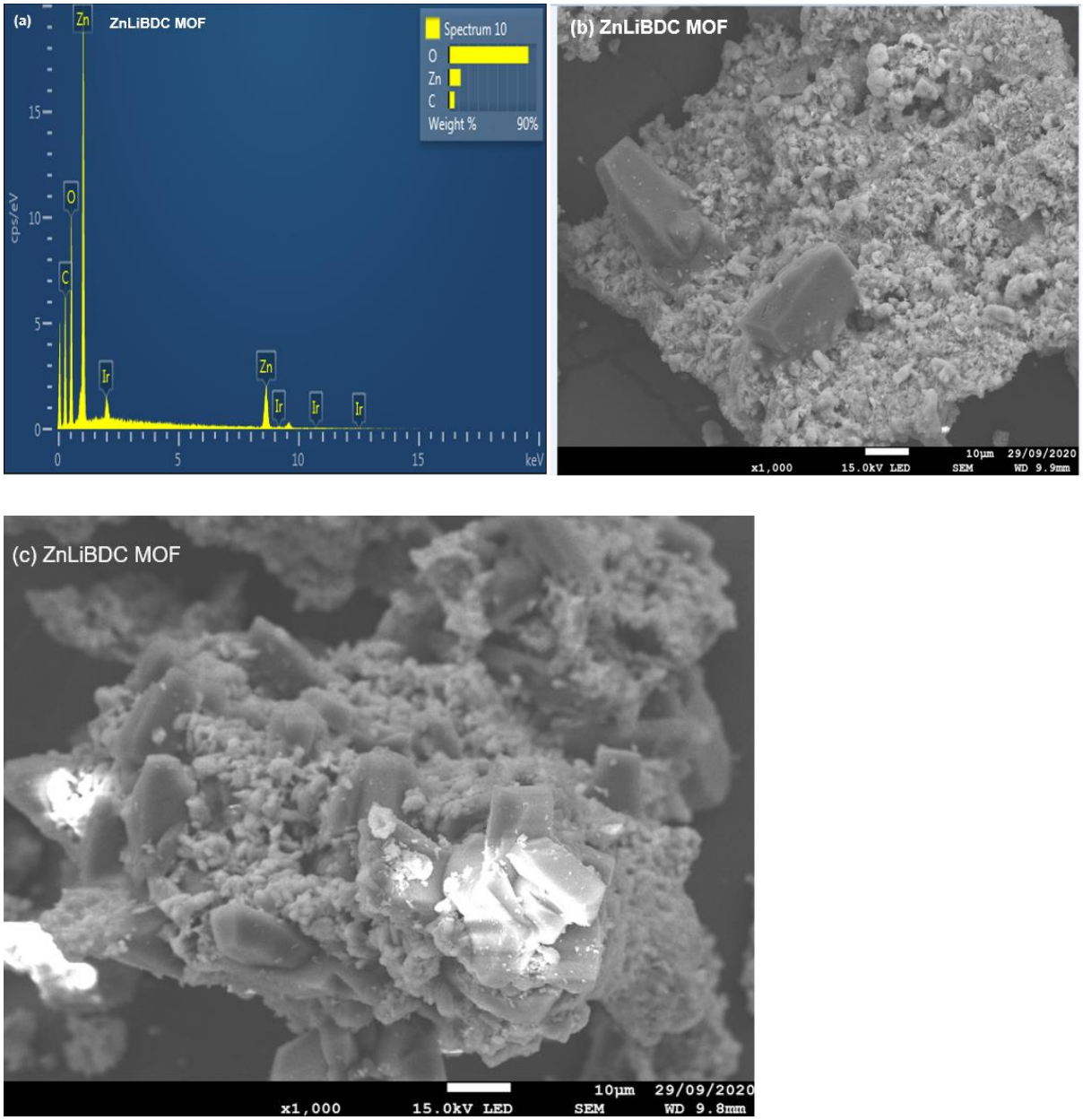


Figure 3.18 EDX Analysis of (a) ZnLiBDC SEM Micrographs of (b) ZnLiBDC (x 1000) (c) ZnLiBDC (x 1000) MOF at different magnifications.

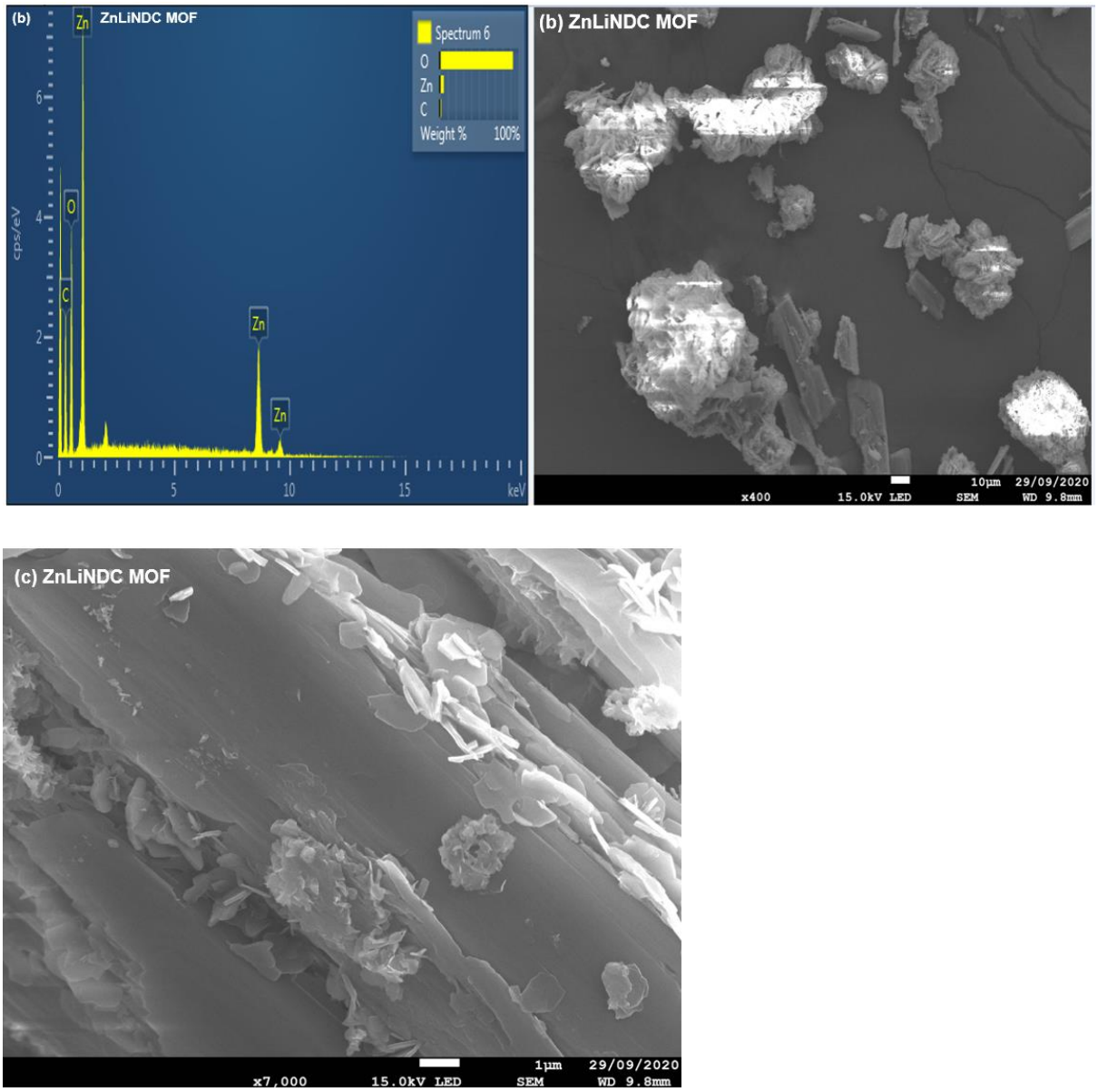


Figure 3.19 EDX Analysis of (a) ZnLiBDC and SEM micrographs of (b) ZnLiNDC MOF at (x400) (c) ZnLiNDC MOF (x7,000) magnification.

Detailed discussion on the adsorption characteristics of the ZnK and ZnLi MOF systems will be discussed in Chapter 4.

3.8 Conclusion and Further Studies

A series of novel bimetallic MM-MOFs were synthesized from a combination of Zinc (Zn) with either Lithium (Li) or Potassium (K) as inorganic metal nodes and three organic linker molecules 1,3,5-Tris(4-carboxyphenyl)benzene (BTB (BTB), benzene-1,4-dicarboxylic acid (Terephthalic acid, BDC), 2,6-Naphthalenedicarboxylic acid (NDC) using hydrothermal methods at temperatures 120 °C and 170 °C. The resulting

MOFs were characterised by single-crystal X-ray diffraction (SCXRD), SEM-EDX, TGA, and FTIR. FTIR results showed no absorptions corresponding to -COOH at 1690-1730 $cm^{-1,}$ confirming complete deprotonation of the dicarboxylic functional group and the formation of ZnKMOFs and ZnLiMOFs. As expected, SEM/EDX results revealed the composition of Zn, K, O, and C atoms within MOFs. The single-crystal X-ray diffraction revealed that MOF crystallizes in the ZnKBDC and ZnLiBDC crystalises in the orthorhombic, FDD2 and monoclinic systems, $P2_1/c$ space group, respectively. The ZnKNDC and ZnLiNDC both crystalize in the triclinic system and P-1 space group, while ZnKBTB and ZnLiBTB both adopted a monoclinic system but with different C2/c and I2/a space groups respectively. A study of the coordination environment of ZnBDC and ZnKBTB MOF shows that in both cases, the Zn(II) displayed tetrahedral coordination geometry with a coordination number of 4, while Potassium, K ion possesses the coordination number of 8, coordinated in a distorted square antiprismatic geometry. It is only in ZnKNDC MOF that Zn displayed both tetrahedral and octahedral coordination geometry by having coordination numbers of 4 and 6, while Potassium possesses the coordination numbers of 3 and 7 coordinated in a trigonal pyramidal and pentagonal pyramidal geometry, respectively. However, In all ZnLiMOFs systems (ZnLiBDC, ZnLINDC and ZnLiBTB) studied, the Zn(II) and Li cations are O-coordinated tetrahedrally.

Additionally, the examination of the coordination mode adopted by the carboxylates in the MOFS shows that in the ZnKBDC MOF, the BDC ligands acted as a bridging tridentate agent, (μ_3-η^1:η^2) binding two Zn and one K at the SBU whereas in ZnLiBDC the ligand binds in the bis bidentate bridging (syn-syn, μ_2-η^1:η^1) mode. While in ZnKNDC, NDC acts as bis-tridendate bridging (μ_3-η^1:η^2) and bis-tetradentate (octadentate) (μ_4-η^1:η^3) bridging ligand in the pentanuclear SBU. Both bidentate bridging (μ_2-η^1:η^1) mode and bis tridentate bridging (μ_3-η^1:η^2) mode are displayed in the ZnLiNDC MOF. In ZnKBTB, BTB^{2-} carboxylate -COO- ligand adopted two different coordinating modes with Zn and K atoms, which include one tridentate bridging (anti-syn-anti, μ_3-η^1:η^2) and two bidentate bridging (syn-syn, μ_2-η^1:η^1) mode with the metal ions in the SBU. Interestingly in ZnLiBTB, the -COO- adopted only bidentate bridging modes with the Zn/Li. The next chapter 4 of this thesis study will focus on the Gas adsorption experiment on the synthesized MOFs.

3.9 References

1. A.P. Peedikakkal, A.A. Jimoh, M.N. Shaikh and B.E. Ali, *Arab J Sci Eng.*, 2017, **42**,4383–4390.

2. S. Schuster, E. Klemm and M. Bauer, *Chem. Eur. J.*, 2012, **19**, 15831–15837.

3. J. L. Long, L.M. Wang and X.F. Gao, *Chem. Commun.*, 2012, **48**, 12109–12111.

4. S. Horike, M. Dinc˘a, K. Tamaki and J.R. Long, *J. Am. Chem. Soc.* 2008.**130**, 5854– 5855.

5. C. Chizallet, S. Lazare and D. Bazer-Bachi, *J. Am. Chem. Soc.* 2010,**132**, 12365–12377.

6. Y. Liu, T. Zhang and W. Wu, *RSC Adv.* 2015, **5**, 56020–56027.

7. Y.P. He, Y.X. Tan and J. J. Zhang, *Mater. Chem. C*. 2014, **2**, 4436−4441.

8. D. Sun, F. Sun, X. Deng, and Z. Li, *Inorg. Chem.* 2015, **54**, 8639−8643.

9. C. K. Brozek and M. Dincă, *J. Am. Chem. Soc.* 2013, **135**, 12886− 12891.

10. F. Gul-E-Noor, B. Jee and M. Mendt, *J. Phys. Chem.* 2012, **116**, 20866–20873.

11. M.A. Gotthardt, R. Schoch and S. Wolf, *Dalton Trans.* 2015, **44**, 2052–2056.

12. P.S. Sagara, V. Varma and J.K. Randhawa, *ChemPlusChem*, 2019, **84**, 13.

13. C. H. Lau, R. Babarao and M. R. Hill, *Chem. Commun.* 2013, **49**, 3634−3636.

14. N. Li, Z. Chang, H. Huang, R. Feng, W. He, M. Zhong, D. G. Madden, M. J. Zaworotko and X. Bu, *Small,* 2019, **15**, 1900426.

15. R. Babarao, R and J.W. Jiang, *Langmuir*, 2008, **24**, 6270–6278.

16. Z. H. Xiang, Z. Hu, D. P. Cao, W. T. Yang, J. M. Lu, B. Y. Han, and W. Wang, *Angew. Chem. Int. Edit.*, 2011, **50**, 491–494.

17. M. Almasi, A. Sharma and T. Zelenka, *Inorganica Chimica Acta*, 2021, **526**, 120505.

18. R. Zou, A. I. Abdel-Fattah, H. Xu, A. K. Burrell, T. E. Larson, T. M. McCleskey, Q. Wei, M. T. Janicke, D. D. Hickmott, T. T. Timofeeva and Y. Zhao, *Cryst. Growth Des*., 2010, Vol. **10**(3), 1301 – 1306.

19. S. S. Kaye, A Dailly, O. M. Yaghi and J. R. Long, *J. Am. Chem. Soc.* 2007, **129**, 14176–1417.

20. W. Mu, D. H. Liu, and C. L. Zhong, *Microporous Mesoporous Mater.,* 2011, **143**, 66–72.

21. L. Song, C. Xue, H. Xia, S. Qiu, L. Sun and H. Chen, *Materials,* 2019, **12**, 844.

22. O.V. Dolomanov, L. J. Bourhis, R. J. Gildea, J. A. K. Howard and H. Puschmann, *J. Appl. Cryst.,* 2009, **42**, 339-341.

23. G. M. Sheldrick, *Acta Cryst. A,* 2015, **71**, 3-8.

24. G. M. Sheldrick, *Acta Cryst. C,* 2015, **71**, 3-8.

25. B. M. Omkaramurthy, G. Krishnamurthy and N. Prasad, *Mater. Today Proc*., 2020, **22**, 2179–2190.

26. S. Ullaha, M. A. Bustamb , M. A. Assiria , A. G. Al-Sehemia, M. Sagir , F. A. Abdul Kareem, A. E. I. Elkhalifahe, A. Mukhtarb and G. Gonfa, *Microporous and Mesoporous Mater.,* 2019, **288**, 109569.

27. S. Ullah, M. Bustam, A. Shariff, A.E. Elkhalifah, G. Murshid and N. Riaz, *AIP Conf. Proc.,* 2014, pp. 34–39.

28. D. Saha and S. Deng, *Int. J. Hydrogen Energy, 2000,* **34**, 2670–2678.

29. N. H. Batubara and A. Zulys*, IOP Conf. Series*: *Mater. Sci. Eng.,* 2019, **546**, 042005.

30. W. Shang, X. Kang, H. Ning, J. Zhang, X. Zhang, Z. Wu, G. Mo, X. Xing and B. Han, *Langmuir*, 2013, **29**, 13168−13174.

31. J. K. Magtaan, M. Devocelle and F. Kelleher, *J Pept Sci*. 2019, **25**, 3139.

32. A. A. Sapianik, M. A. Kiskin, K. A. Kovalenko, D. G. Samsonenko, D. N. Dybtsev, N. Audebrand, Y. Sun and V. P. Fedin, *Dalton Trans*., 2019, **48**, 3676.

33. A. A. Sapianik, E. N. Zorina-Tikhonova, M. A. Kiskin, D. G. Samsonenko, K. A. Kovalenko, A. A. Sidorov, I. L. Eremenko, D. N. Dybtsev, A. J. Blake, S. P. Argent, M. Schroder and V. P. Fedin, *Inorg. Chem*., 2017, **56**, 1599– 1608.

34. S. Kayal and A. Chakraborty, *J. Indian Chem. Soc*., 2022, **99,** 100493.

35. D. E. Newbury, *Scanning*, 2009, **31**, (3), 91-101.

36. K. Vellingiri, D. C.W. Tsang, K. Kim, A. Deep, T. Dutta and D. W. Boukhvalov, *J. Clean. Prod*., 2018, **199**, 995-1006.

Chapter 4: Gas Adsorption and Separation Studies of Novel Bimetallic Metal-Organic Frameworks Synthesized from Zinc and Alkali Metals (Potassium and Lithium)

4.1 Introduction

The need for continuous development of efficient porous materials for gas storage applications cannot be overemphasised due to their potential industrial usage. In recent times, bimetallic MOFs have displayed a promising potential for gas adsorption due to the possession of modifiable pore sizes, open metal sites and large surface areas. Moreover, the adsorption strength of a specific adsorbate in bimetallic MOFs can be optimized by tuning the composition of these MOFs. Many bimetallic MOFs have been designed as excellent gas sorbents. Gas storage, too, has become economically important to industry. Recent applications of porous materials include the capture of gases carbon dioxide (CO_2), methane (CH_4) and hydrogen (H_2) for storage or energy use. Nanoporous materials such as ordered carbons and metal-organic frameworks (MOFs), bimetallic MOFs, and covalent organic frameworks (COFs) are being studied for the storage of gases such as nitrogen (N_2), carbon dioxide (CO_2), CH_4, O_2 and H_2 because of their large pore volumes and high surface areas.

The structure of bimetallic MOFs has been examined to correlate favourable structural features to gas storage performance. Structural characterization includes X-ray diffraction (XRD), FTIR and scanning electron microscopy (SEM) methods. Gas sorption experiments help us to evaluate the entire micropore and mesopore range in the bulk material.[1-5]

Gas adsorption is a tool for characterising the texture of porous solids and fine powders. In 1985, an IUPAC manual was issued on “Reporting Physisorption Data for Gas/Solid Systems”, specifically determining surface area and porosity. The conclusions and recommendations in the 1985 document have since been updated with recommendations regarding physical adsorption characterization, including the classification of isotherm.[1] Figure. 2.2 (chapter 2) shows the IUPAC isotherm groupings to enable us to interpret adsorption isotherms for structural characterisation. Six different categories identified are summarily described in the following paragraphs.

Like microporous materials, most nanoporous materials lead to Type I isotherms; Type II isotherms typically come from nonporous or macroporous adsorbents; Type III and V isotherms signify cases whereby no identifiable multilayer formation exists, denoting that there are relatively weak adsorbent-adsorbate interactions. Mesoporous materials yield Type IV and Type VI isotherms that indicate layer-by-layer adsorption onto a smooth, nonporous surface.[1]

Precise evaluation of the pore size distribution within the material can be achieved through the choice of an adequate adsorptive analyte and pore size calculations based on statistical mechanics [(molecular simulation or density functional theory (DFT)]. Analyzing the isotherm hysteresis curves broadens our knowledge about the pore shape and connectivity in the porous network and can explain storage and transport properties.[6]

Selecting suitable adsorptives is critical for studying porous materials' surface area and pore structure. Previously, nitrogen (N_2) adsorption at 77 K was accepted as the standard analyte for micropore and mesopore size analysis. However, recent studies have proved that nitrogen is not always appropriate for this application. Whilst nitrogen at 77 K has been used successfully for accurate analysis of nonpolar materials (for instance, non-functionalized carbons), interactions between the quadrupole moment of the nitrogen molecule and many surface functional groups and exposed ions that exist in Zeolite or MOF materials can result in inaccurate analysis. This affects both the orientation of the adsorbed nitrogen molecules and the micropore-filling pressure. Such specific interactions shift the pore-filling pressure of nitrogen to very low relative pressures (a P/P_0 equal to about 10^{-7} bar); consequently, the pore-filling pressure is not correlated with micropore size.[1,2]

The International Union of Pure and Applied Chemistry, IUPAC, recommended Argon (Ar) for micropore characterization in adsorption studies.[1] This is because, in contrast to the issues with nitrogen adsorption mentioned above, argon at 87 K (the boiling temperature of argon) does not display any specific interactions with surface functionality or uncertainty in orientation.[1] Besides using liquid argon, various commercially available cryostats and cryo-coolers make it possible to control the experimental temperature at 87 K with high precision.

The tuning of MOFs by the mixed-metal (MM) approach is expected to enhance adsorption properties towards designing adsorbents for selective gas storage, separation and release. This section selected examples of MM-MOFs for gas adsorption and separation. Some of the gas adsorption experiments discussed here were carried out at the University of Nottingham by Prof. Mokaya's group, and other studies were carried out at the University of Cambridge by Dr. Madden as part of a collaboration. Gas adsorption tests were performed on Zinc-Potassium and Zinc-Lithium MOF samples using O_2, N_2, CH_4, H_2 and CO_2. Adsorption tests were conducted at three chosen temperatures (77 K, 273 K and 298 K). The MM-MOFs were subjected to the activation process before the analysis at a temperature of 150 °C for 10 h under vacuum to eradicate the moisture content.

4.2 Hydrogen Adsorption Studies

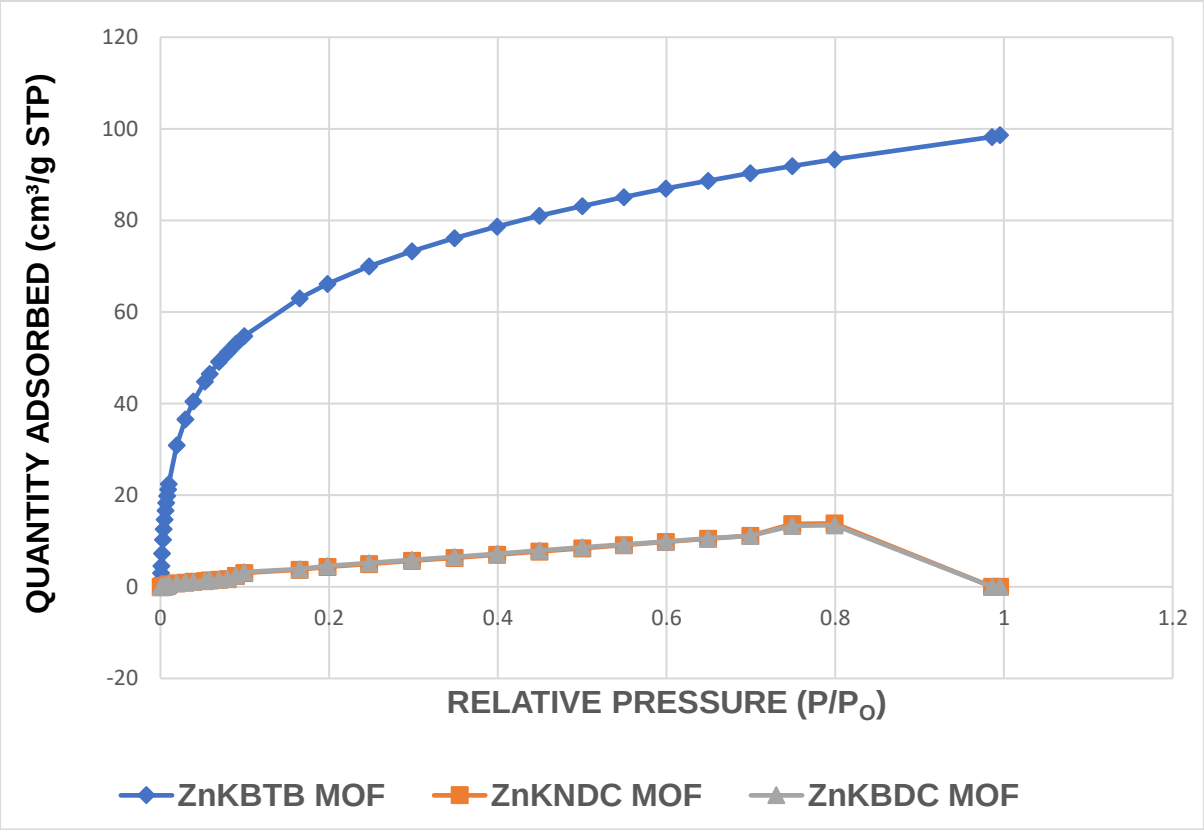


Figure 4.1: Hydrogen Adsorption-Desorption Isotherms at 77 K of ZnKBTB, ZnKBDC and ZnKNDC MOF.

In this study, inorganic metal cations (zinc (II) ions) and organic linkers (BTB, H_2BDC and NDC) have been utilized to tune the structure, pore size, and surface area of MOFs for hydrogen adsorption. Of the three MOF compounds studied for H_2

adsorption capacities at 77 K, ZnKBTB exhibited the highest loading of H_2 at low pressure, as shown in Figure 4.1. ZnKBTB exhibited a reversible Type I Isotherm depicting microporosity (having cavities less than 2 nm in size) to hydrogen adsorption. No hysteresis was observed upon desorption of gas from the pores, indicating the stability of the pores. The BET surface areas obtained were 179 m^2/g (ZnKNDC), 15 m^2/g and 16 m^2/g (ZnKBDC); thus, the H_2 uptake on both prepared ZnKBDC and ZnKNDC adsorbents was an order of magnitude lower than for ZnKBTB under the same temperature and pressure. ZnKBDC and ZnKNDC displayed a Type III isotherm, showing a linear relationship between quantity adsorbed and relative pressure, although only a very low H_2 uptake capacity was shown.

The key factors determining hydrogen adsorption and desorption are the surface area of the adsorbents and the interaction between hydrogen and the adsorbents. According to Zhang and Hu,[15] at a temperature of 77 K and high H_2 pressure, hydrogen uptake by most MOFs largely depends on their total surface areas, a conclusion also reported by Yaghi et al. for Zinc-carboxylate MOFs (Figure 4.2).[16] These MOFs include MOF-5 ($Zn_4O(BDC)_3$) and IRMOF-8, ($Zn_4O(NDC)_3$) and MOF-177 ($Zn_4O(BTB)_2$ and do not contain any alkali metals (e.g. K, Li, Na)). Of all these MOFs, MOF-177 possesses the highest apparent BET surface area of 4746 m^2g^{-1} and the highest hydrogen uptake of 7.5 wt % at 77 K and 70 bar. Our results agree with these reports, where surface area and Hydrogen uptake in the materials follow the ZnKBTB > ZnKNDC ≈ ZnKBDC trend. The inclusion of alkali metal potassium in the framework could not increase the BET surface area as well as hydrogen uptake significantly but the type of organic linker does have an effect.

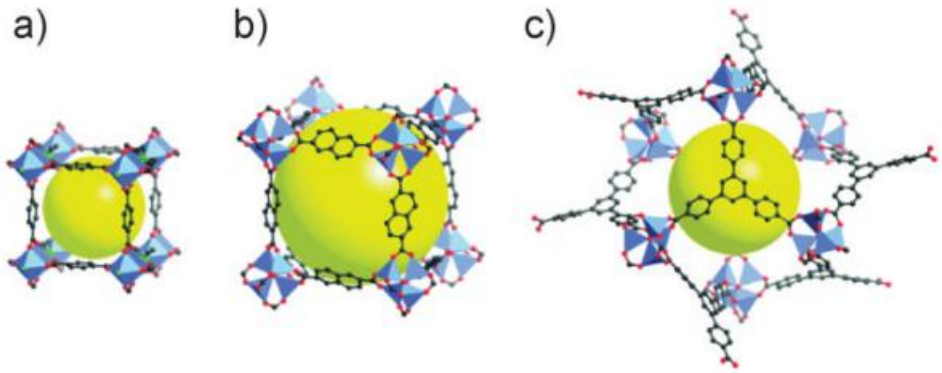


Figure 4.2: Zinc-carboxylate MOFs (a) MOF-5, $Zn_4O(BDC)_3$, (b) IRMOF-8, $Zn_4O(NDC)_3$, and (c) MOF-177, $Zn_4O(BTB)_2$.[16]

4.3 Oxygen Adsorption Studies

The results obtained from the oxygen adsorption isotherms do not align with the CO_2 adsorption results. Instead, the adsorption curve is categorized as type III isotherms. This demonstrates a weak interaction between MOF and the oxygen molecules. The most notable adsorption occurred at very high pressure, as shown in Figure 4.3. There was no identifiable monolayer formation; the adsorbent-adsorbate (MOF – O_2) interactions are now relatively weak, and the adsorbed O_2 molecules are clustered around the most favourable sites on the surface of a nonporous or microporous solid.

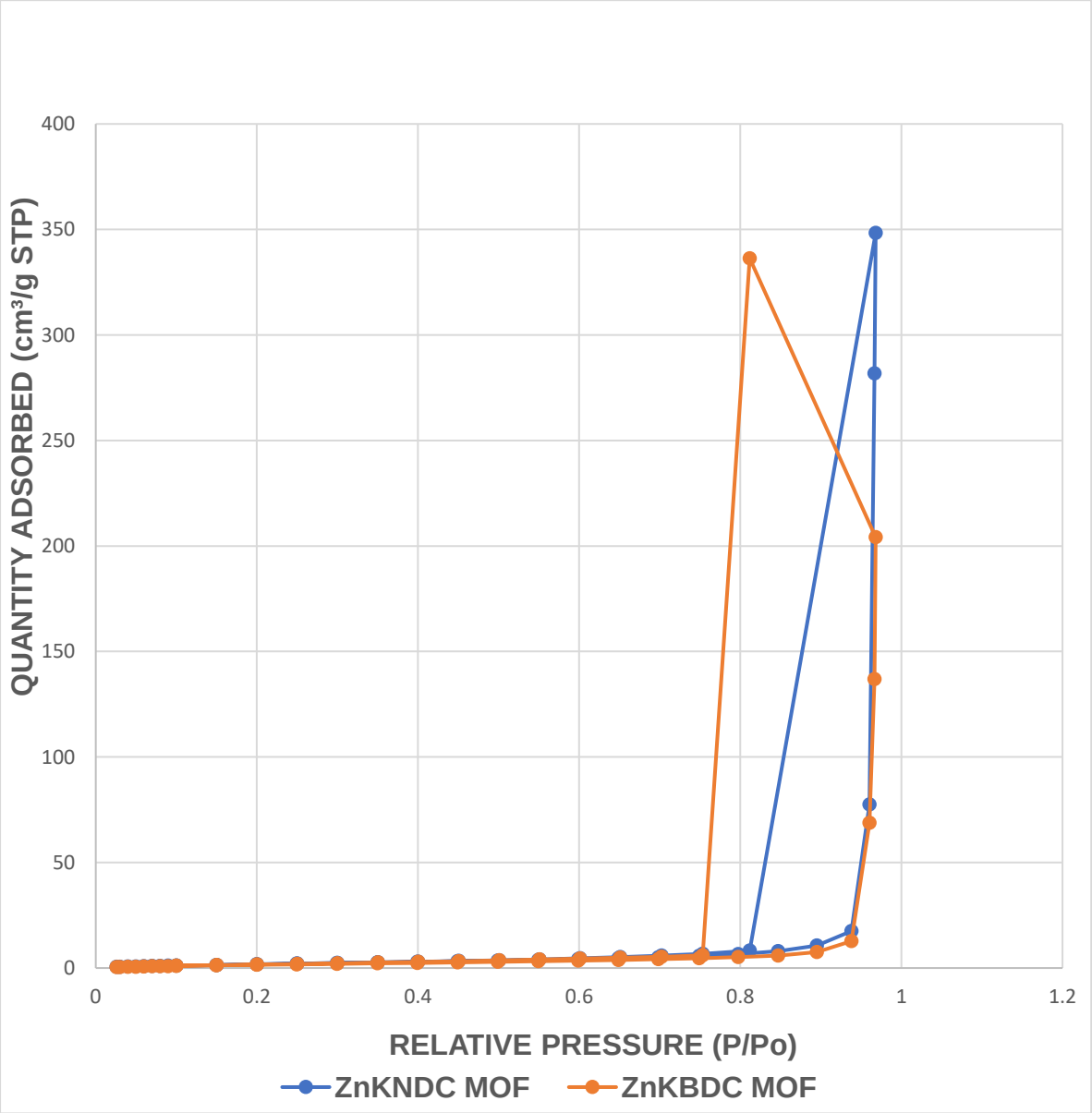


Figure 4.3: Oxygen Adsorption profiles at 77 K.

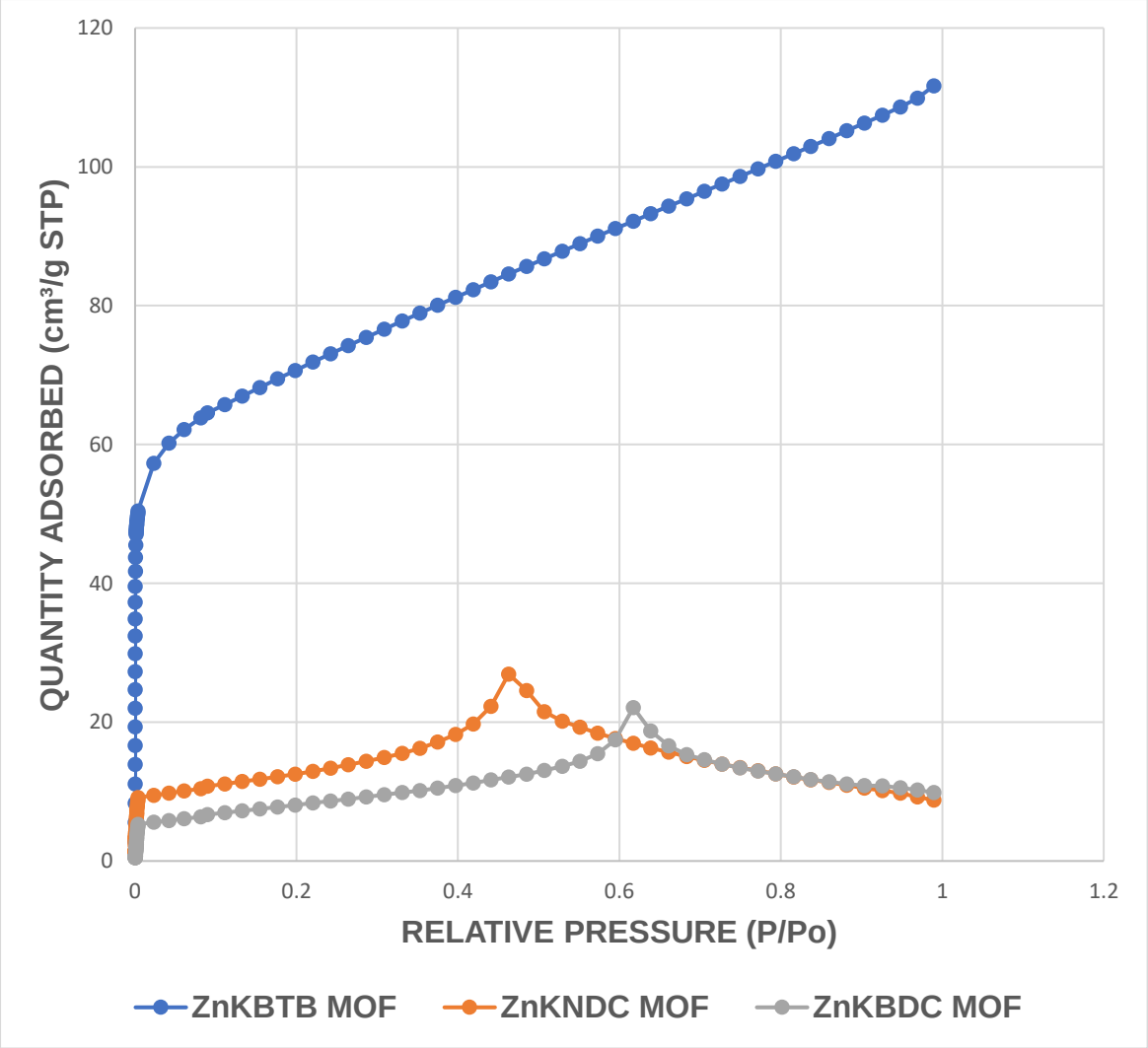


Figure 4.4: Nitrogen Adsorption Profiles at 77 K.

4.4 BET Surface Area Analysis

The porosities of these ZnKBTB, ZnKBDC and ZnKNDC MOF materials were measured by hydrogen, oxygen, and nitrogen adsorption at 77 K (Figures 4.1, 4.3 and 4.4, respectively). ZnKBTB exhibited permanent microporosity, as evidenced by reversible type I H_2 and N_2 adsorption isotherms at 77 K. The H_2, N_2 and O_2 uptake on both prepared ZnKBDC and ZnKNDC adsorbents was much lower than of ZnKBTB under the same temperature and pressure. The comparison of the BET surface area of the bimetallic MOFs against some selected MOFs like MOF-5 and MOF-177 are summarised in Tables 4.1, 4.2 and 4.3 based upon N_2 , H_2 and O_2 adsorption isotherm studies. The BET surface area and Langmuir surface area of the ZnKBTB, ZnKBDC and ZnKNDC were lower than those reported in some studies,[7–10,13-15,] suspected to be due to insufficient activation.[11] We deduced that lowered measured surface areas

may have resulted from blockage of pores, reducing access to some portions of the framework. Zhong et al.[12] supported this assertion: according to their report, the surface area of HKUST-1 moderately doped with alkali metals Li, Na and K increased initially, only decreasing with excessive Li, Na and K doping.[11] They concluded that the dramatic decrease in surface area at higher doping levels suggests

Table 4.1: Comparison of BET Surface Area Analysis Published ZnBDC MOF and ZnKBDC MOF (Nitrogen Physisorption)

S/No	MOF	Apparent Surface Area (BET), $m^2 g^{-1}$	References
1.	MOF-5	3800 to 3100	13, 14, 15.
2.	ZnKBTB	219	This Study
3.	ZnKBDC	68	This Study
4.	ZnKNDC	63	This Study
5	MOF 177	3100	13, 14, 15.

that the Li^+, Na^+ and K^+ ions may have blocked the pores and prevented access to some portions of HKUST-1, particularly when the doping ions are present with solvent molecules.[11] Likewise, we deduced that the combined effect of potassium ions lining the pores and an increased molecular weight may have contributed to decreased BET surface area.

Table 4.2: Comparison of BET Analysis published ZnBDC, ZnNDC, ZnBTB MOF and ZnKBDC, ZnKNDC and ZnKBTB MOF respectively (Based upon Hydrogen Adsorption Isotherm Studies)

S/No	MOF	Apparent Surface Area (BET), $m^2 g^{-1}$	Max H_2 Capacity, wt%	Pressure (bar)	Reference
1.	MOF-5, cubic $Zn_4O(BDC)_3$ framework.	2000	4.5 – 5.2 wt%	0.7	13, 14, 15.
2.	MOF-177	4746	7.5 wt% at 77 K and 70 bar	70	13, 14, 15.
3.	ZnKBDC	16	-	-	This Study
4.	$Zn_4O(NDC)_3$	1466	1.5	1	13. 14, 15
5.	ZnKNDC	15	-	-	This Study
6.	$Zn_4O(BTB)_2$	4526	1.25	1	13, 14, 15.
7.	ZnKBTB	179	-	-	This Study

Table 4.3: The BET Analysis of ZnNDC MOF and ZnKNDC MOF Based upon Oxygen Adsorption Isotherm Studies

S/No	MOF	Apparent surface area (BET), $m^2 g^{-1}$	Remarks
1.	ZnKBDC	6.6	This Study
2.	ZnKNDC	7.8	This Study

4.5 Carbon Dioxide adsorption properties of ZnKMOF and ZnLiMOF

Carbon dioxide (CO_2) emissions are one of the most serious environmental concerns facing the world today.[18] Most industrial processes and other human activities contribute to the environmental load of CO_2. Notable sources of emissions are mainly oil and natural gas, coal combustion, other energy generation activities and daily life affairs. It is expected that CO_2 emissions will continue to increase with economic growth and industrial development. Whilst scientists are focused on research and development towards achieving cleaner alternative energy, research efforts geared toward the capture and sequestration of CO_2 are also important to minimise the environmental impact of the existing CO_2 emissions.[18]

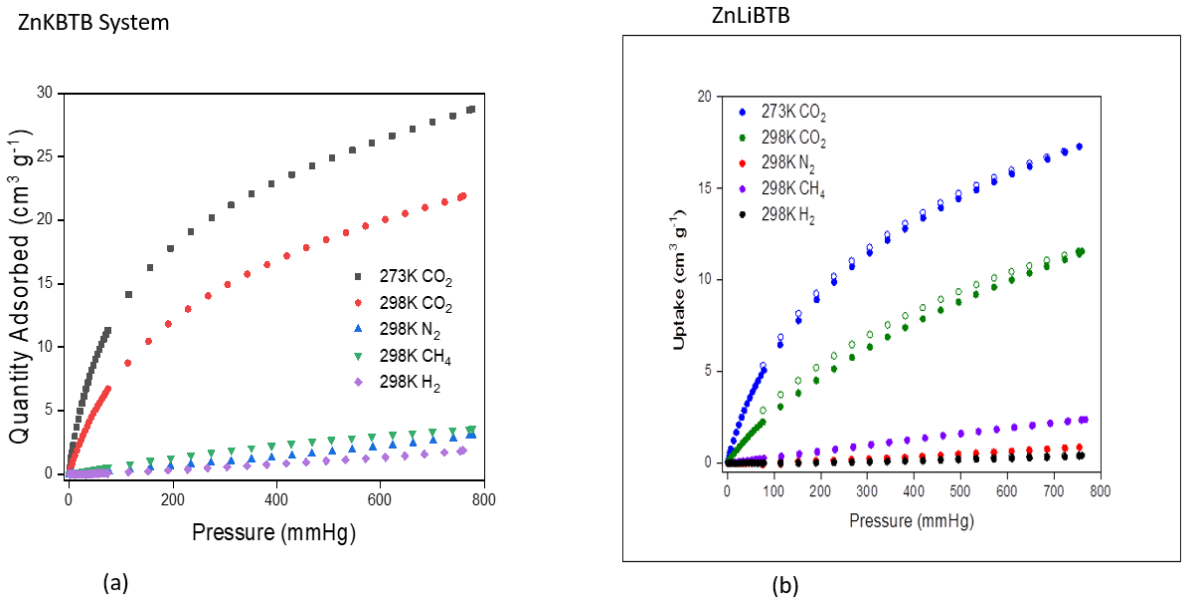


Figure 4.5: CO_2, N_2, CH_4 and H_2 Adsorption - desorption Isotherms for (a) ZnKBTB (b) ZnLiBTB at 273 K and 298 K.

Figures 4.5 and 4.6 show the CO_2 adsorption isotherms of ZnKBTB, ZnLiBTB, ZnKBDC, ZnLiBDC and ZnKNDC and ZnLiNDC at 298 K, 273 K and different pressures in the range of 0−800 mmHg. There is a high probability for selective CO_2 adsorption because of the occurrence of intermolecular interactions between the CO_2 molecules and the coordinated solvent(s), that is, the DMF (in ZnLiBDC and ZnLiBTB) or DMA (in ZnLiNDC) molecules identified on the surface of the channel. [18,35] Carbon dioxide CO_2 physisorption is a characterisation technique used to determine porosity, surface area and pore volume. For ZnKBTB and ZnLiBTB MOFs, the CO_2 isotherms at 273 K and 298 K are classified as type I and do not have diffusion limitations.[1]

As seen from Figure 4.5, the adsorption and desorption isotherms follow the same path, inferring that the adsorption process is reversible and the adsorbed molecules can be recovered during the desorption process when required.[1,2] CO_2 adsorption capacity rapidly increased with pressure at 298 K and 273 K. The ZnKBTB and ZnLiBTB compounds exhibited a high loading of CO_2 at low pressure, comparable to values attained by MOFs with open metal sites.

The adsorption capacity of ZnKBTB was higher than that of ZnLiBTB at the same temperature and pressure. However, the graph further shows that temperature affects CO_2 adsorption. The CO_2 adsorption capacities of the two samples were not too significantly different from each other, but CO_2 uptake at 298 K was lower than at 273 K. Consequently, lower temperature favours CO_2 adsorption. For all temperature ranges, the uptake capacities in ZnKBTB were higher than that of ZnLiBTB. Therefore, for BTB linker-based MOFs studied here, the uptake of CO_2 increases with pressure but is greater for ZnKBTB than ZnLiBTB. This trend was supported by the Song group,[12] who reported that the CO_2 uptake of 1K-HKUST-1 was 8.64 mmol/g, which is significantly higher than that of 2Li-HKUST-1 (7.89 mmol/g), 1Na-HKUST-1 (8.11 mmol/g) and HKUST-1 (7.72 mmol/g). The adsorption of CO_2 in ZnKBTB and ZnLiBTB MOF materials depends on the specific surface area, the size and charge of the balancing cations and the distribution of the cations located in the framework structures and the micropore volume of the adsorbent.

Another trend of CO_2 adsorption uptake was observed with uptake capacity of ZnLiNDC > ZnKNDC and ZnLiBDC > ZnKBDC even though all exhibited Type III Isotherms, which depicts non-porosity as shown in Figures 4.5 and 4.6.

The effect of the linker's conjugation system on the CO_2 uptake capacity followed the trend ZnKBTB > ZnKNDC > ZnKBDC. The same uptake capacity trend was repeated when the alkali metal was changed to lithium: ZnLiBTB > ZnLiNDC > ZnLiBDC, validating our point that CO_2 uptake capacity was primarily based on the type of organic linker and not necessarily the alkali metal.

4.6. N_2 Adsorption Studies

Experimental N_2 uptake experiments were performed at 77 K for ZnKBTB, ZnKBDC and ZnKNDC to determine the effect of the type of alkali metal on their surface areas and uptake capacity (Figures 4.5 and 4.6, and Table 4.1). The N_2 uptake capacity for ZnKBTB was 219m^2/g greater than ZnKBDC (68 m^2/g) and ZnKNDC (63 m^2/g) as shown in Table 4.1 above. The adsorption space and adsorption sites for N_2 is highest for ZnKBTB. The ordering of surface area matches the ordering of N_2 adsorption somewhat. As for CO_2, N_2 uptake at 298 K was lower than at 273 K. The Type III isotherm curves for ZnKBDC and ZnKNDC signified non-porosity as shown in the linear relationship between the quantity adsorbed and the relative pressure. The Zinc-Lithium system displayed the same sorption characteristics (Figures 4.5 and 4.6).

Therefore, in this series of MM-MOF studies, N_2, CH_4 and H_2 uptake capacity at 298K were very low compared to CO_2 adsorption at the same temperature, irrespective of the nature of the organic linker. The BTB linker-based MOFs performed the best, with CO_2 uptakes of ca. 25-30 cm^3/g. The BDC and NDC-based MM-MOF materials appear to be on the borderline between porosity and non-porosity. We also observed that lowering the BET surface area could also be traced to incomplete activation. The lower-than-expected surface areas appear to result from inaccessible pore space rather than structural collapse.

The CO_2 adsorption capacity in MOFs (e.g., in M-HKUST-1) depends on the size and charge of the balancing cations and the distribution of the cations located in the framework structures. Other factors included the specific surface area and the micropore volume of the adsorbent.[12] Generally, the capacity for CO_2 adsorption is higher than for N_2 because the quadruple moment of CO_2 is larger than that of N_2. Due to the similar N_2 capacities of the two samples, the addition of potassium ions within the framework improves selectivity for CO_2 over N_2 in HKUST-1.[12]

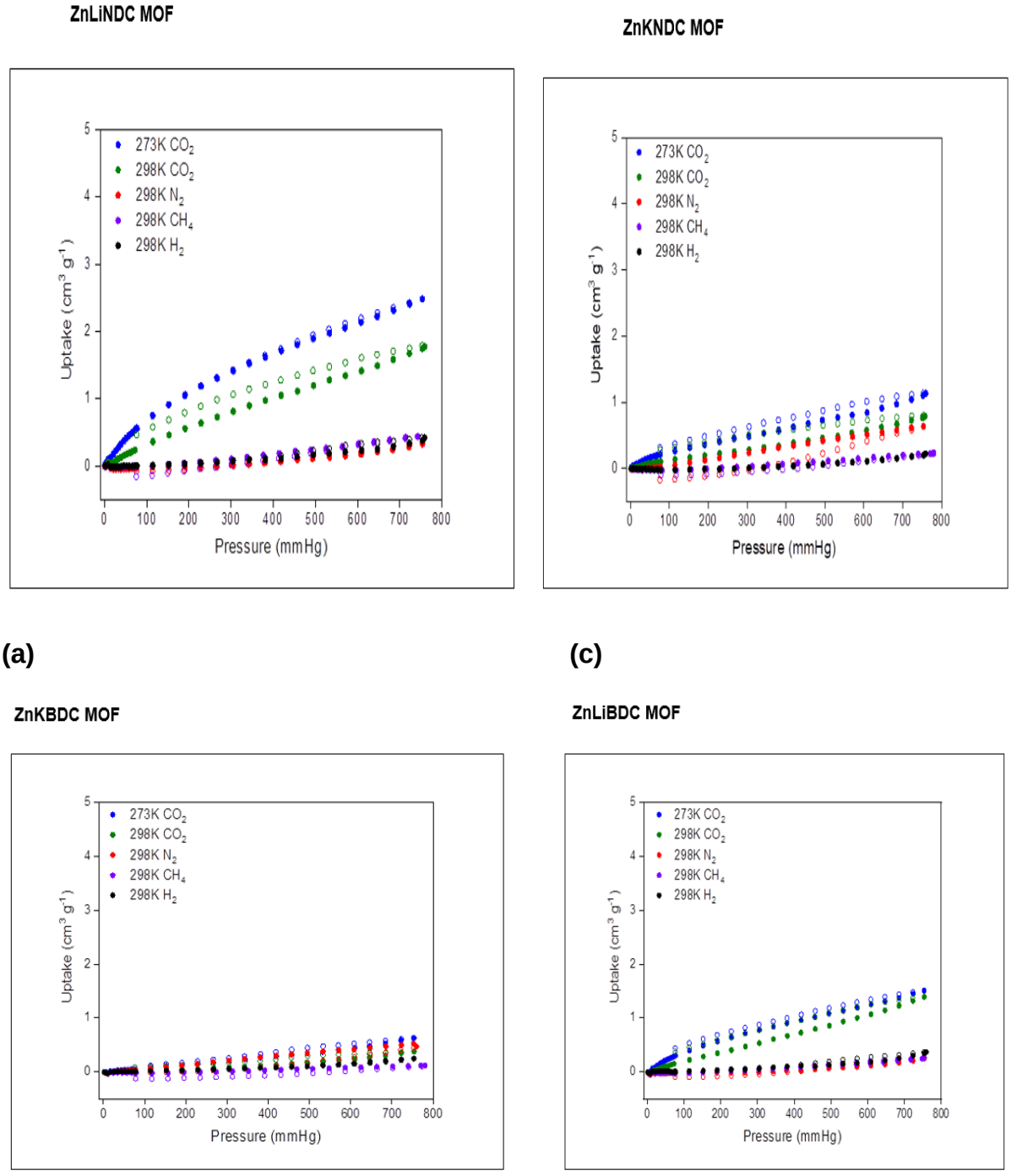


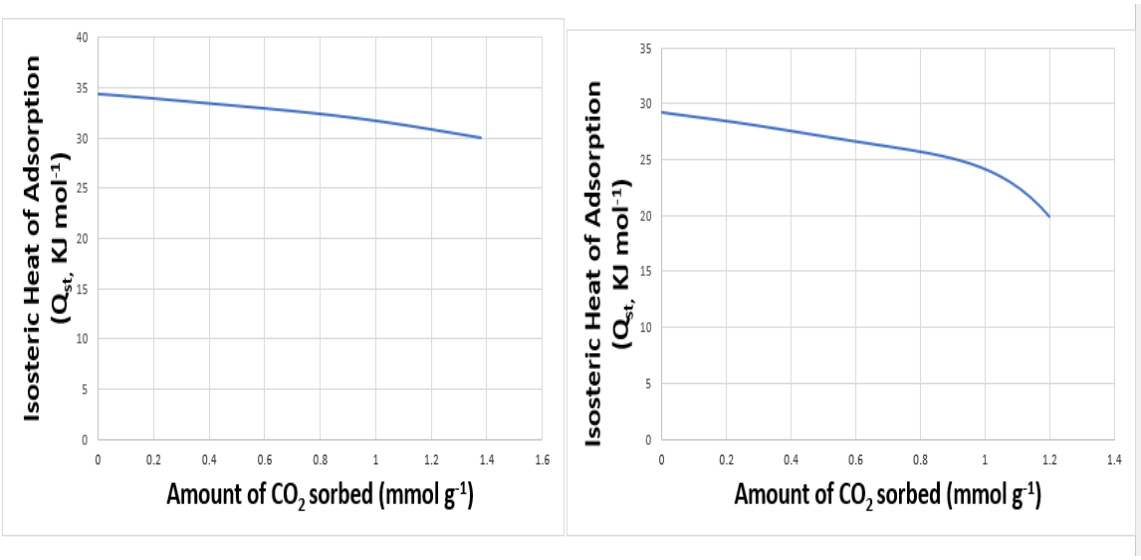
Figure 4.6: CO_2, N_2, CH_4 and H_2 adsorption isotherms for (a) ZnLiNDC, (b) ZnKNDC, (c) ZnLiBDC and (d) ZnKBDC at 273 K and 298 K.

4.7 The Isosteric Heat of Adsorption, Q_{st} ZnKBTB and ZnLiBTB

Isosteric heat (enthalpy) of adsorption (Q_{st}) is a crucial criterion for characterizing the interaction between the adsorbate molecules and the adsorbent surfaces. To further enhance our understanding of the CO_2 adsorption properties and interaction strengths

of ZnKBTB and ZnLiBTB MOFs, the Q_{st} for CO_2 was determined. The heat of CO_2 adsorption of ZnKBTB and ZnLiBTB materials was calculated using the Clausius-Clapeyron equation (Figure 4.7). Peak Q_{st} values were obtained at 34 kJ.mol^{-1} and 29 kJ.mol$^{-1,}$ respectively, which demonstrated a remarkable affinity to the CO_2 molecule at low pressures, falling within the ranges: ZnKBTB; 34.38 - 30.83 kJmol^{-1} and ZnLiBTB; 29.17 - 19.85 kJ.mol^{-1}, typical for physisorption as demonstrated in the literature.[19-21] Generally, physisorption involves weak van der Waals forces between the adsorbed molecules and the surfaces of the adsorbent, which is relatively easy to reverse with either the application of thermal energy (thermal swing) or lowering pressure (pressure swing).[20,21]

In both adsorbent–adsorbate pairs ZnKBTB-CO_2 and ZnLiBTB-CO_2, the isosteric heat reduces as CO_2 uptake increases. Therefore, the decrease in isosteric heat at higher uptake or loading indicates the variability in energetic heterogeneity and weaker bonding at multi-layer adsorption sites. This means all the available adsorption sites do not have the same adsorption energy for the probing CO_2 molecules. It is important to note that MOF-5 (without alkali metal ions in the framework) showed the same relationship trend between the Q_{st} and the CO_2 loading.[28-30] However, the study of the isosteric heat of adsorption of CO_2 for MOF-177, by Long et al.,[34] based on the single-site Langmuir fit, revealed that MOF-177 has a constant isosteric heat of adsorption of 14 kJ.mol^{-1}, indicative of the relatively weak CO_2-adsorbent interaction observed in the CO_2 isotherms and lack of strong adsorption sites in the framework.



(a) (b)

Figure 4.7: Heat of CO_2 adsorption for (a) ZnKBTB-MOF and (b) ZnLiBTB estimated using the Clausius-Clapeyron equation.

The Q_{st} value of the prepared adsorbents is calculated according to the CO_2 adsorption obtained at both 273 K and 298 K, as shown in Figure 4.7. The presence of open metal sites enhanced the CO_2 affinity of the MOFs, especially at low surface loading or CO_2 partial pressures. However, as the absorption continues to increase, the Q_{st} value decreases significantly until the Zn^{2+} and K^+ or Li^+ adsorption sites are completely occupied and the adsorption is stabilized. Applying Blom and co-worker's[22] explanation in similar Q_{st} versus gas loading of MOF-74(Ni) and MOF-5,[25,] we can explain the decrease in Q_{st} values. At the beginning of the adsorption process, the adsorption sites of Zn^{2+}, K^+ and Li^+ metal ions are unoccupied and energized to adsorb CO_2. As the CO_2 uptake increases, these sites are gradually occupied, leading to the decrease of adsorption strength.[22]

A comparison of Q_{st} values from different MOF characterization studies shows the potential of our MOFs for CO_2 capture. According to our results, the Q_{st} value of ZnKBTB (34.38 - 30.83 kJ.mol^{-1}) is higher than ZnLiBTB (29.17 - 19.85 kJ.mol^{-1}), slightly lower than the Q_{st} value recorded for MOF-74(Ni) (30.0 - 52.0 kJ.mol^{-1}) but higher than that of MOF-74(Ni) (20.0 - 41.0 kJ.mol^{-1}).[22] Higher Q_{st} values are attributed to synergistic interactions between the adsorbed CO_2 molecules and unsaturated metal ion sites of the micropore walls.[22] Quite interestingly, the Q_{st} values of ZnKBTB and ZnLiBTB are slightly higher than carbon materials (20-30 kJ.mol^{-1})[24] and also fall

within the same range as other leading MOFs (25-35 kJ.mol^{-1}).[25] The values are lower than those of most chemically active soluble adsorbents such as aqueous amines (usually greater than 70 kJ.mol-1) and amino-functionalized materials (up to 98 kJ.mol^{-1}). The Q_{st} of the chemisorption processes begins at around 50 kJ.mol^{-1}, indicating a stronger interaction strength between the substrate and adsorbent.

Mijowska and co-workers [28] report the same trend of the isosteric heat of adsorption for CO_2 on MOF-5. The direction of the Q_{st} curve indicates the negligible intermolecular interaction between CO_2 molecules. Mijowska et al.[28] asserted that the disappearance of favourable adsorption sites was responsible for the decrease in the isosteric heat of adsorption with increased surface coverage. The magnitude of the Q_{st} values of ZnKBTB and ZnLiBTB MOFs can be categorized as moderate CO_2 binding strength, with the potential to demand enhanced capture capacity as well as less energy required for sorbent regeneration.[22,27,28]

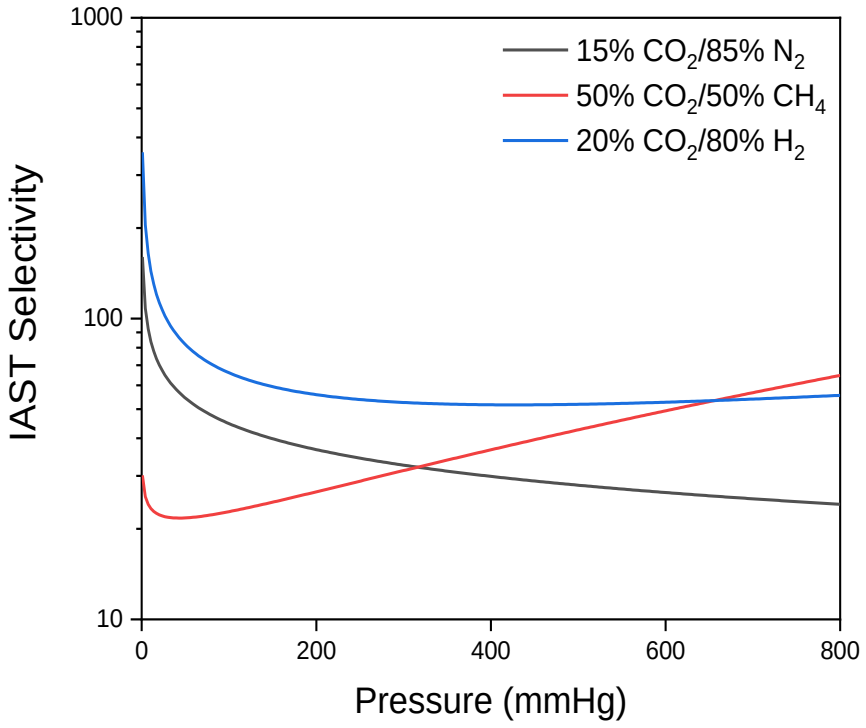
4.8 Ideal Adsorbed Solution Theory for ZnKBTB and ZnLiBTB MOFs

The adsorption selectivity (S_{ads}) is required to investigate the adsorption preference for one adsorbate over another. This selectivity was calculated from single-component gas adsorption data through the ideal adsorption solution theory (IAST) equation:

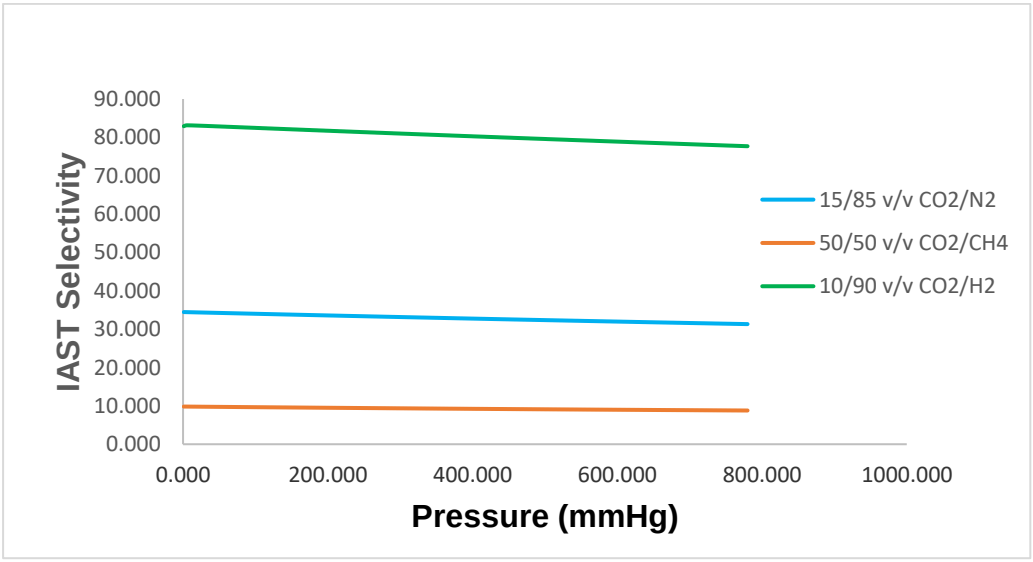
$$S_{ads} = \frac{q_1/q_2}{P_1/P_2}$$

Where q_1 and q_2 represent the number of moles of adsorbate and p_1 and p_2 represent the partial pressures of each species in a binary gas mixture.

IAST was used to evaluate the separation performance of MOF ZnKBTB. The single-component CO_2 capacities for ZnKBTB have been described in the previous section, but here they are contrasted with pure component CH_4 isotherms and data obtained for the binary mixtures of CO_2/H_2, CO_2/CH_4 and CO_2/N_2 at 298 K. As shown in Figure 4.8(a), the S_{ads} recorded for ZnKBTB was 64.72 (at 800 mmHg and 298 K) for CO_2 over CH_4 in a 50:50 mixture, decreasing to 30.12 as pressure decreases. The selectivity is higher than those of CO_2/H_2 (20:80), at 55.57 and CO_2/N_2 (15:85), at 24.13 (at 800 mmHg and 298 K).



(a)



(b)

Figure 4.8: Comparison of IAST selectivities for CO_2/H_2, CO_2/CH_4 and CO_2/N_2 mixtures on (a) ZnKBDC MOF and (b) ZnLiBDC MOFs.

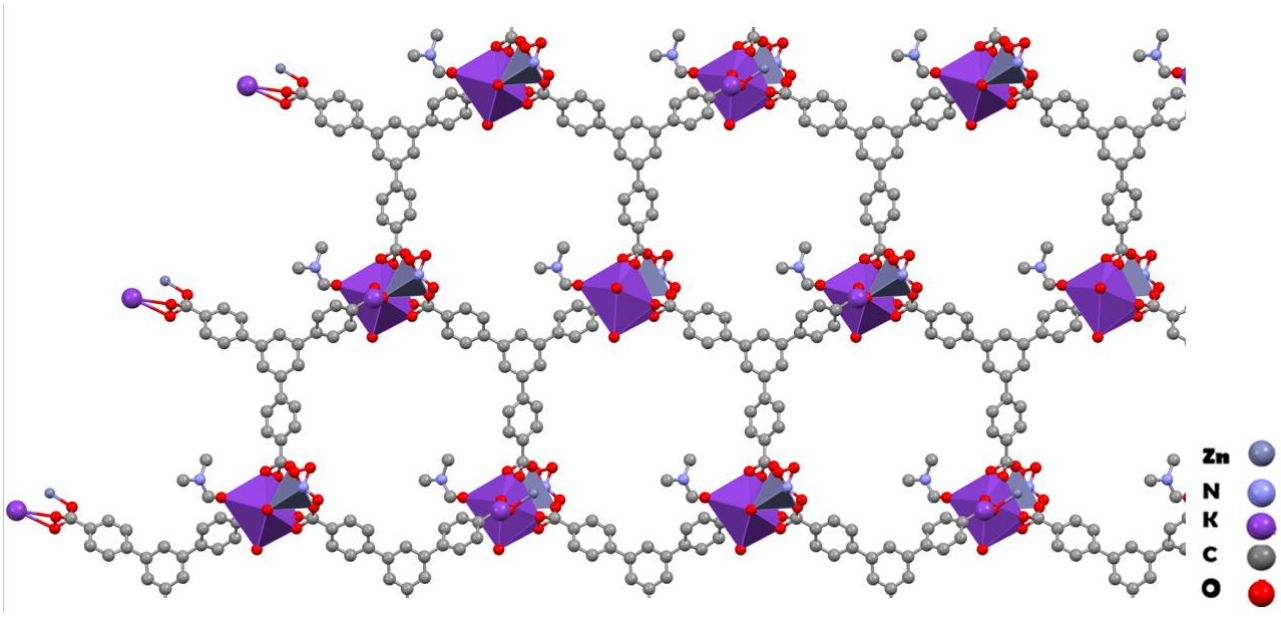
The CO_2/CH_4 selectivity increases sharply with pressure, contrary to the decreasing trend observed for CO_2/N_2 and CO_2/H_2 mixtures. The performance of an adsorbent is

highly dependent on the uptake capacity and separation selectivity. The high selectivity of CO_2 over CH_4 and the high CO_2 adsorption capacity of ZnKBTB suggest an application in gas separation.

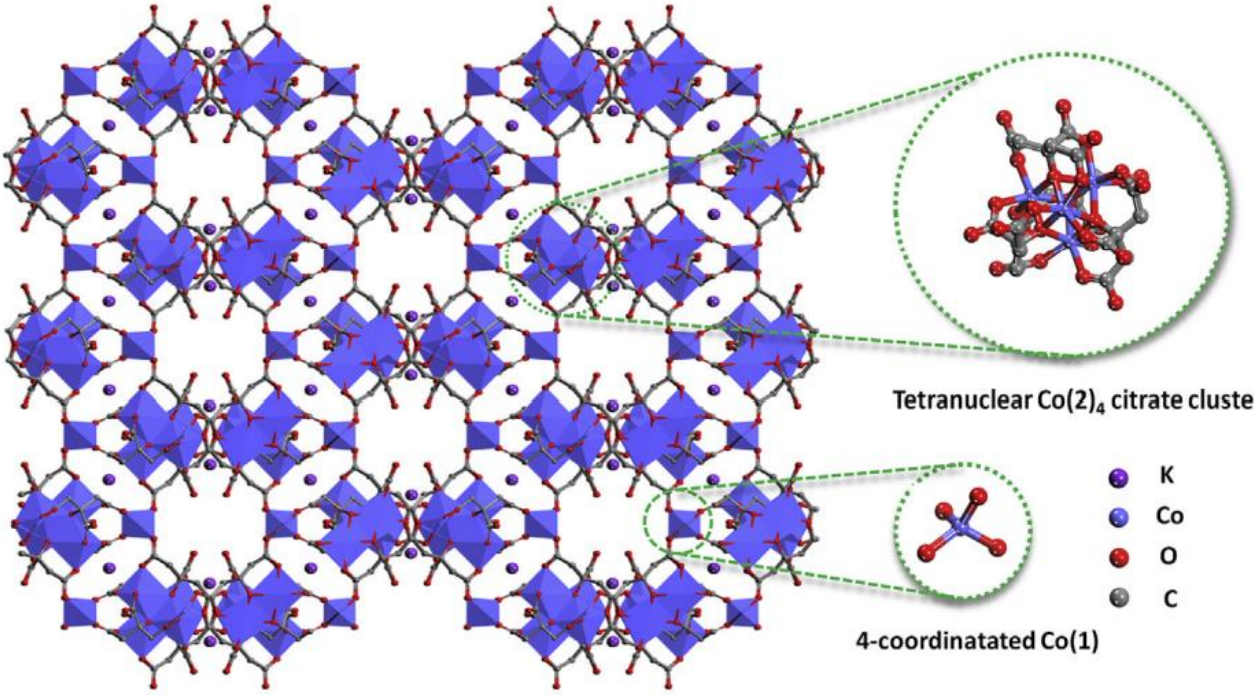
Table 4.6: The BET surface areas, heats of adsorption, textural properties and adsorbate selectivity from gas mixtures for various Mixed-Metal Metal Organic Frameworks[29,32,33]

S/No	Sample	BET (m^2 /g)	Q_{st} at lower pressure region (kJ/mol)	The ionic radius of group 1 element (nm)	CO_2/N_2 Selectivity	CO_2/CH_4 Selectivity	CO_2/H_2 Selectivity	References
1	Li- UTSA -16	519.4	21.57	0.076	---	--	-	32
2	ZnLiBTB	--	29.17	0.076	34.45 31.32	8.79	77.69	This study
3	Na-UTSA-16	544.1	24.19	0.102	--	--	-	32
4	K- UTSA -16	874.0	25.32	0.138	--	--	-	32
5	ZnKBTB	219.0	34.38	0.138	24.13	64.72	55.57	This study
6	Rb-UTSA-16	461.5	26.04	0.152	---	--	-	32
7	Cs-UTSA-16	291.3	31.67	0.167	---	--	--	32
8	Li-BEA	474.0	53.0	--	20.0	--	--	33
9	K-BEA	508.0	56.5	--	16.8	--	--	33
10	Na-BEA	446.0	59.6	--	14.7	--	--	33
11	Cs-BEA	411.0	89.6	--	24.0	--	--	33
12	MOF-5	--	--	-	17.48	15.53	--	29
13	MOF-177	--	--	--	17.73	4.43	--	29
14	Zeolite	--	--	-	240.56	256.47	--	29

4.9 Comparative Studies with other Mixed Metal Metal-Organic Frameworks



(a)



(b)

Figure 4.9: (a) Polyhedral structural representation of ZnKBTB (having pore volume ranging 21.3 – 148.2A) viewed along crystallographic 'b' axis, and (b) polyhedral structural representation of M-UTSA-16, formed from tetrahedral Co(I) atoms and tetranuclear Co(II) citrate clusters in octahedral geometry. Note that K^+ ions are located in the channels of the framework.[32]

Alkali metal cations have a high affinity and activation ability for CO_2. Zhang et al.[32] and Yang et al.[33] investigated the impact of the inclusion of alkali metal ions in M-UTSA-16 ($MCo_3(C_6H_4O_7)(C_6H_5O_7)(H_2O)_2$, where M = Li^+, Na^+, Rb^+, Cs^+) and M-BEA (Zeolite beta with high aluminium content (BEA, Si/Al = 7.4)) on N_2 and CO_2 adsorption and textural properties. The series of M-UTSA-16 synthesized by ion exchange were evaluated as ''catalyst for the transformation of CO_2 and epoxide to cyclic carbonate in the absence of co-catalyst''.[32] Li-UTSA-16 exhibited the highest efficiency of catalytic activity compared with other alkali metals.[32]

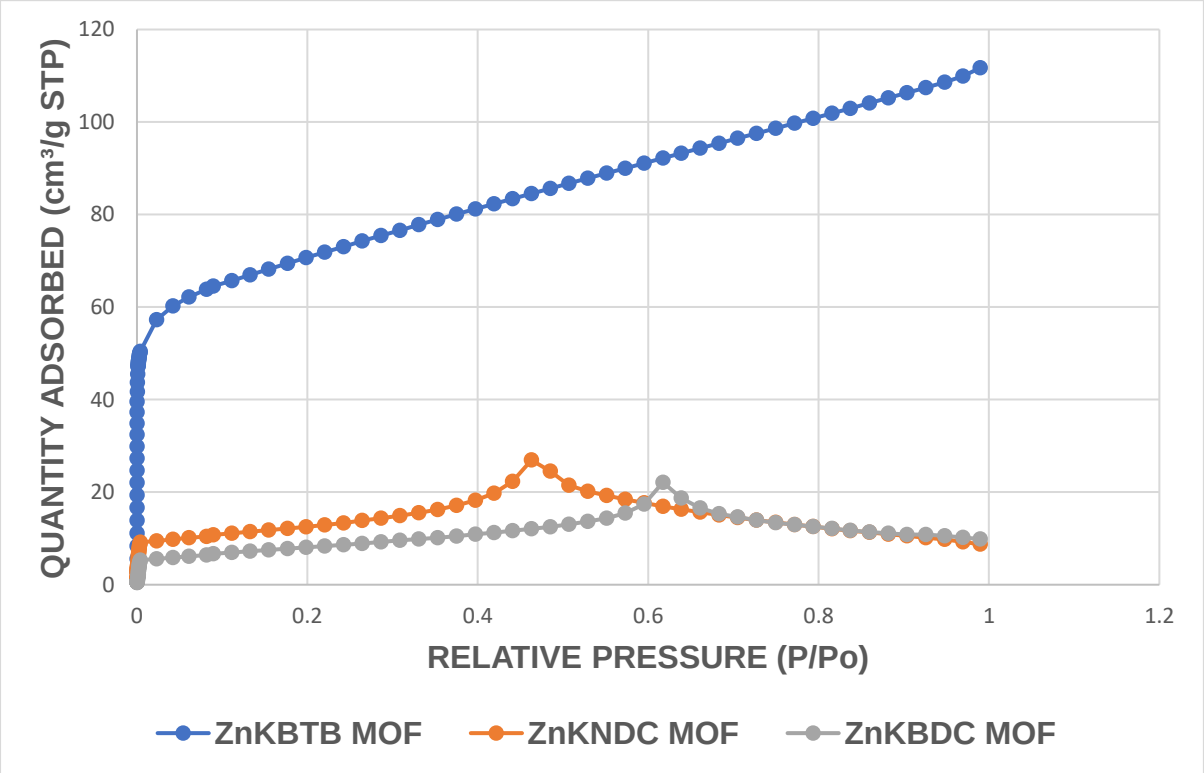


Figure 4.10: Nitrogen Adsorption Profiles of ZnKBTB MOF at 77 K showing similarities with K-UTSA-16[32]

Nitrogen adsorption analysis by Zhang et al.[32] and our studies have shown a similar pattern in the characterization of the porous structures of ZnKBTB and M-UTSA-16 (Figures 4.10 and 4.11, respectively). The adsorption isotherms of these materials exhibited typical type I curves at 77 K, 273 K and 298 K and displayed a significant amount of adsorption at low relative pressures, which indicates the existence of a substantial quantity of micropores, in agreement with our pattern of N_2 adsorption analysis for ZnKBTB.

The special surface area calculated by BET in the relative pressure (P/P_0) range of 0.05 - 0.3 (Table 4.6) shows K-UTSA-16 has a higher surface area than ZnKBTB, as well as a significant decrease in BET Surface area in the order of K-UTSA-16 > Na-UTSA-16 > Li-UTSA-16 > Rb-UTSA-16 > Cs-UTSA-16, an unexpected trend because it is not in direct agreement with the sequence of increasing ionic radius up the group (Cs>Rb>K>Na>Li).

Zhang et al.[32] also report the CO_2 gas adsorption performances of M-UTSA-16 at 273K and 298 K, respectively. We compare this result with our studies on ZnKBTB and ZnLiBTB as shown in Figure 4.5. The adsorption isotherms of the materials revealed that M-UTSA-16 had a high affinity and adsorption capacity for CO_2 (Figure 4.10b and c).[32] The equilibrium adsorption capacity for CO_2 decreases in the order of K^+>Na^+>Li^+>Rb^+>Cs^+, in agreement with our result, where the adsorption capacity for CO_2 is greater for K^+ than Li^+.

Yang et al.[33] prepared zeolite beta (M-BEA) with high aluminium content (Si/Al = 7.4) and tested for CO_2 adsorption after ion exchange with Li^+, K^+, Cs^+, Mg^{2+}, Ca^{2+} and Ba^{2+}. They further confirmed the superiority of K-BEA for CO_2 adsorption capacity. However, they asserted that the CO_2 adsorption capacity relied on the charge compensating cations,[33] and the adsorption capacity for CO_2 increased in the order of K^+> Na^+> Li^+> Ba^{2+}> Ca^{2+}; Cs^+ > Mg^{2+} The heat of adsorption fell in a range of 23 to 34 kJ.mol^{-1} at high loading conditions. Regarding selectivity studies, Yang and coworkers [33] also reported that group II cations showed higher selectivity than group I cations, with K-BEA giving the lowest selectivity for CO_2/N_2. This trend in CO_2/N_2 selectivity shows that for M-BEA, the higher the CO_2 adsorption capacity, the lower the CO_2/N_2 selectivity.[33] ZnLiBTB possesses higher CO_2/N_2 selectivity than ZnKBTB at 800 mmHg and 298 K and higher than the selectivity reported by Yang et al.[33] Thus, we can boldly establish that our results correspond to studies by Zhang et al.[32] and Yang et al.[33] for gas adsorption features and that our MOFs perform well for gas selection applications.

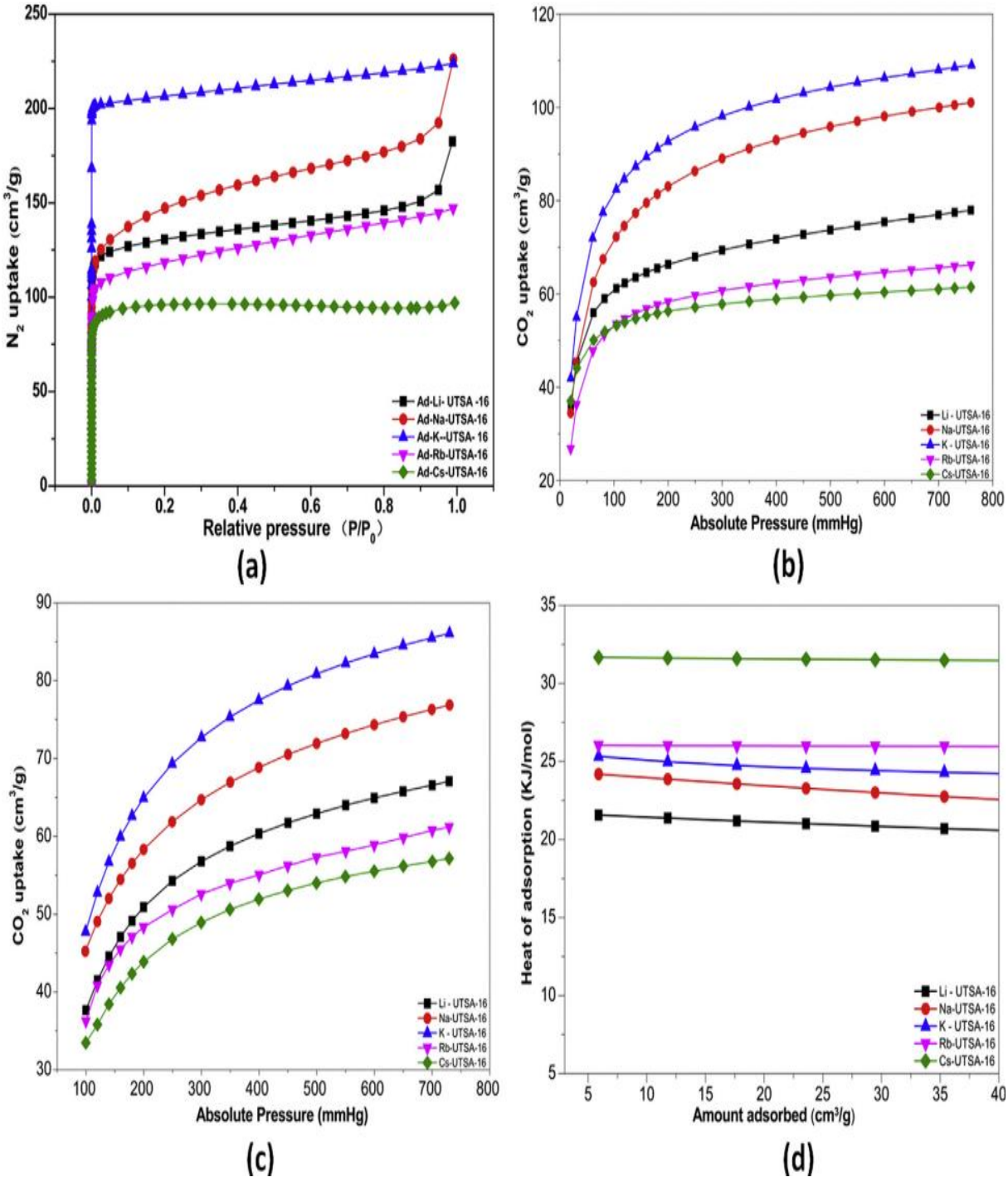


Figure 4.11: Adsorption isotherms of various cation-exchanged M-UTSA-16 MOFs (a) N_2 at 77 K, (b) CO_2 at 273 K, (c) CO_2 at 298 K, and (d) corresponding heats of adsorption for CO_2 at lower pressure.[32]

4.10 Conclusion

The synthesis of bimetallic framework materials formed between the transition metal zinc and group I alkali metals potassium and lithium was confirmed by several

analytical techniques such as XRD, TGA, SEM, and EDX. ZnKBTB MOF exhibits a straightforward type I isotherm for N_2 and H_2, indicating microporosity (width < 2 nm) with a BET surface area of around 200 $m^2 g^{-1}$ and pore volume of around 0.17 $cm^3 g^{-1}$. While ZnKBTB and ZnLiBTB displayed strong CO_2 adsorption capacities, depicted by a concave curve at all temperature and relative pressure ranges, ZnKBDC and ZnKNDC MOFs displayed linear plot associated with a type III isotherm, indicating non-porosity for the adsorption of H_2, N_2 and CH_4 gases at both 273 K and 298 K. Interestingly, both ZnKBDC and ZnKNDC MOFs showed minimal type I adsorption (described by lower concave curve) at 77 K. We then deduced that the adsorption in this experiment is dependent mostly on the ligand employed and not on the amount of the alkali metal in the MOF. The CO2/N2 selectivity trend study shows that the higher the CO2 adsorption capacity in ZnKBTB and ZnLiBTB MOFs, the lower the CO_2/N_2 selectivity. The adsorption capacity for CO_2 is higher for K^+ than for Li^+. The heat of CO_2 adsorption at high loading conditions indicates strong physisorption (ZnKBTB; 34.38 - 30.83 $kJ.mol^{-1}$ and ZnLiBTB; 29.17 - 19.85 $kJmol^{-1}$), comparable to values attained by other MOFs having open metal sites due to the presence of polar groups along the pore channels.

4.11 References

1. M. Thommes, K. Kaneko, A. V. Neimark, J. P. Olivier, F. Rodriguez-Reinoso and J. Rouquerol, *Pure Appl. Chem.*, 2015, **87**, 9–10:1051–69.

2. J. Cˇejka, H. Van-Bekkum, A. Corma and F. Schüth, *Amsterdam: Elsevier Ltd.,* 2007, 495–523.

3. M. Thommes and K. A. Cychosz, *Adsorption*., 2014, **20**, 233–50.

4. K. A. Cychosz, R. Guillet-Nicolas, J. Garcia-Martinez and M. Thommes, *Chem. Soc. Rev*., 2017, **46(2)**, 389–414.

5. M. Thommes, K. A. Cychosz and A. V. Neimark, *Amsterdam: Elsevier Ltd.,* 2012, 107 - 139.

6. K. A. Cychosz, P. Llewellyn, M. Thommes and S. Kaskel, *Adsorption methodology*. In: S. Kaskel, ed., New York: John Wiley & Sons; 2016, 575–605.

7. S. S. Y. Chui, S. M. F. Lo, J. P. H. Charmant, A. G. Orpen and I. D. Williams, *Science*, 1999, **283**, 1148.

8. C. Prestipino, L. Regli, J. G. Vitillo, F. Bonino, A. Damin, C. Lamberti, A. Zecchina, P. L. Solari, K. O. Kongshaug and S. Bordiga, *Chem. Mater.*, 2006, **18**,1337.

9. J. Moellmer, A. Moeller, F. Dreisbach, R. Glaeser and R. Staudt, *Microporous Mesoporous Mater*., 2011, **138,** 140.

10. A. R. Millward and O. M. Yaghi, *J. Am. Chem. Soc.*, 2005, **127**, 17998.

11. Y. X. Zhao, M. Seredych, Q. Zhong and T. J. Bandosz, *RSC Adv*., 2013, **3**, 9932.

12. Y. Cao, Y. Zhao, F. Song and Q. Zhong, *J. Energy Chem*., 2014, **23,** 468–474.

13. L. Zhang, Q. Wang and Y. C. Liu, *J. Phys. Chem.*, B 2007, **111**, 4291.

14. T. Sagara, J. Klassen and E. Ganz, *J. Chem. Phys.,* 2004, **121**, 12543.

15. Y. H. Hu and L. Zhang, *Adv. Mater.*, 2010, **22**, E117–E130.

16. A. G. Wong-Foy, A. J. Matzger and O. M. Yaghi, *J. Am. Chem. Soc.,* 2006, **128**, 3494.

17. J. L. C. Rowsell and O. M. Yaghi, *Angew. Chem. Int. Ed.,* 2005, **44**, 4670.

18. S. Xiang, Y. He, Z. Zhang, H. Wu, W. Zhou, R. Krishna and B. Chen, *Nat. Commun*., 2012, 3, 954.

19. N. Al-Janabi, P. Hill, L. Torrente-Murciano, A. Garforth, P. Gorgojo, F.R. Siperstein and X. Fan, *Chem. Eng. J.*, 2015, **281** 669–677.

20. G. E. Cmarik, M. Kim, S. M. Cohen and K. S. Walton, *Langmuir.,* 2012, **28**, 15606–15613.

21. J. H. Cavka, C. A. Grande, G. Mondino and R. Blom, *Ind. Eng. Chem. Res.,* 2014, **53,** 15500–15507.

22. L. Lei, Y. Cheng, C. Chen, M. Kosari, Z. Jiang and C. He, *J. Colloid Interface Sci.*, 2022, **612,** 132–145.

23. P. D. Dietzel, V. Besikiotis and R. Blom, *J. Mater. Chem.*, 2009, **19 (39),** 7362–7370.

24. C. Chen, X. Feng, Q. Zhu, R. Dong, R. Yang, Y. Cheng and C. He, *Inorg. Chem.*, 2019, **58 (4)**, 2717–2728.

25. H. J. Park and M. P. Suh *Chem. Sci.*, 2013, **4 (2)**, 685–690.

26. N. A. Dogan, E. Ozdemir and C. T. Yavuz, *ChemSusChem,* 2017, **10 (10),** 2130–2134.

27. H. A. Patel, J. Byun and C. T. Yavuz, *ChemSusChem.,* 2017, **10 (7)**, 1303–1317.

28. W. Kukulka, K. Cendrowski, B. Michalkiewicz and E. Mijowska, *RSC* Adv., 2019, **9**, 18527–18537.

29. D. Saha, Z. Bao, F. Jia and S. Deng, *J. Environ. Sci. Technol*., 2010, 44, **5**, 1820–1826.

30. Z. Li, P. Liu, C. Ou and X. Dong, *ACS Sustainable Chem. Eng.*, 2020, **8**, 15378−15404.

31. N. A. Dogan, E. Ozdemir and C. T. Yavuz, *ChemSusChem.,* **2017**, **10** (10), 2130–2134.

32. X. Zhang, Z. Chen, X. Yang, M. Li, C. Chen and N. Zhang, *Microporous and Mesoporous Mater.,* 2018, **258**, 55 – 61.

33. S. Yang, Jun Kima and W. Ahn, *Microporous and Mesoporous Mater.,* 2010, **135**, 90–94.

34. J. A. Mason, K. Sumida, Z. R. Herm, R. Krishna and J. R. Long, *Energy Environ. Sci.,* 2011, **4**, 3030.

Chapter 5: Adsorption Studies of Lanthanum/Alkali Metal-Organic Frameworks

5.0 Introduction

In 2014, Plessius et al.[1] reported a new lanthanide MOF comprised of lanthanum nodes and pyrazine-2,5-dicarboxylate linkers, which were highly hydrophilic in nature.[1]

It is believed that to search for new water-stable MOFs, lanthanide-based materials should attract more focus because lanthanum metal ions possess high coordination numbers, hence large coordination spheres and flexible coordination geometries, which can enable structural rearrangement without resulting in disorder of the entire MOF framework.[1,2] The presence of more accessible d-orbitals and f-orbitals in lanthanide-based MOFs allows more possibilities for coordination and binding with various ligands towards aiding the discovery of novel and rare network topologies.[3-5]

La^{3+} fabricated composite materials have also been shown to be good composite materials for toxic ion removal because of specific affinity and desired structural properties due to high coordination, with Zhang et al. reporting LaMOF composites for arsenate and phosphate removal, thus contributing huge potential to toxic waste management.[6] The Ligands possessing carboxylate functional groups such as 1,3,5-tris(4-carboxyphenyl)benzene (BTB), 2,6-naphtalenedicarboxylate acid (NDC), and Benzene 1,4- dicarboxylic acid (BDC) have proved to be excellent bridging ligands in constructing novel MOFs with attractive structural topologies and unique properties because of its various coordinating modes, high symmetry, and structural rigidity. The La cation has an affinity for the carboxylate oxygen atoms found in these ligands.

The BDC ligand exhibits a variety of binding modes from mono- to tetradentate as illustrated in Figure 1.6 of Chapter 1. For instance, in a report by Abdelbaky et al. reported the synthesis of lithium-lanthanide-containing MOFs,[7] $LiLn(BDC)_2(H_2O)\cdot 2(H_2O)]$ (where Ln = Dy, Ho, Er, Yb, $Y_{0.96}Eu_{0.04}$, and $Y_{0.93}Tb_{0.07}$ and $[LiTb(BDC)_2]$. In the series of MOFs synthesised, the carboxylate group gave interesting coordination modes: (a) bis-tridentate bridging, (b) pentadentate bridging, (c) tetradentate (bis-bidentate) chelate and bridging[7] as illustrated in Figure 5.1 below.

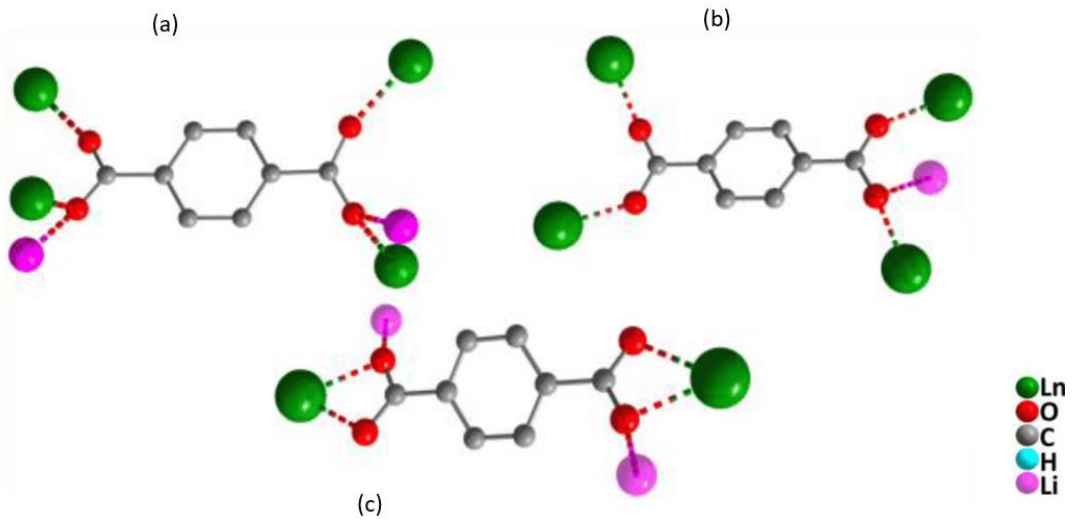


Figure 5.1: Coordination modes of BDC ligand in LnLiBDC [$LiLn(BDC)_2(H_2O)\cdot 2(H_2O)$] (Ln = Dy, Ho, Er, Yb, $Y_{0.96}Eu_{0.04}$, and $Y_{0.93}Tb_{0.07}$ and [$LiTb(BDC)_2$]. (a) bis-tridentate bridging (b) pentadentate bridging (c) tetradentate (bis-bidentate) chelate and bridging.[7]

In addition, in [Ni(DMF)(L)Ln(bdc)1.5] (Ln=La (1) and Nd (4)) reported by Zhang et al. La(III) atom was nine-coordinated, bearing a distorted tricapped trigonal prism. The BDC ligand coordinated in two different modes when two carboxylate $-COO^-$ groups acted as a bidentate ligand, and another served as a tetradentate ligand.[8]

In the present work, we report the synthesis of a new lanthanum-based bimetallic MOF system, LaK-MOF and LaLi-MOF, containing K(I) and Li(I), respectively. Three linkers were employed, 1,4-BDC, 1,3,5-tris(4-carboxyphenyl) benzene (BTB), and 2,6-naphthalenedicarboxylic acid (2,6-NDC), each showing variation in length and connectivity. The study examines hybrid mixed valent MOFs' physicochemical properties and potential applications. Potassium tert-butoxide and lithium tert-butoxide, were used as sources of potassium and lithium in this study. We further investigated the effects of monovalent alkali cations on CO_2, N_2, H_2, O_2 and CH_4 adsorption properties in LaK-MOF systems.

5.1 Experimental

5.1.1 Materials

Chemicals and solvents were purchased from Alfa Aesar, Fluorochem, Sigma-Aldrich, and VWR and used without further purification. Pirossigeno supplied single gases at a minimum purity of 99.9995%. Certified gas mixtures were supplied by Sapio at a

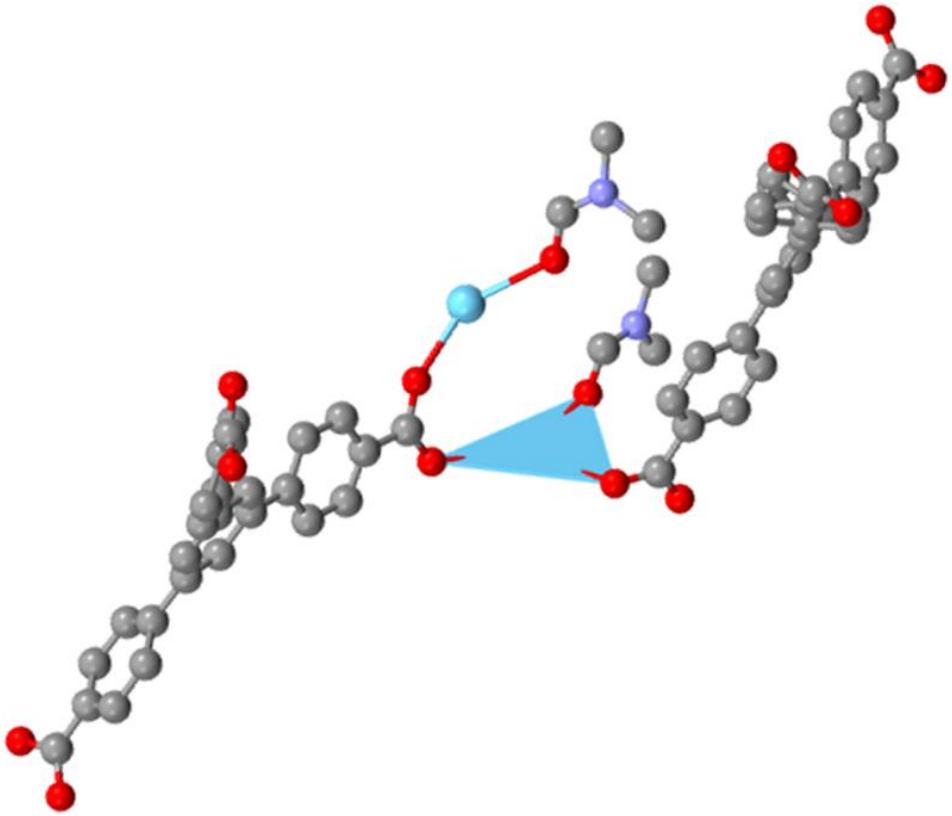
purity of ±0.01% from the certified concentration (CO_2/CH_4 mixture with 47.89 mol.% CH_4, and $N_2/CO_2/O_2$ mixture with 10.10 mol.% CO_2 and 10.02 mol.% O_2).

5.1.2 Attempt to Synthesis of LaKNDC MOF

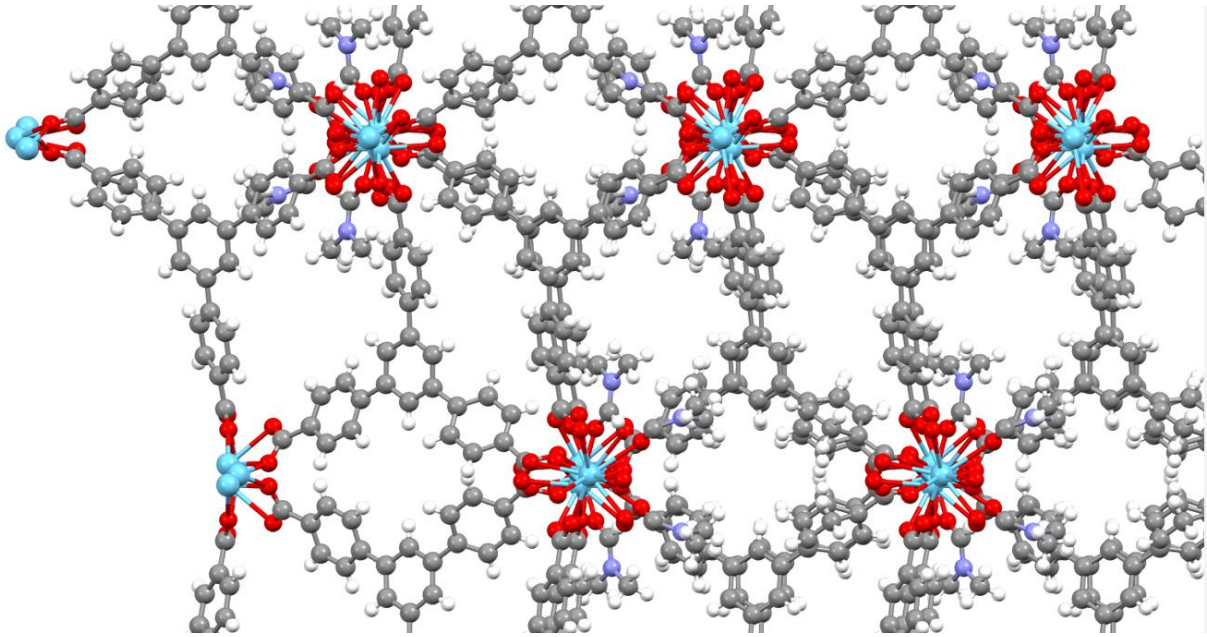
Lanthanum (III) nitrate hexahydrate (200 mg, 0.462 mmol), 2,6-naphthalenedicarboxylic acid, (75 mg, 0.35 mmol), potassium tert-butoxide (59 mg, 0.53 mmol) and DMF (6 mL) was sonicated for 30 mins. The reaction mixture was heated at 120 °C for 72 h in a 23 mL Teflon Stainless Steel lined autoclave vessel. Hexagonal-shaped colourless crystals and a white microcrystalline solid were obtained; the crystals were separated manually from the bulk product, suitable for single-crystal X-ray diffraction. The same reaction was repeated at 170 °C. The mixture was cooled at a rate of 0.2 °C min^{-1} to room temperature. Hexagonal-shaped crystals were formed and isolated by washing with DMF (4 x 2 ml) and dried overnight in air. However, these synthesised crystals could not be certified to have achieved the mixed metal/alkali metal MOF, LaKNDC MOF system intended. The structure could not be solved as the crystal was not well diffracting.

5.1.3 Attempt to Synthesis of LaKBTB MOF

Lanthanum (III) nitrate hexahydrate (200 mg, 0.462 mmol), 1,3,5-Tris(4-carboxyphenyl)benzene (154 mg, 0.35 mmol), potassium tert-butoxide (60 mg, 0.53 mmol) and DMF (6 mL) was sonicated for 30 mins. The reaction mixture was heated at 120 °C for 72 h in a 23 mL Teflon Stainless Steel lined autoclave vessel. Ellipsoidal-shaped colourless crystals and a white microcrystalline solid were obtained; the crystals were separated manually from the bulk product, suitable for single-crystal X-ray diffraction. The same reaction was repeated at 170 °C. The mixture was cooled at a rate of 0.2 °C min^{-1} to room temperature. Ellipsoidal-shaped crystals were formed and isolated by washing with DMF (4 x 2 ml) and dried overnight in air. However, these synthesised crystals could not achieve the mixed metal/alkali metal MOF, LaKBTB system intended only lanthanum coordination with BTB ligands identified by single crystal X-ray diffraction as described in the asymmetric and packed unit shown in Figure (5.2) and crystal data in Table (5.1). Also, no trace of potassium, K ion found using SEM/EDX techniques. Hence, further characterization was stopped.

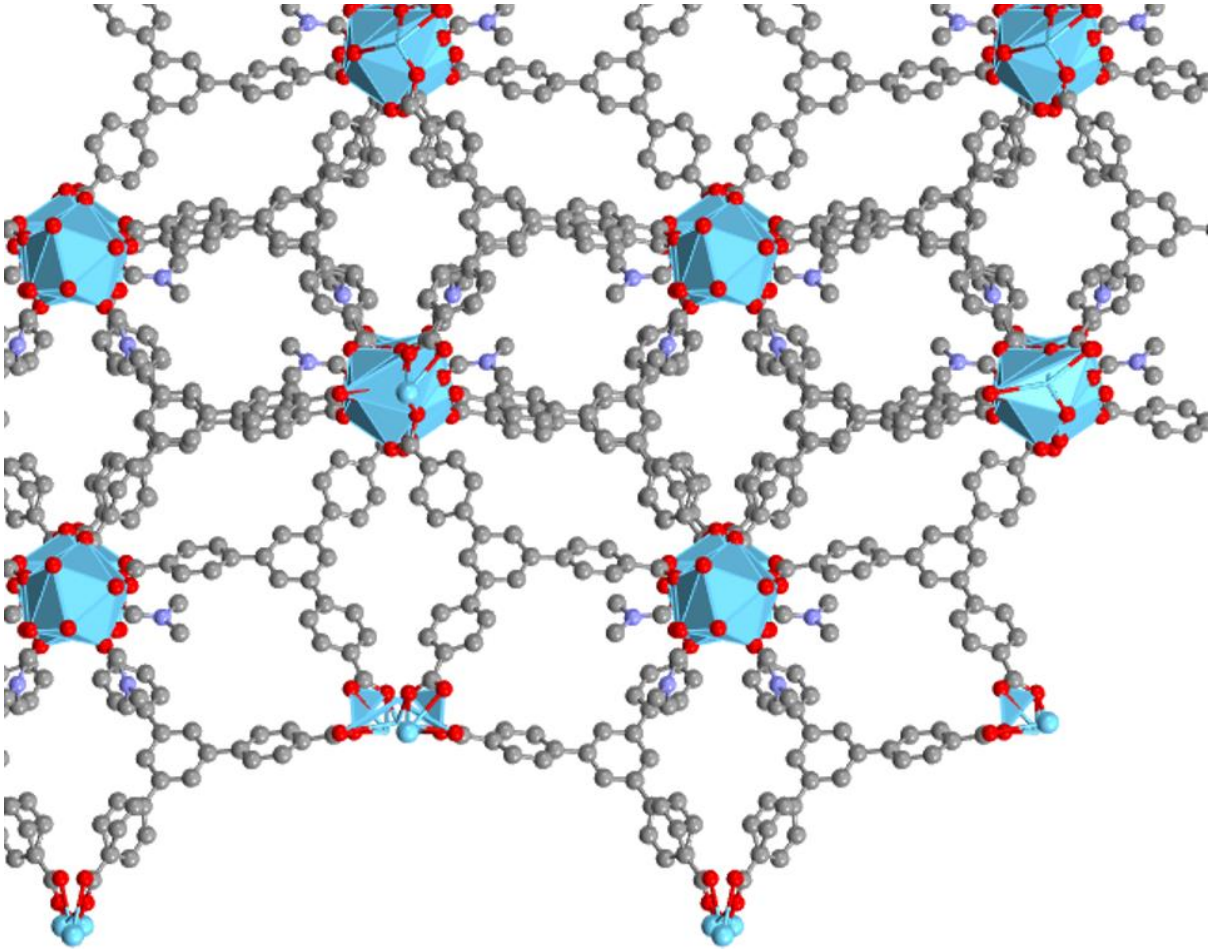


(a)



(b)

Figure: 5.2 Crystal structure (a) Asymmetric unit (b) Autocentre (c) Packed unit of LaBTB MOF viewed along crystallographic 'b' axis (grey = C, cyan = La, red = O, blue = N, H = light grey, hydrogen atoms have been removed in (a) and (b) for clarity).



(c)

Figure 5.2c: Crystal structure (a) Asymmetric unit (b) Autocentre (c) Packed unit of LaBTB MOF viewed along crystallographic ‘b’ axis (grey = C, cyan = La, red = O, blue = N, H = light grey, hydrogen atoms have been removed in (a) and (b) for clarity).

Table 5.1: Crystal data and structure refinement for synthesised LaBTB MOF.

Empirical formula	$C_{120}H_{86.58}La_4N_4O_{28}$
Formula weight	2588.15
Temperature/K	293(2)
Crystal system	Monoclinic
Space group	$P2_1/c$
a/Å	15.13450(10)
b/Å	28.7595(2)
c/Å	16.34780(10)
α/°	90
β/°	96.8920(10)
γ/°	90
Volume/Å^3	7064.14(8)
Z	2
ρ_{calc}g/cm^3	1.217
μ/mm^{-1}	1.155
F(000)	2573.0
Radiation	Cu Kα (λ = 0.6889)
2Θ range for data collection/°	2.628 to 66.08
Index ranges	$-13 \leq h \leq 14$, $-24 \leq k \leq 24$, $-25 \leq l \leq 24$
Reflections collected	20487
Independent reflections	8745 [R_{int} = 0.8819, R_{sigma} = 1.4303]
Data/restraints/parameters	8745/634/726
Goodness-of-fit on F^2	0.742
Final R indexes [I>=2σ (I)]	R_1 = 0.8639, wR_2 = 0.7994
Final R indexes [all data]	R_1 = 0.9722, wR_2 = 0.8669
Largest diff. peak/hole / e Å^{-3}	0.77/-2.56

5.1.4 Attempt to Synthesis of LaLiBDC MOF

Lanthanum (III) nitrate hexahydrate (200 mg, 0.462 mmol), benzene-1,4-dicarboxylic acid (59 mg, 0.36 mmol), lithium tert-butoxide (42 mg, 0.053 mmol) and DMF (6 mL) was sonicated for 30 mins. The reaction mixture was heated at 120 °C for 72 h in a 23 mL Teflon Stainless Steel lined autoclave vessel. Boat-hexagonal shaped colourless crystals and a white microcrystalline solid were obtained; the crystals were separated manually from the bulk product, suitable for single crystal X-ray diffraction. The same reaction was repeated at 170 °C. The mixture was cooled at a rate of 0.2 °C min^{-1} to room temperature. Boat-hexagonal-shaped colourless crystals were formed and isolated by washing with DMF (4 x 2 ml) and dried overnight in the air. These synthesised crystals could not achieve the mixed metal/alkali metal MOF, LaLiBDC

MOF system expected; only lanthanum coordination with BDC ligands identified by single crystal X-ray diffraction according to the polyhedral asymmetric and packed units shown in Figure (5.3) and crystal data in Table (5.2). Also, no trace of lithium Li ion was found using SEM/EDX techniques. Hence, further characterization was stopped.

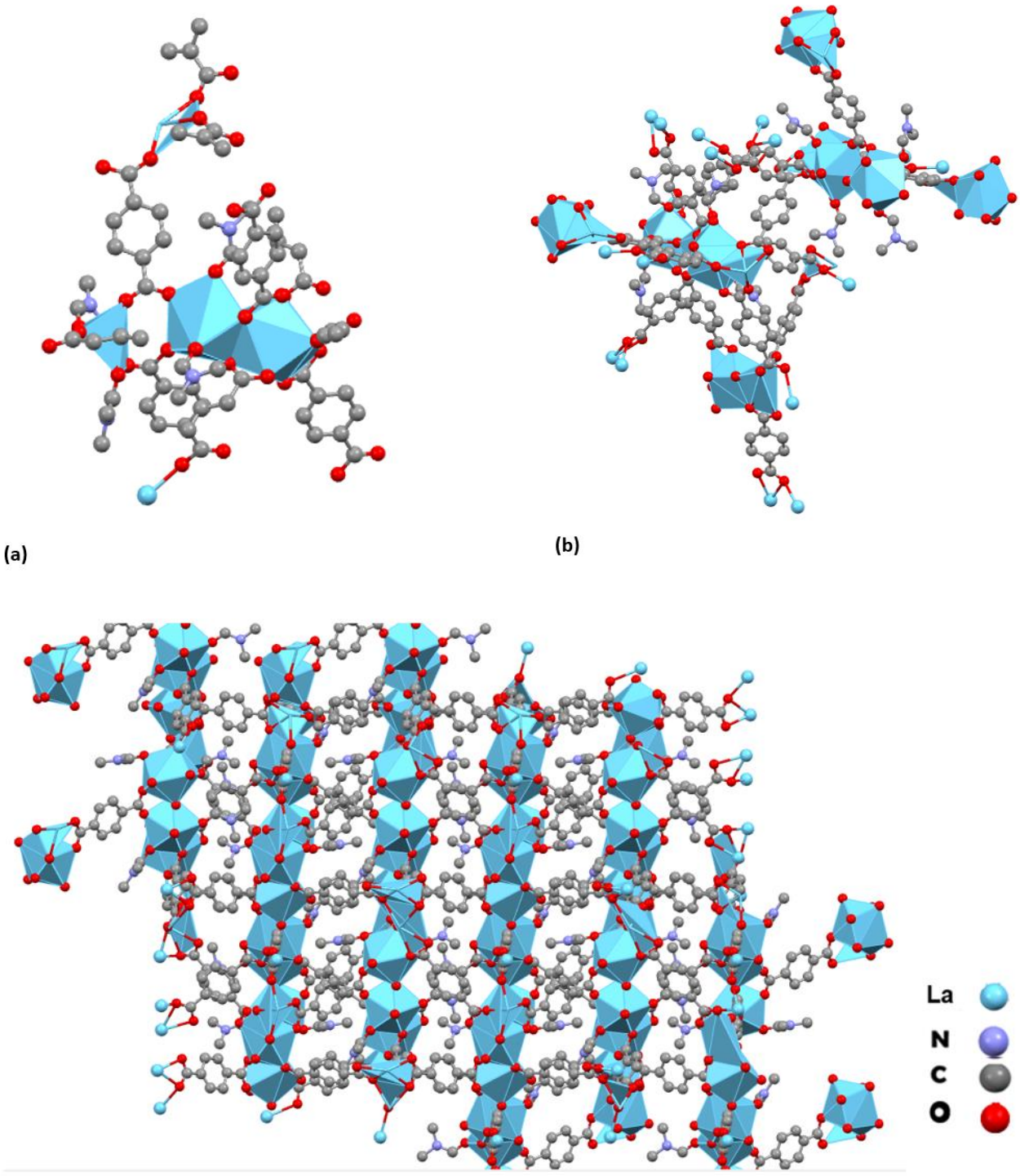


Figure 5.3: Polyhedral Crystal structure (a) Asymmetric unit (b) Autocentre (c) Packed

unit of LaBDC MOF viewed along crystallographic 'b' axis **(**grey = C, cyan = La, red = O, blue = N, H = light grey, hydrogen atoms have been removed for clarity**).**

Table 5.2: Crystal data and structure refinement for synthesised LaBDC MOF

Empirical formula	**$C_{72}H_7La_5N_4O_{34}$**
Formula weight	577.15
Temperature/K	293(2)
Crystal system	Triclinic
Space group	P-1
a/Å	14.0296(4)
b/Å	15.2897(4)
c/Å	17.8781(4)
α/°	90.116(2)
β/°	93.082(2)
γ/°	90.879(2)
Volume/Å^3	3828.99(17)
Z	2
ρ_{calc}g/cm^3	0.501
μ/mm^{-1}	2.013
F(000)	478.0
Radiation	Cu Kα (λ = 0.6889)
2Θ range for data collection/°	2.818 to 51.004
Index ranges	$-13 \leq h \leq 14$, $-19 \leq k \leq 19$, $-22 \leq l \leq 22$
Reflections collected	16947
Independent reflections	9752 [R_{int} = 0.8192, R_{sigma} = 1.2774]
Data/restraints/parameters	9752/1631/1014
Goodness-of-fit on F^2	0.728
Final R indexes [I>=2σ (I)]	R_1 = 0.7823, wR_2 = 0.8037
Final R indexes [all data]	R_1 = 0.9590, wR_2 = 0.8633
Largest diff. peak/hole / e Å^{-3}	1.38/-3.08

5.1.5 Attempt to Synthesis of LaLiNDC MOF

Lanthanum (III) nitrate hexahydrate (200 mg, 0.462 mmol), 2,6-naphthalenedicarboxylic acid (76 mg, 0.35 mmol), lithium *tert*-butoxide (42 mg, 0.5 mmol) and DMF (6 mL) was sonicated for 30 mins. The reaction mixture was heated at 120 °C for 72 h in a 23 mL Teflon Stainless Steel lined autoclave vessel. Hexagonal-shaped colourless crystals and a white microcrystalline solid were obtained; the crystals were separated manually from the bulk product, suitable for single-crystal X-ray diffraction. The same reaction was repeated at 170 °C. The mixture was cooled at a rate of 0.2 °C min^{-1} to room temperature. Hexagonal-shaped crystals were formed

and isolated by washing with DMF (4 x 2 ml) and dried overnight in the air (5 mg, 32% based on lanthanum nitrate hexahydrate). These synthesised crystals were not the mixed metal/alkali metal MOF, LaLiNDC MOF system expected, only lanthanum coordination with NDC ligands identified by single crystal X-ray diffraction as shown in Figure (5.4) and crystal data in Table (5.3). Also, no trace of lithium Li ion was found using SEM/EDX techniques. Hence, further characterization was stopped.

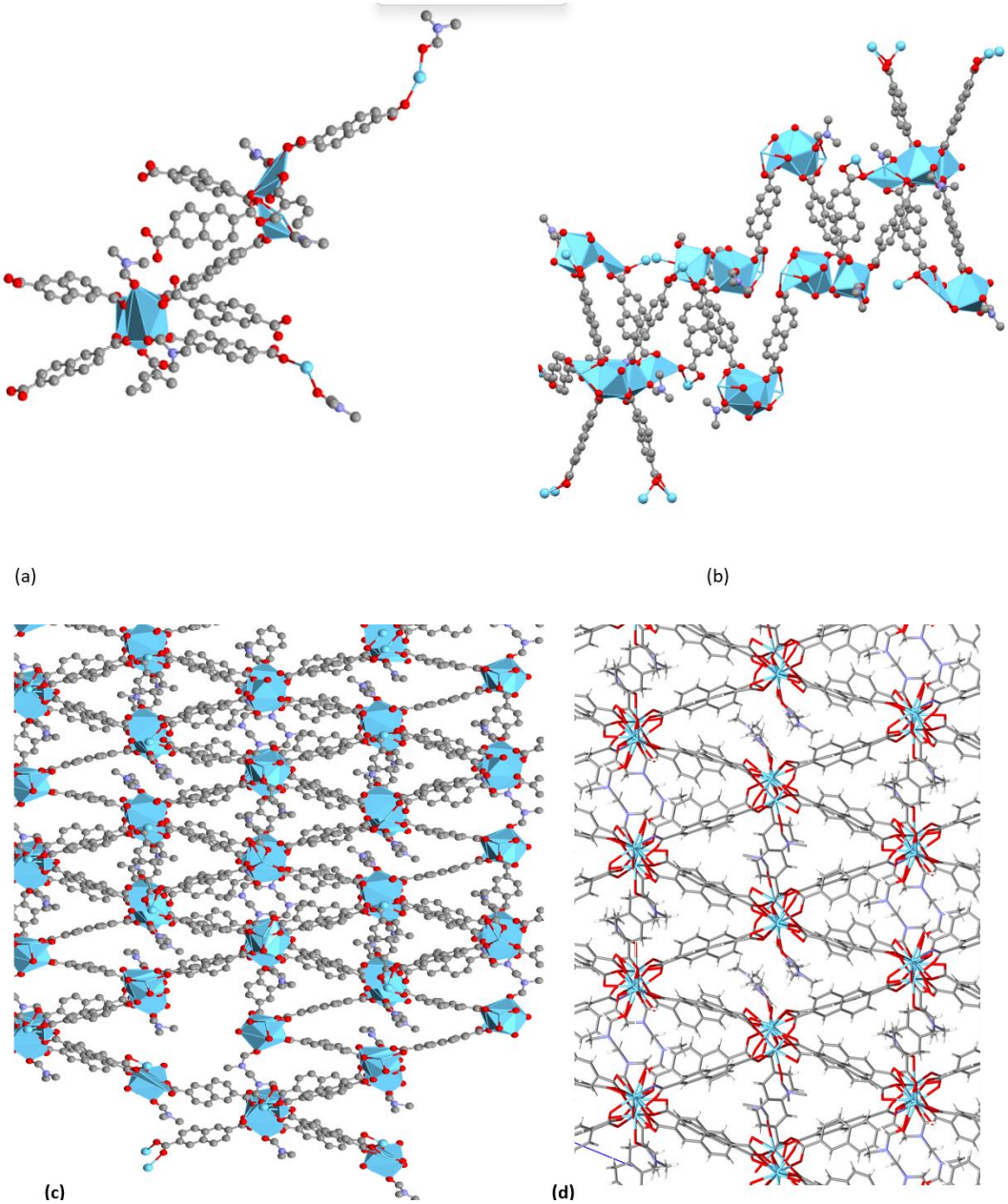


Figure 5.4: Polyhedral Crystal structure (a) Autocentre (b) Asymmetric unit (c) polyhedral packed unit (d) Stick representation of LaNDC MOF Packed unit viewed along crystallographic 'b' axis **(**grey = C, cyan = La, red = O, blue = N, H = light grey, hydrogen atoms have been removed for clarity).

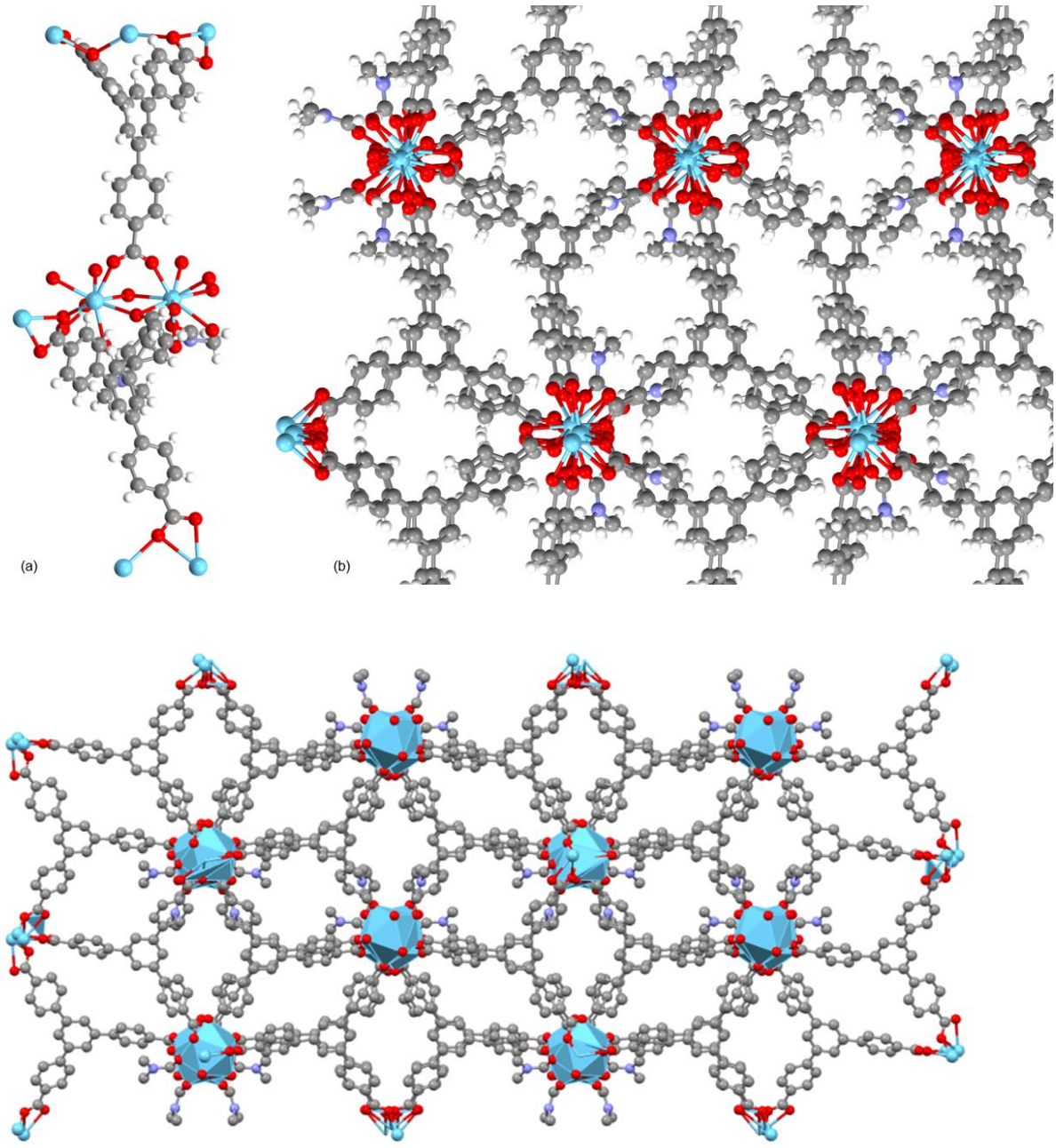
Table 5.3: **Crystal data and structure refinement for synthesised LaNDC MOF**

Empirical formula	$C_{252}H_{178}La_{12}N_{14}O_{82}$
Formula weight	6380.99
Temperature/K	293(2)
Crystal system	Triclinic
Space group	P-1
a/Å	12.2868(6)
b/Å	21.7882(11)
c/Å	25.3515(10)
α/°	109.951(4)
β/°	94.656(4)
γ/°	105.698(4)
Volume/Å^3	6027.6(5)
Z	1
ρ_{calc}g/cm^3	1.758
μ/mm^{-1}	2.009
F(000)	3128.0
Radiation	Cu Kα (λ = 0.6889)
2Θ range for data collection/°	2.094 to 51
Index ranges	$-13 \leq h \leq 14$, $-24 \leq k \leq 24$, $-25 \leq l \leq 24$
Reflections collected	20749
Independent reflections	12604 [R_{int} = 0.8502, R_{sigma} = 1.3380]
Data/restraints/parameters	12604/1465/1605
Goodness-of-fit on F^2	1.003
Final R indexes [I>=2σ (I)]	R_1 = 0.8123, wR_2 = 0.8197
Final R indexes [all data]	R_1 = 0.9721, wR_2 = 0.8928
Largest diff. peak/hole / e Å^{-3}	1.25/-1.83

5.1.6 Attempt to Synthesis of LaLiBTB MOF

Lanthanum (III) nitrate hexahydrate (200 mg, 0.462 mmol), 1,3,5-Tris(4-carboxyphenyl)benzene (154 mg, 0.35 mmol), lithium *tert*-butoxide (59 mg, 0.53 mmol) and DMF (6 mL) was sonicated for 30 mins. The reaction mixture was heated at 120 °C for 72 h in a 23 mL Teflon Stainless Steel lined autoclave vessel. Colourless-cylindrical shaped crystals and a white microcrystalline solid were obtained; the crystals were separated manually from the bulk product, suitable for single crystal X-ray diffraction. The same reaction was repeated at 170 °C. The mixture was cooled at a rate of 0.2 °C min^{-1} to room temperature. Cylindrical-shaped crystals were formed and isolated by washing with DMF (4 x 2 ml) and dried in air overnight. These

synthesized crystals were not the mixed metal/alkali metal MOF LaLiBTB MOF system expected. Only lanthanum coordination with BTB ligands forming LaBTB MOFs was identified by single crystal X-ray diffraction according to the asymmetric and packed unit shown in Figure (5.5) and crystal data in Table (5.4).



(c)

Figure 5.5: Crystal structure (a) Asymmetric unit (b) packed (c) Polyhedral Packed unit of LaBTB MOF viewed along crystallographic 'b' axis (grey = C, cyan = La, red = O, blue = N, H = light grey**).**

Also, no trace of Lithium Li-ion was found using SEM/EDX techniques. Hence, further characterization was stopped.

Table 5.4: Crystal data and structure refinement for synthesised LaBTB MOF

Empirical formula	**$C_{120}H_{88}La_4N_4O_{28}$**
Formula weight	2589.58
Temperature/K	293(2)
Crystal system	Monoclinic
Space group	$P2_1/c$
a/Å	15.13840(10)
b/Å	28.80650(10)
c/Å	16.354
α/°	90
β/°	96.50
γ/°	90
Volume/Å^3	7085.88(5)
Z	2
ρ_{calc}g/cm^3	1.214
μ/mm^{-1}	1.151
F(000)	2576.0
Radiation	Cu Kα (λ = 0.6889)
2Θ range for data collection/°	2.624 to 66.114
Index ranges	$-13 \leq h \leq 14$, $-24 \leq k \leq 24$, $-25 \leq l \leq 24$
Reflections collected	20487
Independent reflections	8745 [R_{int} = 0.8819, R_{sigma} = 1.4303]
Data/restraints/parameters	8745/663/726
Goodness-of-fit on F^2	0.901
Final R indexes [I>=2σ (I)]	R_1 = 0.8257, wR_2 = 0.7639
Final R indexes [all data]	R_1 = 0.9488, wR_2 = 0.8421
Largest diff. peak/hole / e Å^{-3}	0.92/-2.16

5.1.7 Synthesis of LaKBDC

Lanthanum (III) nitrate hexahydrate (50 mg, 0.12 mmol), benzene-1,4-dicarboxylic acid (12 mg, 0.06 mmol), potassium *tert*-butoxide (13 mg, 0.12 mmol) and DMF (3 mL) was sonicated for 30 mins. The reaction mixture was heated at 120 °C for 72 h in a 23 mL Teflon Stainless Steel lined autoclave vessel. Boat-shaped colourless crystals and a white microcrystalline solid were obtained; the crystals were separated manually from the bulk product, suitable for single-crystal X-ray diffraction. The same reaction was repeated at 170 °C. The mixture was cooled at a rate of 0.2 °C min^{-1} to room

temperature. Block-shaped crystals were formed and isolated by washing with DMF (4 x 2 ml) and dried overnight in the air (5 mg, 32% based on lanthanum nitrate hexahydrate). The bulk product was identified as $[LaK(BDC)_2].DMF$ $\{C_{19}H_{18.4}K_2NLa_2O_9\}n$ by powder x-ray diffraction. Yield: 30%. Elemental analysis (exp %): C: 29.90%; H: 1.94%; N: 1.79%; (calc %): C: 30.00%; H: 2.44%; N: 1.84%. Crystal data is found in Table 5.5 below.

5.2.0 Results and Discussions

This series of mixed metal MOFs is intended as a family of lanthanum-alkali metal (K, Li) terephthalate-based metal-organic frameworks. There were several attempts at synthesizing other varieties of lanthanum-alkali metal MOF systems. Hence, synthesis of LaLiBDC, LaKNDC, LaLiBTB, LaLiNDC and LaKBTB were unsuccessful (as described in Sections 5.1.1., 5.1.2., 5.1.3., 5.1.4. and 5.1.5. respectively) with the single crystal structures of the resulting MOF crystals clearly showing the absence of alkali metal coordination within the frameworks (as previously shown in Figures 5.2 – 5.5 above). Therefore, we could not proceed with further characterization and adsorption studies as planned. Consequently, only LaKBDC MOF was further characterised, and adsorption properties were studied, as presented in the following paragraphs.

5.2.1 PXRD Analysis of LaKBDC MOF

Single crystal X-ray diffraction analysis revealed the formation of a 3D framework which crystallises in the cubic space group, Ia-3. The 3D framework is built by lanthanum and potassium ions coordinated by oxygen atoms, forming layers interconnected by BDC molecules. The asymmetric and packed units are shown in Figure 5.6(a, b, c, d), polyhedral crystal packed structures in Figure 5.7 (a and b), and Table 5.5 reveals the crystal data parameters. Each unit cell contains two non-equivalent lanthanum atoms (La00 and La1) coordinated by oxygen atoms from BDC. The asymmetric unit (5.6a) consists of one full BDC carboxylate linker, with one of the two carboxylate O atoms coordinating to one K, while the two carboxylate O (in a chelating mode) also coordinate to La. According to figures 5.6b and 5.7a, the LaKBDC MOF autocentre shows that each metal centre unit consists of three crystallographic independent Lanthanum, La ions (La00 between two La1). The central La ion (La00) is bridged by six carboxylate groups of the six different BDC

ligands possessing a total of 12 oxygen atoms, thus making central La(III) ion, (La00) to possess the coordination number of 12 (and the polyhedron approximates a cuboctahedron in Figure 5.7a). The other two vertex La ions (La01) are each coordinated by six oxygen atoms (three O donated by three neighbouring BDC ligands and the remaining three O from the K-O bond) and possess the coordination number of 6 in an octahedral coordination geometry. Likewise, the metal centre consists of six (6) vertex potassium (in a distorted square pyramidal geometry), K ions (K2), each of which is bonded by three oxygen atoms from three neighbouring BDC ligands, a La-O bridge and a carboxylate C-K bond) from one BDC ligand with a coordination number of 5 (Figure 5.7a).

Table 5.5: Crystal data and structure refinement for LaKBDC.

Empirical formula	$C_{19}H_{18.4}K_2NLa_2O_9$
Formula weight	**760.762**
Temperature/K	120(2)
Crystal system	cubic
Space group	Ia-3
a/Å	27.012
b/Å	27.012
c/Å	27.012
α/°	90
β/°	90
γ/°	90
Volume/Å^3	19709.3
Z	48
ρ_{calc}g/cm^3	0.997
μ/mm^{-1}	2.606
F(000)	5704.0
Crystal size/mm^3	0.188 × 0.111 × 0.075
Radiation	CuKα (λ = 0.9028)
2Θ range for data collection/°	5.418 to 71.96
Index ranges	-35 ≤ h ≤ 33, -34 ≤ k ≤ 33, -34 ≤ l ≤ 34
Reflections collected	90599
Independent reflections	3733 [R_{int} = 0.0536, R_{sigma} = 0.0168]
Data/restraints/parameters	3733/0/126
Goodness-of-fit on F^2	1.196
Final R indexes [I>=2σ (I)]	R_1 = 0.0442, wR_2 = 0.1987
Final R indexes [all data]	R_1 = 0.0466, wR_2 = 0.2010
Largest diff. peak/hole / e Å^{-3}	1.91/-0.47

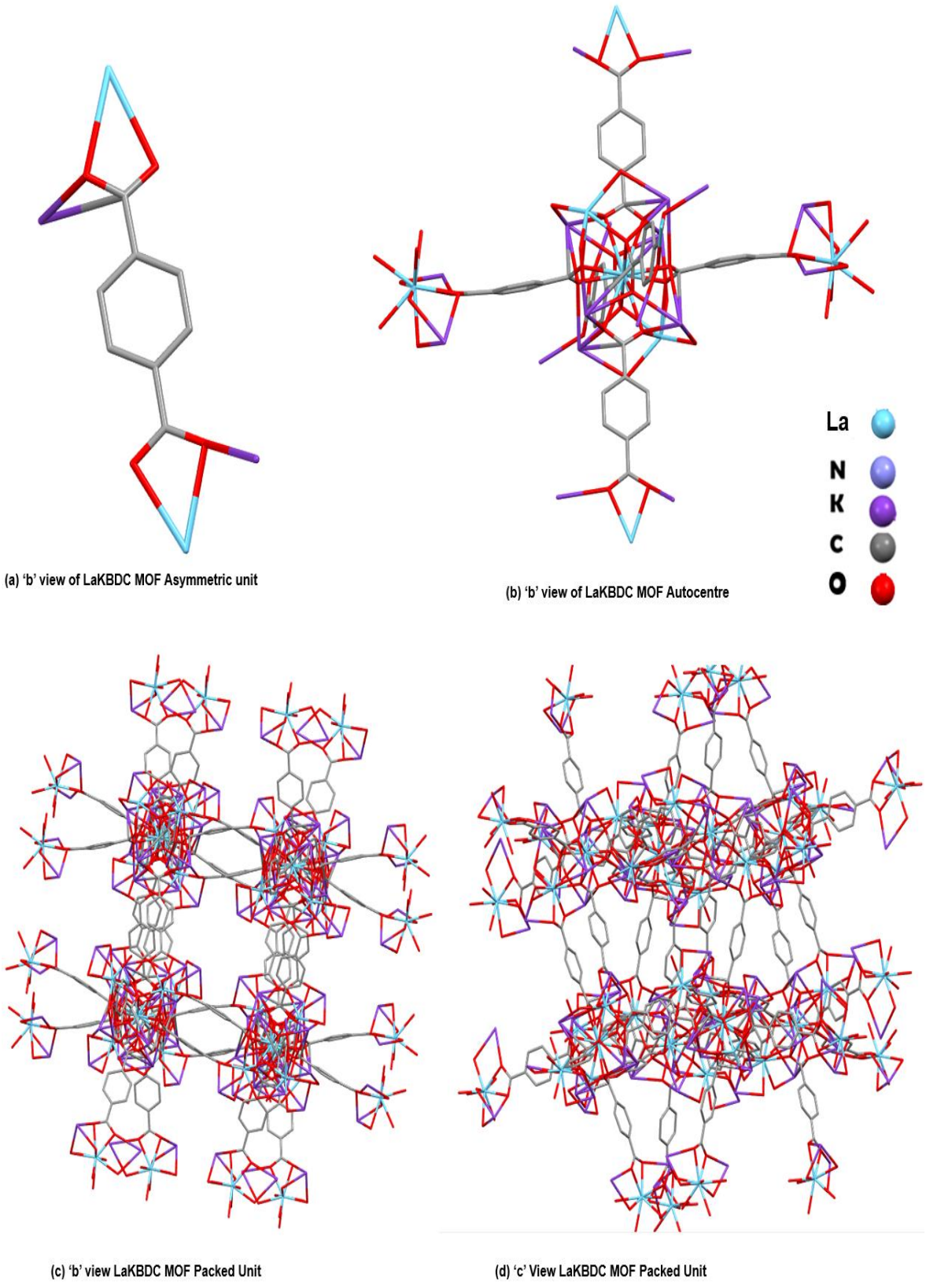
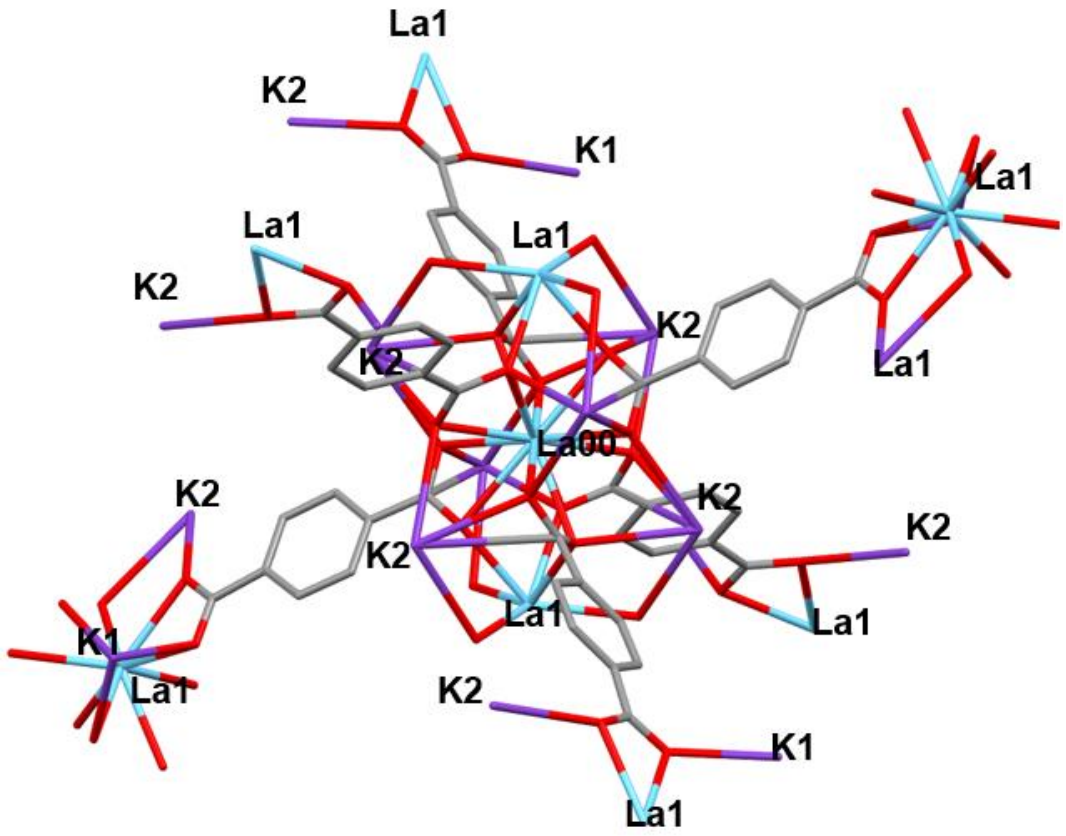
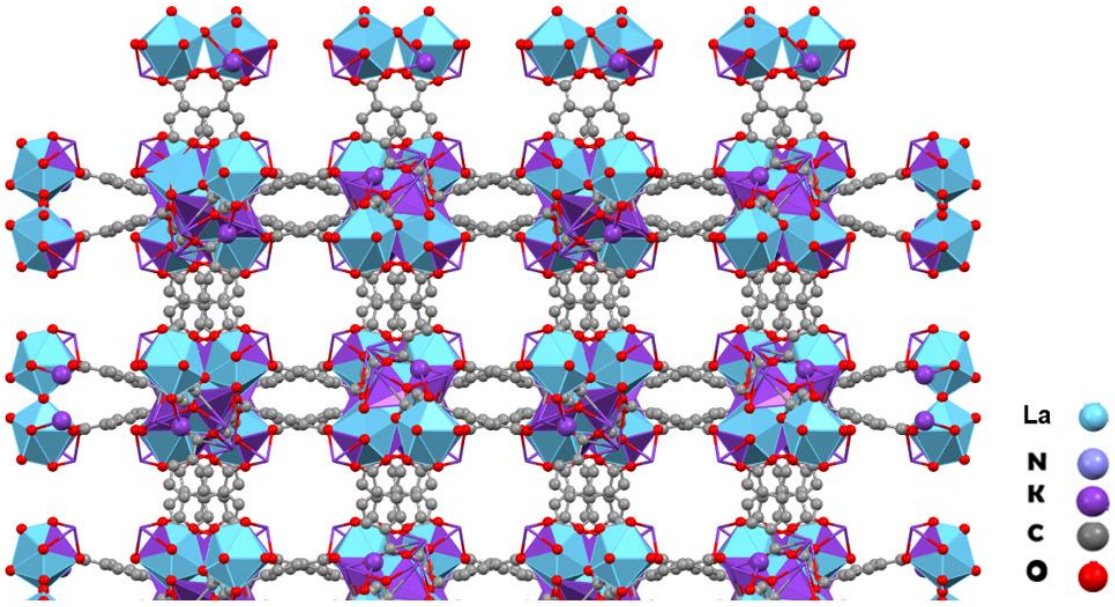


Figure 5.6: Crystal strucure of LaKBDC MOF (grey = C, cyan = La, purple = K, red = O, blue = N, H = light grey, hydrogen atoms have been removed for clarity**).**



(a)



(b)

Figure 5.7: (a) Stick representation of 'b' view of LaKBDC MOF Autocentre (b) Polyhedral representation of Packed LaKBDC MOF viewed along the crystallographic

'b' axis. (grey = C, cyan= La, purple = K, red = O, blue = N, H = light grey; La(III) cation are presented as octahedral and cuboctahedron, K presented as distorted square pyramidal geometry, La as cyan, and K as purple).

To bind La and K ions, two distinct coordinating modes (Figure 5.8) are adopted by carboxylates in the BDC linker, which include heptadentate (Figure 5.8b) and tetradentate (Figure 5.8c) chelating/bridging coordination modes. For the unusual heptadentate bridging/chelating mode, μ_7-η^3:η^2:η^2 carboxylate anion (-COO-), one O of -COO- is coordinated by two K(I) ion (purple node) (that is, K2, K2) while the metal centre shows that each of the terephthalate dianion oxygen in bidentate coordination chelates the central Lantanum, La00. Additionally, the second O of -COO- binds with potassium, K(I) and a La(III) ions (La1) (cyan colour nodes) (Figure 5.7a) giving rise to the existence of seven (7) different bonds namely, K2-O003, two K2-O005 bonds, La1-O003, La00-O003, La00-O005 and K2-C008 (see Figure 5.8b).

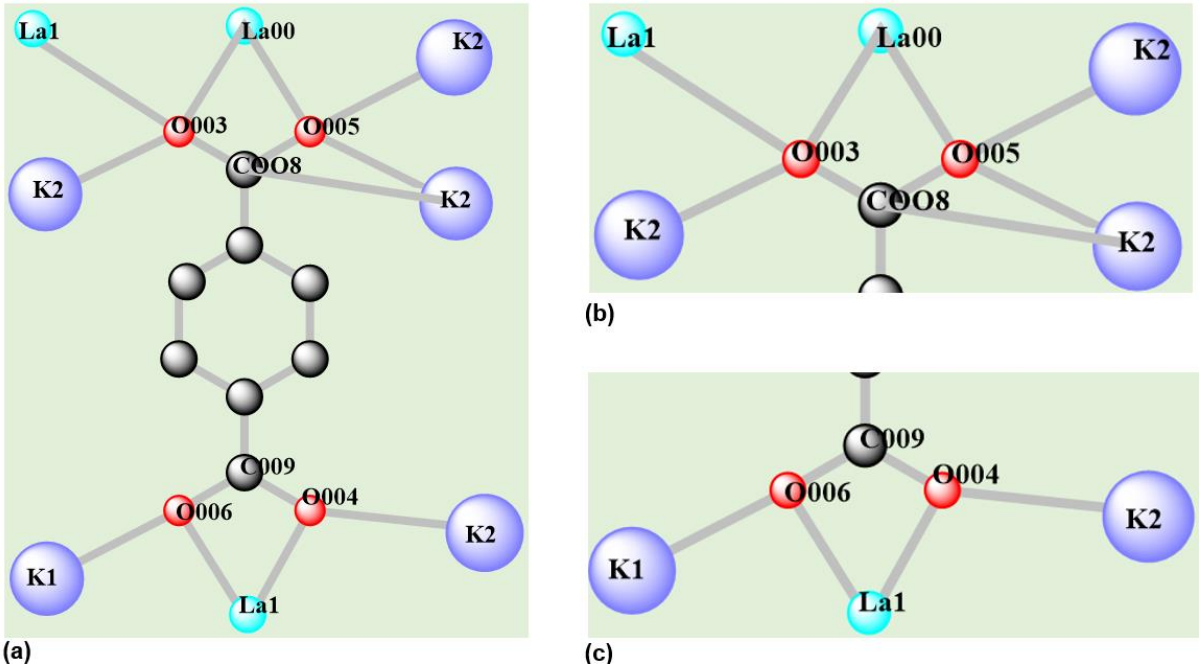


Figure 5.8: Coordination modes of BDC in LaKBDC MOF (a) BDC Ligand in LaKBDC (b) heptadentate bridging/chelating mode, μ_7-η^3:η^2:η^2 (c) tetradentate chelating / bridging mode, μ_4-η^1:η^2:η^1.

The tetradentate chelating / bridging type coordination mode (Figure 5.8c) was exhibited by all the carboxylate groups of the BDC ligands acting as a bridging ligand to K1 and K2 and as a chelating ligand to the Lanthanum ion, La1 (that is, where two

oxygen atoms of one carboxylate group chelate one La(III) ion) as shown in Figure 5.7a. The carboxylate groups of the BDC linkers exhibited the tetradentate chelating/bridging coordination mode. This chelating/bridging tetradentate binding mode, μ_4-η^1:η^2:η^1 has also been observed and reported in carboxylate-bridged dimmers.[9,10] The La - O bond lengths are in the range of 2.529(3) - 2.677(3) Å (agreeing with earlier report)[1], and the K - O bond lengths are in the range of 2.839(5)-2.943(5) Å (see Appendix VI for detailed bond distances and bond angles).

5.2.2 FTIR and TGA Analysis

The TGA profile (recorded in air, 30 - 700 °C, heating rate 10 °C/min) of LaKBDC MOF shows three degradation steps (Figure 5.9a) involving weight loss in the temperature range 30–178 °C due to 2.3% water desorption the first degradation step around 178-281 ^{o}C most likely corresponds to the decomposition, loss and desorption of included solvent molecules such as DMF, the second step corresponds to the BDC ligand decomposition (288-463 ^{o}C) takes 17% weight loss and therefore MOF structural damage, and the final decomposition (from 463-525 °C) leads to the formation of oxides of lanthanum and potassium. LaKBDC is, therefore, thermally stable up to 650 °C, the onset degradation temperature. The optimum degradation temperature (ODT) was 485 °C.[21,22.]

FTIR spectroscopy was utilized throughout the region of wavenumbers 400-4000 cm-1 (mid-infrared) to identify the functional groups within the mixed metal MOFs. As shown in Figure 5.9b, two strong peaks were observed at 1360 cm^{-1} and 1536 cm^{-1}, which indicated the existence of both symmetric and asymmetric vibrations of C=O, respectively. The 1602–1560 cm-1 and 1402–1364 cm-1 peaks may be attributed to bridging and chelating carboxyl groups.[2,11-13] Additionally, an intense peak at 1536 cm^{-1} showed the complex interaction of the C=O with metals La^{3+} and K^{+}. The vibration C=O stretching mode of DMF shifted to the lower wavenumbers (1649 cm^{-1}) relative to the free amide value (1680 cm^{-1}), showing that the ligations of all DMF molecules with their carbonyl groups were successfully formed. Generally, the absorption band was absent in the region of 1700 cm-1, indicating that the ligand's carboxylic acid groups were completely deprotonated. Also, the absence of –OH absorption at ~ 2500 cm^{-1}, a distinct functional group in carboxylic acid, was eliminated in the LaKBDC MOFs. This indicated that the carboxylate groups of the BDC ligand are coordinated to metal ion (La^{3+}) nodes. The typical vibration at 501.68 cm^{-1} (~ 502 cm^{-1}) is attributed

to La-O stretching vibration, in which the oxygen atom was coordinated to La.[22] The absence of the O-H stretching vibrations from water molecules (two peaks, sharp peak and broad peak, at 3460 cm^{-1} and 3220 cm^{-1}, respectively) shows the absence of water molecules in the frameworks.[2,15]

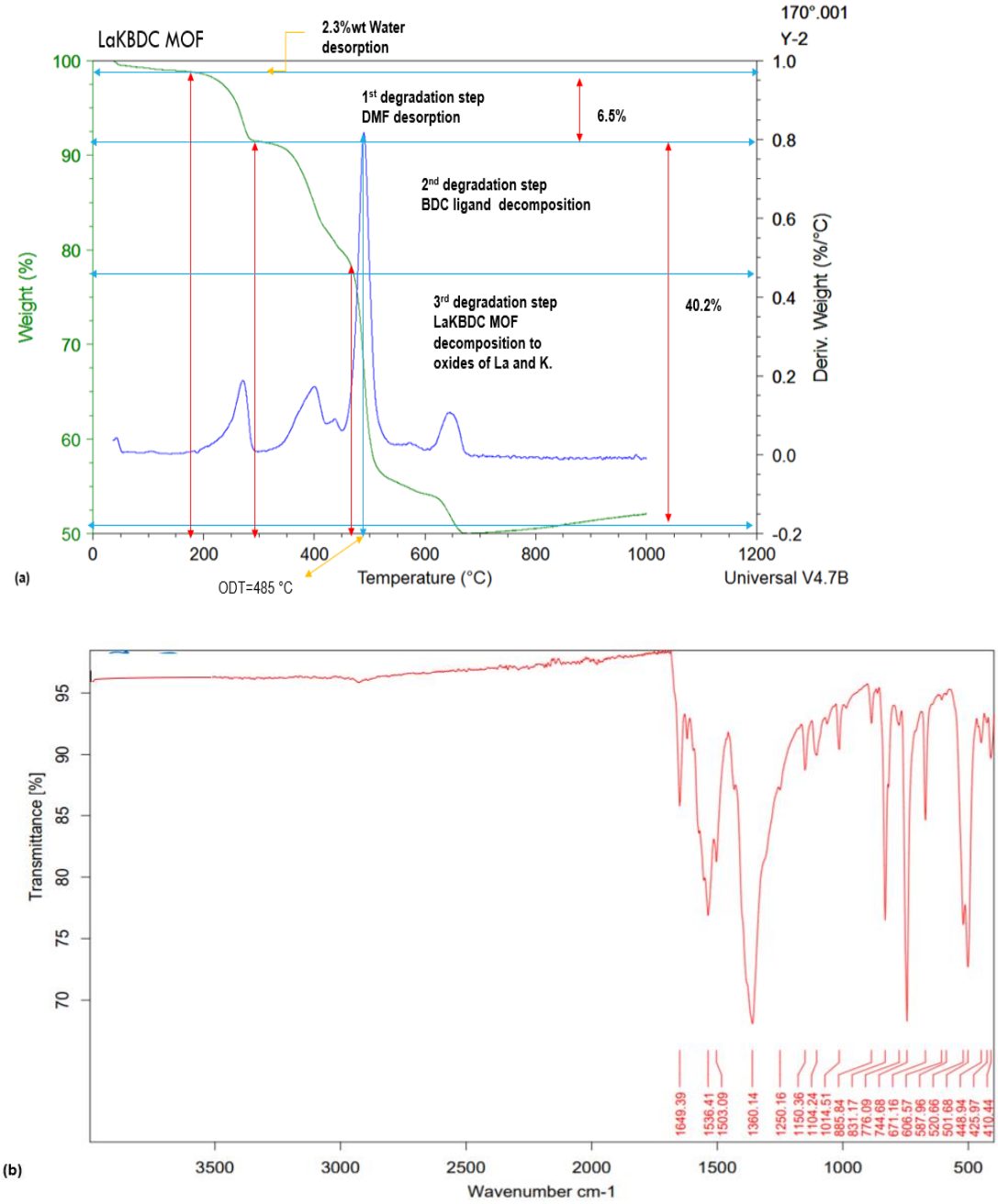


Figure 5.9: (a) TGA curve and (b) FTIR-ATR spectra for LaKBDC MOF.

5.2.3 SEM/EDX analysis of LaKBDC MOF

The lanthanum MOFs were characterised by PXRD to observe and record the diffraction pattern on the resulting diffractogram. Figure 5.10 shows the diffraction

pattern of LaKBDC. The diffraction pattern of LaKBDC shows sharp peaks with high intensity, indicating the material's high crystallinity. The pattern in Figure 5.10 is consistent with the peak positions found in the MOF with the same BDC ligand where characteristic peaks were observed at 2Θ = 7.92 °, 9.47 °, 10.8 °, 12.43 °, 16.70 °, 19.54 °.[13,14] The broad peak and its miller indexes at 2Θ = 16.52 °, 23.51 °, 33.37 °, 41.22 °, 44.82 °, 47.95 ° indicates lanthanum (III) nitrate in LaKBDC.

To observe the particle morphology, LaKBDC samples were examined with a scanning electron microscope (SEM) and the recorded images are illustrated in Figure 5.11, shown below. The LaKBDC sample showed the presence of V-hull-shaped particles with 100 µm width.

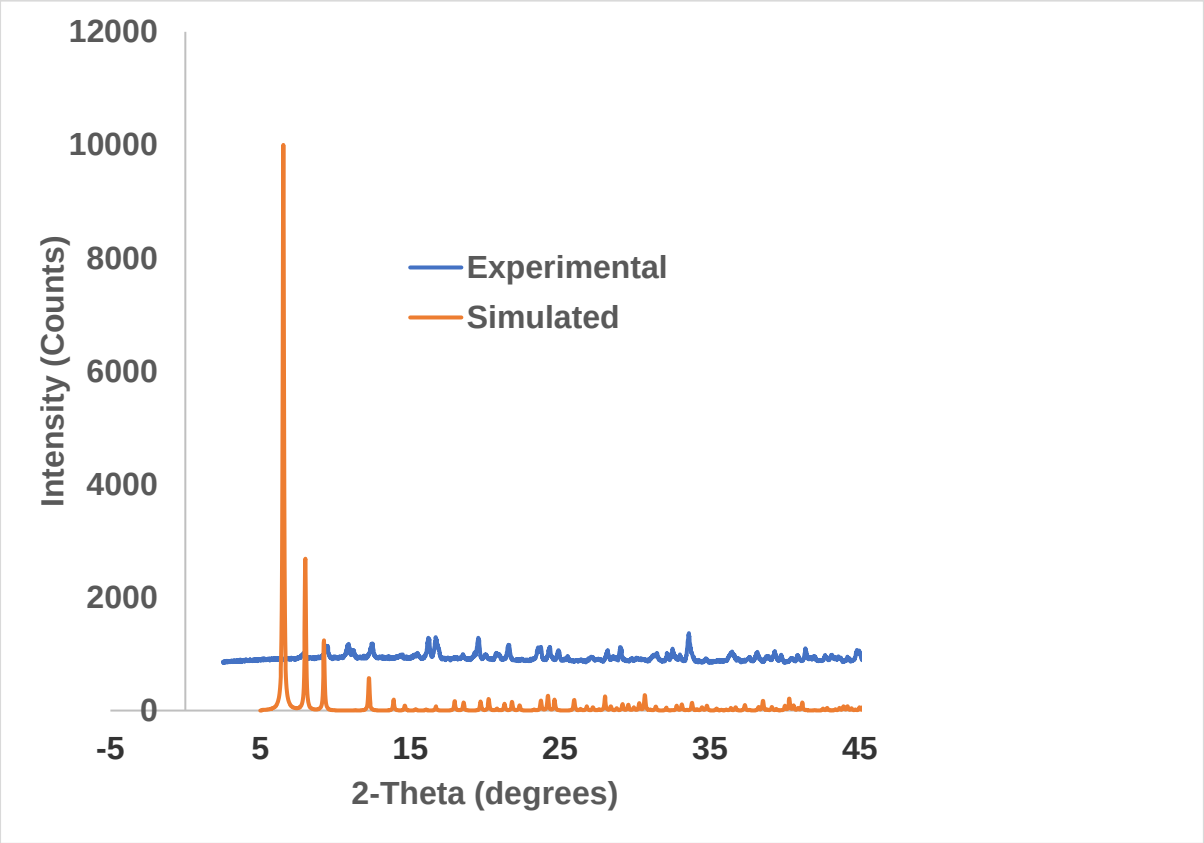


Figure 5.10: PXRD pattern of LaKBDC MOF.

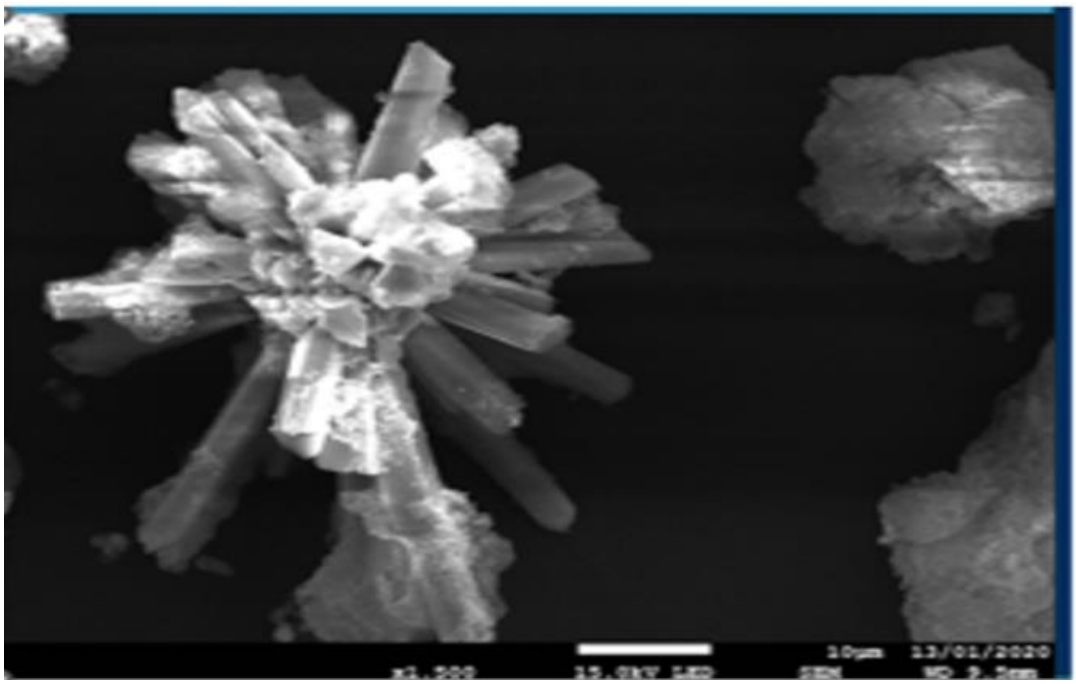


Figure 5.11: SEM micrograph showing the morphology of LaKBDC MOF**.**

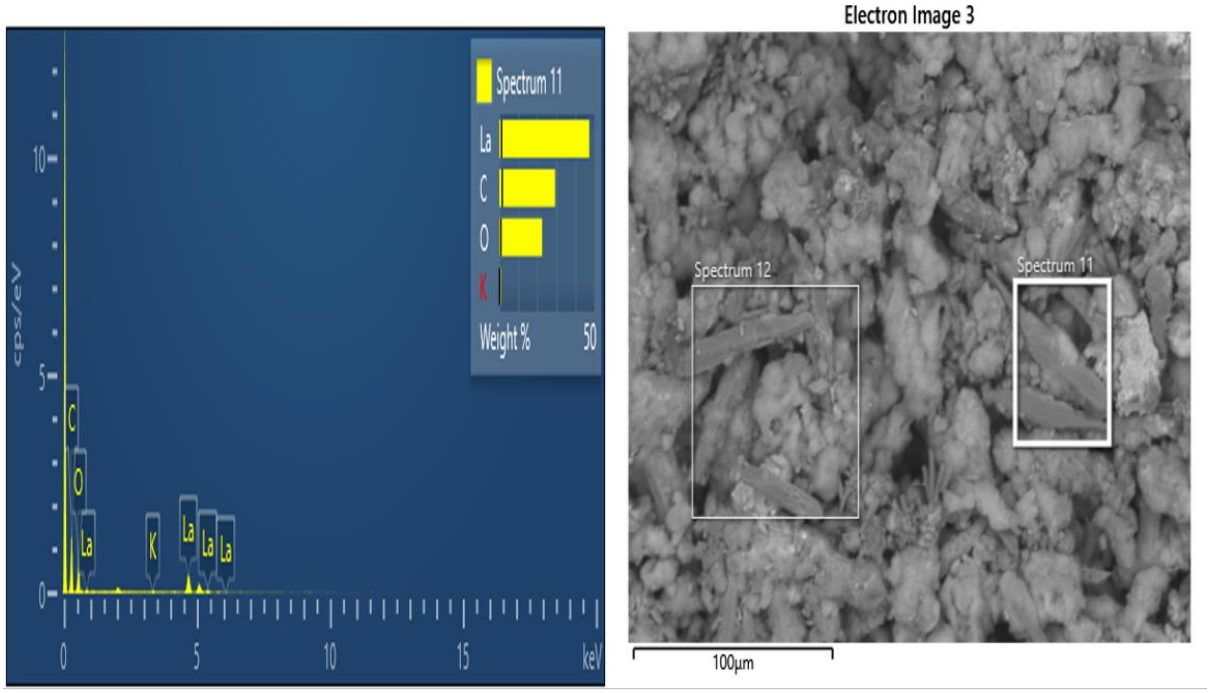


Figure 5.12: SEM images and EDX analysis of LaKBDC MOF EDS spectrum showing the peaks for the elements C, O, K and La.

This regular but tiny structure confirmed the good crystallinity of the materials, which XRD patterns had already demonstrated. LaKBDC exhibited relatively small, uniform crystals, as observed in Figure 5.12, with smaller particles joined together to form a

sheet of woven string-like material. The smooth surfaces and uniform-like structural morphology suggest impressive crystallinity and thermal stability with the lowest possible surface area.

Table 5.6: EDX analysis of LaKBDC MOF

Element	Line Type	Apparent Concentration	k Ratio	Wt%	Wt% Sigma	Standard Label	Factory Standard
C	K series	0.10	0.00103	21.59	1.50	C Vit	Yes
O	K series	0.40	0.00133	24.59	0.81	SiO_2	Yes
K	K series	0.02	0.00014	1.11	0.18	KBr	Yes
La	L series	0.61	0.00544	52.71	1.23	LaB_6	Yes
Total:				100.00			

LaKBDC showed V-hull shapes that were widely distributed throughout the sample. The corresponding EDS analysis (Figures 5.12) confirmed the expected C and O from the BDC ligand, and most importantly, both metals, La and K, were observed in the MOF sample. EDS results in Table 5.6 and Figure 5.12 state the percentage of La incorporation as 52.71%. It also shows about 1.11% of K inside the material. Although the exact amount of doped K in the structure cannot be calculated precisely from the result because the EDS was largely semi-quantitative, the inclusion of K within the structure is proved. It should also be noted that although the reactant mixture of La and K was a ratio of 1:1.5, a very small amount of K was fixed in the mixed MOF material.

5.3 Gas Adsorption Studies

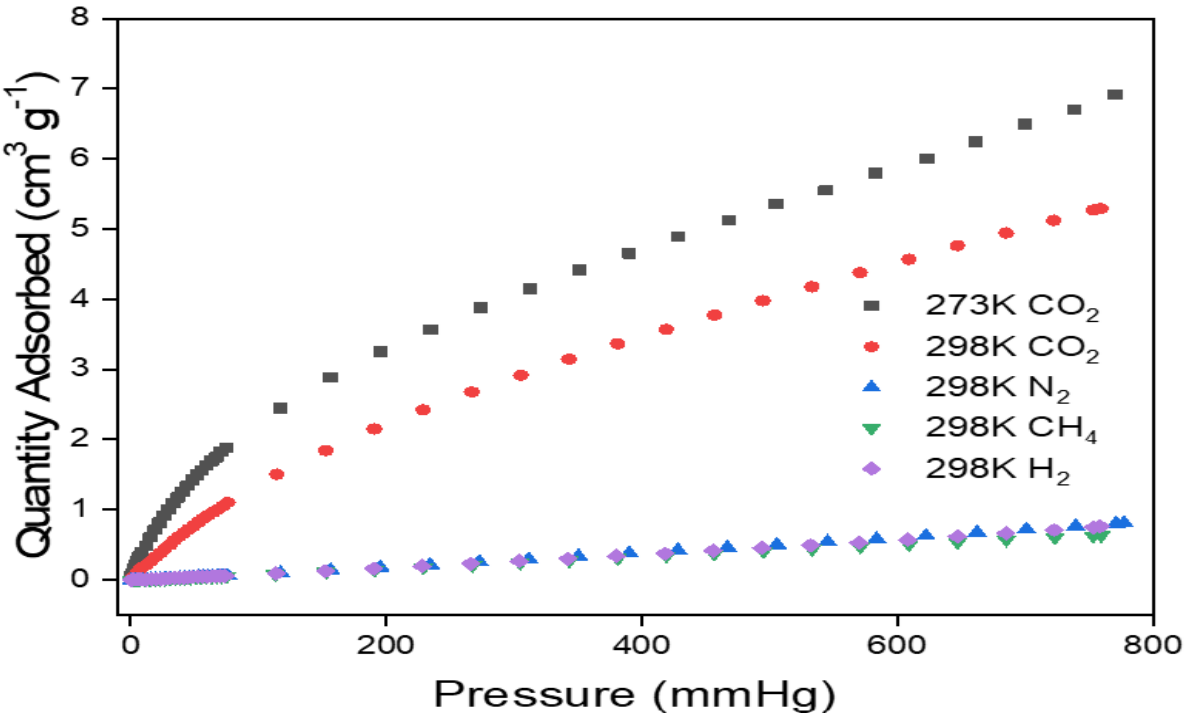


Figure 5.13: CO_2, N_2, CH_4 and H_2 Adsorption Isotherms for LaKBDC at 273 K and 298 K of LaKBDC MOF.

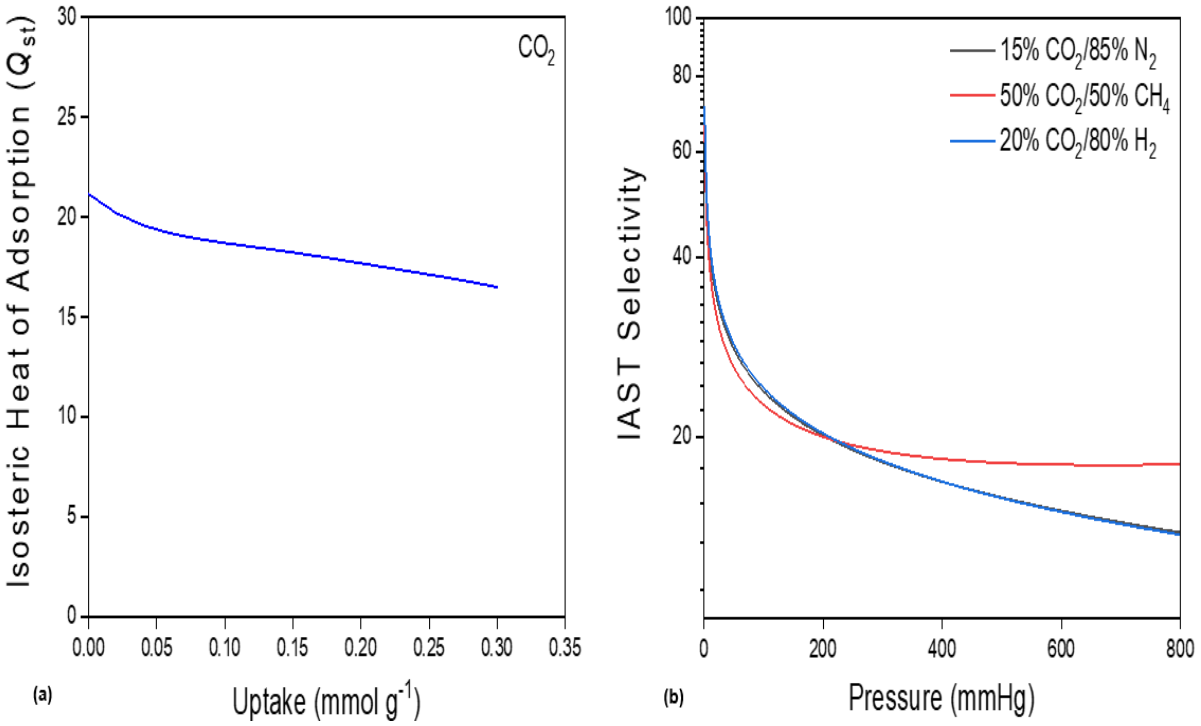


Figure 5.14: (a) Isosteric Heat of adsorption, Q_{st} (b) IAST Selectivity of LaKBDC MOF.

5.3.1 CO_2, N_2, CH_4 and H_2 Adsorption Isotherms for LaKBDC at 273 K and 298 K of LaKBDC MOF

The gas adsorption properties of LaKBDC were studied to examine the pore characteristics. The samples were degassed at 150 °C for 10 h under vacuum before the adsorption experiments. The CO_2 adsorption capacity of LaKBDC at 273 K and 298 K shows a type I isotherm of a microporous material. The experimental adsorption isotherms of CO_2 and CH_4, H_2, and N_2 on LaKBDC MOF were measured over a pressure range of 0–800 mmHg at 273 K and 298 K, respectively, as shown in Figure 5.13. The adsorption capacity of LaKBDC MOF decreases with the increase in temperature for all gases. LaKBDC MOF has a higher affinity towards CO_2 than to CH_4, H_2, and N_2, as shown by the significant difference in adsorption capacities at any pressure. The compound exhibited high CO_2 uptakes at 273 K and 298 K and comparatively lower H_2, CH_4 and N_2 uptakes at 298 K with increasing pressure.

The experiment further showed that LaKBDC has a stronger affinity toward CO_2 at 273 K when compared to 298 K, while the adsorption of N_2, H_2 and CH_4 at 298 K is much lower and showed almost no interaction with the adsorbent. Therefore, only a negligible surface area (<1 cm^3g^{-1}) was observed. The adsorption isotherm curve for 298 K CH_4 and H_2 exhibits Type III Isotherm describing a linear relationship between quantity adsorbed and relative pressure. This result agrees with the assertion of Li et al.[12] that achieving room-temperature H_2 storage with MOFs was still a daunting task because of the weak interaction between H_2 and MOFs. For example, van der Waals interactions are too weak to bring in much H_2 uptake of MOFs because of the zero-dipole moment of H_2. Hence, researchers should focus more on synthesising MOFs with high densities of strong H2 adsorption sites and producing MOFs with high room temperature H_2 capacities. This same van der Waals interaction requirement applies to N_2 and CH_4. Hence, van der Waals interactions are the dominant force accounting for its H_2, N_2, and CH_4 storage.

5.3.2 Isosteric Heat for CO_2 on LaKBDC MOF

Figure 5.14a is the isosteric heat for CO_2 on LaKBDC, showing that the adsorption of CO_2 on LaKBDC exhibits a decreasing trend with higher uptake (thus higher pressure). In this adsorbent–absorbate pair, isosteric heat reduces as uptake increases. Therefore, isosteric heat decreases at higher uptake or loading (from 21.16 $kJmol^{-1}$ -

16.50 kJmol^{-1} at 0 mmol g^{-1} - 0.3 mmol g$^{-1,}$ respectively) due to variability in energetic heterogeneity and weaker bonding at multi-layer adsorption. This means all the available adsorption sites do not have the same adsorption energy for the probing gases, CO_2.[18]

5.3.3 Ideal Adsorbed Solution Theory (IAST)

Thermodynamic analysis by ideal adsorbed solution theory (IAST) was used to determine the adsorbed phase's and bulk gas's equilibrium composition for binary systems.[18] The IAST is based on the thermodynamic equilibrium properties of the pure components of the system studied. It helps to predict the selectivity of adsorbents, including porous materials, to separate a particular mixture.[12]

IAST was used to compute the adsorption selectivity required to evaluate the separation performance of LaKBDC. The single-component CO_2 capacities for the LaKBDC sample have been described in the previous section, but here they are contrasted with pure component CH_4 isotherms and data obtained for the binary mixture of CO_2/H_2, CO_2/CH_4 and CO_2/N_2. The selectivities for three different compositions of CO_2/H_2, CO_2/CH_4 and CO_2/N_2 mixtures were calculated at 298 K. As shown in Figure 5.14b, at 800 mmHg and 298 K, the selectivity decreases drastically with increased pressure. The CO_2/CH_4 (50:50) mixture selectivity of LaKBDC is 18.03, in the range of 18.03 – 66.75. The selectivity is higher than those of CO_2/H_2 (20:80) (13.78) range 13.78 – 71.29 and CO_2/N_2 range (13.91– 68.22) having similar IAST selectivity (13.91) at 800 mmHg and 298 K. The performance of an adsorbent is highly dependent on the uptake capacity and separation selectivity. The high selectivity of CO_2/CH_4 (50:50) and the high CO_2 adsorption capacity of LaKBDC predict its useful separation potential for CO_2/CH_4.

In summary, the isosteric heat for CO_2 on LaKBDC shows that the adsorption of carbon dioxide (CO_2) on LaKBDC exhibits a decreasing trend with higher uptake (thus higher pressure), which is common to all potassium-based MOFs studied in selected literature as referenced in Table 5.3 Selectivity studies show LaKBDC showed similar selectivity for CO_2/N_2 and CO_2/H_2 around 13.9 while displaying higher selectivity for CO_2/CH_4 thus predicting its useful separation potential for CO_2/CH_4.

5.3.4 Comparative Studies of LaKBDC MOF with other Mixed Metal–Alkali Metal-Organic Frameworks

We compared our adsorption data (LaKBDC MOF) with the textural properties of some reported mixed metal MOFs summarised in Table 5.7 above. Zhang et al.[16] and Yang et al.[17] investigated the impact of the inclusion of alkali metal in mixed alkali MOF, UTSA-16 ($KCo_3(C_6H_4O_7)(C_6H_5O_7)(H_2O)_2$ where M= (M = Li+, Na+, Rb+, Cs+))

Table 5.7: The BET surface area, heat of adsorption, textural properties and heats of adsorption over some selected Mixed-Alkali Metal based MOFs[16,17,18]

S/No	Sample	BET (m^2 /g)	Q_{st} at lower pressure region (kJ/mol)	The ionic radius of group 1 element (nm)	CO_2/N_2 Selectivity	CO_2/CH_4 Selectivity	CO_2/H_2 Selectivity	References .
1	Li- UTSA -16	519.4	21.57	0.076	---	--	-	16
2	ZnLiBTB	--	29.17	0.076	31.32	8.79	77.69	This Study
3	Na-UTSA-16	544.1	24.19	0.102	--	--	-	16
4	K- UTSA -16	874.0	25.32	0.138	--	--	-	16
5	ZnKBTB	219.0	34.38	0.138	24.13	64.72	55.57	This Study
6	Rb-UTSA-16	461.5	26.04	0.152	---	--	-	16
7	Cs-UTSA-16	291.3	31.67	0.167	---	--	--	16
8	Li-BEA	474.0	53.0	--	20.0	--	--	17
9	K-BEA	508.0	56.5	--	16.8	--	--	17
10	Na-BEA	446.0	59.6	--	14.7	--	--	17
11	Cs-BEA	411.0	89.6	--	24.0	--	--	17
12	MOF-5	--	--	-	17.48	15.53	--	18
13	MOF-177	--	--	--	17.73	4.43	--	18
14	Zeolite	--	--	-	240.56	256.47	--	18
15	LaKBDC MOF		21.0		13.91	18.03	13.78	This Study

to form M-UTSA-16[16] and M-BEA[17] (Zeolite beta with high aluminium content (BEA, Si/Al = 7.4)) on N_2 and CO_2 adsorption. The basic alkali metal K+ cation was observed to possess a high affinity and activation ability for CO_2.[16-18.] The M-UTSA-16 frameworks synthesized by ion exchange were evaluated as 'catalysts for transforming CO_2 and epoxide to cyclic carbonate without co-catalysts.[17] CO_2 adsorption isotherm follows type I isotherm characteristic of a microporous material.

The Isosteric heat of adsorption, $Q_{st,}$ decreases with increased loading in agreement with our reports in Chapter 4 and Zhang et al.[16] and Yang et al.[17]

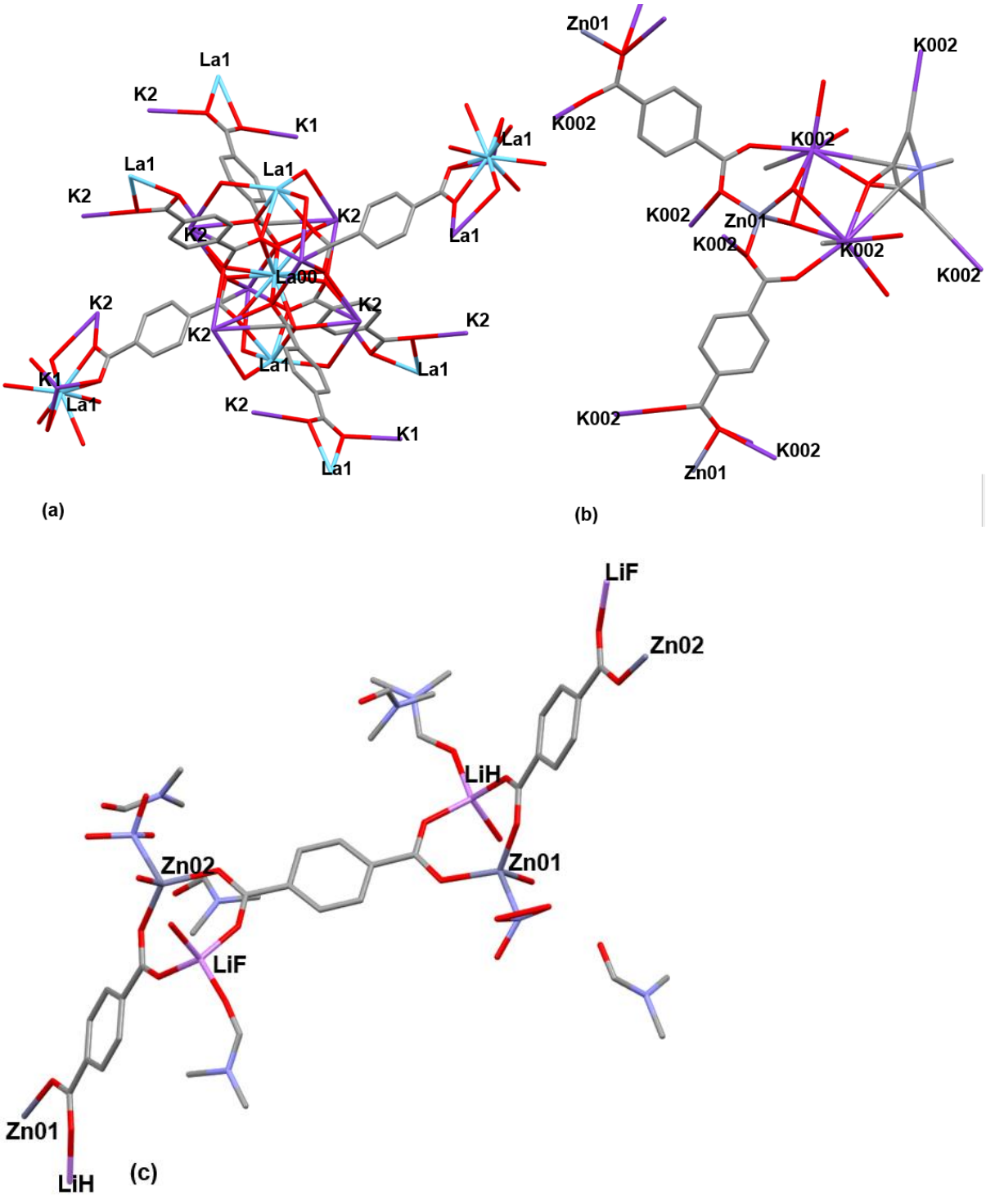


Figure 5.15: Coordination Environment of La and K atoms in (a) Stick representation of 'b' view of LaKBDC MOF Autocentre (b) b' view ZnKBDC MOF Autocenter (c) 'b' view ZnLiBDC MOF Autocenter.

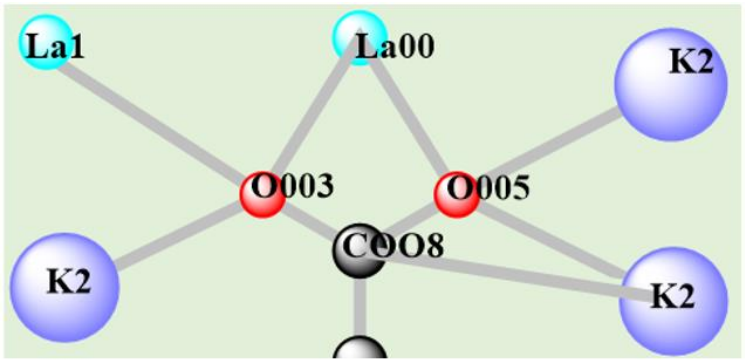
Additionally, comparing the coordination environment and structural data LaKBDC MOF with MM-MOFs (ZnKMOF and ZnLiMOFs) constructed with the same carboxylate linker, benzene-1,4-dicarboxylic acid (BDC), that is the LaKBDC MOF with ZnKBDC and ZnLiBDC MOF (see Figure 5.15a,b,c) synthesized in Chapter 3. A study of the coordination environment of ZnKBDC MOF (Figure 5.15b) shows that the Zn(II) (Zn01) displayed tetrahedral coordination geometry with a coordination number of 4, while Potassium, K ion (K002) possesses the coordination number of 8, coordinated in a distorted square antiprismatic geometry. Also, for the ZnLiBDC (Figure 5.15c) studied, the Zn(II) (Zn01 and Zn02) and Li cations (LiH and LiF) are O-coordinated tetrahedrally with a coordination number of 4. However, for LaKBDC (Figure 5.15a), the coordination numbers of K ions are 3 (for K1) and 5 (for K2). The three lanthanum atoms within the metal centre, vertex La1, central La00, and vertex La1, possessed the coordination number of 6, 12 and 6, respectively. The coordination characteristics are common to many lanthanides.[19,20]

Many MOF structures have been reported with multiple coordination modes co-existing in the same polymeric structure. The carboxylates, -COO- in LaKBDC MOF, display two different coordination modes, namely the heptadentate chelating/bridging, μ_7-η^3:η^2:η^2 (Figures 5.15a and 5.16a) and tetradentate (Figure 5.16b) chelating/bridging coordination (μ_4-η^1:η^2:η^1)[9,10] modes. Just like in our structural study, observing some uncommon coordination modes is not unusual. Dong et al.[24] in 2002 reported a $[Ba_9(MeCO_2)_{14}](ClO_4)_4$ (Figure 5.17a) three-dimensional (3D) framework which displayed multiple acetate groups bridging modes coexisting in the same polymeric structure. These include the μ_5-η^3:η^3 (a), μ_4-η^2:η^2 (b), and μ_3-η^2:η^2 bridging modes. The central barium atom [Ba(3)] is coordinated by eight oxygen atoms from four μ_5-η^3:η^3 (Figure 5.17a).[24]

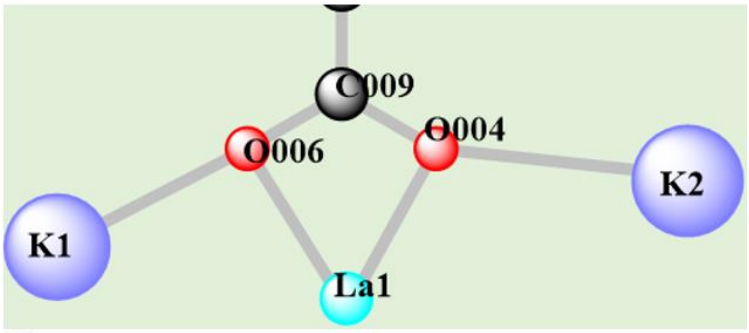
The comparison of coordination modes of bimetallic MOF, LaKBDC and monometallic, LaBDC MOF was examined from the literature.[25,26] For LaBDC MOFs synthesized without a second metal, such as an alkali metal, more than one coordination mode exists in some Lanthanum-based MOFs. For instance, Just like in LaKBDC MOF, where we have reported two distinct BDC ligand carboxylate coordination modes, Gil-Mateo and co-workers[25] reported a pure LaBDC MOF, $La_2(BDC)_3(H_2O)_4$, where BDC coordination mode acted as both bidentate chelate and bidentate bridging ligand. In

the same article, another pure LaBDC MOF, $La_3BDC_2(OH)_5$, exhibited the lanthanum atoms having two distinctive coordination environments: bidentate bridging and bidentate chelating mode. Furthermore, Chule and coworker[26] reported the construction of another Lanthanum-based MOF, [La(1,4-BDC)(H_2O)].(H_2O) which displayed three coordination sites of 1,4-BDC namely monodentate-, bidentate chelating- and bidentate bridging modes which are involved in bonding with La(III) ions.

However, it must be noted that the study of the coordination mode adopted by the BDC carboxylates, -COO- in ZnKBDC and ZnLiBDC MOFs was only bridging without any chelation observed. Therefore, in ZnKBDC MOF (Figure 5.15b), the BDC ligands acted as a tridentate bridging agent (syn, syn, anti; μ_3-η^1:η^2) binding two K (K002) and one Zn (Zn01) at the SBU whereas in ZnLiBDC the ligand binds Zn (Zn01 and Zn02) and Li (LiH and LiF) cations in the bis bidentate bridging (syn -syn, μ_2-η^1:η^1) mode (Figure 5.15c).



(a)



(b)

Figure 5.16: The coordination modes of benzene-1,4-dicarboxylic acid (BDC) in the La/K core in LaKBDC MOF (a) The heptadentate bridging/chelating mode, anti, syn, anti μ_7-η^3:η^2:η^2 (b) tetradentate bridging/chelating mode.

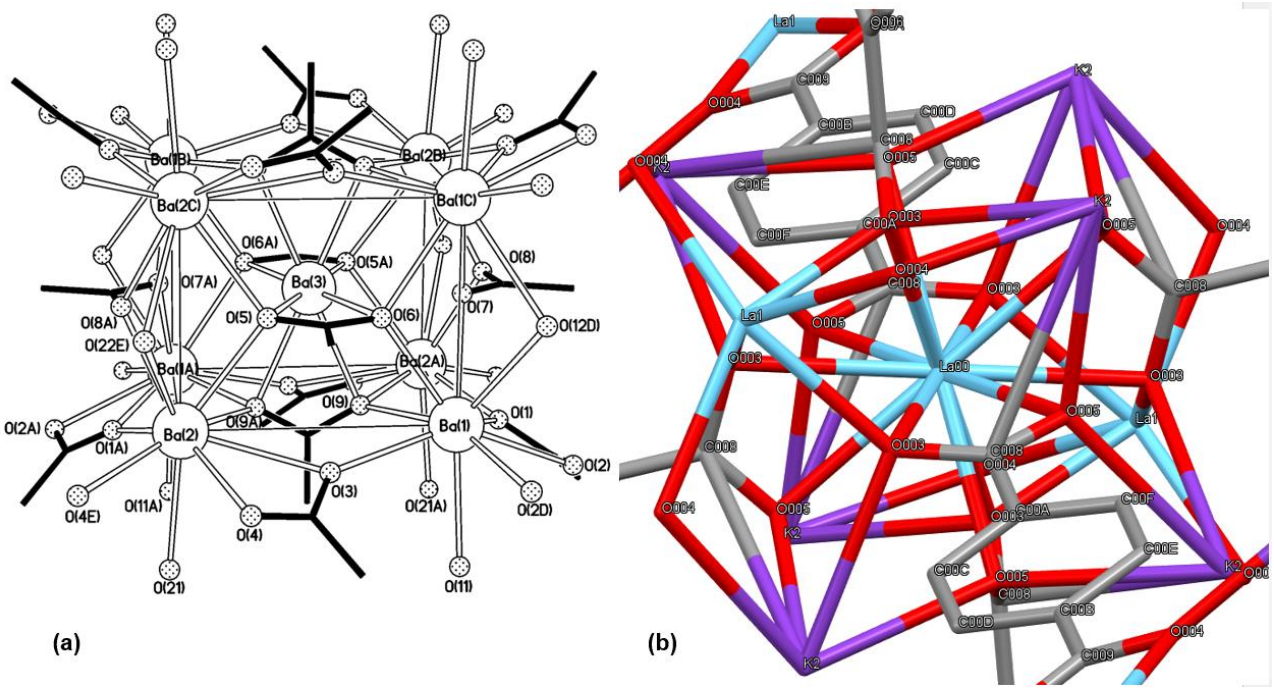


Figure 5.17: (a) The coordination geometries of the three kinds of barium atom in the Ba_9 core, acetate ions display a novel hexadentate μ_5-η^3:η^3 -bridging / chelating coordination mode [23,24] (b) The distorted binuclear $[La_3K_6(COO)_6]$ motif showing heptadentate bridging/chelating mode, μ_7-η^3:η^2:η^2 carboxylate anion, -COO- in LaKBDC MOF.

5.4 Conclusion

In conclusion, all attempts to synthesize LaLiBDC, LaLiNDC, LaLiBTB, LaKNDC and LaKBTB MOFs by several of our methods failed at various stages of characterization. The Lanthanum / Alkali Metal-organic framework, LaKBDC MOF, made of Lanthanum ion, Potassium metal ion and benzene-1,4-dicarboxylic acid (BDC) ligand, was synthesized using solvothermal methods at temperatures 120 °C and 170 °C. The characterization of LaKBDC was also investigated as well. According to the FTIR results, the dicarboxylic acid functional groups (−COOH) were completely deprotonated due to the absence of the absorption band in the region of 1700 cm^{-1}. In addition, the characterization of the MOFs using XRD, TGA, SEM, and EDS affirmed the formation of the mixed–metal MOFs in this research. LaKBDC MOF crystallized in the cubic system, space group Ia-3. La(III) cations adopted octahedral and cuboctahedron, while K (with a coordination number of 5)adopted a distorted square pyramidal coordination geometry within the MM-MOF. As observed in many lanthanide

complexes, the Lanthanum achieved high coordination up to 12.[19,20.] The carboxylates, -COO- in LaKBDC MOF, display two different coordination modes, namely the heptadentate chelating/bridging, μ_7-η^3:η^2:η^2 and tetradentate chelating/bridging coordination, μ_4-η^1:η^2:η^1. The isosteric heat for CO_2 on LaKBDC shows that carbon dioxide adsorption (CO_2) on LaKBDC exhibits a decreasing trend with higher uptake (thus higher pressure), common to all potassium-based MOFs studied. Selectivity studies show LaKBDC showed similar selectivity for CO_2/N_2 and CO_2/H_2 around 13.9 while displaying higher selectivity for CO_2/CH_4, thus predicting its useful separation potential for CO_2/CH_4.

5.5 References

1. R. Plessius, R. Kromhout, A. L. D. Ramos, M. Ferbinteanu, M. C. Mittelmeijer-Hazeleger, R. Krishna, G. Rothenberg and S. Tanase, *Chem. – Eur. J.*, 2014, **20**, 7922–7925.

2. N. H. Batubara and A. Zulys, *IOP Conf. Series: Mater. Sci. Eng.,* 2019, **546**, 042005.

3. S. M. Ginting, D. Handayani, R. Elvia, I. D. Lestari and U. Rosidah, NITRIC 2022, *AHCPS*, 2023, **4**, pp. 97–106. Available at: https://doi.org/10.2991/978-94-6463-130-2_12, Accessed 18 July 2023.

4. D. L. Long, A J. Blake, N. R. Champness, C. Wilson and M. Schröder, *J. Am. Chem. Soc*., 2001, **123**, 3401–2.

5. S. M. Prabhu, S. Imamura and K. Sasaki*, ACS Sustainable Chem. Eng*., 2019, **7**, 6917−6928.

6. X. Zhang, F. Sun, J. He, H. Xu, F. Cui and W. Wang, *Chem. Eng*., J. 2017, **326**, 1086−1094.

7. M. S. M. Abdelbaky, Z. Amghouz, S. García-Granda and J. R. García, *Polymers*., 2016, **8**(3):86. Available at: https://doi.org/10.3390/polym8030086, Accessed 16 July 2023.

8. Y. Zhang, Y. J. Li, S. Z. Guo, T. Fu and L. Zhao, *Transit Met Chem.*, 2020, **45**, 485–492.

9. G. E. Kostakis, G. Abbas, C.E. Anson and A.K. Powell, *CrystEngComm.*, 2008, **10**, 1117–1119.

10. S. Nayak, G. Kostakis, C.E. Anson and A.K. Powell, *CrystEngComm*, 2010, **12** 3008– 3011.

11. A. Jeyaseelan and N. Viswanathan, *J. Chem. Eng. Data*, 2020, **65**, 5328−5340.

12. H. Li, K. Wang, Y. Sun, C. T. Lollar, J. Li and H. Zhou, *Mater. Today*, 2018, vol. **21**, 2, pp. 108–121.

13. M. Safnejad, A. Rigi, M. Zeraati, Z. Heidary, S. Jahani, N. P. S. Chauhan and G. Sargazi, *BMC Chemistry*, 2022, **16**, 93, 1-9.

14. N. Riezzati, Y. K. Krisnandi and A. Zulys., *IOP Conf. Ser.: Mater. Sci. Eng.,* 2020, **902**, 012044.

15. A. L. Myers and J. M. Prausnitz, *AIChE J.,* 1965, **11**, 121–130.

16. X. Zhang, Z. Chen, X. Yang, M. Li, C. Chen and N. Zhang, *Microporous and Mesoporous Mater.*, 2018, **258**, 55 – 61.

17. S. Yang, Jun Kima and W. Ahn, *Microporous and Mesoporous Mater.*, 2010, **135**, 90–94.

18. D. Saha, Z. Bao, F. Jia and S. Deng, *Environ. Sci. Technol*., 2010, **44**, 5, 1820–1826.

19. S.A. Cotton, *C. R. Chimie,* 2005, **8**, 129–145.

20. G. C. Dugoni, M. Mori, V. Dichiarante, A. Sacchetti and F. Meneghetti, *J. Mol. Struct.,* 2022, **1265**, 133398.

21. S. Wang, Z. Ma, X. Du, S. Zhang and Z. Chen, *Mater. Express*, 2018, **8**(4), 381-387.

22. P. M. Thabede, N. D. Shooto and S. J. Modise, *Dig. J. Nanomater. Bios.,* 2023, **18**(1), 157 – 163.

23. J. Goura and V. Chandrasekhar, *Chem. Rev.* 2015, **115**, 6854−69.

24. G. Dong, Z. Bing-guang, D. Chun-ying, P. Ke-liang and M. Qing-jin, *J. Chem. Soc., Dalton Trans*., 2002, 3783–3784.

25. P. Gil-Mateo, X. Wang and A. J. Jacobson, *MRS Online Proceedings Library,* 2008, **1148**, 802.

26. S. Chule and S. Jonnalagadda, *Preprints*, 2018, 2018110244.

Chapter 6: Conclusions and Future Directions

In this work, a comprehensive study on the synthesis, characterization and application of ZnKBDC, ZnKNDC, ZnKBTB, ZnLiBDC, ZnLiNDC, ZnLiBTB and LaKBDC MOF for the adsorption of CO_2, N_2, CH_4 and H_2 at 77 ^oC, 273 ^oC and 298 ^oC conditions have been investigated. The MM-MOFs have successfully been synthesized and characterized by XRD, PXRD, FT-IR, TGA and BET techniques.

In this study, several attempts to synthesize Zinc/Alkali metal-organic frameworks yielded materials with very interesting properties. Attempts at synthesising some other combinations, such as Cu/K, Ni/K, Cr/K, Co/K, Co/Li, Ni/Li, Cu/K, Cd/K and Zn/Na, failed during the research. Therefore, a series of novel mixed metal–organic frameworks (MM-MOFs) ZnKMOFs and ZnLiMOFs were synthesized from a combination of Lithium (Li) or Potassium (K) with Zinc (Zn) as inorganic metal nodes and three organic linker molecules 1,3,5-tris(4-carboxyphenyl)benzene (BTB), benzene-1,4-dicarboxylic acid (terephthalic acid, BDC), 2,6-naphthalenedicarboxylic acid (NDC) using solvothermal methods at temperatures 120 °C and 170 °C which produced related MOFs. All MOFs described are stable up to 350 °C. FTIR results showed no vibrational modes at 1690-1730 $cm^{-1,}$ confirming complete deprotonation of the dicarboxylic functional group and the formation of ZnKMOFs and ZnLiMOFs. All Li/Zn in all ZnLiMOFs systems synthesised adopted distorted tetrahedral coordination with bond distances in agreement with published literature. However, in ZnKMOF systems, Zn mostly adopted tetrahedral coordination except in ZnKNDC MOF, where the second Zn ion (at the metal centre) possesses a coordination number of 6 (an octahedral coordination). The potassium K ion displayed varied coordination up to 8 in a trigonal pyramidal, pentagonal pyramidal, distorted square antiprismatic coordination geometry. SEM/EDX revealed the composition of Zn, K, O, and C atoms within MM-MOFs.

In line with our aims and objectives, we performed various gas adsorption experiments and the adsorptive performance of the synthesized Zinc/Alkali-metal organic frameworks were performed.[1,2] The interesting study describes the potential future application of our MOFs as adsorptive materials. ZnKBTB MOF exhibits a straightforward type 1 isotherm for N_2 and H_2, indicating microporosity (width < 2nm) with a BET surface area around 200 $m^2 g^{-1}$ and pore volume ~ 0.17 cm^3. While

ZnKBTB and ZnLiBTB displayed strong CO_2 adsorption capacity depicted by a concave curve at all temperature and relative pressure ranges, ZnKBDC and ZnKNDC MOFs displayed linear adsorption profiles associated with Type III Isotherm indicating non-porosity for the adsorption of H_2, N_2 and CH_4 gases at both 273K and 298K. Interestingly, ZnKBDC and ZnKNDC MOFs showed minimal Type I adsorption (described by a lower concave curve) at 77 K.

We then deduced that the adsorption in this experiment is dependent on the ligand employed and that there is a high probability that the K and Li ions may be blocking the pore channels, thus resulting in low apparent BET surface area compared to some reported MOFs (without alkali metals within their frameworks) where higher apparent surface areas were reported (for instance, MOF-5, MOF-177). The study of the trend in CO_2/N_2 selectivity shows that the higher the CO_2 adsorption capacity in both ZnKBTB and ZnLiBTB MOFs, the lower the CO_2/N_2 selectivity because ZnLiBTB possesses higher CO_2/N_2 selectivity of 32.32 in comparison to ZnKBTB (24.13 at 800 mmHg at 298 K). Therefore, the adsorption capacity for CO_2 increased in the order of $K^+>Li^+$. The heat of adsorption, $Q_{st,}$ falls in a range of 30.83 to 19.85 kJ/mol at high loading conditions (ZnKBTB; 34.38 - 30.83 $kJmol^{-1}$ and ZnLiBTB; 29.17 $kJmol^{-1}$ – 19.85 $kJmol^{-1}$). Thus, our MOFs exhibit features favouring high loading of CO_2 at low pressure and high heat of adsorptions, which are comparable to values attained by MOFs having open metal sites. A comparative study between our MOFs and alkali metal-based MOFs, M-UTSA and M-BEA synthesised by Yang et al.[3] and Zhang et al.[4] showed the same trend in CO_2 adsorption, IAST selectivity studies as well as trend in Isosteric heat of adsorption. It is worthy of note and exciting that our MOFs ZnKBTB and ZnLiBTB show similar trends in all the properties described above.[5-8]

In Conclusion, this study examined the synthesis, characterization, and gas adsorption performance of the Lanthanum/Alkali metal-organic framework, LaKBDC. The LaKBDC MOF made of carboxylate linker, namely benzene-1,4-dicarboxylic acid (terephthalic acid, BDC), was synthesized using solvothermal methods at 120 °C and 170 °C. The two coordination modes exhibited by BDC ligand carboxylates, -COO- in LaKBDC MOF were heptadentate chelating/bridging, μ_7-η^3:η^2:η^2 and tetradentate chelating/bridging coordination (μ_4-η^1:η^2:η^1) modes. In this study, Lanthanum achieved a high coordination number up to 12, which is common to lanthanide complexes.[9] The coordination environment of La(III) and K ion showed that lanthanum ion possesses a

coordination number of 6 and 12 in octahedral and cuboctahedron coordination, respectively. Potassium ion K adopted a distorted square pyramidal coordination. Interestingly, the isosteric heat of adsorption for CO_2 by LaKBDC exhibits a decreasing trend with higher uptake. LaKBDC MOF exhibited similar selectivity for CO_2/N_2 and CO_2/H_2 but recorded a higher selectivity for CO_2/CH_4, indicating its potential separation for CO_2/CH_4 mixture.[10]

Future Development: This research work may give way for research interest in the following:

1. Computational and simulation studies to allow the development of potential MOF adsorbents.
2. Electrochemical applications of Metal/Alkali metal and lanthanides/alkali metal-organic frameworks.
3. Application of metal/alkali metal and lanthanides/alkali metal-organic frameworks as heterogenous catalysts in organic synthesis.
4. Synthesis of mixed metal-organic frameworks (MOF) Gel and Monoliths.
5. Further characterization and application of synthesized MM-MOFs: ZnKBDC, ZnKNDC, ZnKBTB, ZnLiBTB, ZnLiNDC, ZnLiBDC and LaKBDC MOF.
6. Synthesis, characterisation and application studies of possible lanthanides / alkali-metal organic frameworks. Exploring possibilities of constructing MM-MOF from lanthanides such as lanthanum (La), cerium (Ce), praseodymium (Pr), neodymium (Nd), promethium (Pm), samarium (Sm), europium (Eu), gadolinium (Gd), terbium (Tb), dysprosium (Dy), holmium (Ho), erbium (Er), thulium (Tm), ytterbium (Yb), and lutetium (Lu).

6.1 References

1 M.A. Gotthardt, R. Schoch, S. Wolf, M. Bauer and W. Kleist, *Dalton Trans*. 2015, **44**, 2052–2056.

2. P.S. Sagara, V. Varma and J.K. Randhawa, *ChemPlusChem*, 2019, **84**, 136–141.

3. S. Yang, Jun Kima and W. Ahn, *Microporous and Mesoporous Mater.,* 2010, **135**, 90–94.

4. X. Zhang, Z. Chen, X. Yang, M. Li, C. Chen and N. Zhang, *Microporous and Mesoporous Mater.,* 2018, **258**, 55 – 61.

5. Lei, Y. Cheng, C. Chen, M. Kosari, Z. Jiang and C. He, *J. Colloid Interface Sci.*, 2022, **612**, 132–145.

6. D. Saha, Z. Bao, F. Jia and S. Deng, *Environ. Sci. Technol*., 2010, **44**, 1820–1826.

7. Z. Li, P. Liu, C. Ou, and X. Dong, *ACS Sustainable Chem. Eng.*, 2020, **8**, 15378−15404.

8. N.A. Dogan, E. Ozdemir and C.T. Yavuz, *ChemSusChem.,* **2017**, **10** (10), 2130–2134.

9. S.A. Cotton, *C. R. Chimie,* 2005, **8**, 129–145.

10. L. S. Blankenship and R. Mokaya, *Mater. Adv.,* 2022, **3,** 1905–1930.

Appendix

Appendix I Crystallographic information for ZnKBDC

Table of Bond Lengths around Zn(II) in ZnKBDC

Atom	Atom	Length/Å	Atom	Atom	Length/Å
Zn1	K1	3.6687(12)	K1	K1^{3}	4.240(2)
Zn1	K1^{1}	3.9177(11)	K1	O2^{6}	2.828(4)
Zn1	K1^{2}	3.9177(11)	K1	O4^{7}	2.686(4)
Zn1	K1^{3}	3.6687(12)	K1	O3^{4}	2.880(4)
Zn1	O2	1.958(4)	K1	O3^{5}	3.103(4)
Zn1	O2^{3}	1.958(4)	K1	O1	2.598(4)
Zn1	O3^{4}	1.994(4)	K1	O5	2.710(4)
Zn1	O3^{5}	1.994(4)	K1	C8	3.381(15)
K1	C9^{2}	3.346(14)			

Table of Bond Angles around Zn(II) and K in ZnKBDC

Atom	Atom	Atom	Angle/˚	Atom	Atom	Atom	Angle/˚
K1^{1}	Zn1	K1	70.59(4)	O5	K1	O3^{5}	75.12(12)
K1^{1}	Zn1	K1^{2}	103.688(7)	O5	K1	O3^{4}	78.97(12)
K1^{3}	Zn1	K1^{2}	109.72(4)	O5	K1	C8	21.5(2)
K1^{1}	Zn1	K1^{3}	134.656(15)	O5	K1	C9^{3}	120.4(3)
K1	Zn1	K1^{3}	103.689(7)	C8	K1	Zn1^{6}	85.1(2)
K1	Zn1	K1^{2}	134.656(15)	C8	K1	Zn1	113.9(2)
O2^{1}	Zn1	K1^{1}	90.16(11)	C8	K1	K1^{1}	59.5(2)

O2	Zn1	K1[1]	159.98(11)	C9[3]	K1	Zn1	78.4(2)
O2[1]	Zn1	K1	159.98(11)	C9[3]	K1	Zn1[6]	94.4(2)
O2	Zn1	K1	90.16(11)	C9[3]	K1	K1[1]	106.7(2)
O2[1]	Zn1	K1[2]	43.20(10)	C9[3]	K1	C8	128.0(4)
O2[1]	Zn1	K1[3]	93.69(11)	Zn1	O2	K1[3]	108.51(14)
O2	Zn1	K1[2]	93.69(11)	C1	O2	Zn1	115.0(3)
O2	Zn1	K1[3]	43.20(10)	C1	O2	K1[3]	121.1(3)
O2[1]	Zn1	O2	109.5(2)	C00E	O4	K1[8]	136.3(3)
O2[1]	Zn1	O3[4]	113.90(15)	Zn1[9]	O3	K1[10]	95.96(14)
O2	Zn1	O3[4]	114.47(15)	Zn1[9]	O3	K1[9]	89.34(12)
O2	Zn1	O3[5]	113.90(15)	K1[10]	O3	K1[9]	90.17(11)
O2[1]	Zn1	O3[5]	114.47(15)	C00E	O3	Zn1[9]	110.7(3)
O3[4]	Zn1	K1[3]	151.00(12)	C00E	O3	K1[9]	135.2(3)
O3[4]	Zn1	K1[2]	86.70(11)	C00E	O3	K1[10]	124.9(3)
O3[4]	Zn1	K1[1]	57.75(11)	C1	O1	K1	146.1(4)
O3[4]	Zn1	K1	51.33(11)	K1	O5	K1[1]	102.9(2)
O3[5]	Zn1	K1[1]	51.33(11)	C8	O5	K1	109.4(5)
O3[5]	Zn1	K1	57.75(11)	C8	O5	K1[1]	144.3(5)
O3[5]	Zn1	K1[2]	151.00(12)	C8[1]	O5	K1[1]	109.4(5)
O3[5]	Zn1	K1[3]	86.70(11)	C8[1]	O5	K1	144.3(5)
O3[5]	Zn1	O3[4]	89.6(2)	O2[6]	K1	C9[3]	113.2(2)
O2[6]	K1	Zn1	139.82(8)	O4[7]	K1	Zn1[6]	45.73(8)
O2[6]	K1	Zn1[6]	28.29(7)	O4[7]	K1	Zn1	144.27(8)

O2[6]	K1	K1[1]	139.54(9)	O4[7]	K1	K1[1]	113.21(8)
O2[6]	K1	O3[5]	172.49(11)	O4[7]	K1	O2[6]	73.23(10)
O2[6]	K1	O3[4]	119.20(11)	O4[7]	K1	O3[5]	113.22(11)
O2[6]	K1	C8	89.7(2)	O4[7]	K1	O3[4]	160.14(12)

Appendix II Crystallographic information for ZnKNDC

Table of Bond lengths around Zn(II) and K in ZnKNDC

Atom	Atom	Length/Å	Atom	Atom	Length/Å
Zn01	Zn02	3.1316(4)	Zn02	O005	1.989(2)
Zn01	Zn02[1]	3.1316(4)	Zn02	O006	1.951(2)
Zn01	K003[1]	3.9296(7)	Zn02	O009	1.964(2)
Zn01	K003	3.9296(7)	K003	K003[2]	3.8653(15)
Zn01	O004[1]	1.970(2)	K003	O004	2.673(2)
Zn01	O004	1.970(2)	K003	O005[2]	2.859(2)
Zn01	O008[1]	2.142(2)	K003	O007	2.776(2)
Zn01	O008	2.142(2)	K003	O007[2]	2.711(2)
Zn01	O00A	2.230(2)	K003	O00A	3.071(2)
Zn01	O00A	2.230(2)	K003	O00B	2.684(3)
Zn02	K003	3.6119(9)	K003	C00F[1]	3.314(3)
Zn02	O004	1.913(2)	K003	C00V	3.532(5)

Table of Bond Angles around Zn(II) and K in ZnKNDC

Atom	Atom	Atom	Angle/^{0}	Atom	Atom	Atom	Angle/^{0}
Zn021	Zn01	Zn02	179.999(11)	O004	K003	O0052	157.03(7)
Zn021	Zn01	K003	119.722(14)	O004	K003	O007	76.99(7)
Zn02	Zn01	K003	60.277(13)	O004	K003	O0072	112.48(7)
Zn02	Zn01	K0031	119.722(13)	O004	K003	O00A1	60.05(6)
O004	Zn01	O0041	180.0	O004	K003	O00B	69.45(9)
O004	Zn01	O0081	88.43(9)	O004	K003	C00F1	110.17(8)
O0041	Zn01	O008	88.43(9)	O004	K003	C00V	76.86(9)
O0041	Zn01	O0081	91.57(9)	O0052	K003	Zn01	163.09(5)
O004	Zn01	O008	91.57(9)	O0052	K003	Zn02	127.17(5)
O0041	Zn01	O00A1	93.09(9)	O0052	K003	K0032	67.15(5)
O004	Zn01	O00A	93.09(9)	O0052	K003	O00A1	140.22(7)
O0041	Zn01	O00A	86.91(9)	O0052	K003	C00F1	92.60(8)
O004	Zn01	O00A1	86.91(9)	O007	K003	O0052	80.04(7)

Appendix III Crystallographic information for ZnKBTB MOF

Table of Bond lengths around Zn(II) and K in ZnKBTB

Atom	Atom	Length/Å	Atom	Atom	Length/Å
Zn01	K002	3.719(2)	K002	O008	2.647(7)
Zn01	O003[1]	1.952(6)	K002	O014[2]	2.639(13)
Zn01	O004	1.926(6)	K002	O017	2.79(4)
Zn01	O006[2]	1.936(6)	K002	O1	2.588(13)
Zn01	N00P	2.053(12)	K002	O1A	2.696(12)
K002	O003[1]	2.723(6)	K002	O0[2]	2.864(18)
K002	O005[3]	2.648(7)			

Table of Bond Angles around Zn(II) and K in ZnKBTB

Atom	Atom	Atom	Angle/^{0}	Atom	Atom	Atom	Angle/^{0}
O003^1	Zn01	K002	45.22(16)	O005^3	K002	Zn01	128.60(14)
O003^1	Zn01	N00P	118.0(4)	O005^3	K002	O003^1	158.88(19)
O004	Zn01	K002	88.9(2)	O005^3	K002	O017	82.1(8)
O004	Zn01	O003^1	117.6(3)	O005^3	K002	O1A	87.1(3)
O004	Zn01	O006^2	108.6(3)	O005^3	K002	O0^2	106.3(5)
O004	Zn01	N00P	100.0(4)	O008	K002	Zn01	109.37(18)
O006^2	Zn01	K002	88.7(2)	O008	K002	O003^1	92.6(2)
O006^2	Zn01	O003^1	109.3(3)	O008	K002	O005^3	95.5(2)
O003^1	K002	O017	113.5(8)	O008	K002	O017	109.4(8)
O003^1	K002	O0^2	67.0(4)				

Appendix IV Crystallographic information for ZnLiBDC MOF

Table of Bond lengths around Zn(II) and Li ion in ZnLiBDC

Atom	Atom	Length/Å	Atom	Atom	Length/Å
Zn01	O00A[1]	1.941(6)	Zn02	Li1F	3.183(12)
Zn01	O00C	1.938(5)	O008	Li1H	1.901(13)
Zn01	O005	1.926(5)	O009	Li1F	1.926(13)
Zn01	N00G	2.086(7)	O00B	Li1H	1.892(12)
Zn01	Li1H	3.247(16)	O00E	Li1H[3]	1.953(13)
Zn02	O00D	1.933(6)	O00F	Li1F	1.865(11)
Zn02	O003	1.926(5)	O00H	Li1H	1.858(17)
Zn02	O006[2]	1.947(5)	O004	Li1F	1.896(10)
Zn02	N00I	2.047(8)	O007	Li1F[4]	1.929(11)

Table of Bond Angles around Zn(II) and K in ZnLiBDC

Atom	Atom	Atom	Angle/^{0}	Atom	Atom	Atom	Angle/^{0}
O00A^1	Zn01	N00G	100.0(3)	O01L	N00G	Zn01	103.1(10)
O00A^1	Zn01	Li1H	74.3(3)	O01R	N00G	Zn01	107.6(8)
O00C	Zn01	O00A^1	114.5(3)	O02B	N00G	Zn01	110.5(8)
O00C	Zn01	N00G	101.7(3)	O1	N00I	Zn02	111.5(12)
O00C	Zn01	Li1H	79.9(3)	O4	N00I	Zn02	115.4(10)
O005	Zn01	O00A^1	120.0(3)	O6	N00I	Zn02	115.2(10)
O005	Zn01	O00C	115.3(2)	O00F	Li1F	Zn02	70.3(4)
O005	Zn01	N00G	100.6(3)	O00F	Li1F	O004	110.2(6)
O005	Zn01	Li1H	83.7(2)	O00F	Li1F	O007^2	110.6(5)
N00G	Zn01	Li1H	174.1(3)	O00F	Li1F	O009	105.1(5)
O00D	Zn02	O006^2	115.0(2)	O004	Li1F	Zn02	71.1(4)
O00D	Zn02	N00I	101.7(3)	O004	Li1F	O007^2	109.7(5)
O00D	Zn02	Li1F	79.5(3)	O004	Li1F	O009	107.4(5)
O003	Zn02	O00D	116.1(2)	O007^2	Li1F	Zn02	72.4(4)
O003	Zn02	O006^2	118.0(2)	O009	Li1F	Zn02	173.7(5)
O003	Zn02	N00I	102.2(3)	O009	Li1F	O007^2	113.7(6)
O003	Zn02	Li1F	79.2(2)	O00B	Li1H	Zn01	64.0(5)

O006[2]	Zn02	N00I	99.5(3)	O00B	Li1H	O00E[1]	109.9(7)
O006[2]	Zn02	Li1F	78.0(3)	O00B	Li1H	O008	108.7(7)
N00I	Zn02	Li1F	177.5(3)	O00E[1]	Li1H	Zn01	75.5(5)
O00A[1]	Zn01	N00G	100.0(3)	O008	Li1H	O00E[1]	105.1(6)

Appendix V Crystallographic information for ZnLiNDC

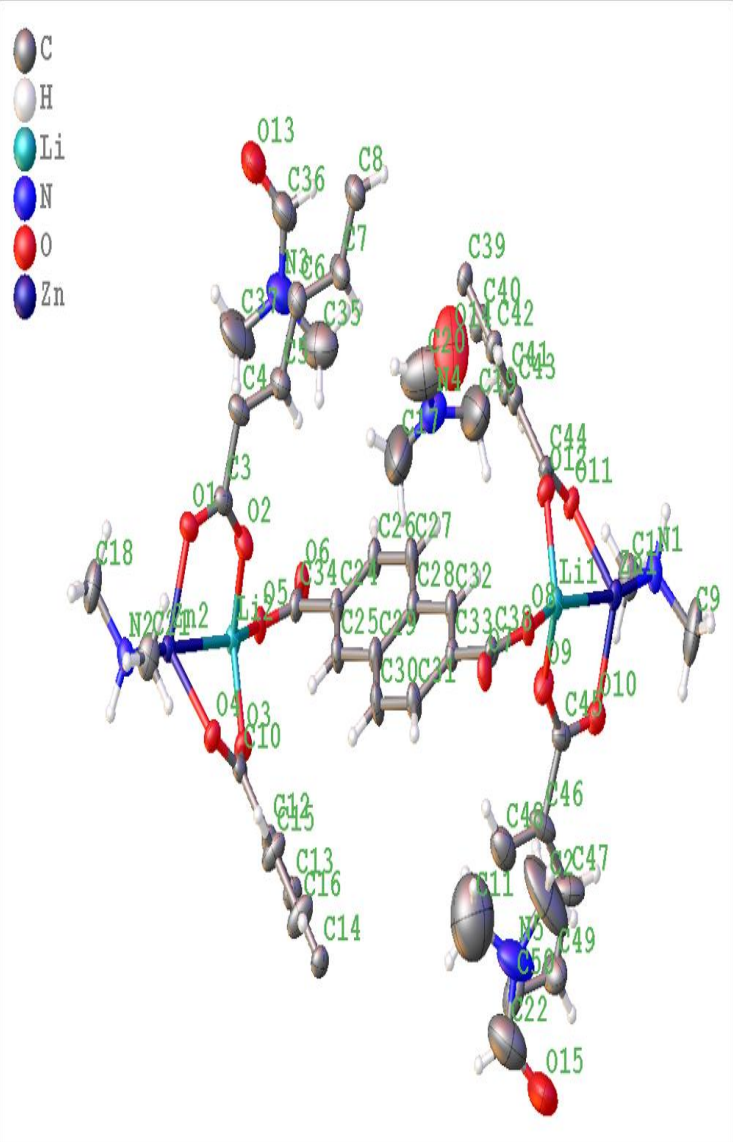


Table of Bond Lengths around Zn(II) and Li ion in ZnLiNDC

ATOM	ATOM	Length/Å	ATOM	ATOM	Length/Å
Zn1	O003	1.949(2)	O004	Li1	1.919(5)
Zn1	O008	1.968(2)	O004	Li2[1]	1.972(5)
Zn1	O00B[1]	1.962(2)	O005	Li1[2]	1.949(5)
Zn1	N1	2.048(3)	O005	Li2	1.935(5)
Zn1	Li1	3.113(5)	O00A	Li1	1.889(5)
Zn2	O9	1.942(2)	O11	Li2	1.897(5)
Zn2	O007[2]	1.960(2)	O2	Li2	1.885(5)
Zn2	O1	1.944(2)	O00E	Li1	1.873(5)
Zn2	N17	2.037(3)			
Zn2	Li2	3.141(5)			

Table of Bond Angles around Zn(II) and Li in ZnLiNDC

Atom	Atom	Atom	Angle/^{0}	Atom	Atom	Atom	Angle/^{0}
O007^{2}	Zn2	N17	100.56(10)	C00P	O005	Li1^{2}	130.3(2)
O007^{2}	Zn2	Li2	77.88(10)	C00P	O005	Li2	139.6(2)
O1	Zn2	O007^{2}	114.79(9)	Li2	O005	Li1^{2}	85.9(2)
O1	Zn2	N17	101.99(10)	C10	O9	Zn2	123.13(19)
O1	Zn2	Li2	79.56(11)	C00L	O007	Zn2^{1}	125.62(18)
N17	Zn2	Li2	178.19(12)	C00X	O008	Zn1	112.1(2)
C00N	O003	Zn1	125.23(18)	C3	O1	Zn2	121.6(2)
C00L	O004	Li1	139.9(2)	C00N	O00A	Li1	128.3(2)
C00L	O004	Li2^{1}	132.2(2)	C00P	O00B	Zn1^{2}	127.44(19)
Li1	O004	Li2^{1}	85.7(2)	C10	O11	Li2	133.8(3)
C3	O2	Li2	136.9(3)	C3	O2	Li2	136.9(3)
C00X	O00E	Li1	142.9(3)	C00X	O00E	Li1	142.9(3)
C21	N17	Zn2	112.7(2)	C21	N17	Zn2	112.7(2)
C18	N17	Zn2	111.0(2)	C18	N17	Zn2	111.0(2)
C18	N17	C21	110.8(3)	C18	N17	C21	110.8(3)
C1	N1	Zn1	111.3(2)	C1	N1	Zn1	111.3(2)
C1	N1	C9	110.3(3)	C1	N1	C9	110.3(3)
C9	N1	Zn1	113.2(2)	C9	N1	Zn1	113.2(2)
O004	Li1	Zn1	167.5(2)	O005^{1}	Li1	Li2^{1}	46.83(16)

O004	Li1	O005[1]	94.6(2)	O00A	Li1	Zn1	74.22(17)
O004	Li1	Li2[1]	48.00(16)	O00A	Li1	O004	117.3(3)
O005[1]	Li1	Zn1	75.16(16)	O00A	Li1	O005[1]	115.6(3)
O00A	Li1	Li2[1]	127.4(3)	O00E	Li1	O005[1]	108.5(3)
O00E	Li1	Zn1	63.27(16)	O00E	Li1	O00A	105.8(3)
O00E	Li1	O004	114.8(3)	O00E	Li1	Li2[1]	126.5(3)

Appendix VI Crystallographic information for LaKBDC

Table of Bond Lengths for LaKBDC

Atom	**Atom**	**Length/Å**	**Atom**	**Atom**	**Length/Å**
La00	O003[1]	2.669(3)	O004	K2[7]	2.947(5)
La00	O003[2]	2.669(3)	O005	K2[3]	2.841(5)
La00	O003[3]	2.669(3)	O005	K2[2]	2.946(5)
La00	O003[4]	2.669(3)	O006	La1[6]	2.543(3)
La00	O003[5]	2.669(3)	O006	K1	2.893(11)
La00	O003	2.669(3)	C008	K2[3]	3.345(6)
La00	O005	2.677(3)	C009	La1[6]	2.904(5)
La00	O005[2]	2.677(3)			
La00	O005[1]	2.677(3)			

La00	O005[3]	2.677(3)			
La00	O005[5]	2.677(3)			
La00	O005[4]	2.677(3)			
O003	La1	2.528(3)			
O003	K2	2.919(5)			
O004	C009	1.266(6)			
O004	La1[6]	2.552(3)			

Table of Bond Angles around La(III) and K in LaKBDC

Atom	Atom	Atom	Angle/˚		Atom	Atom	Atom	Angle/˚
O003[1]	La00	O003[2]	180.00(11)		C00F	C00A	C00C	120.3(4)
O003[3]	La00	O003[4]	115.11(10)		C00D	C00B	C009	119.5(4)
O003[3]	La00	O003	64.89(10)		C00E	C00B	C009	120.2(4)
O003[5]	La00	O003[4]	64.89(10)		C00E	C00B	C00D	120.3(4)
O003[2]	La00	O003	64.89(10)		C00D	C00C	C00A	119.6(4)
O003[5]	La00	O003	115.11(10)		C00C	C00D	C00B	120.2(4)
O003[1]	La00	O003[3]	115.11(10)		C00B	C00E	C00F	119.8(4)
O003[1]	La00	O003[5]	64.89(10)		C00A	C00F	C00E	119.8(4)
O003[2]	La00	O003[3]	64.89(10)		O003	La1	O003[3]	68.99(11)
O003[1]	La00	O003	115.11(10)		O003	La1	O003[2]	68.99(11)

O003^{5}	La00	O003^{3}	180.0		O003^{3}	La1	O003^{2}	68.99(11)
O003^{2}	La00	O003^{5}	115.11(10)		O003	La1	O004^{8}	72.67(11)
O003^{1}	La00	O003^{4}	64.89(10)		O003^{2}	La1	O004^{8}	135.97(11)
O003^{2}	La00	O003^{4}	115.11(10)		O003	La1	O004^{9}	77.76(10)
O003^{4}	La00	O003	180.0		O003^{2}	La1	O004^{9}	72.67(11)
O003^{4}	La00	O005^{3}	105.56(10)		O003^{2}	La1	O004^{10}	77.76(10)
O003^{3}	La00	O005^{4}	68.19(10)		O003^{3}	La1	O004^{8}	77.76(10)